UN/JP0003V2
*REV. 01*

# Propagation Effects Handbook for Satellite Systems Design

*Fifth Edition*

# Section 2
# Prediction

**Dr. Louis J. Ippolito**
**STANFORD TELECOM *ACS***
**45145 Research Place**
**Ashburn, Virginia 20147**

***prepared for***
**JPL**
**Jet Propulsion Laboratory**
**4800 Oak Grove Drive**
**Pasadena, CA 91109**

*February 1999*

STANFORD TELECOM®

# PREFACE

This Fifth Edition of the Propagation Effects Handbook for Satellite Systems Design continues the long process of a continuing NASA commitment to provide a comprehensive reference document which provides the latest information on atmospheric propagation effects and how they impact satellite communications system design and performance. The First Edition of the Handbook was published in March 1980, the Second Edition in December 1981, the Third Edition in June 1983, and the Fourth Edition in February 1989. I have been fortunate to have been involved with the Propagation Handbook project since its inception, and this Fifth Edition continues on with the process.

I would like to acknowledge the contributions of the many members of the staff at Stanford Telecom who helped with the development of this handbook. The contributions of Dr. Lynn Ailes, Glenn Feldhake, Dr. Frank Hastings, Chris Pearson, Jennifer Pinder, and John Weinfield are gratefully appreciated. The contributions of previous members of the staff, Jay Gibble, Julie Feil, and Chris Hofer are also acknowledged. The assistance of Ivy Cooper and Marian Montigny in the production of the handbook is also appreciated.

Louis J. Ippolito
Stanford Telecom
Ashburn, Virginia
October 1998

# PREFACE TO REVISION 1

This first revision, REV. 01, of the Fifth Edition of the Propagation Effects Handbook for Satellite Systems Design, incorporates the results of a peer review process on the original Fifth Edition, published in October 1998. Revisions consisted, for the most part, of misspellings, omissions and corrections to the original text and graphics. In addition, clarifications and further discussions were added where indicated in the peer review.

Section 1, Background, had revisions to 16 pages, out of the total of 119 pages. Section 2, Prediction, had revisions to 104 pages out of the total of 226 pages. Four missing exhibits were added to Section 2. The reference lists for both Sections have been completely updated and re-formatted. Corrected pages are indicated by an 'R1' in the file name on the right side of the page footer. Section 3, Applications, was not revised at this time.

I would like to thank the reviewers for their thoroughness and diligence in the review process. A special thanks goes to Dr. Ernest K. Smith for his excellent comprehensive review and comments. I also would like to acknowledge the contributions of Warren Flock, Ken Davies, and Glen Feldake to the review process.

Louis J. Ippolito
Stanford Telecom
Ashburn, Virginia
February 1999

# INTRODUCTION

## I.1 INTRODUCTION TO THE HANDBOOK

The Fifth Edition of the Propagation Effects Handbook for Satellite Systems Design provides, in one complete reference source, the latest information on atmospheric propagation effects and how they impact satellite communications system design and performance. The National Aeronautics and Space Administration, NASA, which has supported a large part of the experimental work in radiowave propagation on space communications links, recognized the need for a reference handbook of this type, and initiated a program in the late 1970's to develop and update a document that will meet this need. This Fifth Edition provides, in a single document, an update to two previous NASA handbooks; the fourth edition of a handbook which focused on propagation effects from 10 to 100 GHz (Ippolito, 1989), and the second edition of a companion handbook which covered propagation effects on satellite systems at frequencies below 10 GHz (Flock, 1987). This Fifth Edition covers the full range of radiowave frequencies that are in use or allocated for space communications and services, from nominally 100 MHz up to 100 GHz.

The basic intention of the Fifth Edition is to combine the scope of the previous handbooks into a single document, with elimination of duplication as much as possible. This Fifth Edition has a completely new outline, different from either of the two previous handbooks. The intent is to provide a more cohesive structure for the reader. The handbook incorporates a unique, new concept with several levels of "entrance" into the handbook.

Several major developments in satellite communications and the study of propagation effects have occurred since publication of the prior NASA handbooks. New propagation measurement campaigns have been completed or are in progress, providing new data for the evaluation of link degradations on satellite links. New propagation models and prediction techniques are available, covering the traditional propagation effects along with several new areas. New satellite applications have been thrust into the forefront of the satellite communications industry, requiring new approaches for the evaluation of propagation effects. The proliferation of new and competing applications in the frequency bands allocated to space communications has increased the importance and priority of understanding spectrum sharing and interference mitigation. Propagation conditions are a critical component of a viable sharing and interference process.

Section I.2 describes the handbook structure. Section I.3 describes how to apply the handbook for the most efficient use of the resource, depending on the readers' needs and level of interest.

## I.2 HANDBOOK STRUCTURE

The Propagation Effects Handbook for Satellite Systems Design, Fifth Edition, is divided into three sections. Section 1 provides the background, historical development, theory, and basic concepts of the propagation effects of concern to the satellite systems engineer. The prediction techniques developed to address the critical propagation effects are presented in Section 2. Information on how to apply the prediction methods for specific satellite systems applications is provided in Section 3.

**Section 1** begins with an overview of propagation effects on satellite communications. The propagation effects are then introduced and background theory and developments are described. The frequency dependence of radiowave propagation is recognized, and the effects are divided into two groups; ionospheric effects, influencing systems operating at frequencies below about 3 GHz, and tropospheric effects, influencing systems operating at frequencies above about 3 GHz. Radio noise, which can affect satellite systems in all operating bands, is then described. The section concludes with a comprehensive description of propagation databases, including points of contact and electronic addresses.

**Section 2** provides descriptions of prediction models and techniques for the evaluation of propagation degradation on satellite links. Step-by-step procedures are provided where available. The first two subsections present propagation effects for ionospheric effects and for tropospheric effects, respectively. The third subsection presents prediction methods for radio noise. The fourth subsection describes several general modeling procedures, including statistical considerations, frequency scaling and elevation angle scaling. The final subsection presents models for the restoration of links subject to propagation impairments, including site diversity, orbit diversity and adaptive FEC.

**Section 3** provides roadmaps for the application of the prediction models given in Section 2 to specific satellite systems and applications. Suggested approaches to evaluating link propagation effects and their impact on system design and performance are provided.

## I.3 HOW TO USE THE HANDBOOK

The Fifth Edition of the Propagation Effects Handbook for Satellite Systems Design is intended for the systems engineer and link designer who is interested in the latest and most accurate methodology available for the evaluation of radiowave propagation effects on satellite communications. The handbook is structured with several levels of "entrance" into the handbook, as highlighted by the chart below.

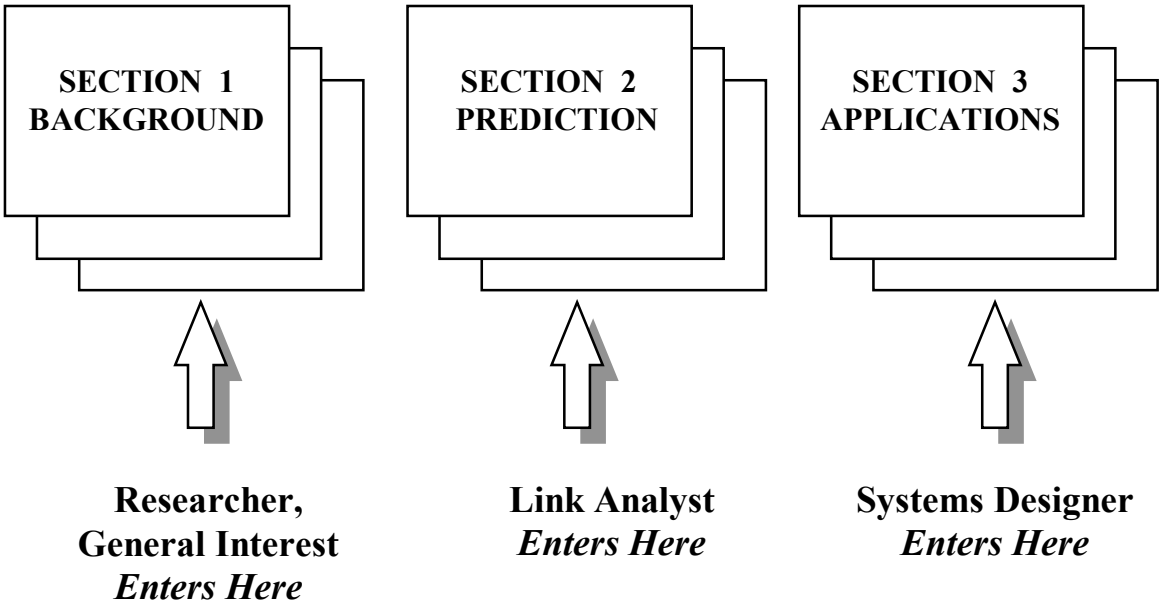


The general researcher or someone new to the subject who may not have a full awareness of the background and history of propagation effects and their impact on satellite communications could enter in Section 1, which provides an overview of propagation effects and the background theory involved in the prediction methodology. Section 1 also provides an extensive listing of resources for additional information and backup data important to the area of propagation effects and satellite communications.

The link analyst or engineer who is familiar with propagation and satellite communications issues and knows which propagation effects are of interest would enter into Section 2 where concise step-by-step procedures for each effect are available. Section 2 also includes general modeling procedures, including statistical considerations, frequency scaling and elevation angle scaling. Section 2, in addition, presents models for the restoration of links subject to propagation impairments, including site diversity, orbit diversity and adaptive FEC.

The system designer who has a good understanding of the system aspects of satellite communications but may not know just which propagation impairments are important to the particular system or application under consideration would enter through Section 3. Here the reader will find roadmaps for the application of the prediction models given in Section 2 to specific satellite systems and applications. Suggested approaches to evaluating link propagation effects and their impact on system design and performance are also provided in Section 3.

These entrance levels are only suggestions for the reader, to avoid unnecessary reading and to optimize the use of the handbook. Suggestions on ways to improve the document structure, or on specific additional information that would be useful to the reader to include in later editions of the handbook, are always welcome by the author.

# Propagation Effects Handbook for Satellite Systems Design

## Section 2 Prediction

***Table of Contents***

# SECTION 2
# PREDICTION

## 2. INTRODUCTION TO SECTION 2

The Propagation Effects Handbook for Satellite Systems Design, Fifth Edition, is divided into three sections. This section, Section 2, provides descriptions of prediction models and techniques for the evaluation of propagation degradation on satellite links. Step-by-step procedures are provided where available. Section 1 provides the background, historical development, theory, and basic concepts of the propagation effects of concern to the satellite systems engineer. The section includes theory and basic concepts, propagation measurements, and available databases. Information on how to apply the prediction methods for specific satellite systems applications is provided in Section 3.

The development of reliable propagation effects prediction models requires measured data to validate the predictions. New propagation measurements in several frequency bands have been accomplished since the last handbook publication. Exhibit 2.0-1 lists some of the satellites which had beacons on board specifically intended for the evaluation of propagation effects. Propagation data has also been developed from other sources including terrestrial links, tracking beacons, and from direct measurement of information bearing signals. For example, land mobile propagation data in the 1.5 GHz region was obtained in the Eastern U.S. from MARECS-B2 and in Australia from ETS-V and INMARSAT.

| Satellite | Organization | Launch Date | Frequency (GHz) | Polarization | Measurement Region(s) |
|---|---|---|---|---|---|
| Olympus | ESA | 1989 | 12.5<br>19.7<br>29.7 | LP<br>Dual Switched LP @933 Hz<br>LP | Europe<br>And<br>Eastern U.S. |
| Italsat F1 | Italy | 1991 | 18.685<br>39.592<br>49.49 | Dual LP<br>CP with ± 500 MHz sidebands<br>Dual switched LP @ 933 Hz | Europe |
| ACTS | NASA | 1993 | 20.185<br>27.5 | LP<br>LP | CONUS<br>Alaska<br>Canada |

Exhibit 2.0-1
Recent Satellites Providing Propagation Measurements

Propagation research since publication of the last handbooks has resulted in the development and publication of propagation prediction models in several new areas. These include:

- Tropospheric Scintillation
- Cloud Attenuation and Scintillation
- Ice Depolarization
- Wet Surface Effects
- Combined Effects

In addition, extensive modeling updates and revisions have been developed for the traditional propagation factors such as

- Rain Attenuation
- Atmospheric Gaseous Attenuation
- Ionospheric Scintillation
- Frequency Scaling
- Worst Month, and
- Site Diversity.

Section 2 provides detailed step-by-step procedures for all of the new models and for the updated procedures as provided by the authors.

The first two subsections of Section 2 present prediction methods for satellite links operating below 3 GHz (primarily ionospheric effects), and prediction methods for satellite links operating above 3 GHz (primarily tropospheric effects), respectively. The third subsection presents prediction methods for radio noise. The fourth subsection describes several general modeling procedures, including statistical considerations, frequency scaling and elevation angle scaling. The final subsection presents models for the restoration of links subject to propagation impairments, including site diversity, orbit diversity and adaptive FEC.

The principal topics and associated subsection numbers for Section 2 are listed below.

## 2.1 PREDICTION METHODS FOR SATELLITE LINKS OPERATING BELOW 3 GHZ

This section presents a compilation of analysis and prediction methods for the evaluation of propagation effects on earth-space links operating in the frequency bands below 3 GHz. The significant effects observed in the frequency bands below about 3 GHz occur primarily in the ionosphere. The ionosphere is the region of ionized gas or plasma that extends from roughly 50km to a not very well defined upper limit of about 500 km to 2000 km about the Earth's surface. The ionosphere is ionized by solar radiation in the ultraviolet and x-ray frequency range and contains free electrons and positive ions so as to be electrically neutral. Only a fraction of the molecules, mainly oxygen and nitrogen, are ionized, and large numbers of neutral molecules are also present. It is the free electrons that affect electromagnetic wave propagation for satellite communications.

The objective of Section 2.1 is to provide a concise summary of accepted prediction techniques that are available to the systems designer for the evaluation of propagation impairments that effect earth-space communications in the frequency bands below about 3 GHz. Detailed background information on the underlying ionospheric effects and their causes is provided in Section 1.2 of this handbook.

The prediction methods are grouped into three areas, reflecting ionospheric conditions and the interaction of the radiowave with the ionosphere:

- Effects Due to Background Ionization
  - Total Electron Content (Section 2.1.1)
  - Faraday Rotation (Section 2.1.2)
  - Group Delay (Section 2.1.3)
  - Dispersion (Section 2.1.4)
- Effects Due to Ionization Irregularities
  - Ionospheric Scintillation (2.1.5)
- Ionospheric Absorption
  - Auroral Absorption (2.1.6)
  - Polar Cap Absorption (2.1.7)

The complex nature of ionospheric physics and the interaction of communications system parameters affected by ionospheric effects listed above cannot always be succinctly summarized in simple closed form analytical models or prediction methods. In many cases the only recourse available to the systems engineer is to review limited measured data if available, and attempt to summarize the effects into ranges or bounds for the expected degradations. This section will point out those situations where a complete 'prediction' may not be available, and provide the best available measured data or analysis to allow for system performance assessments.

### 2.1.1 Total Electron Content

A number of ionospheric effects, including refraction, group delay, and dispersion are directly dependent on total electronic content, TEC. Faraday rotation is also approximately proportional to TEC, with the contributions from different parts of the ray path weighted by the longitudinal component of magnetic field. Therefore knowledge of the TEC is required before many important ionospheric effects can be estimated quantitatively estimated.

The TEC is determined by integration of the electron concentration along the propagation path,

$$TEC = \int_s n_e(s)\, ds \qquad (2.1.1\text{-}1)$$

where:

$n_e$ : electron concentration, in el/$m^3$.

s : propagation path, in m

The electron concentration varies as a function of altitude, geomagnetic latitude, diurnal cycle, yearly cycle, and solar activity (among others). Most U.S. ground station-satellite paths pass through the mid-latitude electron density region, which is the most homogeneous region. Representative plots of electron density distributions, at the extremes of the sunspot cycle, are shown in Exhibit 2.1.1-1.

Analytical expressions are not available for integration of the TEC, however, under conditions of low to moderate solar activity numerical techniques may be used to derive values for any location, time and chosen set of heights up to 1000 km.

For satellite path effects prediction, the TEC value is usually quoted for a zenith path having a cross-section of 1 $m^2$. The TEC of this vertical column can vary between $10^{16}$ and $10^{18}$ electrons/$m^2$, with the peak occurring during the sunlit portion of the day. For many purposes it is sufficient to estimate electron content by multiplication of the peak electron density with an equivalent slab thickness value of 300 km.

A recommended zenith path value to use for the determination of maximum typical values for satellite path effects is

$$TEC = \underline{1 \times 10^{18}} \text{ electrons/m}^2 \qquad \text{(zenith path)}$$

This estimate is based on a typical high value of TEC encountered at low latitudes in day-time with high solar activity.

Where instantaneous values are required, real-time data may be obtained, for example, using signals from the Global Positioning System (GPS).

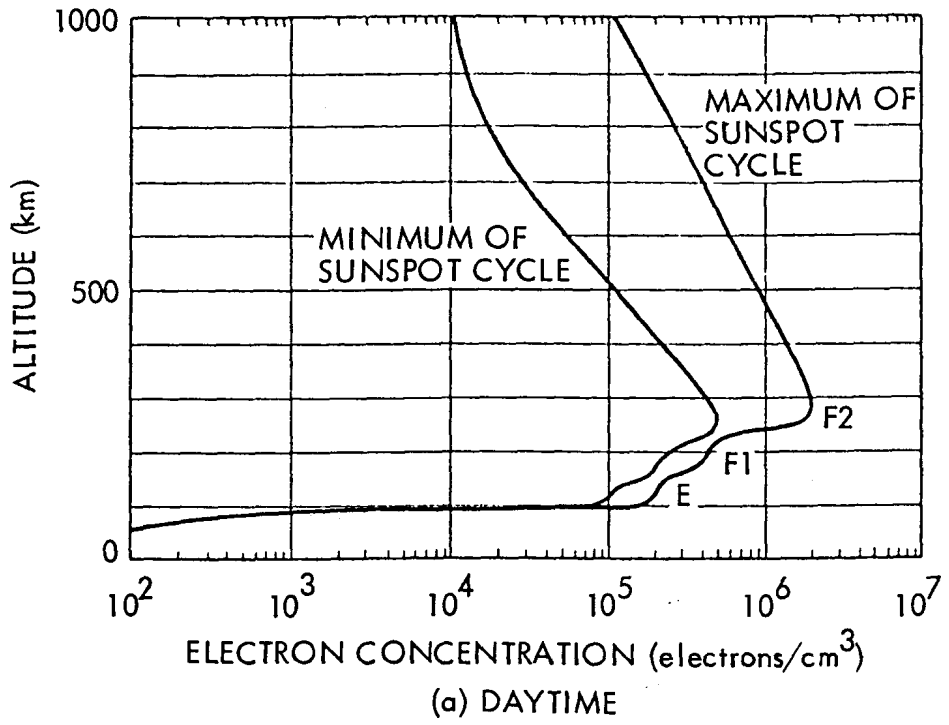


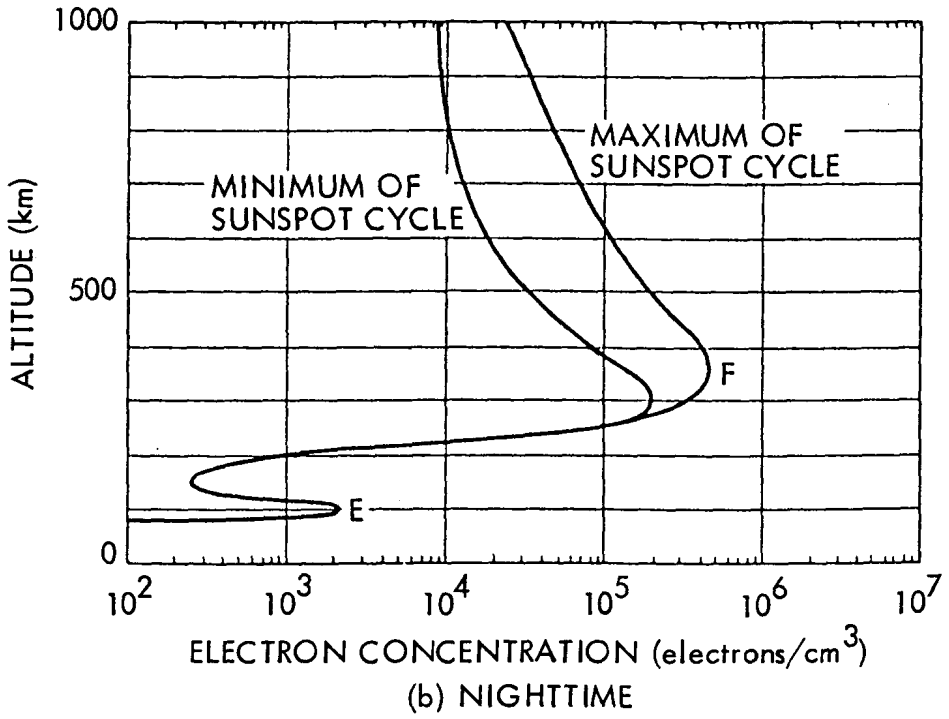


Exhibit 2.1.1-1
Electron density distribution at the extremes of the sunspot cycle (from Hanson, W.B., "Structures of the Ionosphere" in Johnson, F.S. (ed.), Satellite Environment Handbook, Stanford U. Press, 1965).
*[Source: Flock (1987), Fig 1.4]*

### 2.1.2 Faraday Rotation

Faraday Rotation is a rotation of the polarization sense of a radio wave, caused by the interaction of a radio wave with electrons in the ionosphere in the presence of the Earth's magnetic field. For satellite systems that employ circular polarization, Faraday rotation is not a concern; however, this condition can seriously affect VHF space communication systems that use linear polarization. A rotation of the plane of polarization occurs because the two rotating components of the wave progress through the ionosphere with different velocities of propagation.

The parameters required for the determination of Faraday rotation angle are:

f: frequency of operation, in GHz
TEC: total electron content, in electrons/$m^2$
$B_L$: average Earth magnetic field, in Wb/ $m^2$

The Faraday rotation angle $\phi$, in rad, is then estimated from,

$$\phi = \frac{2.36 \times 10^2}{f^2} B_L \ TEC \qquad (2.1.2\text{-}1)$$

Typical values of Faraday rotation as a function of ionospheric TEC and frequency, from 100 MHz to 10 GHz, for a northern mid latitude earth station viewing a geostationary satellite near the station meridian, are shown in Exhibit 2.1.2-1.

A practical consequence of Faraday rotation is that, in the frequency range where Faraday rotation is significant, one cannot transmit using one linear polarization and receive using an antenna with the same linear polarization without a high probability of a significant polarization loss. Among the techniques for avoiding or dealing with the problem are using a sufficiently high frequency that Faraday rotation is negligible, using a receiving antenna that can accept both orthogonal linear polarizations so that no polarization loss occurs, and using circular rather than linear polarization. As a right or left circularly polarized wave is a characteristic wave, it does not change polarization as it propagates and thus presents no problem, as long as both antennas of the link are designed for the same circular polarization. Another possibility, if Faraday rotation is not too great or highly variable, is to vary the orientation of a linear transmitting or receiving antenna to compensate for the Faraday rotation expected along the path, as a function of time of day, season, and period of the sunspot cycle (see Section 1.2.2.3).

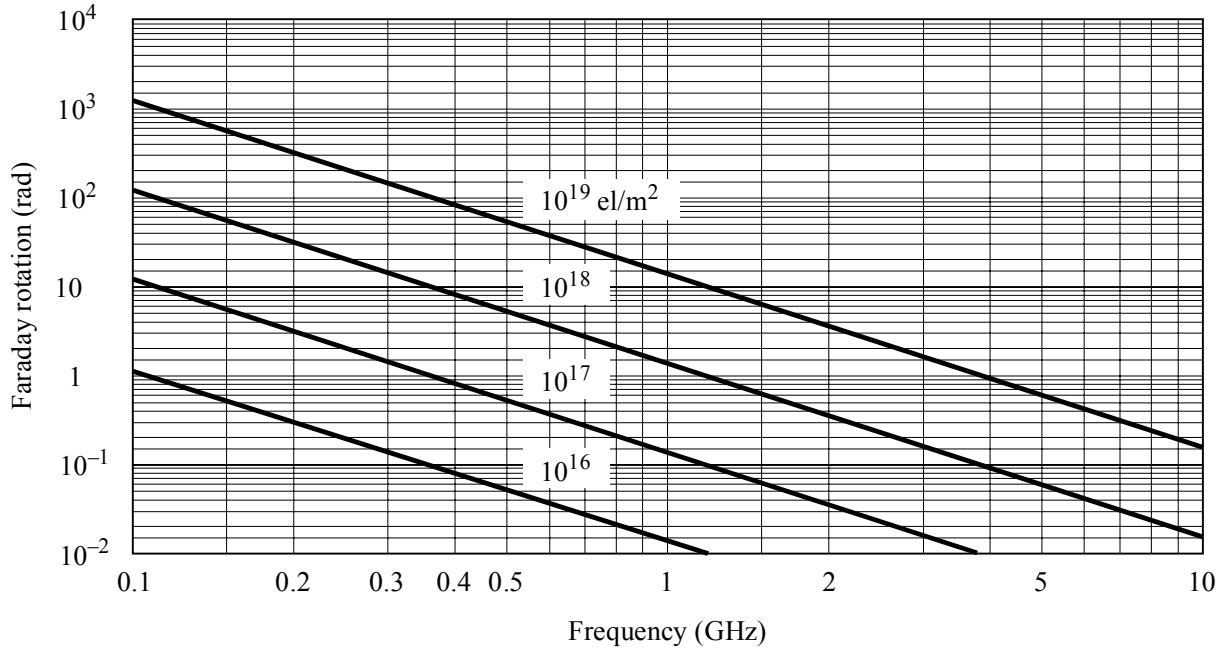


Exhibit 2.1.2-1
Faraday rotation as a function of ionospheric TEC and frequency (after Klobuchar, 1978)
[Source: ITU-R Rec. P.531-4 (1997)]

### 2.1.3 Time Delay

The presence of charged particles in the ionosphere slows down the propagation of radio signals along the path. The time delay in excess of the propagation time in free space, is commonly referred to as the *time delay* or *excess range delay*. Group delay is an important factor to be considered for MSS systems operating in the 1-3 GHz bands.

The parameters required for the determination of time delay are:

f: frequency of operation, in GHz
TEC: total electron content, in electrons/$m^2$

The time delay, $\Delta t$, in seconds, is then found from (ITU-R Rec. P.531-4, 1997)

$$\Delta t = \frac{1.345 \times 10^{-16}}{f^2} \text{ TEC} \qquad (2.1.3\text{-}1)$$

The time delay, $\Delta t$, found from this expression is referenced to propagation in a vacuum.

Exhibit 2.1.3-1 shows a plot of time delay, $\Delta t$, as a function of frequency, from .1 to 3 GHz, for a range of typical values of electron content along the propagation path. The plots show that for the frequency band around 1.6 GHz, the delay will vary from about 0.5 to 500 nsec for the range of TEC displayed.

The ITU-R (Rec. P.531-4, 1997) provided a plot of global contours of the percentage of yearly average daytime hours when the delay at vertical incidence at 1.6 GHz exceeds 20 nsec. This plot is shown as Exhibit 2.1.3-2. The contours are for a sunspot number of 140, which represents conditions near the upper peaks of the solar cycle.

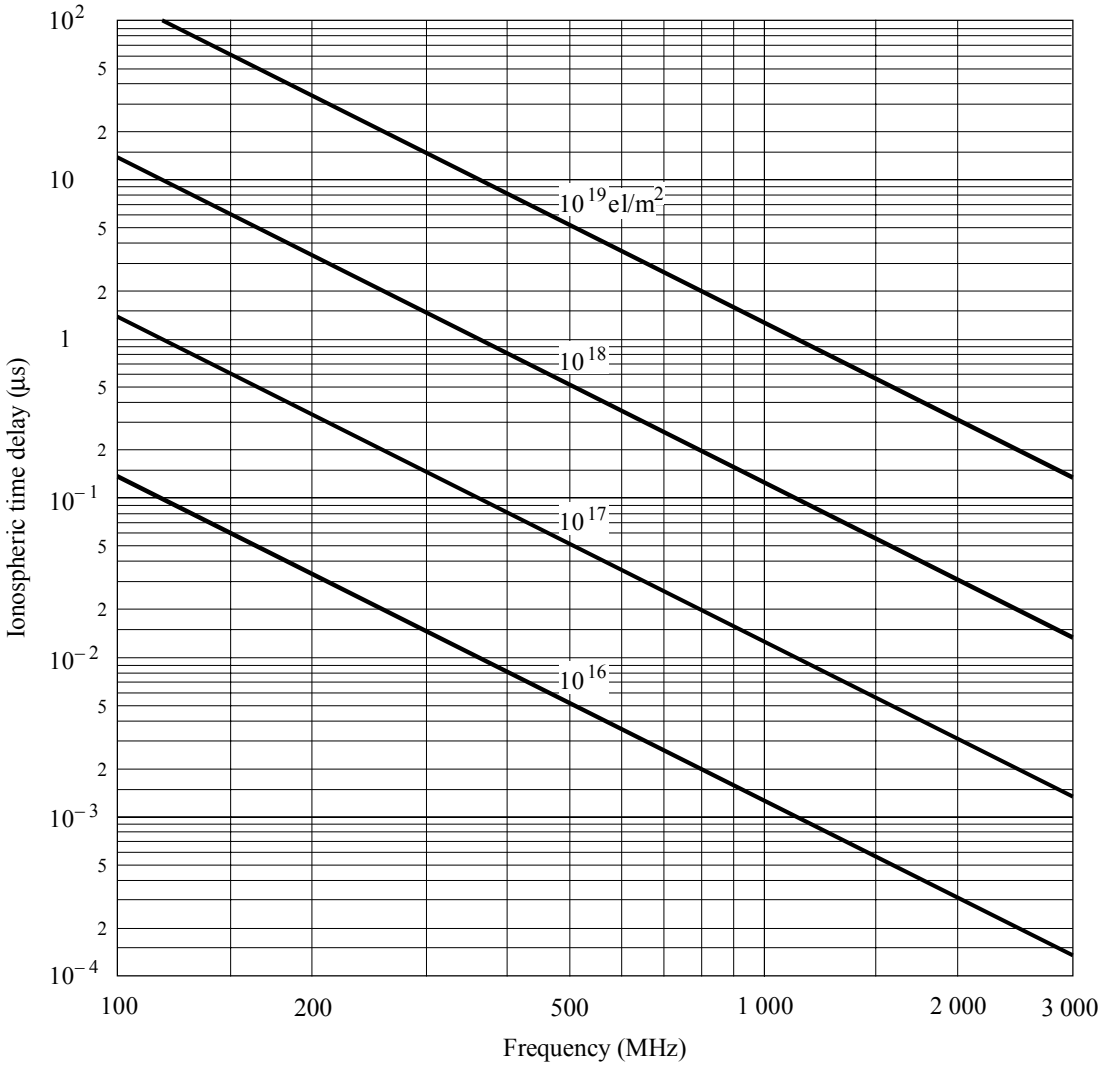


Exhibit 2.1.3-1
Ionospheric time delay, $\Delta t$, in μsec, as a function of ionospheric TEC and frequency (after Klobuchar, 1978).
*[Source: ITU-R Rec. P.531-4 (1997)]*

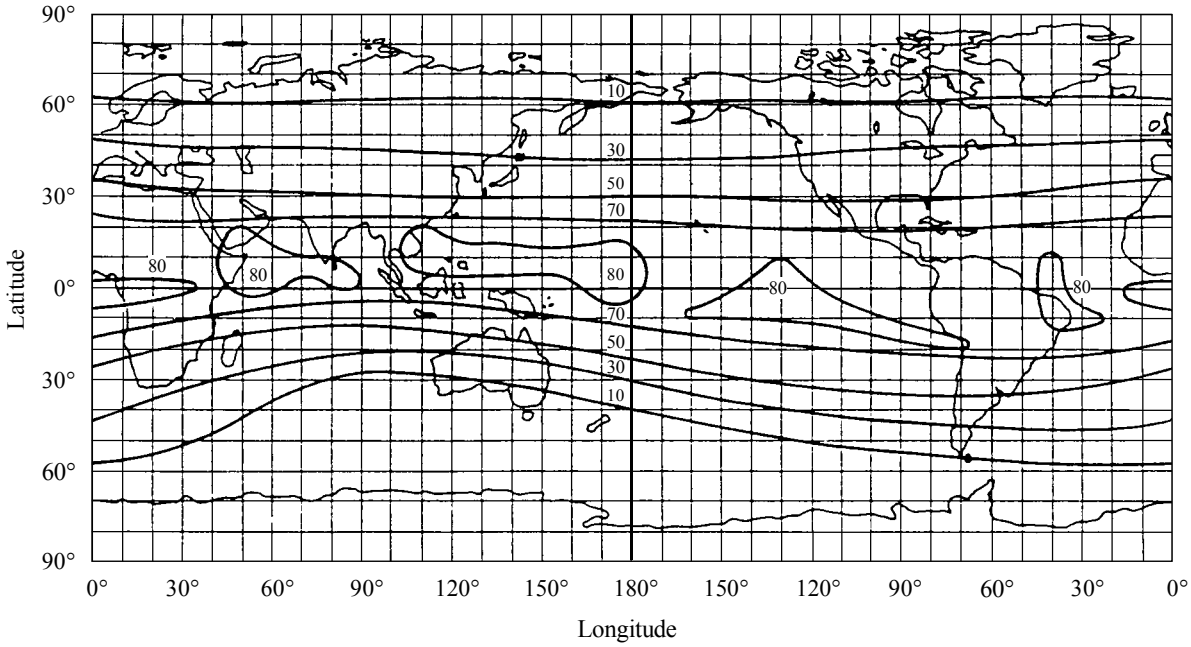


**Contours: % of daytime hours**
**Δt Threshold: ≥ 20 nsec.**
**Frequency: 1.6 GHz**
**Sunspot Number: 140**

Exhibit 2.1.3-2
Contours of Percentage of Yearly Average Daytime Hours when Group Delay Exceeds 20 nsec.
*[Source: ITU-R Rec. P.531-4 (1997)]*

### 2.1.4 Dispersion

**Time Delay Dispersion**

A radiowave propagating through the ionosphere will experience a time delay, as described in Section 2.1.3, which is proportional to $1/f^2$. If the radiowave has a significant bandwidth, the propagation delay will vary across the band and dispersion will be introduced.

The *time delay dispersion* or *differential time delay*, which is the rate of change of time delay with frequency, is determined from the first derivative of the time delay (Equation 2.1.3-1),

$$\boxed{\delta t = \frac{dt}{df} = \frac{-2.69 \times 10^{-16}}{f^3} \text{ TEC}} \qquad (2.1.4\text{-}1)$$

where, as before:

f: frequency of operation, in GHz

TEC: total electron content, in electrons/$m^2$

The differential time delay across the bandwidth is proportional to $1/f^3$. Exhibit 2.1.4-1 shows the differential time delay for the upper and lower frequencies of a transmitted signal for pulse widths $\tau$ of 0.01 to 10 μsec. The TEC is set at the fixed value of $5 \times 10^{17}$ electrons/$m^2$. For example, a signal with a pulse length of 1μsec results in a differential delay of 0.02 μsec at 200 MHz, while at 1.6 GHz the delay would be 0.00008 μsec, or 80 pico-seconds.

**Phase Dispersion**

The rate of change of phase angle with frequency, or the *phase dispersion*, is determined from the rate of change of the phase advance with frequency. The phase advance $\Phi$, in rad, is found from the time delay, $\Delta t$, as

$$\Phi = \frac{2\pi f}{c} \Delta t \qquad (2.1.4\text{-}2)$$

The phase dispersion, $\delta\Phi$, is found as the derivative of $\Phi$,

$$\boxed{\delta\Phi = \frac{d\Phi}{df} = \frac{-8.44 \times 10^{-16}}{f^2} \text{TEC}} \qquad (2.1.4\text{-}3)$$

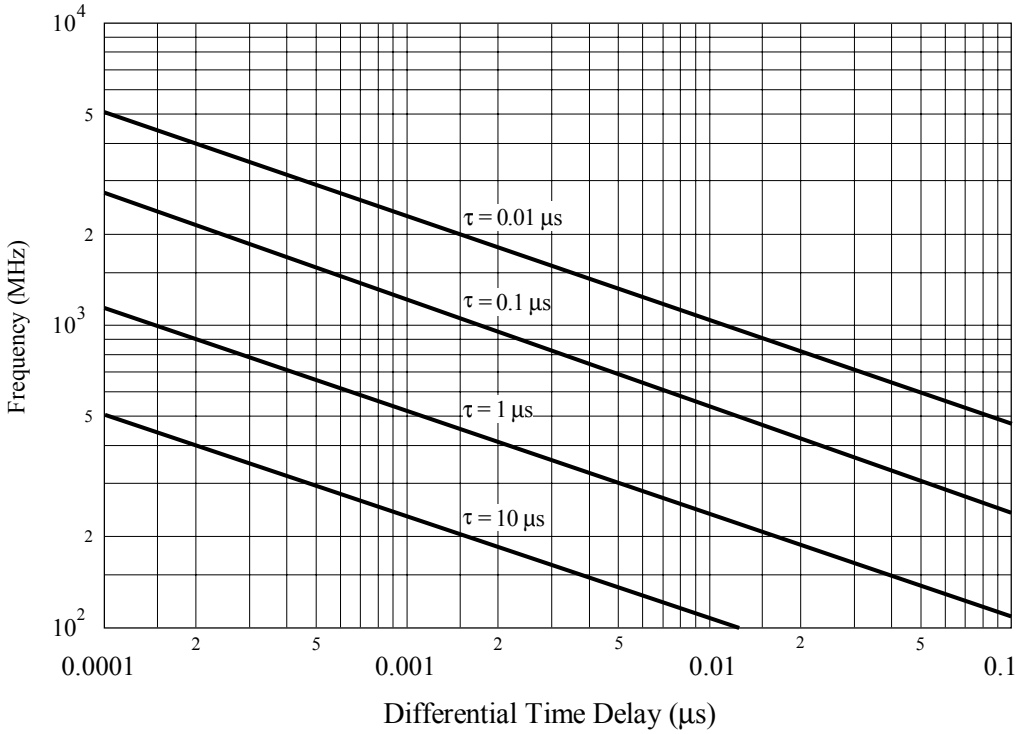


TEC = 5 x $10^{17}$ el/$m^2$

Exhibit 2.1.4-1
Differential Time Delay for Lower and Upper Frequencies of the Spectrum for Pulse Width τ, Transmitted Through the Ionosphere with TEC = $5 \times 10^{17}$ el/$m^2$
*[Source: ITU-R, Rec. P.531-4 (1997), Figure 4]*

### 2.1.5 Ionospheric Scintillation

Although ionospheric scintillation has been the subject of a great deal of theoretical and experimental study over the years and much is understood about the effect, the modeling and prediction methods available are still not at a mature state. [see Section 1.2.3.2 of this handbook for a detailed background description of ionospheric scintillation] A large amount of uncertainty is inherent in scintillation model predictions. The predicted margin requirements continue to evolve as more data, and higher quality data, becomes available.

An empirical method to estimate the effects of ionospheric scintillation developed by the ITU-R is provided in the following section.

#### 2.1.5.1 ITU-R Ionospheric Scintillation Model

The ITU-R developed a procedure to estimate the effects of scintillation on a satellite path (ITU-R Rec. P.531-4, 1997). The procedure is based on extrapolation of direct measurements of ionospheric effects at equatorial locations.

The input parameters required for the ITU-R method are:

f: frequency of operation, in GHz
p: annual percent of time, in %
θ: elevation angle, in degrees
location of ground terminal

The step-by-step procedure follows.

*Step 1)*

Determine a peak-to-peak amplitude fluctuation, $PP_p$ in (dB), for the percent of time of interest, p, from the plots on Exhibit 2.1.5.1-1. The plots are measurements at 4 GHz for satellite links at elevation angle of about $20^o$ (solid line 'P' curves) and an elevation angle of about $30^o$ (dashed line 'I' curves). The plots are for different times of the year and for different sun spot numbers, SSN, as described in the exhibit legend. Select the plot (or plots) most representative of the elevation angle, time of year, and solar conditions (described by the SSN) of interest.

*Step 2)*

Determine the peak-to-peak amplitude fluctuation for the frequency of interest, $PP_p(f)$, from

$$PP_p(f) = PP_p\left(\frac{f}{4}\right)^{-1.5} \qquad (2.1.5.1\text{-}1)$$

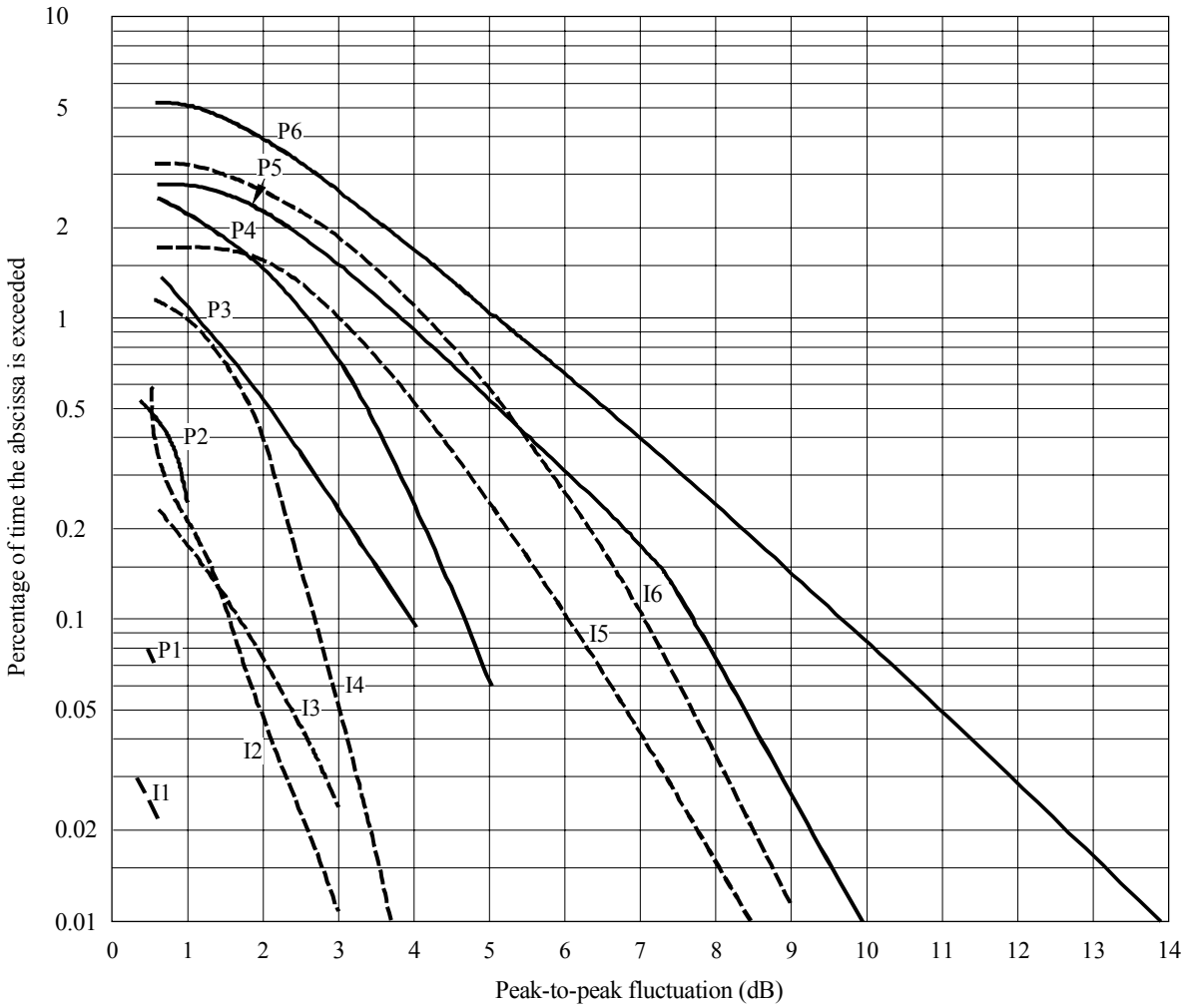


| *Curve* | *Period* | *SSN range* |
|---|---|---|
| I1, P1 | March 75-76 | 10-15 |
| I2, P2 | June 76-77 | 12-26 |
| I3, P3 | March 77-78 | 20-70 |
| I4, P4 | October 77-78 | 44-110 |
| I5, P5 | November 78-79 | 110-160 |
| I6, P6 | June 79-80 | 153-165 |

Exhibit 2.1.5.1-1
Measurements of annual statistics of peak-to-peak ionospheric scintillation
on satellite paths at 4 GHz
Solid Curves (P6, P5, P4, P3, P2, P1): Elevation angle $\phi = 20^0$
Dashed Curves (I6, I5, I4, I3, I2, I1): Elevation angle $\phi = 30^0$
Observations at Hong Kong: (P1, P3-P6). Observations at Taipei: (P2, I2).
*[Source: ITU-R Rec. P.531-4 (1997), Figure 10]*

*Step 3)*

The elevation angle dependence of ionospheric scintillation has not been determined with adequate measurement validation. A rough estimate can be obtained by use of the standard 'cosecant law' approximation for path length. The peak-to-peak scintillation at the desired elevation angle $\theta$ can be estimated from the value at the elevation angle $\phi$ obtained from Exhibit 2.1.5.1-1 by,

$$PP_p(\theta) = \frac{\sin\phi}{\sin\theta} PP_p(\phi) \qquad (2.1.5.1\text{-}2)$$

*Step 4)*

A very rough qualitative estimate of the variation of peak-to-peak scintillation with geographical location and diurnal occurrence can be determined from Exhibit 2.1.5.1-2. The exhibit indicates regions where the value(s) of $PP_p(f)$ found above can be modified based on location of the ground terminal, and for solar maximum and minimum conditions.

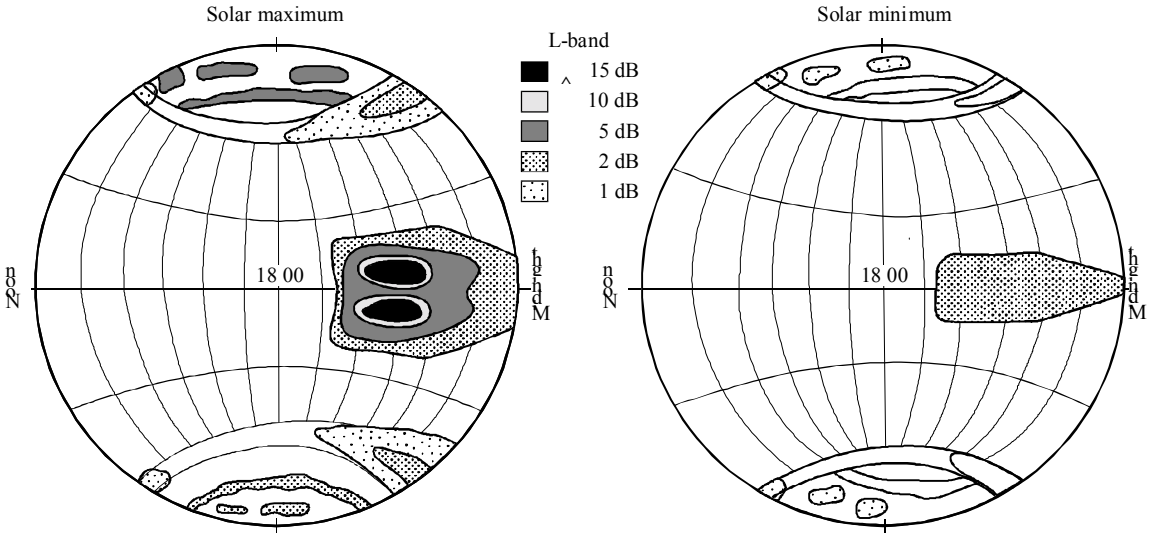


Exhibit 2.1.5.1-2
Pattern of ionospheric scintillation based on observations at L-Band (1.6GHz)
*[Source: ITU-R Rec. P.531-4 (1997), Figure 5]*

*Step 5)*

The signal loss $L_p$, in dB, can by estimated from

$$L_p = \frac{PP_p(f)}{\sqrt{2}} \qquad (2.1.5.1\text{-}3)$$

*Step 6)*

The scintillation index, $S_4$, the most widely used parameter in describing scintillation, can also be estimated from $PP_p(f)$. The index $S_4$ is defined as [see Section 1.2.3.2.1]

$$S_4 = \frac{1}{\overline{E^2}} \left[ \overline{\left( E^2 - \overline{E^2} \right)^2} \right]^{1/2}$$

where E is field intensity.

The index $S_4$ is estimated from $PP_p(f)$ by the conversion table given in Exhibit 2.1.5.1-3.

| **$S_4$** | **$PP_p(f)$** (dB) |
|---|---|
| 0.1 | 1.5 |
| 0.2 | 3.5 |
| 0.3 | 6 |
| 0.4 | 8.5 |
| 0.5 | 11 |
| 0.6 | 14 |
| 0.7 | 17 |
| 0.8 | 20 |
| 0.9 | 24 |
| 1.0 | 27.5 |

Exhibit 2.1.5.1-3
Empirical Conversion table for Scintillation Indices
[Source: ITU-R Rec. P.531-4 (1997), Table 1]

The procedure outlined in the ITU-R model is admittedly very crude. However, given the lack of a validated theoretical or empirical prediction method and the large amount of uncertainty in the conditions that cause ionospheric scintillation, the ITU-R procedure can serve as a coarse qualitative estimate of the range of expected ionospheric degradation on the satellite path.

### 2.1.5.2 Sample Ionospheric Scintillation Evaluation

In this section an example of the application of the ITU-R ionospheric scintillation procedure will be described. The parameters of the link to be evaluated are:

Frequency: f = 2.48 GHz (MSS downlink frequency)
Annual percent of time values, p: 0.05, 0.1, 0.5 %
Elevation Angle: $\theta = 15^o$
Location of ground terminal: Washington, DC 38.9° N. Lat., 77° W. Long.

We wish to evaluate peak-to-peak scintillation and scintillation index $S_4$ for the three annual probability values given.

*Step 1)*
Consider worst case solar activity, at the elevation angle closest to the desired 15 degrees. Curve P6 of Exhibit 2.1.5.1-1 is chosen ($\phi = 20^o$, SSN = 153-165)

The values of peak-to-peak amplitude fluctuation are read off from curve P6:

$$PP_{0.05} = 11 \text{ dB}$$
$$PP_{0.1} = 9.7 \text{ dB}$$
$$PP_{0.5} = 6.5 \text{ dB}$$

*Step 2)*
The frequency conversion factor is found from equation (2.1.5.1-1) as

$$PP_p(f) = PP_p\left(\frac{2.48}{4}\right)^{-1.5} = 2.048\, PP_p$$

Therefore:

$$PP_{0.05}(f) = 11 \text{ x } 2.048 = 22.5 \text{ dB}$$
$$PP_{0.1}(f) = 9.7 \text{ x } 2.048 = 19.8 \text{ dB}$$
$$PP_{0.5}(f) = 6.5 \text{ x } 2.048 = 13.3 \text{ dB}$$

*Step 3)*
The elevation angle conversion factor is found from equation (2.1.5.1-2) as

$$PP_p(15^o) = \frac{\sin(20^o)}{\sin(15^o)} PP_p(20^o) = 1.321\, PP_p(20^o)$$

Therefore:

$$PP_{0.05}(15) = 22.5 \text{ x } 1.321 = 29.7 \text{ dB}$$
$$PP_{0.1}(15) = 19.8 \text{ x } 1.321 = 26.1 \text{ dB}$$
$$PP_{0.5}(15) = 13.3 \text{ x } 1.321 = 17.6 \text{ dB}$$

*Step 4)*
Since the ground terminal of interest is located in a temperate mid-latitude region (39.9° N. Lat.), and the measurements were taken in a lower latitude region (21.7° N. Lat. For Hong Kong), a correction for location is obtained from Exhibit 2.1.5.1-2. The difference between the measurement region and the ground terminal region, for the solar maximum condition (left globe), is seen from the legend values as

$$\frac{\sim 5 \text{ dB}}{\sim 1 \text{ dB}} = \text{a factor of} \sim 5 = \sim 7 \text{ dB}$$

Thus values found in Step 3 are reduced by 7 dB, i.e.

$$PP_{0.05}(15) = \sim 22.7 \text{ dB}$$
$$PP_{0.1}(15) = \sim 19.1 \text{ dB}$$
$$PP_{0.5}(15) = \sim 10.6 \text{ dB}$$

*Step 5)*
The expected signal loss $L_p$ is found from equation (2.1.5.1-3) as

$$L_{0.05} = 16 \text{ dB}$$
$$L_{0.01} = 13.6 \text{ dB}$$
$$L_{0.5} = 7.5 \text{ dB}$$

*Step 6)*
The scintillation index $S_4$ is estimated from Exhibit 2.1.5.1-3 and the values found in Step 4 as

$$S_4(0.05) = 0.85$$
$$S_4(0.01) = 0.80$$
$$S_4(0.5) = 0.48$$

This evaluation, as discussed above, provides a first order, coarse estimate of the effects of ionospheric scintillation on the link.

### 2.1.6 Auroral Absorption

Auroral absorption results from an increase in electron concentration in the D and E regions produced by incident energetic electrons. The absorption is observed over a range of 10° to 20° latitude centered close to the latitude of maximum occurrence of visual aurora. Auroral absorption occurs as a series of discrete absorption enhancements each of relatively short duration, i.e. from minutes up to a few hours, with an average duration of about 30 minutes. The events usually occur with an irregular time structure. Night enhancements tend to consist of smooth fast rises and slow decays (ITU-R Rec. P.531-4, 1997).

A comprehensive model for the estimation of auroral absorption is not available. Auroral absorption measurement have shown that the effect is negligible for frequencies above about 200 MHz (< 0.1 dB).

Exhibit 2.1.6-1 presents a summary of measurements of typical auroral absorption levels at 127 MHz. [see section 1.2.3.1.2 for further information on auroral effects]

| Percentage of Time | Elevation Angle | |
|---|---|---|
| | $20^o$ | $5^o$ |
| 0.1 | 1.5 | 2.9 |
| 1 | 0.9 | 1.7 |
| 2 | 0.7 | 1.4 |
| 5 | 0.6 | 1.1 |
| 50 | 0.2 | 0.4 |

Exhibit 2.1.6-1
Auroral Absorption, in dB, at 127 MHz
*[Source: ITU-R, Rec. P.531-4 (1997)]*

### 2.1.7 Polar Cap Absorption

Polar cap absorption, which may occur at times of high solar activity, does so at geomagnetic latitudes greater than 64° (ITU-R Rec. 531-4, 1997). The absorption is produced by ionization at heights greater than about 30 km. It usually occurs in discrete, though sometimes overlapping, events that are nearly always associated with discrete solar events. The absorption can last for long periods and is detectable over the sunlit polar caps. Polar cap absorption occurs most usually during the peak of the sunspot cycle, when there may be 10 to 12 events per year. Such an event

may last up to a few days. This is in contrast to auroral absorption, which is frequently quite localized, with variations in periods of minutes.

Exhibit 2.1.7-1 is a hypothetical model of the diurnal variation of polar cap absorption following a major solar flare. Polar cap absorption events show a great reduction in the absorption during hours of darkness for a given rate of electron production.

A comprehensive model for the estimation of auroral absorption is not available. Observations indicate that the effects are negligible (< 0.1 dB) for frequencies above about 100 MHz. [see section 1.2.3.1.5 for further information on polar cap absorption]

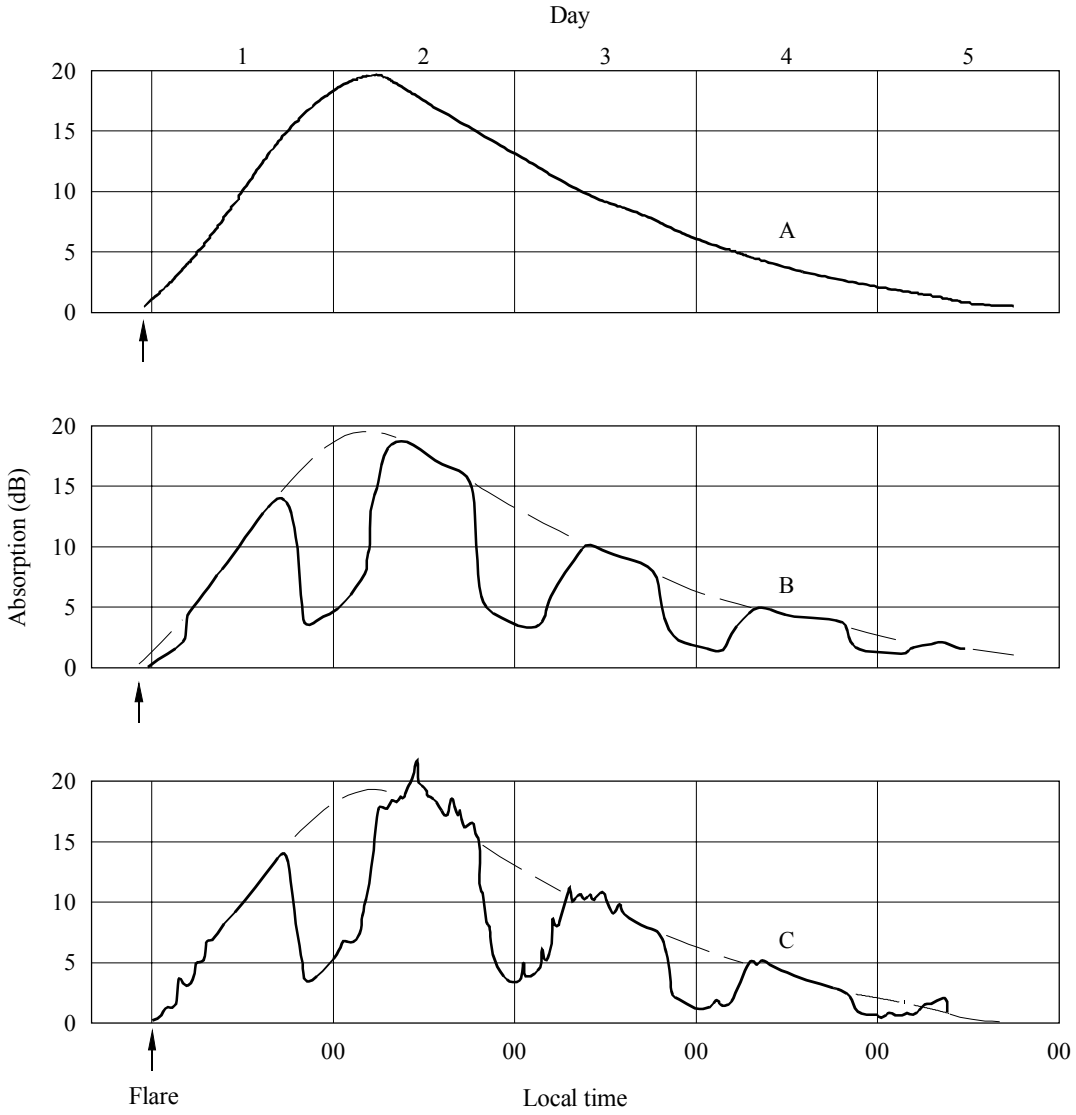


Exhibit 2.1.7-1
Hypothetical model showing polar cap absorption following a major solar flare as expected to be observed on riometers at approximately 30 MHz.

A. High latitudes - 24 h of daylight.
B. High latitudes - equal period day and night.
C. High latitudes - auroral zone.

*[Source: ITU-R Rec. P.531-4, Figure 11]*

### 2.1.8 Summary – Ionospheric Effects Prediction

The prediction methods described in the preceding sections provide a concise set of tools to estimate ionospheric effects on satellite paths. Ionospheric effects are most significant for frequencies of operation below about 3 GHz, i.e. the VHF/UHF, L-band, and S-band frequencies allocated to satellite services.

Exhibit 2.1.8-1 provides a summary of ionospheric effects predictions for frequencies from 100 MHz to 10 GHz, for a one-way link at a $30^0$ elevation angle. The estimates are based on a total electron content (TEC) of 1 x $10^{18}$ electrons/$m^2$, the value recommended in Section 2.1.1. This value corresponds to a typical high value of TEC encountered at low latitudes in day-time with moderate-to-high solar activity.

The summary table shows the sharp drop-off of ionospheric effects with frequency. Faraday rotation, delay, and other effects are reduced to very low values at 3 GHz and above. However, scintillation may still be important for low-latitude high sun-spot numbers (see Exhibit 2.1.5.1-1).

(this page blank)

| Effect | Frequency Dependence | 100 MHz | 250 MHz | 500 MHz | 1 GHz | 3 GHz | 10 GHz |
|---|---|---|---|---|---|---|---|
| Faraday rotation | $1/f^2$ | 30 rotations | 4.8 rotations | 1.2 rotations | 108° | 12° | 1.1° |
| Propagation delay | $1/f^2$ | 25 μs | 4 μs | 1 μs | 0.25 μs | 0.028 μs | 0.0025 μs |
| Refraction | $1/f^2$ | < 1° | < 0.16° | < 2.4′ | < 0.6′ | < 4.2″ | < 0.36″ |
| Variation in the direction of arrival (r.m.s.) | $1/f^2$ | 20′ | 3.2′ | 48″ | 12″ | 1.32″ | 0.12″ |
| Absorption (auroral and/or polar cap) | $\approx 1/f^2$ | 5 dB | 0.8 dB | 0.2 dB | 0.05 dB | $6 \times 10^{-3}$ dB | $5 \times 10^{-4}$ dB |
| Absorption (mid-latitude) | $1/f^2$ | < 1 dB | < 0.16 dB | < 0.04 dB | < 0.01 dB | < 0.001 dB | $< 10^{-4}$ dB |
| Dispersion | $1/f^3$ | 0.4 ps/Hz | 0.026 ps/Hz | 0.0032 ps/Hz | 0.0004 ps/Hz | $1.5 \times 10^{-5}$ ps/Hz | $4 \times 10^{-7}$ ps/Hz |
| Scintillation (1) | | | | | >20 dB peak-to-peak | ≈ 10 dB peak-to-peak | ≈ 4 dB peak-to-peak |

Estimates based on a TEC = $10^{18}$ el/m$^2$

(1) Values observed near the geomagnetic equator during early nighttime hours at equinox under conditions of maximum sunspot number.

Exhibit 2.1.8-1

Summary of ionospheric effects for frequencies from 100 MHz to 10 GHz, for a one-way link at a $30^0$ elevation angle

*[Source: ITU-R Rec. P.680-2 (1997), Table 1]*

## 2.2 PREDICTION METHODS FOR SATELLITE LINKS OPERATING ABOVE 3 GHZ

### 2.2.1 Atmospheric Gaseous Attenuation

Two sources are available to provide predictions of attenuation due to gaseous absorption. They are the Liebe Complex Refractivity Model (Leibe, et.al., 1993), and procedures developed by the ITU-R (ITU-R P.676-3, 1997). The ITU-R presents a detailed line-by-line summation of the spectral lines of water vapor and oxygen, which is similar to the Leibe method. An approximation to the line-by line method is also provided by the ITU-R.

Both the Liebe Complex Refractivity and the ITU-R Models compute specific attenuation, or attenuation rate, in dB/Km. Both models assume a stratified atmosphere and divide it into small layers, for which a description of the moisture (or humidity) content, temperature and barometric pressure is imposed on these layers. The specific attenuation is computed at these layers, and the total path attenuation is obtained by integrating the specific attenuation from the surface of the earth to a zenith height of 30 km typically. This integral gives the total path attenuation vertically, 90° perpendicular to the earth's surface, and is called the zenith attenuation. To obtain the gaseous absorption along the satellite path the zenith attenuation is scaled as a function of the elevation angle, measured relative to the local horizontal. The scaling is the cosecant of the elevation angle for angles between 10° and 90°. The barometric pressure, air temperature and humidity at various levels in the atmosphere are needed to compute specific attenuation. Actual measurements of these weather parameters, obtained by launching a balloon with ambient temperature, humidity and pressure instruments attached (radiosonde), at these levels would be ideal, but are not practical to obtain on a regular basis. In lieu of these measurements, a set of "profiles" describing functionally how each of these weather parameters varies with height are used. Exhibit 2.2.1-1 compares the profiles to example measurements with height, assuming surface absolute humidity measurements of 7.5g/$m^3$ and 20 g/$m^3$. It is immediately seen that the general trends in the measurement profile and the model profiles are similar; thus, on an average basis, the model profiles are adequate to represent the upper atmosphere. Recommended profiles for the ITU-R models are provided in ITU-R P.835-2 (1997).

The Leibe Complex Refractivity Model and the detailed and approximation procedures of the ITU-R are described in this section. Emphasis is placed on the ITU-R models, since they are based on the original Liebe procedure, and the ITU-R approximation calculation lends itself to relatively easy calculations.

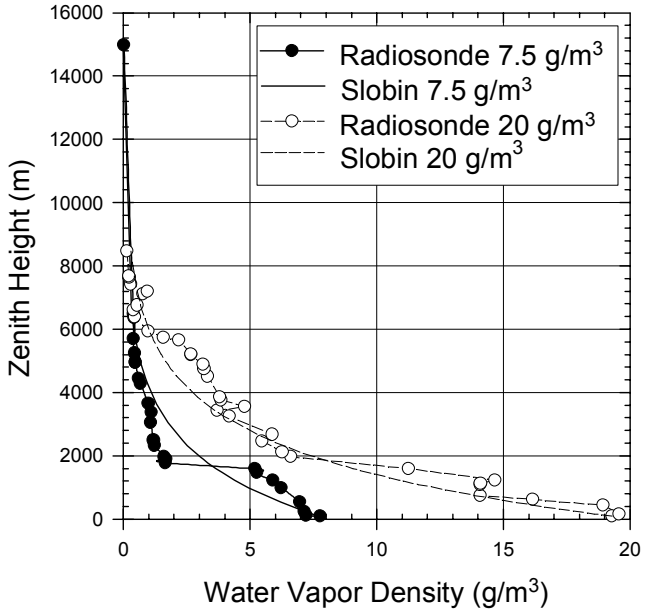


Exhibit 2.2.1-1: Variation of Water Vapor with Zenith Height

### 2.2.1.1 Leibe Complex Refractivity Model

The Liebe Complex Refractivity Model (Leibe, et.al., 1993) will be considered first. This model is designed to give predictions of attenuation due to gaseous absorption for a frequency range from 1 to 1000 GHz. It is based on spectral characteristics of water vapor and oxygen. The inputs that the model depends on are:

- relative humidity
- air temperature, and
- barometric pressure.

Consider a plane wave propagating a distance $z$ at a frequency $v$ described by a field strength,

$$E(z) = exp[ikz(1 + N \bullet 10^{-6})]E(0). \qquad (2.2.1.1\text{-}1)$$

Where E(0) is the initial value, $k = 2\pi v/c$ is the free space wave number and c is the speed of light. The spectral characteristics of the atmosphere are given by complex refractivity,

$$N = N_0 + N' + iN'' \qquad ppm. \qquad (2.2.1.1\text{-}2)$$

Using the imaginary part of this expression as follows,

$$\alpha = 0.1820\, v\, N'' \qquad (2.2.1.1\text{-}3)$$

gives the specific attenuation in dB/Km. The details of computing N″ can be summarized by two expressions: one describing the oxygen contribution, which is based on 44 oxygen spectral lines; and an expression describing the water vapor contribution, based on 34 resonant lines. It is the expression $\alpha$ that is computed at each layer of the atmosphere, using the profiles discussed above, and summed to give the total zenith attenuation through the atmosphere. The final step is the multiplication by a scaling factor, a function of the elevation angle for angles between 0 and 90 degrees, to arrive at the total path attenuation in dB.

#### 2.2.1.2 ITU-R Gaseous Attenuation Models

Two modeling procedures are provided by the ITU-R for the prediction of gaseous attenuation. Both models are presented in this section, with the line-by-line model presented first, followed by the approximation to the line-by-line model. An example computation using the approximate model is also presented here.

##### 2.2.1.2.1 ITU-R Line-by-line Calculation

The line-by-line model is contained in Annex 1 of the ITU-R Recommendation ITU-R P.676-3 (1997). The model assumes input frequencies up to 1000 GHz, elevation angles ≥ 0 as well as < 0 for slant path calculations. Terrestrial paths are also treated. The input weather parameters required are the dry air pressure, water vapor partial pressure and air temperature. Ideally, these should be measured locally, and vertically, through the atmosphere, as well. In the absence of local measurements the ITU has an accompanying recommendation, ITU-R P.835-2 (1997), that provides the Reference Standard Atmospheres.

Calculation of the specific attenuation, $\gamma$, is considered first.

$$\gamma = \gamma_o + \gamma_w = 0.1820 f N''(f) \quad \text{dB/Km} \qquad (2.2.1.2\text{-}1)$$

The $\gamma_o$ and $\gamma_w$ are the specific attenuations (dB/Km) due to dry air and water vapor, respectively. The parameter $f$ is the frequency (GHz) and the $N''(f)$ is the imaginary part of the frequency-dependent complex refractivity:

$$N''(f) = \sum_i S_i F_i + N''_D(f) + N''_W(f) \qquad (2.2.1.2\text{-}2)$$

$S_i$ is the strength of the $i$ th line, $F_i$ is the line shape factor and the sum extends over all the lines. The $N''_D(f)$ and $N''_W(f)$ are the dry and wet continuum spectra.
The line strength is given by:

$$S_i = a_1 \times 10^{-7} p \theta^3 \exp\left[a_2 (1-\theta)\right] \qquad \text{for oxygen} \qquad (2.2.1.2\text{-}3)$$

$$S_i = b_1 \times 10^{-1} e \theta^{3.5} \exp\left[b_2 (1-\theta)\right] \qquad \text{for water vapor}$$

The input weather parameters are given as follows:

p: dry air pressure (hPa)
e: water vapor partial pressure (hPa)
θ: θ = 300/T
T: air temperature (degrees K).

These are the input parameters that need to be measured locally, including vertically. The vertical measurements are usually obtained by using radiosondes. The Reference Standard Atmospheres in Recommendation ITU-R P.835-2 can be used in lieu of actual measurements. One point of clarification needs to be made, however, about these input parameters. The parameters *p* and *e* are not common weather parameters. These may be related to more common parameters as follows:

$$B_p = p + e \qquad \text{(hPa)} \qquad \text{(2.2.1.2-4)}$$

The parameter $B_p$ is called the barometric pressure and is widely available. The parameter, *e*, is the water vapor partial pressure and this may be calculated using the following formula:

$$e = \rho T / 216.7 \qquad \text{(hPa)} \qquad \text{(2.2.1.2-5)}$$

The parameter ρ is the water vapor density ($g/m^3$) and can be calculated using the following formula:

$$\rho = \frac{RH}{5.752} \theta^{6} 10^{(10-9.834\theta)} \qquad \text{(2.2.1.2-6)}$$

Where

RH: relative humidity in %
$T_c$: air temperature measured in degrees C
θ = 300/ ($T_c$ +273.15)

These parameters are also widely available measured weather parameters.

Thus in terms of the more common measured weather parameters the required input parameters are given as follows:

$$p = B_p - (\rho T / 216.7) \text{ (hPa)} \qquad \text{(2.2.1.2-7)}$$

$$e = \rho T / 216.7 \qquad \text{(hPa)} \qquad \text{(2.2.1.2-8)}$$

The coefficients $a_1$ and $a_2$ in equation (2.2.1.2-3) are listed in Exhibit 2.2.1.2-1 for the oxygen contribution. The coefficients $b_1$ and $b_2$ in equation (2.2.1.2-3) are listed in Exhibit 2.2.1.2-2 for the water vapor contribution.

The line-shape factor is given by:

$$F_i = \frac{f}{f_i}\left[\frac{\Delta f - \delta(f_i - f)}{(f_i - f)^2 + \Delta f^2} + \frac{\Delta f - \delta(f_i + f)}{(f_i + f)^2 + \Delta f^2}\right] \qquad (2.2.1.2\text{-}9)$$

where $f_i$ is the line frequency and $\Delta f$ is the width of the line:

$$\begin{aligned} \Delta f &= a_3 \times 10^{-4}(p\theta^{(0.8-a_4)} + 1.1e\theta) && \text{for oxygen} \\ \Delta f &= b_3 \times 10^{-4}(p\theta^{b4} + b_5 e\theta^{b6}) && \text{for water vapor} \end{aligned} \qquad (2.2.1.2\text{-}10)$$

and $\delta$ is a correction factor necessary to compensate for interference effects in oxygen lines:

$$\begin{aligned} \delta &= (a_5 + a_6\theta) \times 10^{-4} p\theta^{0.8} && \text{for oxygen} \\ &= 0 && \text{for water vapor} \end{aligned} \qquad (2.2.1.2\text{-}11)$$

The remaining spectroscopic coefficients are also contained in Exhibit 2.2.1.2-1 and Exhibit 2.2.1.2-2.

The next term, $N''_D(f)$, is called the dry air continuum and this arises from the non-resonant Debye spectrum of oxygen below 10 GHz and a pressure-induced nitrogen attenuation above 100 GHz. This term is given below:

| $f_0$ | $a_1$ | $a_2$ | $a_3$ | $a_4$ | $a_5$ | $a_6$ |
|---|---|---|---|---|---|---|
| 50.474238 | 0.94 | 9.694 | 8.60 | 0 | 1.600 | 5.520 |
| 50.987749 | 2.46 | 8.694 | 8.70 | 0 | 1.400 | 5.520 |
| 51.503350 | 6.08 | 7.744 | 8.90 | 0 | 1.165 | 5.520 |
| 52.021410 | 14.14 | 6.844 | 9.20 | 0 | 0.883 | 5.520 |
| 52.542394 | 31.02 | 6.004 | 9.40 | 0 | 0.579 | 5.520 |
| 53.066907 | 64.10 | 5.224 | 9.70 | 0 | 0.252 | 5.520 |
| 53.595749 | 124.70 | 4.484 | 10.00 | 0 | −0.066 | 5.520 |
| 54.130000 | 228.00 | 3.814 | 10.20 | 0 | −0.314 | 5.520 |
| 54.671159 | 391.80 | 3.194 | 10.50 | 0 | −0.706 | 5.520 |
| 55.221367 | 631.60 | 2.624 | 10.79 | 0 | –1.151 | 5.514 |
| 55.783802 | 953.50 | 2.119 | 11.10 | 0 | −0.920 | 5.025 |
| 56.264775 | 548.90 | 0.015 | 16.46 | 0 | 2.881 | −0.069 |
| 56.363389 | 1 344.00 | 1.660 | 11.44 | 0 | −0.596 | 4.750 |
| 56.968206 | 1 763.00 | 1.260 | 11.81 | 0 | −0.556 | 4.104 |
| 57.612484 | 2 141.00 | 0.915 | 12.21 | 0 | –2.414 | 3.536 |
| 58.323877 | 2 386.00 | 0.626 | 12.66 | 0 | –2.635 | 2.686 |
| 58.446590 | 1 457.00 | 0.084 | 14.49 | 0 | 6.848 | −0.647 |
| 59.164207 | 2 404.00 | 0.391 | 13.19 | 0 | −6.032 | 1.858 |
| 59.590983 | 2 112.00 | 0.212 | 13.60 | 0 | 8.266 | –1.413 |
| 60.306061 | 2 124.00 | 0.212 | 13.82 | 0 | –7.170 | 0.916 |
| 60.434776 | 2 461.00 | 0.391 | 12.97 | 0 | 5.664 | –2.323 |
| 61.150560 | 2 504.00 | 0.626 | 12.48 | 0 | 1.731 | –3.039 |
| 61.800154 | 2 298.00 | 0.915 | 12.07 | 0 | 1.738 | –3.797 |
| 62.411215 | 1 933.00 | 1.260 | 11.71 | 0 | −0.048 | −4.277 |
| 62.486260 | 1 517.00 | 0.083 | 14.68 | 0 | −4.290 | 0.238 |
| 62.997977 | 1 503.00 | 1.665 | 11.39 | 0 | 0.134 | −4.860 |
| 63.568518 | 1 087.00 | 2.115 | 11.08 | 0 | 0.541 | –5.079 |
| 64.127767 | 733.50 | 2.620 | 10.78 | 0 | 0.814 | –5.525 |
| 64.678903 | 463.50 | 3.195 | 10.50 | 0 | 0.415 | –5.520 |
| 65.224071 | 274.80 | 3.815 | 10.20 | 0 | 0.069 | –5.520 |
| 65.764772 | 153.00 | 4.485 | 10.00 | 0 | −0.143 | –5.520 |
| 66.302091 | 80.09 | 5.225 | 9.70 | 0 | −0.428 | –5.520 |
| 66.836830 | 39.46 | 6.005 | 9.40 | 0 | −0.726 | –5.520 |
| 67.369598 | 18.32 | 6.845 | 9.20 | 0 | –1.002 | –5.520 |
| 67.900867 | 8.01 | 7.745 | 8.90 | 0 | –1.255 | –5.520 |
| 68.431005 | 3.30 | 8.695 | 8.70 | 0 | –1.500 | –5.520 |
| 68.960311 | 1.28 | 9.695 | 8.60 | 0 | –1.700 | –5.520 |
| 118.750343 | 945.00 | 0.009 | 16.30 | 0 | −0.247 | 0.003 |
| 368.498350 | 67.90 | 0.049 | 19.20 | 0.6 | 0 | 0 |
| 424.763124 | 638.00 | 0.044 | 19.16 | 0.6 | 0 | 0 |
| 487.249370 | 235.00 | 0.049 | 19.20 | 0.6 | 0 | 0 |
| 715.393150 | 99.60 | 0.145 | 18.10 | 0.6 | 0 | 0 |
| 773.839675 | 671.00 | 0.130 | 18.10 | 0.6 | 0 | 0 |
| 834.145330 | 180.00 | 0.147 | 18.10 | 0.6 | 0 | 0 |

Exhibit 2.2.1.2-1 Spectroscopic Data for Oxygen Attenuation

***[Source: ITU-R P.676-3 (1997)]***

| $f_0$ | $b_1$ | $b_2$ | $b_3$ | $b_4$ | $b_5$ | $b_6$ |
|---|---|---|---|---|---|---|
| 22.235080 | 0.1090 | 2.143 | 28.11 | 0.69 | 4.80 | 1.00 |
| 67.813960 | 0.0011 | 8.735 | 28.58 | 0.69 | 4.93 | 0.82 |
| 119.995941 | 0.0007 | 8.356 | 29.48 | 0.70 | 4.78 | 0.79 |
| 183.310074 | 2.3000 | 0.668 | 28.13 | 0.64 | 5.30 | 0.85 |
| 321.225644 | 0.0464 | 6.181 | 23.03 | 0.67 | 4.69 | 0.54 |
| 325.152919 | 1.5400 | 1.540 | 27.83 | 0.68 | 4.85 | 0.74 |
| 336.187000 | 0.0010 | 9.829 | 26.93 | 0.69 | 4.74 | 0.61 |
| 380.197372 | 11.9000 | 1.048 | 28.73 | 0.69 | 5.38 | 0.84 |
| 390.134508 | 0.0044 | 7.350 | 21.52 | 0.63 | 4.81 | 0.55 |
| 437.346667 | 0.0637 | 5.050 | 18.45 | 0.60 | 4.23 | 0.48 |
| 439.150812 | 0.9210 | 3.596 | 21.00 | 0.63 | 4.29 | 0.52 |
| 443.018295 | 0.1940 | 5.050 | 18.60 | 0.60 | 4.23 | 0.50 |
| 448.001075 | 10.6000 | 1.405 | 26.32 | 0.66 | 4.84 | 0.67 |
| 470.888947 | 0.3300 | 3.599 | 21.52 | 0.66 | 4.57 | 0.65 |
| 474.689127 | 1.2800 | 2.381 | 23.55 | 0.65 | 4.65 | 0.64 |
| 488.491133 | 0.2530 | 2.853 | 26.02 | 0.69 | 5.04 | 0.72 |
| 503.568532 | 0.0374 | 6.733 | 16.12 | 0.61 | 3.98 | 0.43 |
| 504.482692 | 0.0125 | 6.733 | 16.12 | 0.61 | 4.01 | 0.45 |
| 556.936002 | 510.0000 | 0.159 | 32.10 | 0.69 | 4.11 | 1.00 |
| 620.700807 | 5.0900 | 2.200 | 24.38 | 0.71 | 4.68 | 0.68 |
| 658.006500 | 0.2740 | 7.820 | 32.10 | 0.69 | 4.14 | 1.00 |
| 752.033227 | 250.0000 | 0.396 | 30.60 | 0.68 | 4.09 | 0.84 |
| 841.073593 | 0.0130 | 8.180 | 15.90 | 0.33 | 5.76 | 0.45 |
| 859.865000 | 0.1330 | 7.989 | 30.60 | 0.68 | 4.09 | 0.84 |
| 899.407000 | 0.0550 | 7.917 | 29.85 | 0.68 | 4.53 | 0.90 |
| 902.555000 | 0.0380 | 8.432 | 28.65 | 0.70 | 5.10 | 0.95 |
| 906.205524 | 0.1830 | 5.111 | 24.08 | 0.70 | 4.70 | 0.53 |
| 916.171582 | 8.5600 | 1.442 | 26.70 | 0.70 | 4.78 | 0.78 |
| 970.315022 | 9.1600 | 1.920 | 25.50 | 0.64 | 4.94 | 0.67 |
| 987.926764 | 138.0000 | 0.258 | 29.85 | 0.68 | 4.55 | 0.90 |

Exhibit 2.2.1.2-2 Spectroscopic data for water-vapor Attenuation
***[Source: ITU-R P.676-3 (1997)]***

$$N''_D(f) = fp\theta^2 \left[ \frac{6.14\times10^{-5}}{d\left[1+\left[\frac{f}{d}\right]^2\right]} + 1.4\times10^{-12}(1-1.2\times10^{-5} f^{1.5})p\theta^{1.5} \right] \qquad (2.2.1.2\text{-}12)$$

where d is the width parameter for the Debye spectrum given as:

$$d = 5.6\times10^{-4}(p+1.1e)\theta \qquad (2.2.1.2\text{-}13)$$

The last term in equation (2.2.1.2-2) $N''_W(f)$ is the wet continuum and is given as:

$$N''_W(f) = f(3.57\theta^{7.5}e + 0.113p)10^{-7} e\theta^3 \qquad (2.2.1.2\text{-}14)$$

Now that the specific attenuation is given, the next step is to obtain the total path attenuation defined by some system geometry.

For a terrestrial path, or for "slightly inclined paths close to the ground", the path attenuation is given as:

$$A = \gamma r_0 = (\gamma_o + \gamma_w) r_0 \qquad \text{dB} \qquad (2.2.1.2\text{-}15)$$

where $r_0$ is the path length in Km and $\gamma_o$ and $\gamma_w$ are the surface specific attenuation values for oxygen and water vapor, respectively.

For slant paths, the computations are more involved. The specific attenuation must be calculated at various levels of the atmosphere by dividing the atmosphere into horizontal layers and specifying the pressure temperature and humidity along the path. This is where the radiosonde measurements of the profiles, given for example in recommendation ITU-R PN.835-1, come into the picture. The total attenuation along the slant path is obtained by integrating the specific attenuation over the path. Thus the total slant path attenuation from a station with some altitude, h, and elevation angle, $\varphi \geq 0$, is given as:

$$A(h,\varphi) = \int_h^\infty \frac{\gamma(H)}{\sin\Phi} dH \qquad (2.2.1.2\text{-}16)$$

where $\Phi$ is given by:

$$\Phi = \arccos\left(\frac{c}{(r+H)\times n(H)}\right) \qquad (2.2.1.2\text{-}17)$$

and

$$c = (r + h) \times n(h) \times \cos\varphi \qquad (2.2.1.2\text{-}18)$$

The *n(h)* in equation (2.2.1.2-17) is the atmospheric radio refractive index calculated from pressure, temperature and water-vapor pressure along the path using ITU-R Recommendation P.453 (1997). It must be noted that the integral will become infinite at $\Phi = 0$. This problem is alleviated by using the substitution, $u^4 = H - h$ in equation (2.2.1.2-16).

If $\varphi < 0$, then there is a minimum height, $h_{min}$, at which the radio beam becomes parallel with the Earth's surface. The value of $h_{min}$ can be determined by solving the following equation:

$$(r + h_{min}) \times n(h) = c \qquad (2.2.1.2\text{-}19)$$

This can be solved by repeating the following calculation, using $h_{min} = h$, as an initial value:

$$h'_{\min} = \frac{c}{n(h_{\min})} - r \qquad (2.2.1.2\text{-}20)$$

Thus, *A(h, φ)* can be calculated as follows:

$$A(h,\varphi) = \int_{h_{\min}}^{\infty} \frac{\gamma(H)}{\sin\Phi} dH + \int_{h_{\min}}^{h} \frac{\gamma(H)}{\sin\Phi} dH \qquad (2.2.1.2\text{-}21)$$

It must be noted that the integral will become infinite at $\Phi = 0$. This is problem is alleviated by using the substitution, $u^4 = H - h_{min}$ in equation (2.2.1.2-21).

There is a numerical algorithm that can be used instead of using the integral to compute the attenuation due to atmospheric gases and this is given next. The atmosphere is divided into layers and ray bending is accounted for at each layer. Exhibit 2.2.1.2-3 shows the geometry. In the exhibit, $a_n$ is the path length through layer *n,* the layer thickness is given as $\delta_n$ and the refractive index is $n_n$. $\alpha_n$ and $\beta_n$ are the entry and exiting incidence angles, $r_n$ are the radii from the center of the Earth to the beginning of layer *n*. Thus $a_n$ is given as follows:

$$a_n = -r_n \cos\beta_n + \frac{1}{2}\sqrt{4 r_n^2 \cos^2\beta_n + 8 r_n \delta_n + 4\delta_n^2} \qquad (2.2.1.2\text{-}22)$$

It should be noted that the layer thickness should increase exponentially with height to ensure accurate attenuation estimates. For example, accurate results can be obtained with layer thickness that increase from 10 cm for the lower layer to 1 Km at an altitude of 100 Km. For Earth-to-space applications the integration should be performed up to at least 30 Km.

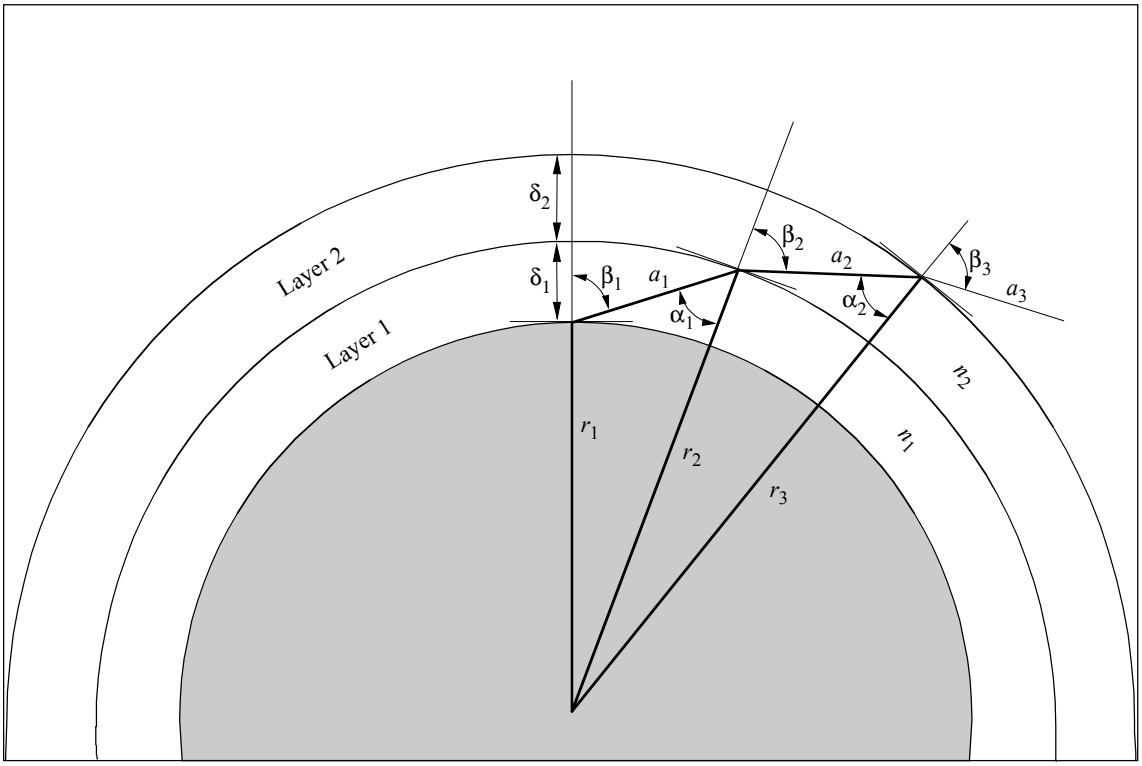


Exhibit 2.2.1.2-3
Gaseous Attenuation Layer Geometry
*[Source: ITU-R P.676-3 (1997), Figure 4]*

The angle $\alpha_n$ is given as:

$$\alpha_n = \pi - \arccos\left(\frac{-a_n^2 - 2r_n\delta_n - \delta_n^2}{2a_n r_n + 2a_n\delta_n}\right) \qquad (2.2.1.2\text{-}23)$$

The angle $\beta_n$ can be computed as follows:

$$\beta_{n+1} = \arcsin\left(\frac{n_n}{n_{n+1}}\sin\alpha_n\right) \qquad (2.2.1.2\text{-}24)$$

where $\beta_1$ is the incident angle at the ground station, and the refractive indexes at layers *n* and *n+1* are $n_n$ and $n_{n+1}$, respectively.

Thus the total path attenuation is given as

$$A_{gas} = \sum_{n=1}^{k} a_n \gamma_n \qquad \text{dB} \qquad (2.2.1.2\text{-}25)$$

where $\gamma_n$ is the specific attenuation given in equation (2.2.1.2-1).

### 2.2.1.2.2 ITU-R Gaseous Attenuation Approximation Method

Even the numerical algorithm given in the previous section to compute the slant path attenuation for the line-by-line attenuation calculation is rather intensive. To provide a reasonably accurate estimate without the computational intensity, the ITU-R has a model to approximate the line-by-line calculation. The approximation model is provided in Recommendation ITU-R P.676-3 (1997) under Annex 2.

This model provides predictions for frequencies from 1 to 350 GHz. There are two geometric scenarios modeled here. The first one pertains to a ground station situated at sea level. The other geometry is for two stations: one situated at an altitude $h_1$ Km. and the other station is situated at an altitude $h_2$ Km. The input weather parameters are barometric pressure, air temperature and water vapor density. The range of permissible elevation angles is $0 \leq \varphi \leq 90$ degrees. For elevation angles less than zero degrees, the line-by-line calculation must be used.

The approximation introduces some departure from the line-by-line calculation. The agreement is to within approximately ± 15 % on average at frequencies away from the centers of major absorption lines. The absolute difference between the results of the approximation and the line-by-line calculation is generally less than 0.1 dB/km and reaches a maximum of 0.7 dB/km near 60

GHz. The ITU-R recommends that the line-by-line calculation be used for altitudes higher than 5 Km and if higher accuracy is required.

The following describes a step-by-step procedure for calculating attenuation due to oxygen and water vapor on a slant path.

The input parameters required for the calculation are:

f: frequency (GHz)
p: pressure (hPa)
T: air temperature (degrees C)
ρ: water vapor density ($g/m^3$).

1) Calculate the specific attenuation for dry air and water vapor.

For dry air the attenuation $\gamma_o$ (dB/Km) is given by:

$$\gamma_o = \left[ \frac{7.27 r_t}{f^2 + 0.351 r_p^2 r_t^2} + \frac{7.5}{(f-5.7)^2 + 2.44 r_p^2 r_t^5} \right] f^2 r_p^2 r_t^2 \times 10^{-3} \qquad \text{for } f \leq 57 \text{ GHz}$$

(2.2.1.2-26)

$$\gamma_o = \left[ 2 \times 10^{-4} r_t^{1.5} \left(1 - 1.2 \times 10^{-5} f^{1.5}\right) + \frac{4}{(f-63)^2 1.5 r_p^2 r_t^5} + \frac{0.28 r_t^2}{(f-118.75)^2 + 2.84 r_p^2 r_t^2} \right] f^2 r_p^2 r_t^2 \times 10^{-3}$$

$$\text{for } 63 \text{ GHz} \leq f \leq 350 \text{ GHz}$$

$$\gamma_o = \frac{(f-60)(f-63)}{18} \gamma_o(f=57) - 1.66 r_p^2 r_t^{8.5} (f-57)(f-63) + \frac{(f-57)(f-60)}{18} \gamma_o(f=63)$$

$$\text{for } 57 \text{ GHz} \leq f \leq 63 \text{ GHz}$$

where:

$r_p$ = p/1013

$r_t$ = 288/(273 + T)

The contribution of water vapor is given by $\gamma_w$ (dB/Km) which is:

$$\gamma_w = \left[ \begin{array}{l} 3.27\times10^{-2} r_t + 1.67\times10^{-3} \dfrac{\rho r_t^7}{r_p} + 7.7\times10^{-4} f^{0.5} + \dfrac{3.79}{(f-22.235)^2 + 9.81 r_p^2 r_t} + .... \\ \dfrac{11.173 r_t}{(f-183.31)^2 + 11.85 r_p^2 r_t} + \dfrac{4.01 r_t}{(f-325.153)^2 + 10.44 r_p^2 r_t} \end{array} \right] f^2 \rho r_p r_t \times 10^{-4}$$

for $f \leq 350$ GHz (2.2.1.2-27)

Before proceeding further, some additional remarks about the input weather parameters are necessary. The parameters P, T and ρ are assumed to be referenced to sea level. Furthermore, if the ground station is situated at sea level then the pressure, temperature and water vapor density are input as measured at that level. If there are two stations, and one station is situated at an altitude of $h_1$ Km. then the pressure and temperature are input as measured, and water vapor density measured there is projected down to sea level. The following equation gives the value for ρ in this case, which is used in equation (2.2.1.2-27):

$$\rho = \rho_1 \times \exp(h_1/2) \quad (2.2.1.2\text{-}28)$$

The parameter $\rho_1$ is the water vapor density corresponding to station altitude $h_1$. The formula approximates the value of the water vapor density assuming the equivalent height of the water vapor density is 2 Km. The formula above is based on recommendation ITU-R P.835-2 (1997), which is the standard atmospheres reference.

2) Compute the zenith attenuation.

The total zenith attenuation is given as:

$$A = h_o \gamma_o + h_w \gamma_w \quad \text{dB} \quad (2.2.1.2\text{-}29)$$

The multipliers, $h_o$ and $h_w$ , are called the equivalent height for dry air and water vapor, respectively. Equivalent height is based on an exponential atmosphere assumption specified by a scale height to describe the decay in density with altitude. Thus for dry air, the equivalent height is given by:

$h_o = 6$ Km for $f < 50$ GHz

(2.2.1.2-30)

$h_o = 6 + 40/((f - 118.7)^2 + 1)$ Km for $70 < f < 350$ GHz

The water vapor equivalent height is given as:

$$h_w = h_{w0}\left[1 + \frac{3.0}{(f-22.2)^2+5} + \frac{5.0}{(f-183.3)^2+6} + \frac{2.5}{(f-325.4)^2+4}\right] \text{ Km} \qquad (2.2.1.2\text{-}31)$$

for $f < 350$ GHz

where $h_{wo}$ is the water vapor equivalent height in the window regions and is dependent on general weather conditions as follows:

$h_{wo}$ = 1.6 Km in clear weather
$h_{wo}$ = 2.1 Km in rain

The above values given for $h_{wo}$ were determined assuming a ground-level temperature of 15 degrees C. For other temperatures the equivalent heights are corrected by 0.1% per degree C in clear weather and 1% per degree C in rain. These corrections apply to the window regions. The correction factors are 0.2% or 2% in the absorption bands (height increasing with increasing temperature). The equations incorporating the corrections just described, for the equivalent heights that apply to the **window regions**, are as follows:

$h_{wo} = 1.6 + 0.001(T - 15) \times 1.6$ Km in clear weather

$h_{wo} = 2.1 + 0.01(T - 15) \times 2.1$ Km in rain

The equations incorporating the corrections just described, for the equivalent heights that apply to the **absorption bands**, are as follows:

$h_{wo} = 1.6 + 0.002(T - 15) \times 1.6$ Km in clear weather

$h_{wo} = 2.1 + 0.02(T - 15) \times 2.1$ Km in rain

The temperature parameter, T degrees C, is measured at the level of the station, as determined in either of the geometry scenarios above.

3) Calculate the attenuation along a slant path.

For a horizontal path, or for paths that are "slightly inclined" and close to the ground, as in terrestrial paths, the attenuation is written as

$$A = \gamma r_0 = (\gamma_o + \gamma_w)\, r_0 \quad \text{dB} \qquad (2.2.1.2\text{-}32)$$

where $r_0$ is the path length (Km).

For space to ground slant path calculations, there are two calculations, based on the range of elevation angle, φ degrees.

3a) Elevation angle range $10 \le \varphi \le 90$ degrees

The first slant path attenuation pertains to elevation angles in the range $10 \le \varphi \le 90$ degrees. This is a simple cosecant law and is given as follows:

$$A_{slant} = ( h_o \gamma_o + h_w \gamma_w )/ \sin \varphi \ \text{dB} \qquad (2.2.1.2\text{-}33)$$

In this case the ground station is assumed to be situated at sea level. The vertical extent is from sea level to 5 Km. In the case where an inclined path exists between a station at an altitude $h_1$ Km. and another at a higher altitude $h_2$ Km. the values $h_o$ and $h_w$ must be replaced by the values, $h'_o$ and $h'_w$ as follows:

$$h'_o = h_o \left[ \exp( -h_1 / h_o ) - \exp( -h_2 / h_o) \right] \quad \text{Km} \qquad (2.2.1.2\text{-}34)$$

$$h'_w = h_w \left[ \exp( -h_1 / h_w ) - \exp( -h_2 / h_w) \right] \quad \text{Km}$$

3b) Elevation angle range $0 \le \varphi < 10$ degrees

The total path attenuation for a system geometry in which the elevation angle is in the interval $0 \le \varphi < 10$ degrees is considerably more involved, for both geometry scenarios. This calculation is used to provide a more accurate representation of the real length of the atmospheric path. Thus for an inclined path between the satellite and a ground station situated at sea level the total path attenuation is given as follows:

$$A_{slant} = \frac{\sqrt{R_e}}{\cos\varphi}\left[ \gamma_o \sqrt{h_o} F\left( \tan\varphi \sqrt{\frac{R_e}{h_o}} \right) + \gamma_w \sqrt{h_w} F\left( \tan\varphi \sqrt{\frac{R_e}{h_w}} \right) \right] \text{dB} \qquad (2.2.1.2\text{-}35)$$

where:

Re: effective radius of the Earth, including refraction. The value is 8500 Km. See Recommendation ITU-R P.834-2 (1997).

φ: elevation angle

F: is a function defined as follows:

$$F(x) = \frac{1}{0.661x + 0.339\sqrt{x^2 + 5.51}} \qquad (2.2.1.2\text{-}36)$$

If the inclined path is defined between an earth station at an altitude $h_1$ and one at a higher altitude $h_2$ ( both altitudes must be less than 1000 m above mean sea level) then the following path attenuation must be used:

$$A = \gamma_o \sqrt{h_o}\left[\frac{\sqrt{R_e + h_1}F(x_1)e^{-h_1/h_o}}{\cos\varphi_1} - \frac{\sqrt{R_e + h_2}F(x_2)e^{-h_2/h_o}}{\cos\varphi_2}\right] + \gamma_w \sqrt{h_w}\left[\frac{\sqrt{R_e + h_1}F(x_1')e^{-h_1/h_w}}{\cos\varphi_1} - \frac{\sqrt{R_e + h_2}F(x_2')e^{-h_2/h_w}}{\cos\varphi_2}\right] \text{ dB} \qquad (2.2.1.2\text{-}37)$$

where

$\varphi_1$: elevation angle at altitude $h_1$.

$$\varphi_2 = \arccos\left(\frac{R_e + h_1}{R_e + h_2}\cos\varphi_1\right) \qquad (2.2.1.2\text{-}37a)$$

$$x_i = \tan\varphi_i \sqrt{\frac{R_e + h_i}{h_o}} \qquad \text{for } i = 1,2 \qquad (2.2.1.2\text{-}37b)$$

$$x_i' = \tan\varphi_i \sqrt{\frac{R_e + h_i}{h_w}} \qquad \text{for } i = 1,2 \qquad (2.2.1.2\text{-}37c)$$

The water vapor density at sea level is given exactly as in equation (2.2.1.2-28).

### 2.2.1.2.3 Sample Calculation – ITU-R Line-by-Line model

This section contains an example calculation using the ITU Approximation to the Line-by-line model. The approximation method was designed to provide reasonably accurate answers with minimal calculation effort.

Assume the following input parameters for a Ka-band link:

| | |
|---|---|
| Frequency: | f = 29.3 GHz |
| Path elevation angle: | $\varphi$ = 38 degrees |
| Surface water vapor density: | $\rho$ = 7.5 g/m$^3$ |
| Surface air temperature: | T = 20 degrees C |
| Surface barometric pressure: | 1013 hPa |
| Station Altitude | 0 km |

Assume clear weather, i.e., no rain.

Step 1:
Compute the specific attenuation

$$f = 29.3 \text{ GHz}, r_p = 1013/1013, r_t = 288/293.$$

Applying eq's. (2.2.1.2-26) and (2.2.1.2-27), $\gamma_o = 0.041498$ dB/km and $\gamma_w = 0.070617$ dB/km.

Step 2:
Compute the total zenith attenuation.

First it is necessary to compute the equivalent heights $h_o$ and $h_w$. Since f < 50 GHz, applying equation (2.2.1.2-30) gives $h_o = 6$.

$h_w$ is obtained by equation (2.2.1.2-31) using $h_{wo} = 1.6 + 0.001(20\text{-}15)\times 1.6$ Km.

Equation (2.2.1.2-29) gives the total zenith attenuation $A = h_o \gamma_o + h_w \gamma_w$ dB.
Thus $A = 0.041498 \times 6 + 0.07061728 \times 1.69544487$.
$= 0.36871889$ dB

Step 3:
Compute the slant path attenuation.

Since $\varphi$ = 38 degrees, equation (2.2.1.2-33) is used. $A_{slant} = ( h_o \gamma_o + h_w \gamma_w )/ \sin \varphi$ dB.

$A_{slant} = 0.36871889/0.61566$ dB.
$= 0.5989$ dB or 0.60 dB

### 2.2.2 Cloud Attenuation

Clouds (and fog) may be categorized generically as hydrosols. Hydrosols are suspended droplets of liquid water, which are typically less than 0.01 cm in diameter. Attenuation models such as the ITU-R model and the Liebe Complex Refractivity Model do not differentiate between clouds and fog though the inputs of typical values for each may be slightly different.

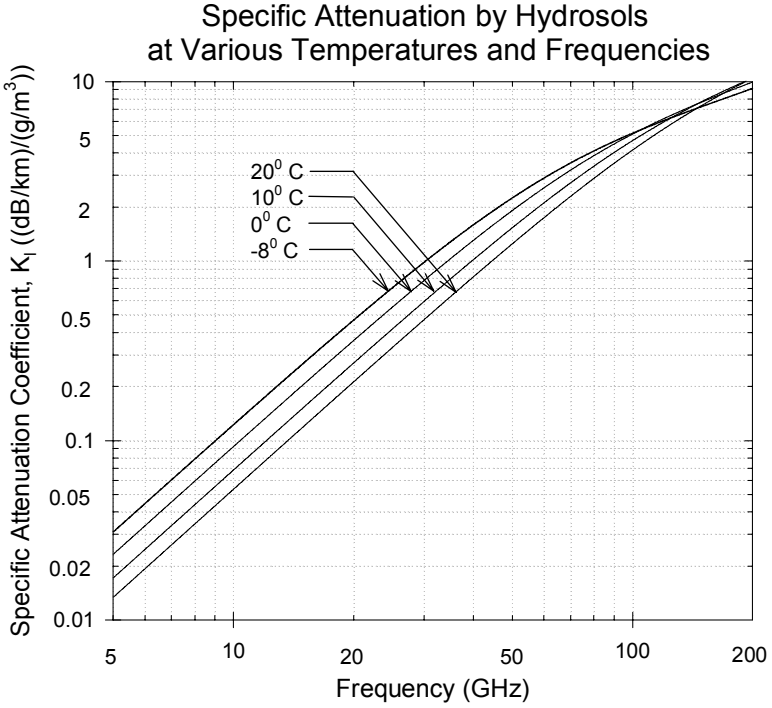


Exhibit 2.2.2-1
Specific Attenuation Due to Hydrosols

The attenuation caused by hydrosols becomes significant particularly for systems operating above 20 GHz. This significance becomes more prominent with increasing frequency and decreasing elevation angle. Portion of clouds and fog that are frozen do not cause significant attenuation though they may be responsible for signal depolarization.

#### 2.2.2.1 The ITU-R Cloud Attenuation Model

The ITU-R provides a simple model to calculate the attenuation along an RF Earth-space path for both clouds and fog in Recommendation ITU-R P.840-2 (1997). The model was originally adopted into Recommendation P.840 in 1992 and has since been updated in 1994 and 1997. It is valid for liquid water only and is applicable for systems operating at up to 200 GHz. Only three

inputs are required: frequency (GHz), elevation angle (°), and the total columnar liquid water content of the cloud or fog ($kg/m^2$).

To begin, the model requires the calculation of the complex dielectric permitivity of water. This is performed in the following steps:

1) Calculate the inverse temperature constant, $\Phi$, according to

$$\Phi=300/T \qquad (2.2.2.1\text{-}1)$$

where T is the temperature in K.

If the model is being performed for clouds, T may be assumed as 273.15K. If the model is being performed for fog, T is equal to the ground temperature.

2) Calculate the principal and secondary relaxation frequencies of the double-Debye model for the dielectric permittivity of water

$$f_p=20.09-142\cdot(\Phi-1)+294\cdot(\Phi-1)^2$$
$$f_s=590-1500\cdot(\Phi-1) \qquad (2.2.2.1\text{-}2)$$

3) Calculate the complex dielectric permittivity of water

$$\varepsilon''(f)=\frac{f\cdot(\varepsilon_0-\varepsilon_1)}{f_p\cdot\left[1+\left(\frac{f}{f_p}\right)^2\right]}+\frac{f\cdot(\varepsilon_1-\varepsilon_2)}{f_s\cdot\left[1+\left(\frac{f}{f_s}\right)^2\right]} \qquad (2.2.2.1\text{-}3)$$

$$\varepsilon'(f)=\frac{\varepsilon_0-\varepsilon_1}{\left[1+\left(\frac{f}{f_p}\right)^2\right]}+\frac{(\varepsilon_1-\varepsilon_2)}{\left[1+\left(\frac{f}{f_s}\right)^2\right]}+\varepsilon_2$$

where

$\varepsilon_0 = 77.6+103.3\cdot(\Phi-1)$,
$\varepsilon_1=5.48$, and
$\varepsilon_2 = 3.51$.

4) Calculate the specific attenuation coefficient, $K_l$ $(dB/km)/(g/m^3)$, by:

$$K_l = 0.819f/(\varepsilon''(1+\eta^2)) \text{ where } \eta=(2+\varepsilon')/\varepsilon'' \qquad (2.2.2.1\text{-}4)$$

The specific attenuation coefficient represents the "point" attenuation at the specified frequency and a given water vapor concentration.

5) The total attenuation due to clouds is then computed by multiplying the specific attenuation coefficient, $K_l$, by the total columnar liquid water content of the cloud, L, and dividing by the sine of the elevation angle.

$$A=L \cdot K_l / \sin(\theta) \qquad (2.2.2.1\text{-}5)$$

In cases where the statistics of cloud liquid water content are not available for the location(s) of interest, the ITU-R provides global maps which show contours of cloud liquid. Exhibits 2.2.2.1-1 through 2.2.2.1-4 present contours of cloud liquid water content not exceeded for 80%, 90%, 95%, and 99% of an average year, respectively. Global contours of fog are not provided, however the ITU-R suggests using 0.05 g/m3 for medium fog and 0.5 g/m3 for thick fog.

### 2.2.2.2 Practical Issues in Using the ITU-R Model

In using the ITU-R cloud attenuation model (or any other cloud attenuation model) a few common "rules of thumb" and insights into the models themselves can prove helpful.

- If more precise estimations of local conditions are desired, statistics of cloud liquid water can also be derived using cloud detection algorithms along with radiosonde data (Barbalicia, 1996). Radiosondes do not explicitly measure cloud liquid water, but these algorithms can provide an empirical relationship between meteorological conditions at a sounding level and the amount of cloud liquid water density present at that location.

- Columnar cloud liquid water is sometimes represented in mm rather than $kg/m^2$. By using the identity that 1 g of water occupies 1 $cm^3$ of space it can be shown that:

  $$1kg/m^2 = 1000\ g/m^2 = 1000\ cm^3/m^2 = 1000\ cm^3 / 10000\ cm^2 = .1\ cm = 1mm.$$

  Some models such as those referenced in (Slobin, 1982) and (Salonen, 1990) discuss cloud liquid water content in terms of water density in units of $g/m^3$. In this case the density must be multiplied by the clouds overall thickness. Assuming no local cloud thickness data is available a good typical values is about 1km. When quick, "back of the envelope" calculations of cloud attenuation are desired for a generic location it is suggested to use a cloud liquid water content of 0.5 $kg/m^2$. This value represents a good "rule of thumb" though in extreme cases the value could be three to four times higher.

- The elevation angle scaling term in step 5) of the ITU-R model is a simple $1/\sin(\theta)$ relationship. This is a reasonable approximation for elevation angles above about 10°. At elevation angles below about 10° an additional effect must be considered. The $1/\sin(\theta)$ relationship assumes that clouds are infinitely wide. Therefore, as the elevation angle approaches 0°, the cloud attenuation approaches ∞. In reality, clouds typically only extend several km in width. Therefore, a physical limit to the path length should be imposed when performing low elevation angle calculations.

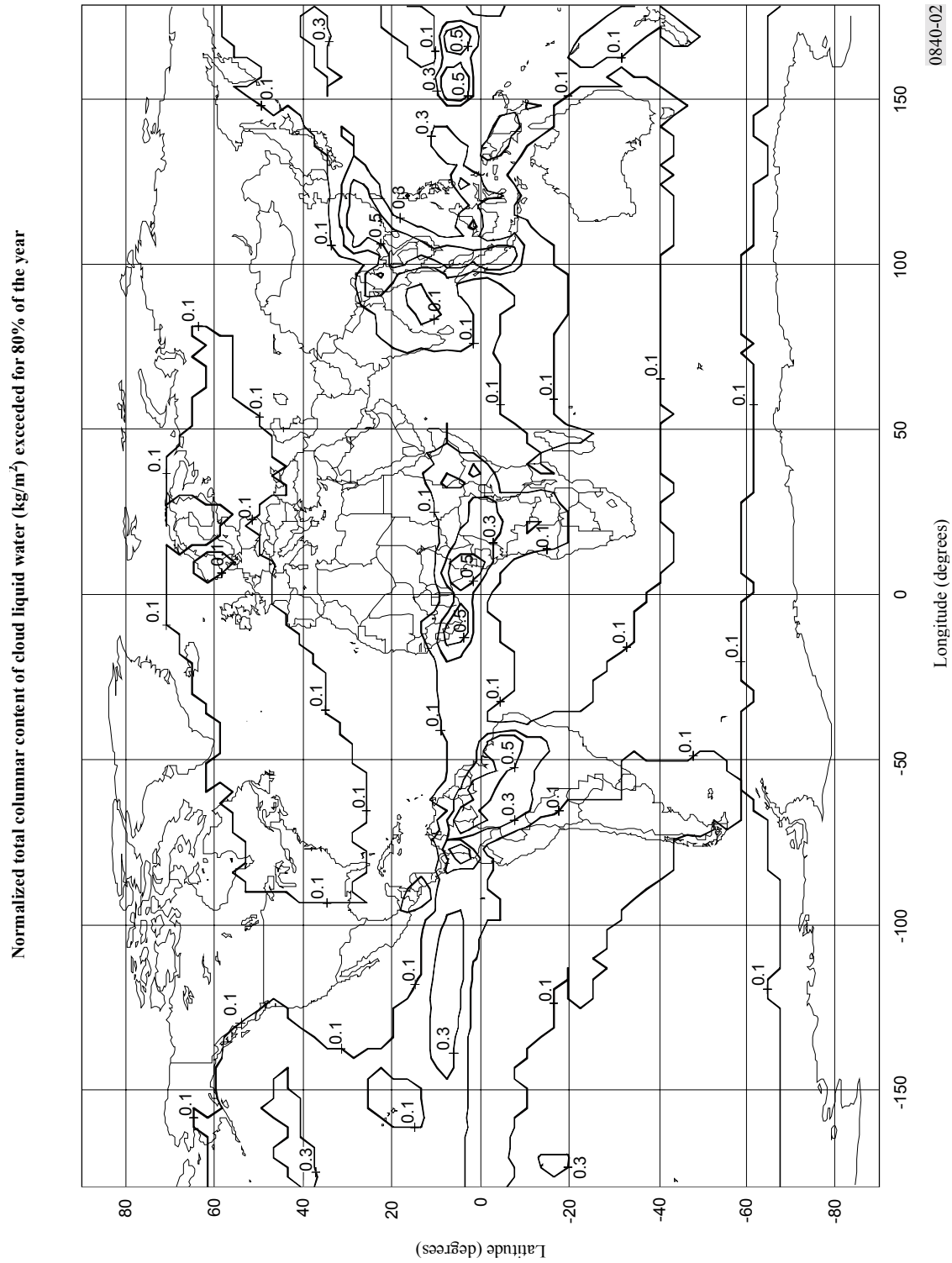


Exhibit 2.2.2.1-1
ITU-R Recommended Contours of Cloud Liquid Water Not Exceeded 80% of the Time
*[Source: ITU-R P.840-2 (1997)]*

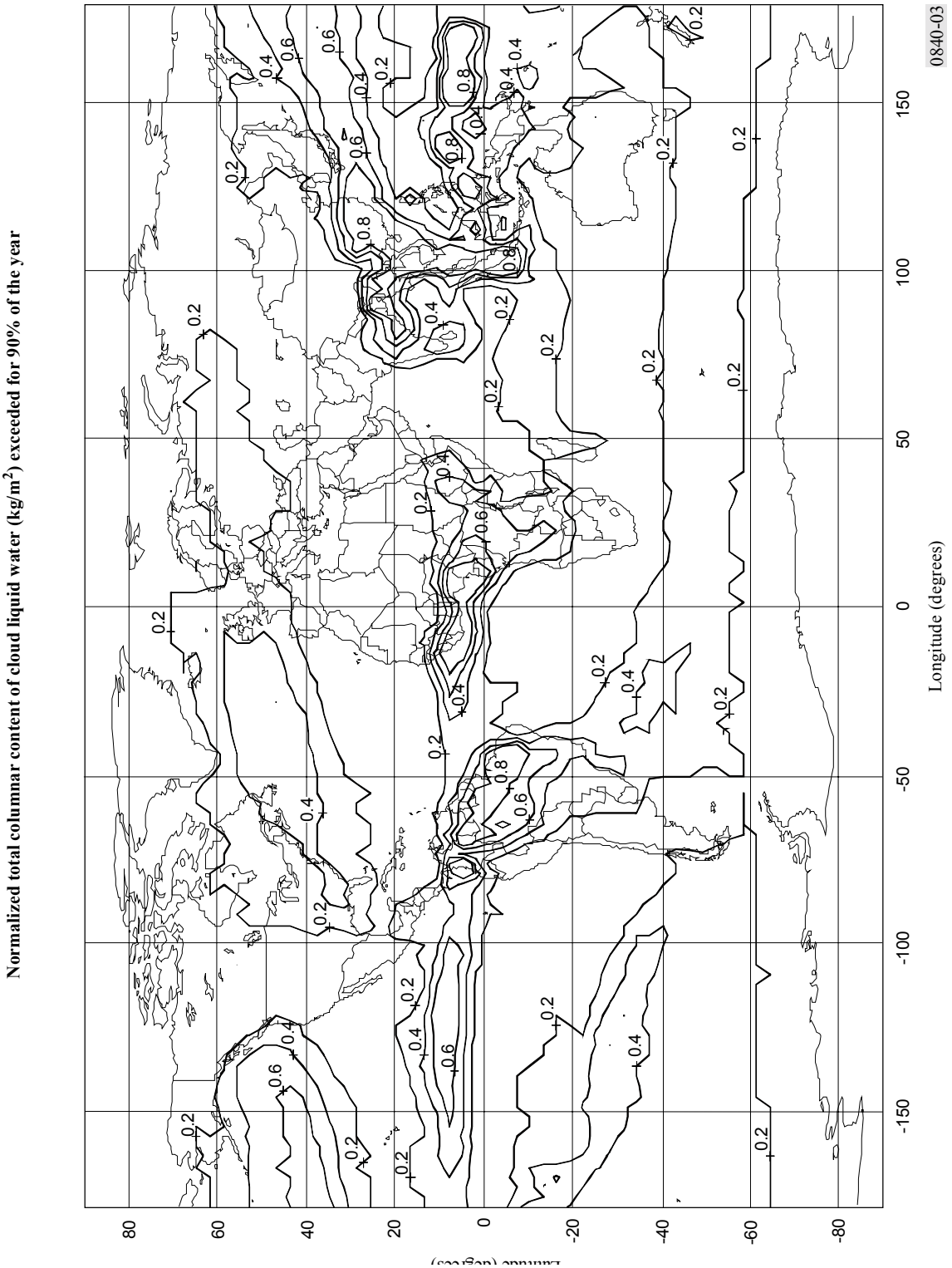


Exhibit 2.2.2.1–2
ITU-R Recommended Contours of Cloud Liquid Water Not Exceeded 90% of the Time
*[Source: ITU-R P.840-2 (1997)]*

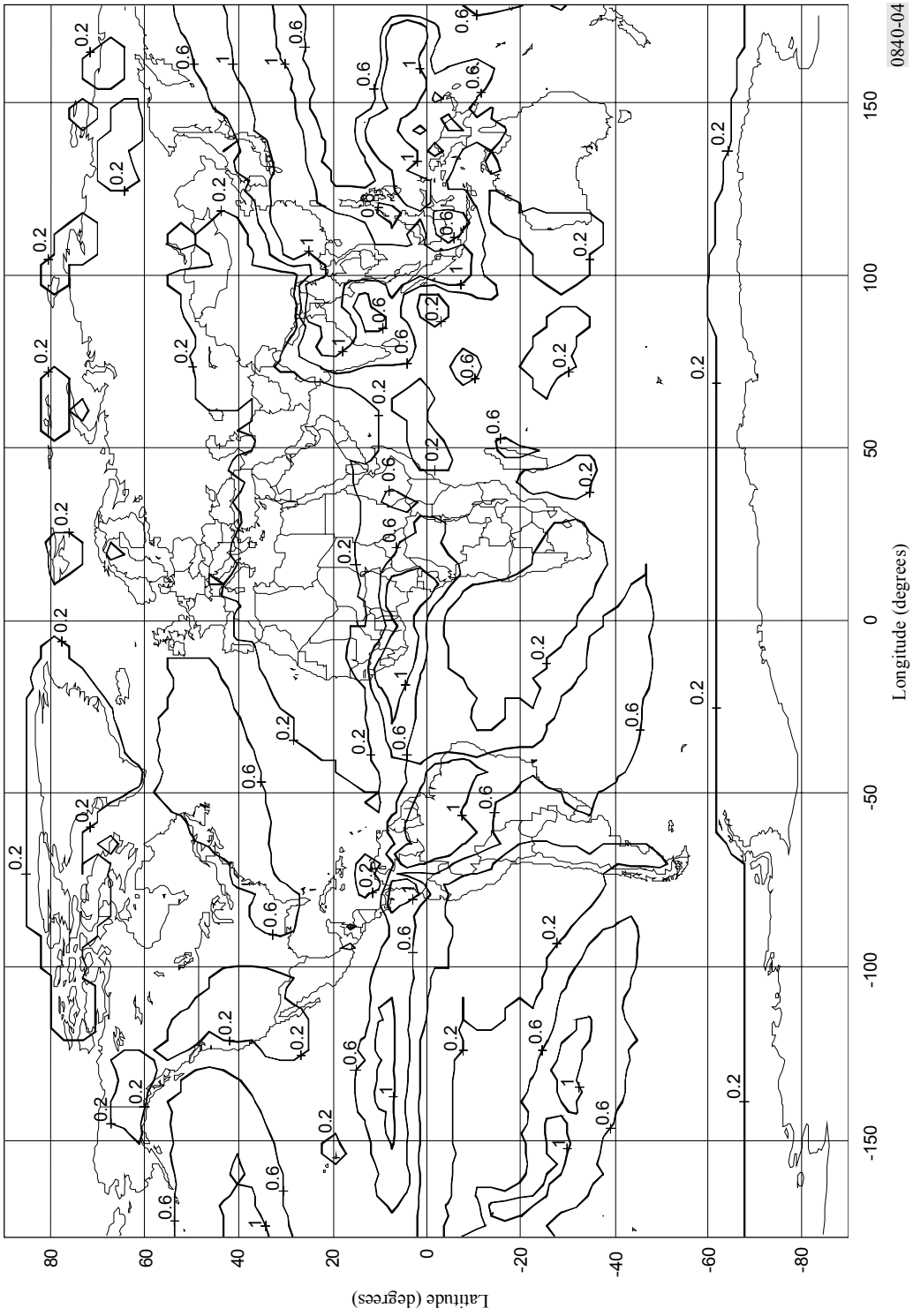


Exhibit 2.2.2.1–3
ITU-R Recommended Contours of Cloud Liquid Water Not Exceeded 95% of the Time
*[Source: ITU-R P.840-2 (1997)]*

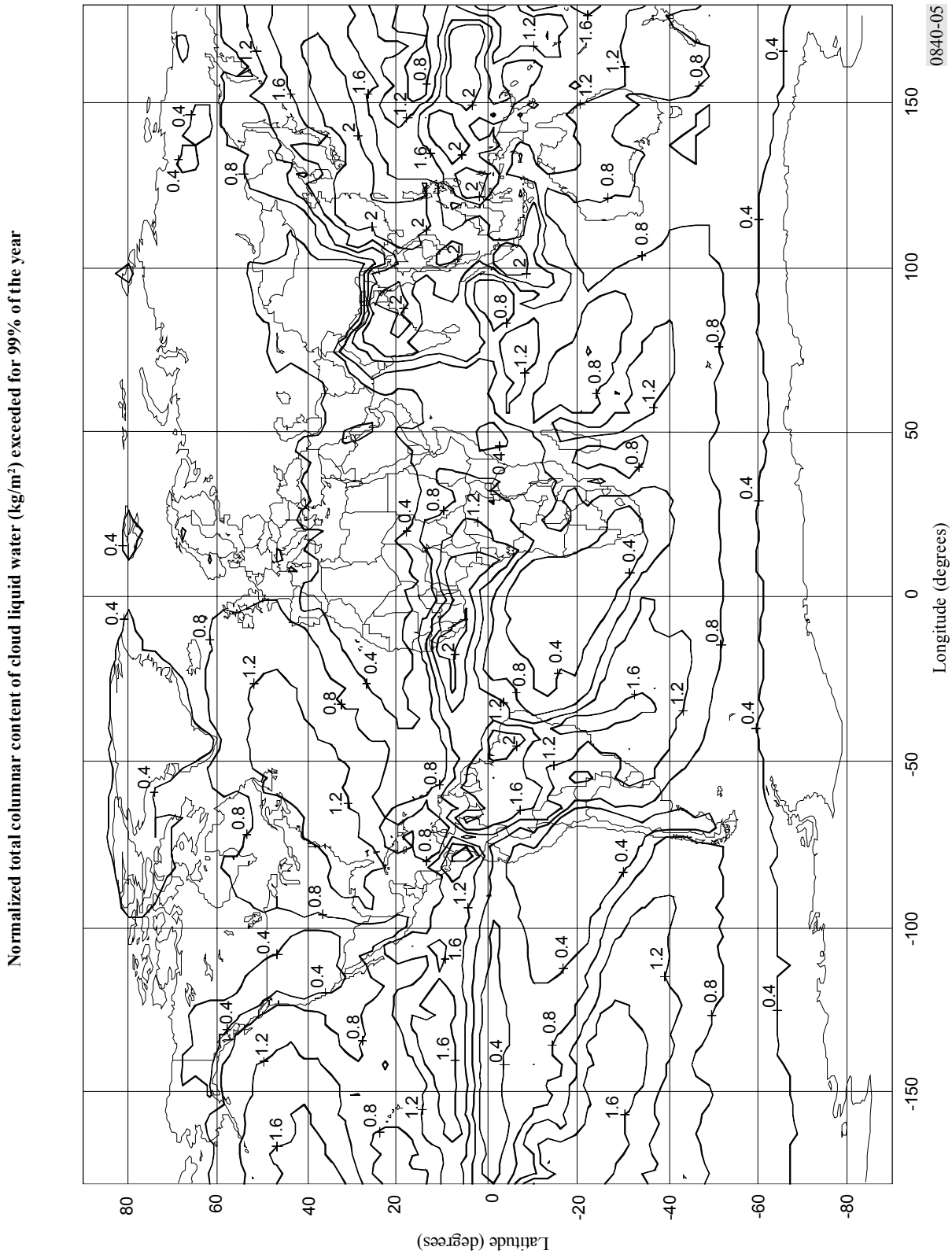


Exhibit 2.2.2.1 – 4

ITU-R Recommended Contours of Cloud Liquid Water Not Exceeded 99% of the Time

*[Source: ITU-R P.840-2 (1997)]*

### 2.2.2.3 Slobin Cloud Model

A detailed study of the radiowave propagation effects of clouds at various locations in the contiguous United States, Alaska, and Hawaii by Slobin (1982) resulted in the development of a cloud model that determines cloud attenuation and noise temperature on satellite paths. Extensive data on cloud characteristics, such as type, thickness, and coverage, were gathered from twice-daily radiosonde measurements and hourly temperature and relative humidity profiles.

Twelve cloud types are defined in the Slobin model, based on liquid water content, cloud thickness, and base heights above the surface. Several of the more intense cloud types include two cloud layers, and the combined effects of both are included in the model. Exhibit 2.2.2.3-1 lists seven of the Slobin cloud types, labeled here from light, thin clouds to very heavy clouds, and shows the characteristics of each. The case numbers listed in the table correspond to the numbers assigned by Slobin.

| Cloud Type | Case No. | Liquid Water ($g/m^3$) | Lower Cloud | | Upper Cloud | |
|---|---|---|---|---|---|---|
| | | | Base (km) | Thickness (km) | Base (km) | Thickness (km) |
| Light, Thin | 2 | 0.2 | 1.0 | 0.2 | -- | -- |
| Light | 4 | 0.5 | 1.0 | 0.5 | -- | -- |
| Medium | 6 | 0.5 | 1.0 | 1.0 | -- | -- |
| Heavy I | 8 | 0.5 | 1.0 | 1.0 | 3.0 | 1.0 |
| Heavy II | 10 | 1.0 | 1.0 | 1.0 | 3.0 | 1.0 |
| Very Heavy I | 11 | 1.0 | 1.0 | 1.5 | 3.5 | 1.5 |
| Very Heavy II | 12 | 1.0 | 1.0 | 2.0 | 4.0 | 2.0 |

Exhibit 2.2.2.3-1
Characteristics of Slobin Model Cloud Types
*[Source: Ippolito (1986)]*

The total zenith ($90^o$ elevation angle) attenuation was calculated by radiative transfer methods for frequencies from 10 to 50 GHz for each of the cloud types. Exhibit 2.2.2.3-2 presents a summary of zenith cloud attenuation for several of the frequency bands of interest. The values include the clear air gaseous attenuation also. The values at C-band and Ku-band are less than 1 dB, even for the most intense cloud types.

| Frequency (GHz) | Light Thin Cloud | Light Cloud | Medium Cloud | Heavy Clouds I | Heavy Clouds II | Very Heavy Clouds I | Very Heavy Clouds II |
|---|---|---|---|---|---|---|---|
| 6 / 4 | <0.1 dB | <0.1 dB | <0.2 dB | <0.2 dB | <0.2 dB | <0.3 dB | <0.3 dB |
| 14 / 12 | 0.1 | 0.15 | 0.2 | 0.3 | 0.45 | 0.6 | 0.9 |
| 17 | 0.2 | 0.22 | 0.3 | 0.45 | 0.7 | 1.0 | 1.4 |
| 20 | 0.25 | 0.3 | 0.4 | 0.6 | 0.9 | 1.4 | 1.8 |
| 30 | 0.3 | 0.4 | 0.5 | 1.0 | 1.7 | 2.7 | 3.9 |
| 42 | 0.7 | 0.9 | 1.2 | 2.1 | 3.5 | 5.5 | 7.9 |
| 50 | 1.5 | 1.9 | 2.3 | 3.6 | 5.7 | 8.4 | 11.7 |

Exhibit 2.2.2.3-2
Cloud Attenuation at Zenith (90$^{o}$ Elevation Angle) from the Slobin Model
*[Source: Ippolito (1986)]*

The Slobin model also developed annual cumulative distributions of cloud attenuation for specified cloud regions at fifteen frequencies from 8.5 to 90 GHz. Slobin divided the U.S. into fifteen regions of statistically "consistent" clouds, as shown in Exhibit 2.2.2.3-3. The region boundaries are highly stylized and should be interpreted liberally. Some boundaries coincide with major mountain ranges (Cascades, Rockies, and Sierra Nevada), and similarities may be noted between the cloud regions and the rain rate regions of the Global Model. Each cloud region is characterized by observations at a particular National Weather Service observation station. The locations of the observation sites are shown with their three-letter identifiers on the map. For each of these stations, an "average year" was selected on the basis of rainfall measurements. The "average year" was taken to be the one in which the year's monthly rainfall distribution best matched the 30-year average monthly distribution. Hourly surface observations for the "average year" for each station were used to derive cumulative distributions of zenith attenuation and noise temperature due to oxygen, water vapor, and clouds, for a number of frequencies ranging from 8.5 to 90 GHz.

The following procedure was employed by Slobin to calculate the cumulative distributions.

- For each hour's observations, the attenuation of each reported cloud layer (up to four) was calculated based on the layer's water particle density, thickness, and temperature. The attenuation due to water vapor and oxygen was also found using the reported surface conditions.

- Total attenuation and noise temperature due to all cloud layers and gases were calculated for sixteen possible cloud configurations, corresponding to all combinations of cloud presence or absence at the four layer heights.

- Cumulative probability distributions for attenuation and noise temperature were calculated using the reported percent-coverage values corresponding to each cloud layer. For example,

if the percentage of coverage was 60 percent for layer 1 and 20 percent for layer 2, then the probability of various configurations of clouds present in the antenna beam would be as follows:

| | |
|---|---|
| no clouds present: | (1-.6) (1-.2) = 0.32 |
| layer 1 clouds only present: | (.6) (1-.2) = 0.48 |
| layer 2 clouds only present: | (1-.6) (.2) = 0.08 |
| clouds in both layers present: | (.6) (.2) = 0.12 |

Exhibit 2.2.2.3-4 shows an example of the distributions at a frequency of 30 GHz for five cloud regions, ranging from very dry, clear Yuma to very wet, cloudy Lihue. Exhibit 2.2.2.3-5, a through d, shows examples of the attenuation distributions for four of the cloud regions, Denver, New York, Miami, and Oakland, at frequencies of 10, 18, 32, 44, and 90 GHz. Plots for all of the cloud regions are available in the Slobin (1982) reference.

The distributions give the percent of the time that cloud attenuation is the given value or less. For example, on the Miami plot, the cloud attenuation was 0.6 dB or less for 0.5 (50 %) of the time at 32 GHz. Values of attenuation in the distribution range 0 to 0.5 (0 to 50 %) may be regarded as the range of clear sky effects. The value of attenuation at 0 % is the lowest value observed for the test year.

It should be noted that the curves apply to zenith paths only, but can be extended to slant paths using a cosecant law. Such extension will probably lead to overestimation at low elevation angles and small time percentages. This is because clouds with large vertical development have less thickness for slant paths than for zenith paths. At time percentages where rain effects become significant (cumulative distributions exceeding about than 5%), the attenuation and noise temperature due to the rain should be considered also.

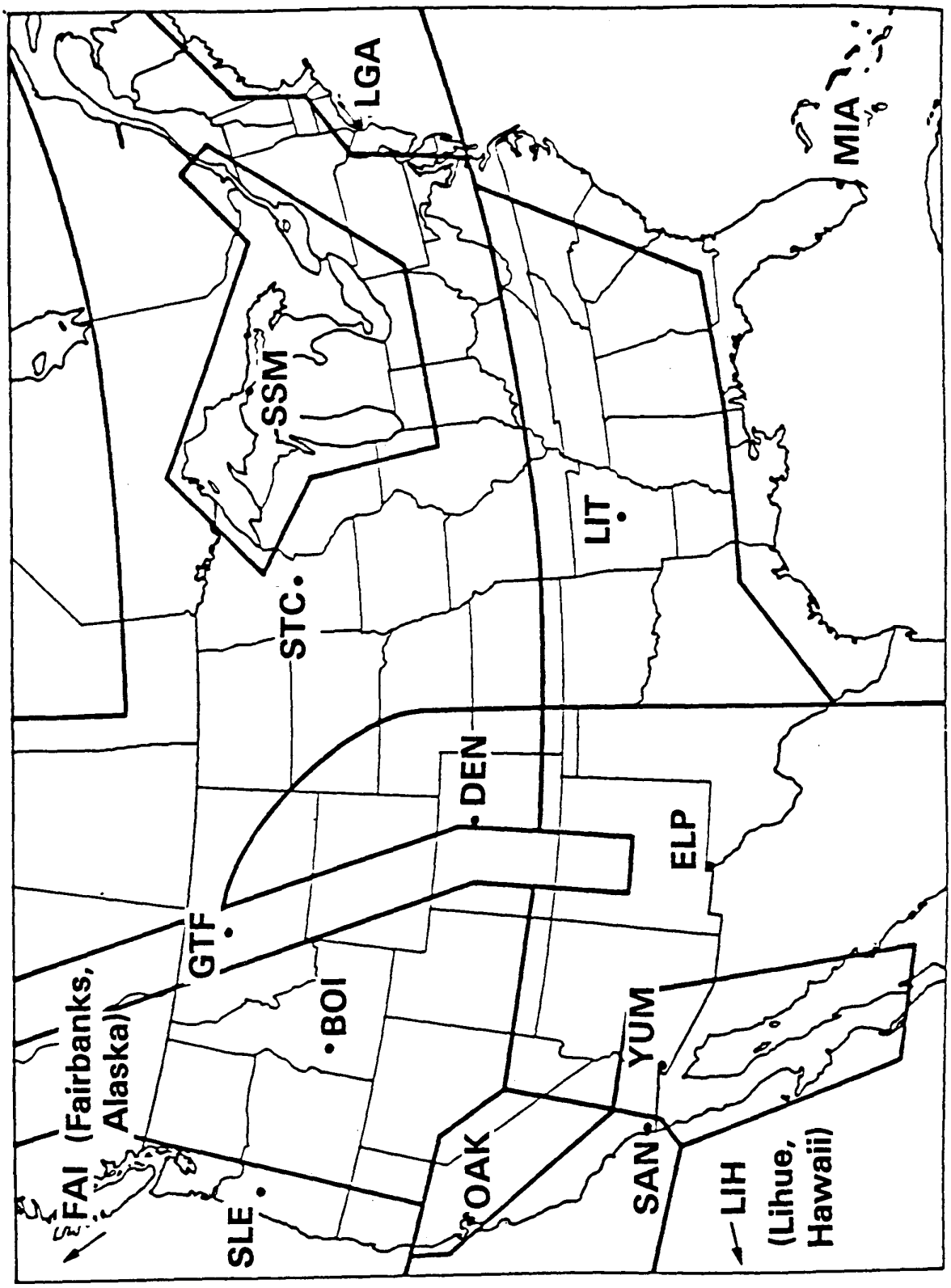


Exhibit 2.2.2.3-3
Slobin Cloud Regions
*[Source: Slobin (1982)]*

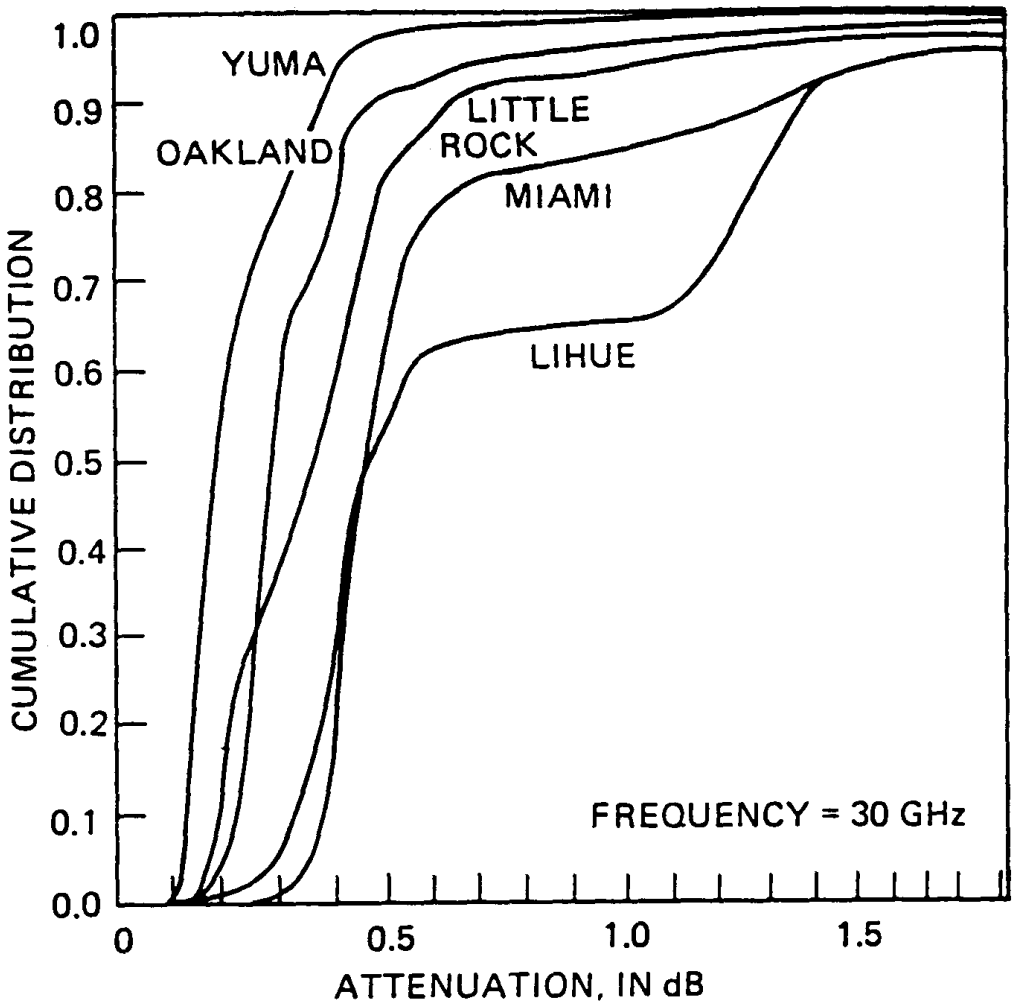


Exhibit 2.2.2.3-4
Zenith Cloud Attenuation at 30 GHz from the Slobin Cloud Model
*[Source: Slobin (1982)]*

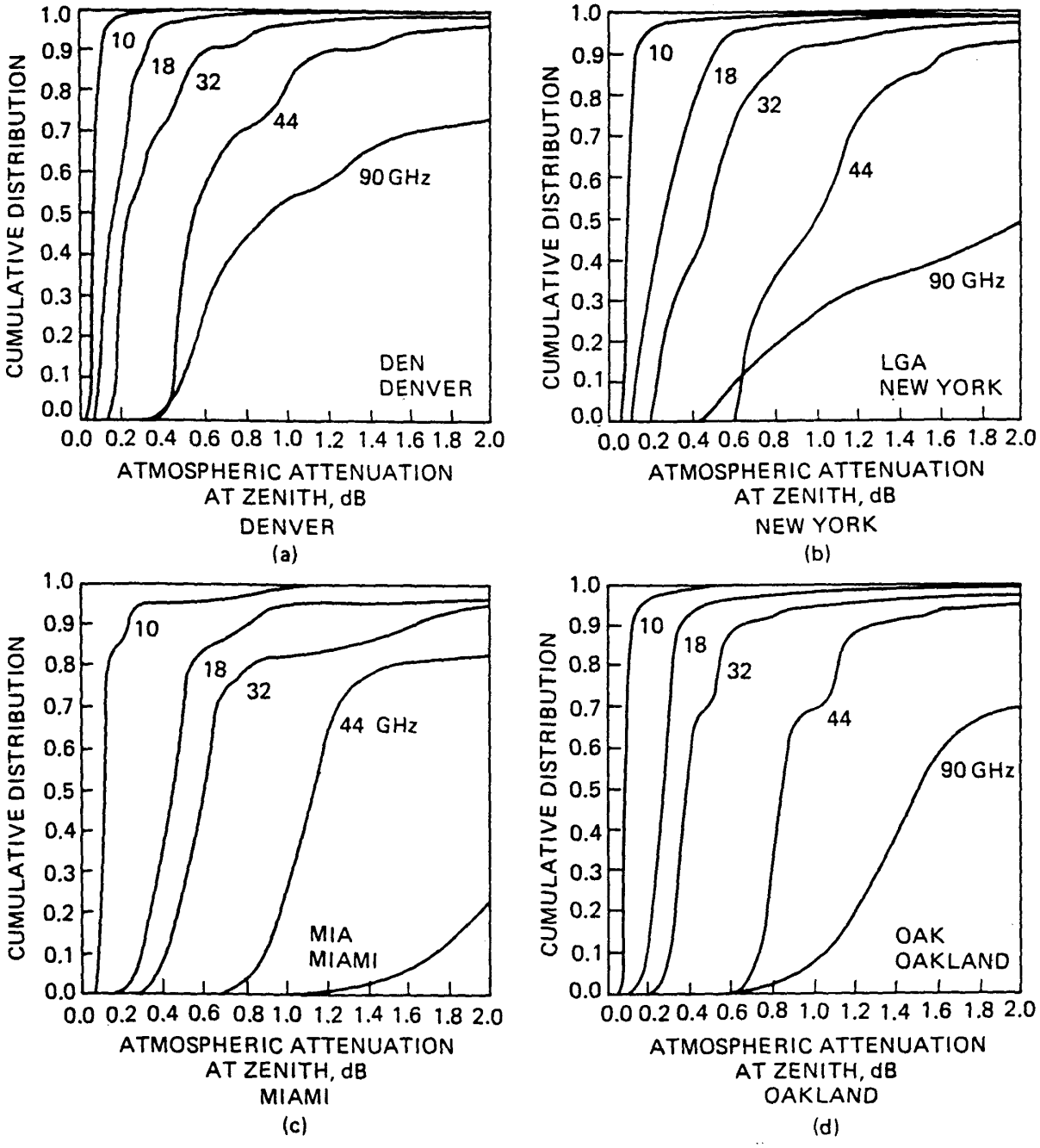


Exhibit 2.2.2.3-5
Cumulative Distributions of Zenith Cloud Attenuation at Four Locations, From the Slobin Cloud Model
*[Source: Slobin (1982)]*

### 2.2.3 Fog Attenuation

Fog results from the condensation of atmospheric water vapor into water droplets that remain suspended in air. Fog is characterized by optical visibility, which is defined as the distance over which a black target against the sky horizon background can just be discerned by the human eye. The international definition of fog is satisfied when visibility is less than one kilometer (Koester and Kosowsky-1970).

There are two main types of fog, differing in the locale and method of formation.

Advection fog is coastal fog that forms when warm, moist air moves over colder water. The liquid water content of advection fog does not normally exceed 0.4 g/m$^3$.

Radiation fog forms inland at night, usually in valleys and low marshes, and along rivers. Radiation fog can have a liquid water content up to 1 g/m$^3$.

Empirical relations have been found (Koester and Kosowsky-1970) between the liquid water content, $\rho_l$, and the visibility, V(km):

$$\rho_l = (18.35\ V)^{-1.43} \quad \text{for advection fog} \qquad (2.2.3\text{-}1)$$

$$\rho_l = (42.00\ V)^{-1.54} \quad \text{for radiation fog} \qquad (2.2.3\text{-}2)$$

#### 2.2.3.1 Altshuler Model

A relatively simple procedure for the estimation of fog attenuation from fog density or fog visibility data has been developed by Altshuler (1984). A regression analysis was performed on a large set of fog attenuation data over a wide range of frequencies (10 to 100 GHz) and temperatures (-8 to 25°C), using tabulated values of indices of refraction. The resulting analysis produced the following expression:

$$a_f = -1.347 + \frac{11.152}{f} + 0.060f - 0.022T \qquad (2.2.3.1\text{-}1)$$

where

$a_f$ is the normalized fog attenuation, in dB/km/g/m$^3$
f is the frequency in GHz, and
T is the temperature in °C

The total fog attenuation is found by multiplying $a_f$ by the fog density, in g/m$^3$, and the fog extent, in km. Unfortunately, the fog density is not easily obtainable, and can vary greatly. Fog, however, is often characterized by visibility, which is much easier to measure than fog density.

The fog density, M, is empirically related to the visibility, V by;

$$M = \left( \frac{0.024}{V} \right)^{1.54} \qquad (2.2.3.1\text{-}2)$$

where V is in km, and M is in $g/m^3$.

The total fog attenuation, $A_f$(dB), is then available from

$$A_f\,(dB) = a_f * M * L_f \qquad (2.2.3.1\text{-}3)$$

where $L_f$ is the fog extent, in km.

The standard error of the estimation procedure described above is 0.14 db. The author recommends in a later publication that the procedure should not be used for frequencies below 30 GHz, since the error is comparable in magnitude to the fog attenuation itself (Altshuler-1986).

### 2.2.3.2 Sample Calculation

As an example of an application of the procedure, consider a link at 44 GHz, with a fog visibility of 120 m (0.12 km). The fog density is then

$$M = \left( \frac{0.024}{0.12} \right)^{1.54} = 0.0839 \qquad g/m^3$$

The normalized fog attenuation, at a temperature of 25°C, will be, from Equation (2.2.3.1-1)

$$a_f = 0.996 \text{ db/km/g/m}^3$$

The total fog attenuation, assuming a fog extent of 2 km, will then be, from Equation (2.2.3.1-3)

$$A_f\,(dB) = (0.996)(0.0839)(2) = 0.167 \text{ dB}$$

The fog attenuation, as expected, is very low, and is not usually a factor in satellite link system design for frequencies below 100 GHz.

## 2.2.4 Rain Attenuation

The most significant impairment to radiowave transmission through the atmosphere in the frequency bands above about 3 GHz is rain attenuation. The evaluation of the effects of rain on a satellite system design requires a detailed knowledge of the attenuation statistics for each ground terminal location at the specific frequency of interest. Direct long-term measurements of rain attenuation for all of the ground terminal locations in an operational network are usually not available, therefore modeling and prediction methods must be used to make a best estimate of the expected rain attenuation for each location. Over the past several years extensive efforts have been undertaken to develop reliable techniques for the prediction of path rain attenuation for a given location and frequency, and the availability of satellite beacon measurements has provided a data base for the validation and refinement of the prediction models. This section presents several of the more promising rain attenuation prediction techniques, and includes step by step procedures where applicable.

Most rain attenuation prediction models use surface measured rain rate as the statistical variable and assume an $aR^b$ relationship to determine the rain induced attenuation, expressed as attenuation per unit length, usually dB per kilomenter (dB/km). The resultant total path attenuation is then of the form

$$A_T(dB) = aR^b L(R) \qquad (2.2.4\text{-}1)$$

where R is the rain rate, a and b are the frequency dependent attenuation coefficients, and L(R) is an `effective' path length parameter, usually a specified function of R. The path length parameter L(R) is the mapping function which provides rain attenuation from a specified rain rate distribution, through Exhibit 2.2.4-1. The major difference between the various rain attenuation prediction methods is in the rationale used to develop the path length parameter L(R).

The rain attenuation prediction methods described here are:

| | Section |
|---|---|
| • ITU-R Rain Model | 2.2.4.1 |
| • Crane Global Model | 2.2.4.2 |
| • Crane Two-Component Model | 2.2.4.3 |
| • DAH Model (“USA Model”) | 2.2.4.4 |
| • ExCell Rain Attenuation Model | 2.2.4.5 |
| • Manning Model | 2.2.4.6 |

### 2.2.4.1 ITU-R Rain Model

The ITU-R rain attenuation model is the most widely accepted model by the international propagation community. The model was first accepted globally in 1982 and is continuously updated as rain attenuation modeling is better understood. The current model has been deliberately kept simple for ease of use. This section describes the ITU-R model as described in the latest version of Recommendation ITU-R P.618-5, (1997).

The input parameters required for the ITU-R Rain Model are:

f: the frequency of operation, in GHz
θ: the elevation angle to the satellite, in degrees
φ: the latitude of the ground station, in degrees N or S.
$h_s$: the altitude of the ground station above sea level, in km.

The step by step procedure follows:

1) Calculate the effective rain height $h_{fr}$ from the latitude of the ground receiver site using the ITU-R rain height procedure.

The freezing rain height (or 0 °C isotherm) is the upper atmosphere altitude at which rain is in the transition state between rain and ice. The rain height is defined in km above sea level. Rain height is calculated as a function of ground station latitude (φ). The rain height, latitude and elevation angle are then used to calculate the slant path $L_S$ through a rain cell and the horizontal component of the slant path $L_G$.

The ITU-R rain height assumes that the rain height, is a function of latitude (φ). The rain height $h_R$ is found as follows:

$$h_R(\varphi) = \begin{cases} 5 - 0.075(\varphi - 23) & \text{for} \quad \varphi > 23^\circ \\ 5 & \text{for} \quad -21^\circ \le \varphi \le 23^\circ \\ 5 + 0.1(\varphi + 21) & \text{for} \quad -71^\circ \le \varphi \le -21^\circ \\ 0 & \text{for} \quad \varphi < -71^\circ \end{cases} \qquad (2.2.4.1\text{-}1)$$

where φ is the latitude of the ground station receiver. Positive φ corresponds to the Northern Hemisphere, and negative φ corresponds to the Southern Hemisphere. The rain height is expressed in km and is expected to be a value greater than zero. The model is only valid for latitudes (φ) less than 89.6° (or greater than -89.6°).

2) Calculate the slant-path length, $L_S$, and horizontal projection, $L_G$, from the rain height, and elevation angle and the altitude of the ground receiver site.

Rain attenuation is directly proportional to the slant path length. The slant path length $L_s$ is defined as the length of the satellite-to-ground path that is affected by a rain cell (see Exhibit 2.2.4.1-1).

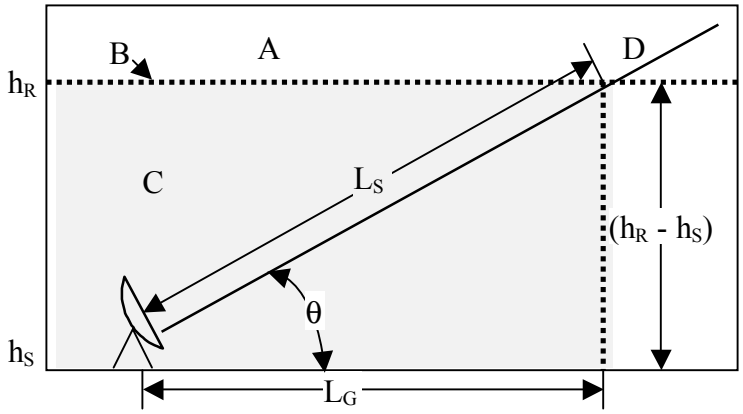


A: frozen precipitation
B: rain height
C: liquid precipitation
D: earth-space path

Exhibit 2.2.4.1-1: Slant Path through Rain

The slant path length $L_S$, expressed in km, is determined from

$$L_S(\theta) = \begin{cases} \dfrac{(h_R - h_S)}{\sin\theta} & for \quad \theta \geq 5° \\ \dfrac{2(h_R - h_S)}{\left[\sin^2\theta + \frac{2(h_R - h_S)}{R_e}\right]^{1/2} + \sin\theta} & for \quad \theta < 5° \end{cases} \qquad (2.2.4.1\text{-}2)$$

where,

$h_R$ = the height of the rain (km), from Step 1
$h_S$ = the altitude of the ground receiver site from sea level (km),
$\theta$ = the elevation angle,
$R_E$= 8500 km (effective earth radius).

For angles greater than or equal to 5°, the slant path length is derived from the geometry from Exhibit 2.2.4.1-1. This equation for $L_S$ can result in negative values when the rain height is smaller than the altitude of the ground receiver site. If a negative value occurs, $L_S$ is set to zero.

The horizontal projection is calculated as

$$L_G = L_S \cos\theta \qquad (2.2.4.1\text{-}3)$$

where $L_S$ and $L_G$ are in kilometers.

3) Determine the rain rate $R_{0.01}$ (for 0.01% of an average year).

Select the value of rain rate at 0.01 % outage from the table below, Exhibit 2.2.4.1-2, for the location of interest. The rain zones (A through Q) are associated with different geographic regions around the world, as shown in Exhibits 2.2.4.1-3, 2.2.4.1-4, 2.2.4.1-5.

| | ITU Rain Regions | | | | | | | | | | | | | | |
|---|---|---|---|---|---|---|---|---|---|---|---|---|---|---|---|
| % Outage | A | B | C | D | E | F | G | H | J | K | L | M | N | P | Q |
| 0.001 | 22 | 32 | 42 | 42 | 70 | 78 | 65 | 83 | 55 | 100 | 150 | 120 | 180 | 250 | 170 |
| 0.003 | 14 | 21 | 26 | 29 | 41 | 54 | 45 | 55 | 45 | 70 | 105 | 95 | 140 | 200 | 142 |
| **0.01** | **8** | **12** | **15** | **19** | **22** | **28** | **30** | **32** | **35** | **42** | **60** | **63** | **95** | **145** | **115** |
| 0.03 | 5 | 6 | 9 | 13 | 12 | 15 | 20 | 18 | 28 | 23 | 33 | 40 | 65 | 105 | 96 |
| 0.1 | 2 | 3 | 5 | 8 | 6 | 8 | 12 | 10 | 20 | 12 | 15 | 22 | 35 | 65 | 72 |
| 0.3 | 0.8 | 2 | 2.8 | 4.5 | 2.4 | 4.5 | 7 | 4 | 13 | 4.2 | 7 | 11 | 15 | 34 | 49 |
| 1 | <0.1 | 0.5 | 0.7 | 2.1 | 0.6 | 1.7 | 3 | 2 | 8 | 1.5 | 2 | 4 | 5 | 12 | 24 |

Exhibit 2.2.4.1-2: ITU-R Rain Regions. Rain Rate in mm/h.

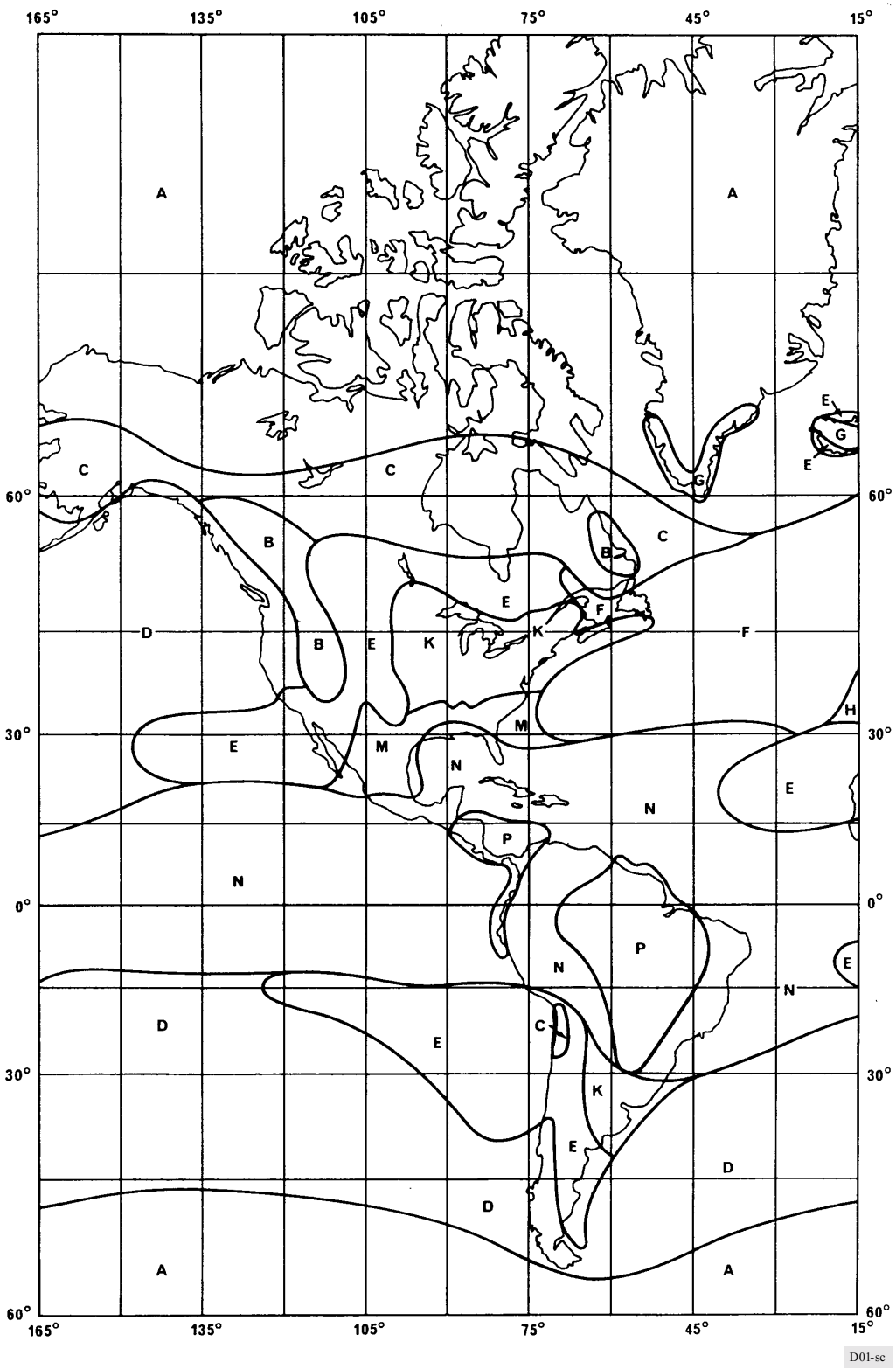


Exhibit 2.2.4.1-3. ITU-R North & South America Rain Regions

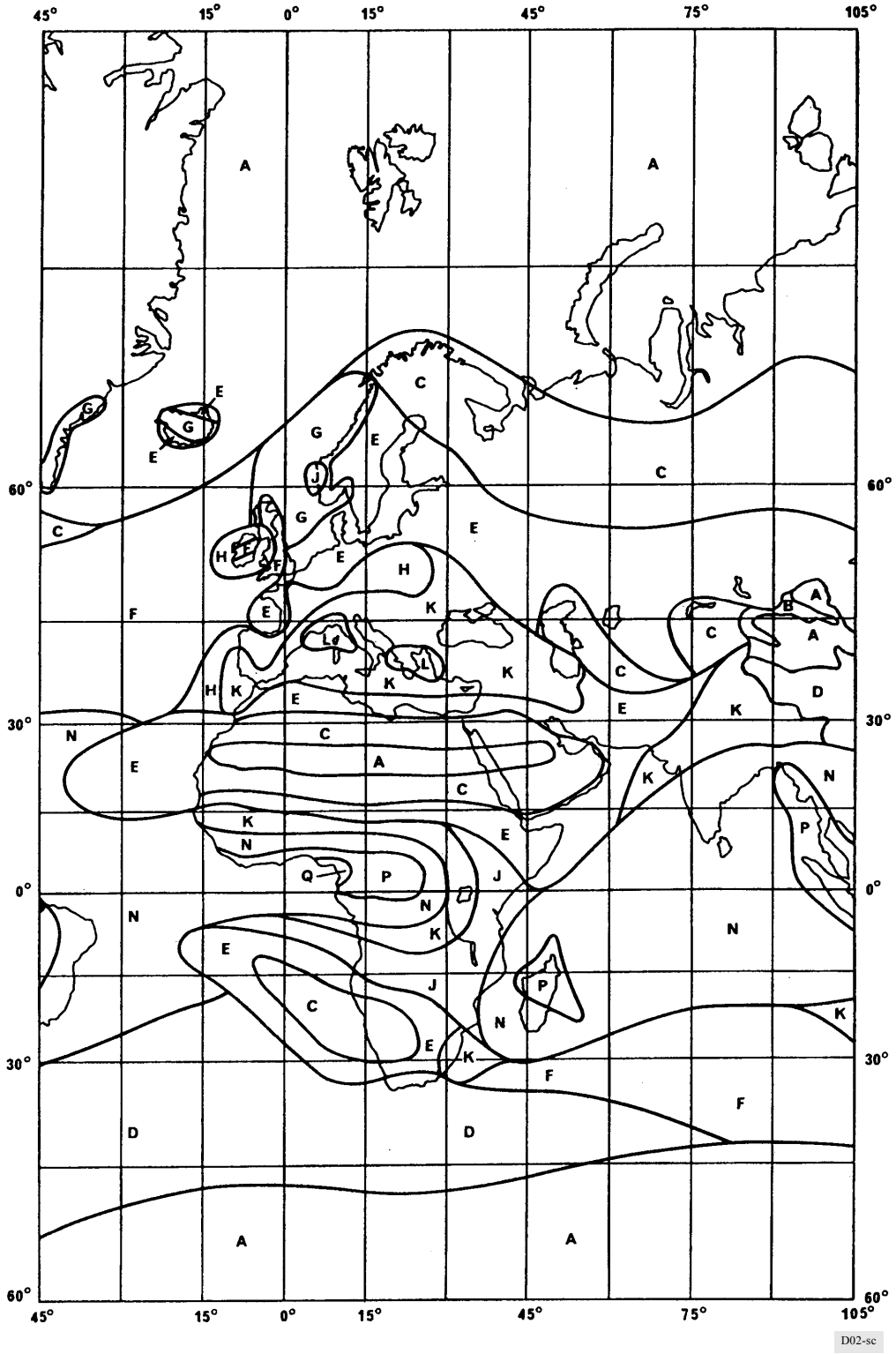


Exhibit 2.2.4.1-4. ITU-R Europe & Africa Rain Regions

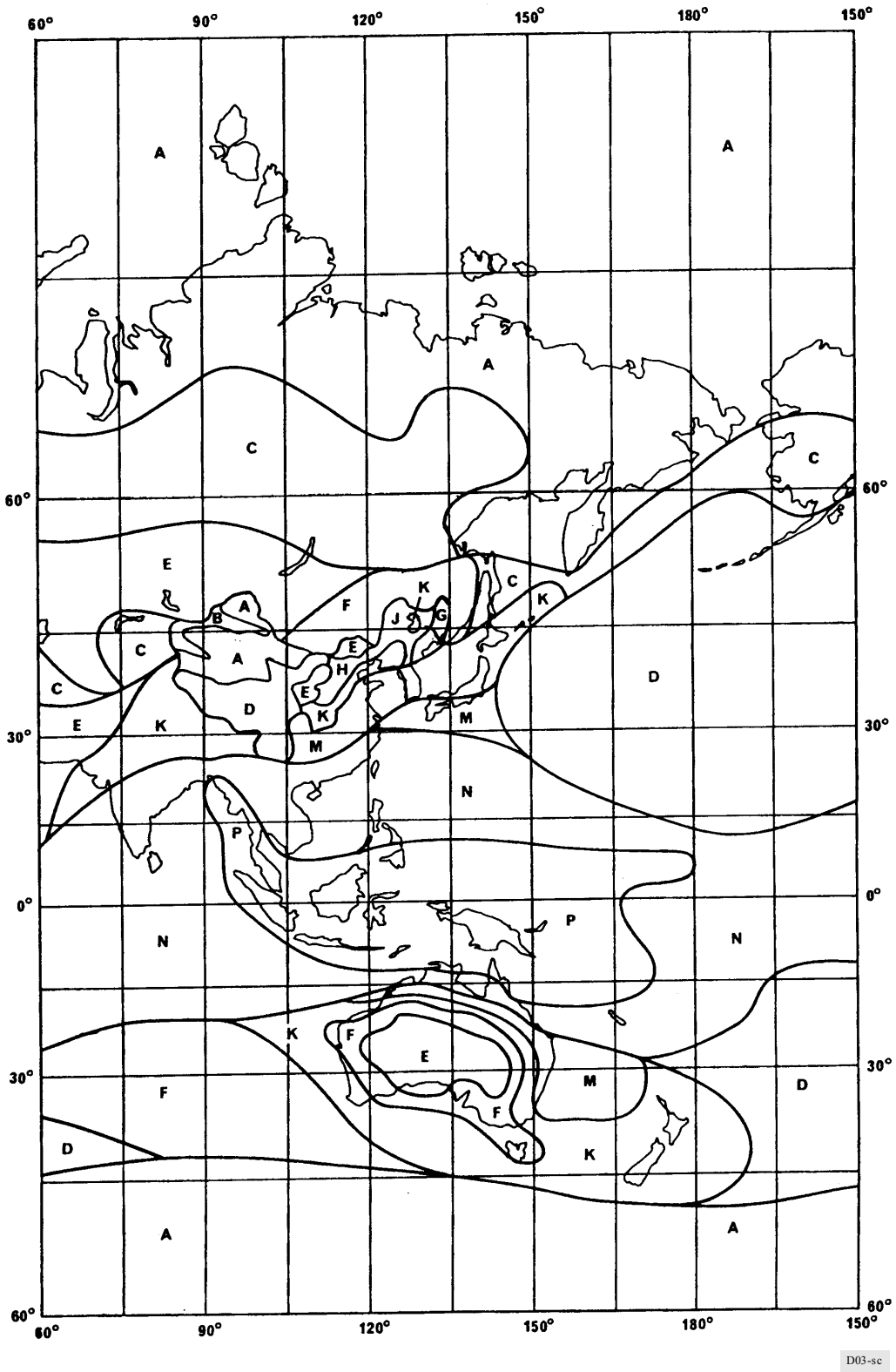


Exhibit 2.2.4.1-5. ITU-R Asia & Australia Rain Regions

4) Calculate the reduction factor $r_{0.01}$ from the rain rate $R_{0.01}$ as follows:

$$r_{0.01} = \frac{1}{1 + L_G / L_0} \tag{2.2.4.1-4}$$

where

$$L_0 = \begin{cases} 35e^{-0.015R_{0.01}} & \text{for} \quad R_{0.01} \le 100\text{mm/h} \\ 35e^{-0.015(100)} & \text{for} \quad R_{0.01} > 100\text{mm/h} \end{cases} \tag{2.2.4.1-5}$$

and $L_G$ is the horizontal projection calculated in step 2.

5) Calculate the specific attenuation $\gamma_R$.

The specific attenuation is based on the relationship:

$$\gamma_R = k\, R^{\alpha} \tag{2.2.4.1-6}$$

where $\gamma_R$ is the specific attenuation in (dB/km) and $\{k, \alpha\}$ are frequency dependent variables calculated using the regression coefficients $k_H$, $k_V$, $\alpha_H$, and $\alpha_V$ from Exhibit 2.2.4.1-5. The subscripts H and V represent horizontal and vertical polarization, respectively. The values have been tested for frequencies up to 40 GHz.

| Frequency (GHz) | $k_H$ | $k_V$ | $\alpha_H$ | $\alpha_V$ |
|---|---|---|---|---|
| 1 | 0.0000387 | 0.0000352 | 0.912 | 0.880 |
| 2 | 0.0001540 | 0.000138 | 0.963 | 0.923 |
| 4 | 0.00065 | 0.000591 | 1.121 | 1.075 |
| 6 | 0.00175 | 0.00155 | 1.308 | 1.265 |
| 7 | 0.00301 | 0.00265 | 1.332 | 1.312 |
| 8 | 0.00454 | 0.00395 | 1.327 | 1.310 |
| 10 | 0.0101 | 0.00887 | 1.276 | 1.264 |
| 12 | 0.0188 | 0.0168 | 1.217 | 1.200 |
| 15 | 0.0367 | 0.0335 | 1.154 | 1.128 |
| 20 | 0.0751 | 0.0691 | 1.099 | 1.065 |
| 25 | 0.124 | 0.113 | 1.061 | 1.030 |
| 30 | 0.187 | 0.167 | 1.021 | 1.000 |
| 35 | 0.263 | 0.233 | 0.979 | 0.963 |
| 40 | 0.350 | 0.310 | 0.939 | 0.929 |
| 45 | 0.442 | 0.393 | 0.903 | 0.897 |
| 50 | 0.536 | 0.479 | 0.873 | 0.868 |
| 60 | 0.707 | 0.642 | 0.826 | 0.824 |
| 70 | 0.851 | 0.784 | 0.793 | 0.793 |
| 80 | 0.975 | 0.906 | 0.769 | 0.769 |
| 90 | 1.06 | 0.999 | 0.753 | 0.754 |
| 100 | 1.12 | 1.06 | 0.743 | 0.744 |
| 120 | 1.18 | 1.13 | 0.731 | 0.732 |
| 150 | 1.31 | 1.27 | 0.710 | 0.711 |
| 200 | 1.45 | 1.42 | 0.689 | 0.690 |
| 300 | 1.36 | 1.35 | 0.688 | 0.689 |
| 400 | 1.32 | 1.31 | 0.683 | 0.684 |

Exhibit 2.2.4.1-5: Regression coefficients for estimating specific attenuation.

For those frequencies not listed in the table, the $k_H$, $k_V$ coefficients are determined by logarithmic interpolation with frequency; and the $\alpha_H$ and $\alpha_V$ terms are determined by linear interpolation with frequency. Finally $k$ and $\alpha$ (for the specific attenuation calculation) are calculated as

$$k = [k_H + k_V + (k_H - k_V)\cos^2\theta \cos 2\tau]/2 \qquad (2.2.4.1\text{-}7)$$

$$\alpha = [k_H \alpha_H + k_V \alpha_V + (k_H \alpha_H - k_V \alpha_V)\cos^2\theta \cos 2\tau]/2k \qquad (2.2.4.1\text{-}8)$$

where $\theta$ is the path elevation angle and $\tau$ is the polarization tilt angle with respect to the horizontal.

6) Calculate the predicted attenuation $A_{0.01}$ exceeded for 0.01% of an average year:

$$A_{0.01} = \gamma_R L_S r_{0.01}. \quad (2.2.4.1\text{-}9)$$

7) Calculate the attenuation $A_P$ exceeded P% of the time where P is the link outage from:

$$A_P = 0.12 A_{0.01} P^{-(0.546+0.043 \log P)} \quad . \quad (2.2.4.1\text{-}10)$$

### 2.2.4.2 Global Model

The first published model that provided a self-contained prediction procedure for global application was developed by R. K. Crane (1980). The Crane developed model, usually referred to as the Global Model, is based on the use of geophysical data to determine the surface point rain rate, point-to-path variations in rain rate, and the height dependency of attenuation, given the surface point rain rate or the percentage of the year the attenuation value is exceeded. The model also provides estimates of the expected year-to-year and station-to-station variations of the attenuation prediction for a given percent of the year. An update of the global model is available in Crane (1996).

The Global model, like the ITU-R model, provides global climate regions, but the 12 climate regions for the Global model differ from the ITU-R model regions previously described (Exhibits 2.2.4.1-3,4,5).

The input parameters required for the Global model are:

f: the frequency of operation, in GHz
$\theta$: the elevation angle to the satellite, in degrees
$\varphi$: the latitude of the ground station, in degrees N or S.
$h_s$: the altitude of the ground station above sea level, in km.
$\tau$ : the polarization tilt angle with respect to the horizontal, in degrees.

The step by step procedure follows:

***Step 1)*** **Determination of the rain rate distribution, Rp**

Determine the global model rain climate region for the ground station of interest from the global maps, Exhibits 2.2.4.2-1, 2.2.4.2-2, and 2.2.4.2-3, which show the climate zones for the Americas, Europe and Africa, and Asia, respectively. Exhibits 2.2.4.2-4 and 2.2.4.2-5 present the climate zones in more detail for North America and for Western Europe, respectively. Once the climate zone has been selected, obtain the rain rate distribution values from the table, Exhibit 2.2.4.2-6.

If long term measured rain rate distributions are available for the location of interest (preferably one-minute average data), they may be used in place of the global model distributions. Caution is recommended in the use of measured distributions if the observations are for a period of less than 10 years (Crane, 1980).

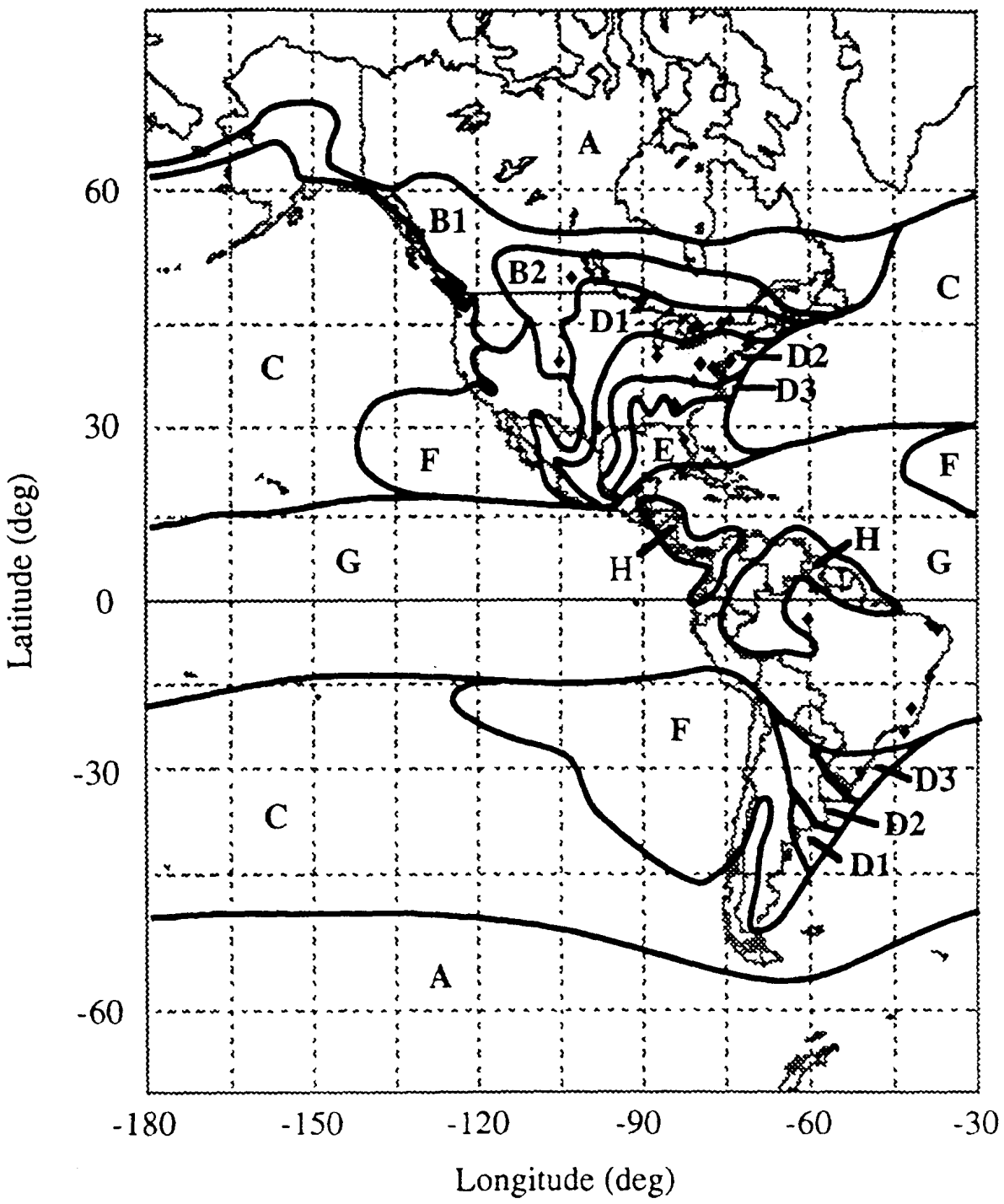


Exhibit 2.2.4.2-1
Global Model Rain Climate Zones for North and South America
*[Source: Crane (1996)]*

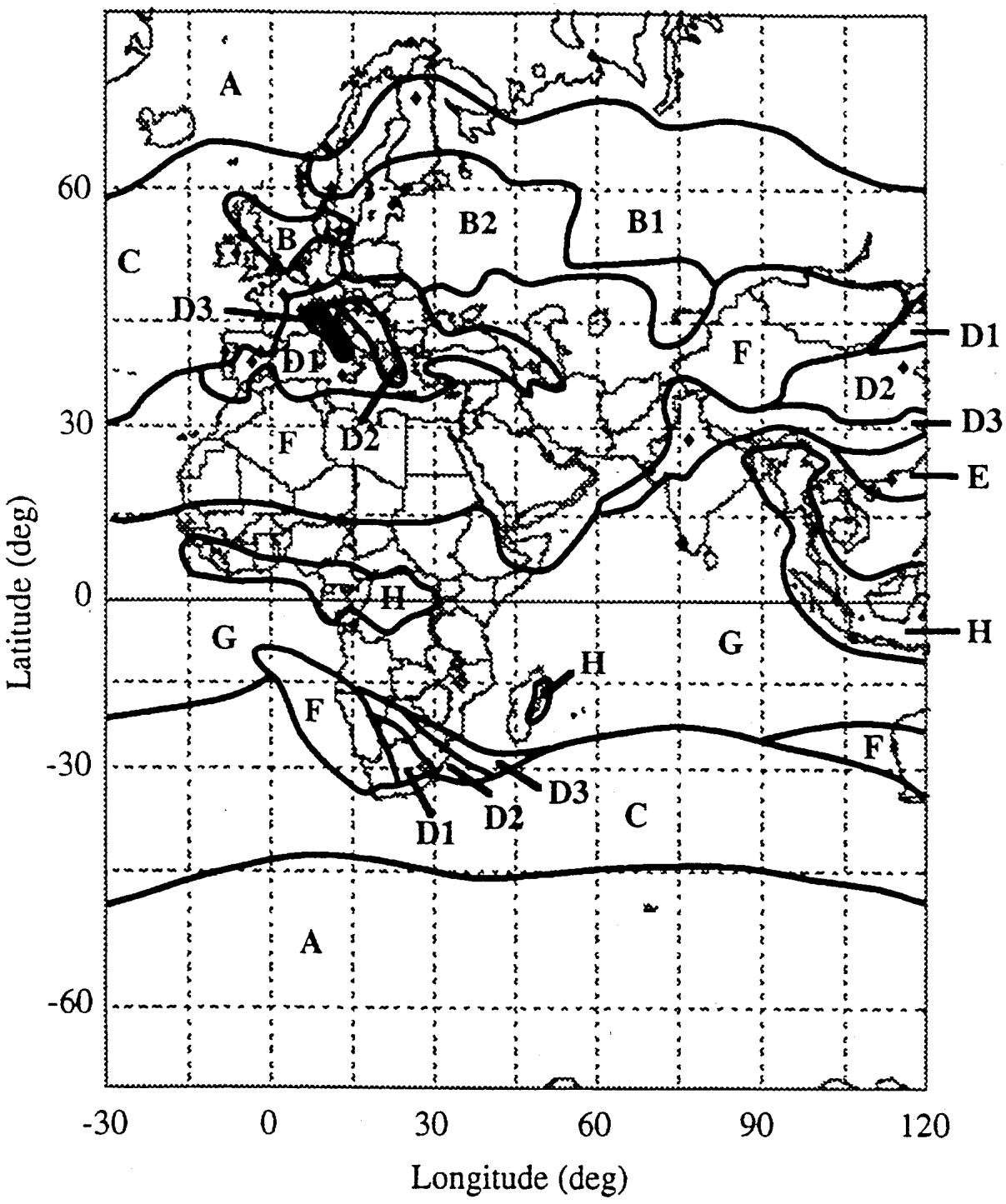


♦ Path locations for rain attenuation measurements

Exhibit 2.2.4.2-2
Global Model Rain Climate Zones for Europe and Africa
*[Source: Crane (1996)]*

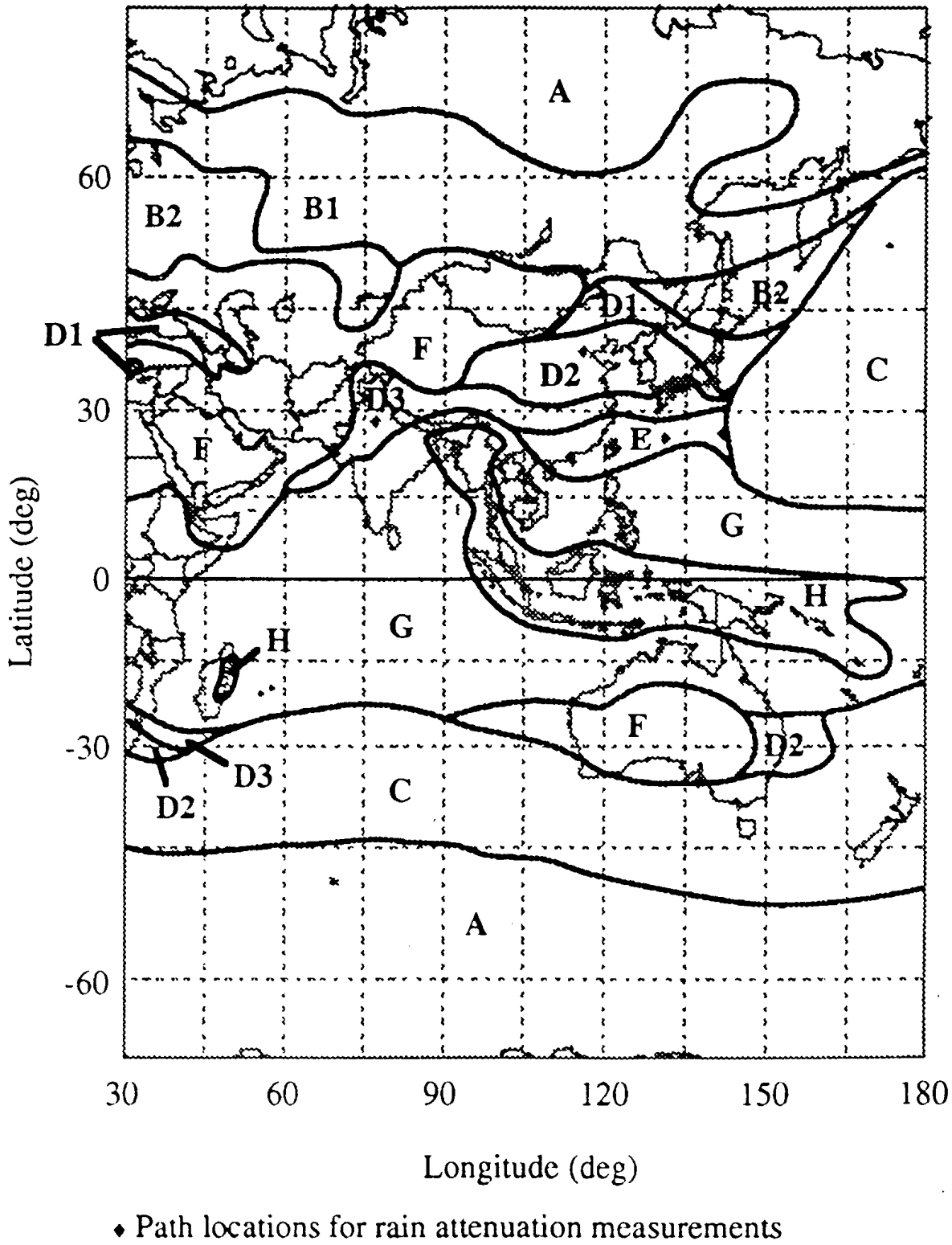


Exhibit 2.2.4.2-3
Global Model Rain Climate Zones for Asia
*[Source: Crane (1996)]*

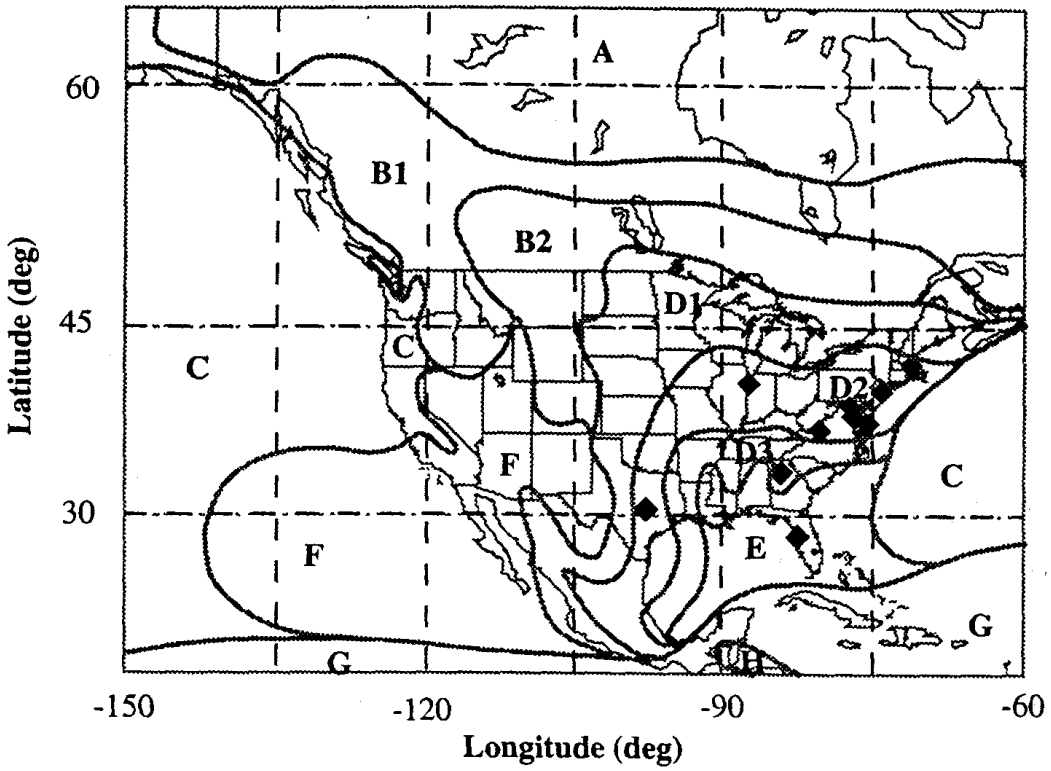


Exhibit 2.2.4.2-4 Global Model Rain Climate Zones for North America
*[Source: Crane (1996)]*

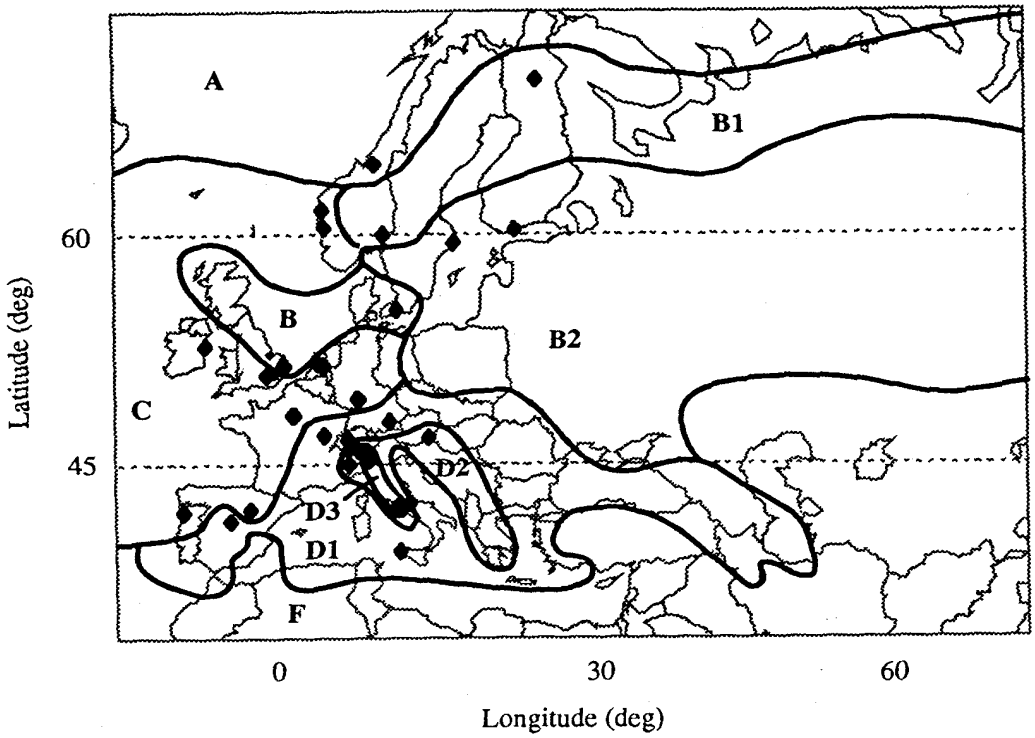


Exhibit 2.2.4.2-5 Global Model Rain Climate Zones for Western Europe
*[Source: Crane (1996)]*

| Percent Of Year | A | B | B1 | B2 | C | D1 | D2 | D3 | E | F | G | H |
|---|---|---|---|---|---|---|---|---|---|---|---|---|
| | mm/h | mm/h | mm/h | mm/h | mm/h | mm/h | mm/h | mm/h | mm/h | mm/h | mm/h | mm/h |
| 5 | 0.0 | 0.2 | 0.1 | 0.2 | 0.3 | 0.2 | 0.3 | 0.0 | 0.2 | 0.1 | 1.8 | 1.1 |
| 3 | 0.0 | 0.3 | 0.2 | 0.4 | 0.6 | 0.6 | 0.9 | 0.8 | 1.8 | 0.1 | 3.4 | 3.3 |
| 2 | 0.1 | 0.5 | 0.4 | 0.7 | 1.1 | 1.2 | 1.5 | 2.0 | 3.3 | 0.2 | 5.0 | 5.8 |
| 1 | 0.2 | 1.2 | 0.8 | 1.4 | 1.8 | 2.2 | 3.0 | 4.6 | 7.0 | 0.6 | 8.4 | 12.4 |
| 0.5 | 0.5 | 2.0 | 1.5 | 2.4 | 2.9 | 3.8 | 5.3 | 8.2 | 12.6 | 1.4 | 13.2 | 22.6 |
| 0.3 | 1.1 | 2.9 | 2.2 | 3.4 | 4.1 | 5.3 | 7.6 | 11.8 | 18.4 | 2.2 | 17.7 | 33.1 |
| 0.2 | 1.5 | 3.8 | 2.9 | 4.4 | 5.2 | 6.8 | 9.9 | 15.2 | 24.1 | 3.1 | 22.0 | 43.5 |
| 0.1 | 2.5 | 5.7 | 4.5 | 6.8 | 7.7 | 10.3 | 15.1 | 22.4 | 36.2 | 5.3 | 31.3 | 66.5 |
| 0.05 | 4.0 | 8.6 | 6.8 | 10.3 | 11.5 | 15.3 | 22.2 | 31.6 | 50.4 | 8.5 | 43.8 | 97.2 |
| 0.03 | 5.5 | 11.6 | 9.0 | 13.9 | 15.6 | 20.3 | 28.6 | 39.9 | 62.4 | 11.8 | 55.8 | 125.9 |
| 0.02 | 6.9 | 14.6 | 11.3 | 17.6 | 19.9 | 25.4 | 34.7 | 47.0 | 72.2 | 15.0 | 66.8 | 152.4 |
| 0.01 | 9.9 | 21.1 | 16.1 | 25.8 | 29.5 | 36.2 | 46.8 | 61.6 | 91.5 | 22.2 | 90.2 | 209.3 |
| 0.005 | 13.8 | 29.2 | 22.3 | 35.7 | 41.4 | 49.2 | 62.1 | 78.7 | 112.0 | 31.9 | 118.0 | 283.4 |
| 0.003 | 17.5 | 36.1 | 27.8 | 43.8 | 50.6 | 60.4 | 75.6 | 93.5 | 130.0 | 41.4 | 140.8 | 350.3 |
| 0.002 | 20.9 | 41.7 | 32.7 | 50.9 | 58.9 | 69.0 | 88.3 | 106.6 | 145.4 | 50.4 | 159.6 | 413.9 |
| 0.001 | 28.1 | 52.1 | 42.6 | 63.8 | 71.6 | 86.6 | 114.1 | 133.2 | 176.0 | 70.7 | 197.0 | 542.6 |
| No. of Station Years | 40 | 102 | 7 | 178 | 29 | 158 | 46 | 25 | 12 | 20 | 3 | 7 |

Exhibit2.2.3.2-6
Rain Rate Distributions For Global Model Rain Climate Regions
*[Source: Crane (1996)]*

***Step 2)*** **Determination of Rain Height, h(p)**

The rain height used for the Global model is a location dependent parameter based on the 0 degree isotherm (melting layer) height. The rain height is a function of station latitude φ and percent of the year p. Exhibit 2.2.4.2-6 gives the Rain Height, h(p), for probabilities of 0.001, 0.01, 0.1, and 1%, for station latitudes from 0 to 70 degrees. (The plot can be used for either North or South latitude locations). A table of rain height for probability values of 0.001 and 1.0%, as provided by Crane(1996), is provided here as Exhibit 2.2.4.2-7. Rain height values for other probability values cam be determined by logarithmic interpolation between the given probability values.

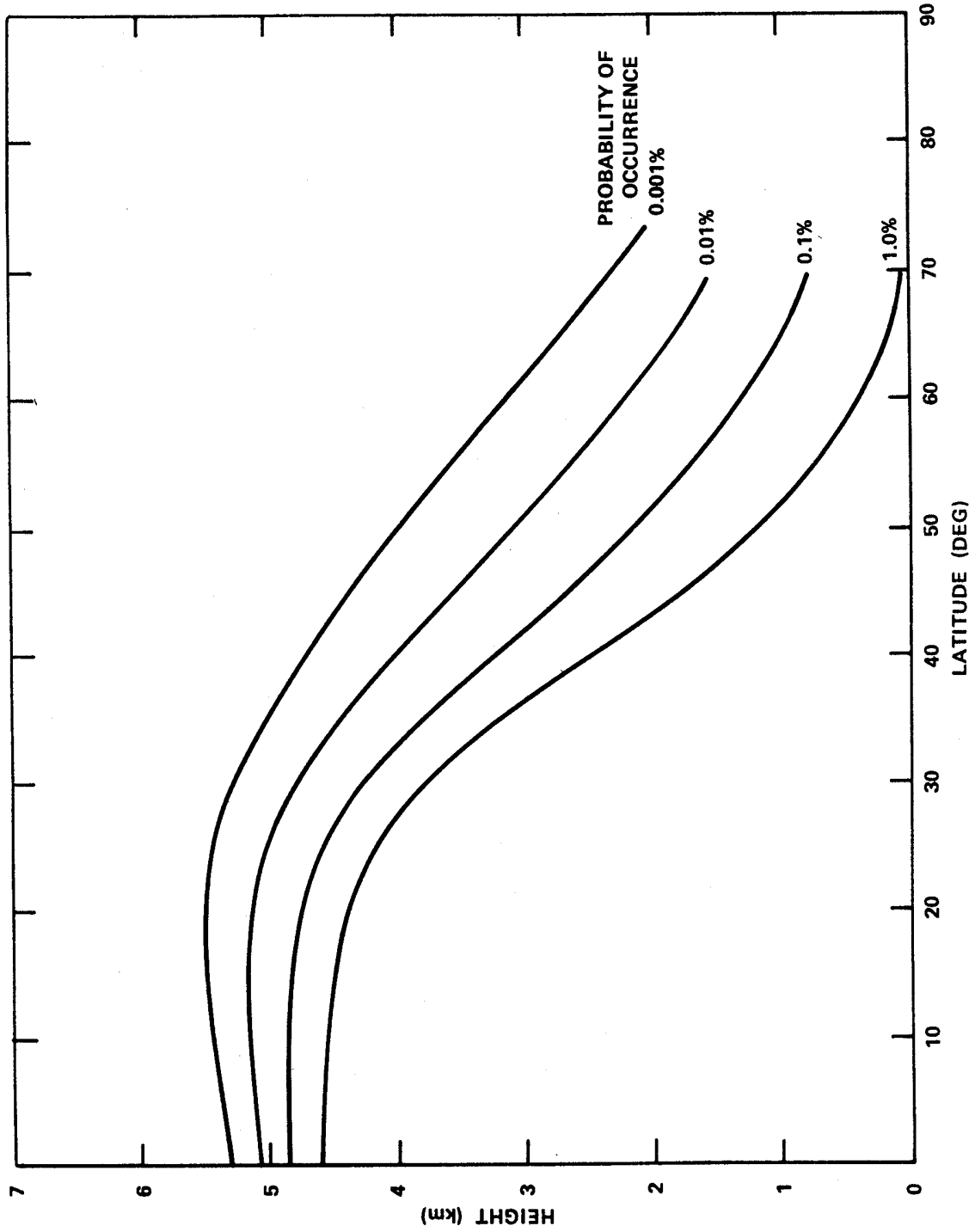


Exhibit 2.2.4.2-6
Rain Height for the Global Rain Attenuation Model
*[Source: Crane 1980)]*

| Ground Station Latitude φ (North or South) in degrees | Rain Height h(p) in km | |
|---|---|---|
| | At 0.001% of Year | At 1.0% of Year |
| ≤ 2 | 5.30 | 4.60 |
| 4 | 5.31 | 4.60 |
| 6 | 5.32 | 4.60 |
| 8 | 5.34 | 4.59 |
| 10 | 5.37 | 4.58 |
| 12 | 5.40 | 4.56 |
| 14 | 5.44 | 4.53 |
| 16 | 5.47 | 4.50 |
| 18 | 5.49 | 4.47 |
| 20 | 5.50 | 4.42 |
| 22 | 5.50 | 4.37 |
| 24 | 5.49 | 4.30 |
| 26 | 5.46 | 4.20 |
| 28 | 5.41 | 4.09 |
| 30 | 5.35 | 3.94 |
| 32 | 5.28 | 3.76 |
| 34 | 5.19 | 3.55 |
| 36 | 5.10 | 3.31 |
| 38 | 5.00 | 3.05 |
| 40 | 4.89 | 2.74 |
| 42 | 4.77 | 2.45 |
| 44 | 4.64 | 2.16 |
| 46 | 4.50 | 1.89 |
| 48 | 4.35 | 1.63 |
| 50 | 4.20 | 1.40 |
| 52 | 4.04 | 1.19 |
| 54 | 3.86 | 1.00 |
| 56 | 3.69 | 0.81 |
| 58 | 3.50 | 0.67 |
| 60 | 3.31 | 0.51 |
| 62 | 3.14 | 0.50 |
| 64 | 2.96 | 0.50 |
| 66 | 2.80 | 0.50 |
| 68 | 2.62 | 0.50 |
| ≥70 | 2.46 | 0.50 |

Exhibit 2.2.4.2-7
Global Model Rain Heights for0.001 % and 1.0 %
*[Source: Crane 1996)]*

***Step 3)*** **Determine the surface projected path length, D**

The horizontal (surface) path projection of the slant path is found from

For $\theta \geq 10^0$

$$D = \frac{h(p) - h_s}{\tan\theta} \qquad (2.2.4.2\text{-}1)$$

For $\theta < 10^0$

$$D = R \sin^{-1}\left[\frac{\cos\theta}{h(p)+R}\left(\sqrt{(h_s+R)^2 \sin\theta + 2R(h(p)-h_s) + h^2(p) - {h_s}^2} - (h_s+R)\sin\theta\right)\right] \qquad (2.2.4.2\text{-}2)$$

where R is the effective radius of the earth, assumed to be 8500 km.

***Step 4)*** **Determine the Specific Attenuation Coefficients a, b**

The specific attenuation is based on the relationship:

$$\gamma_R = a\, R^b \qquad (2.2.4.2\text{-}3)$$

where $\gamma_R$ is the specific attenuation in (dB/km) and a and b are frequency dependent specific attenuation cofficients.

The coefficients are calculated using the regression coefficients $k_H$ , $k_V$ , $\alpha_H$ , and $\alpha_V$ from Exhibit 2.2.4.1-5. The subscripts H and V represent horizontal and vertical polarization, respectively. The values have been tested for frequencies up to 40 GHz.

For those frequencies not listed in the table, the $k_H$, $k_V$ coefficients are determined by logarithmic interpolation with frequency; and the $\alpha_H$ and $\alpha_V$ terms are determined by linear interpolation with frequency. Finally a and b (for the specific attenuation calculation) are calculated as

$$a = [k_H + k_V + (k_H - k_V)\cos^2\theta \cos 2\tau]/2 \qquad (2.2.4.2\text{-}4)$$

$$b = [k_H \alpha_H + k_V \alpha_V + (k_H \alpha_H - k_V \alpha_V)\cos^2\theta \cos 2\tau]/2a \qquad (2.2.4.2\text{-}5)$$

where $\theta$ is the path elevation angle and $\tau$ is the polarization tilt angle with respect to the horizontal.

***Step 5)*** **Determine Empirical Constants**

Determine the following four empirical constants for each probability p of interest:

$$X = 2.3R_p^{-0.17} \quad (2.2.4.2\text{-}6)$$

$$Y = 0.026 - 0.03 \ln R_p \quad (2.2.4.2\text{-}7)$$

$$Z = 3.8 - 0.6 \ln R_p \quad (2.2.4.2\text{-}8)$$

$$U = \frac{\ln\left(Xe^{YZ}\right)}{Z} \quad (2.2.4.2\text{-}9)$$

where Rp is the rain rate at the probability p %, obtained from step 1.

***Step 6)*** **Mean Slant Path Attenuation, A(p)**

The mean slant-path rain attenuation, A(p), at each probability of occurrence, p, is determined from

For $0 < D \leq d$

$$A(p) = \frac{a\,R(p)^b}{\cos\theta}\left[\frac{e^{UbD} - 1}{Ub}\right] \quad (2.2.4.2\text{-}10)$$

For $d < D \leq 22.5$

$$A(p) = \frac{a\,R(p)^b}{\cos\theta}\left[\frac{e^{Ubd} - 1}{Ub} - \frac{X^b e^{Ybd}}{Yb} + \frac{X^b e^{YbD}}{Yb}\right] \quad (2.2.4.2\text{-}11)$$

For $D > 22.5$, calculate A(p) with $D = 22.5$, and the rain rate R'(p) at the probability value

$$p' = \left(\frac{22.5}{D}\right)p \quad (2.2.4.2\text{-}12)$$

***Step 7)*** **Upper and Lower Bounds**

The Crane Global Model provides for an estimate of the upper and lower bounds of the mean slant path attenuation. The bounds are determines as the standard deviation of the measurement about the average and are estimated from:

| Percent of Year | Standard Deviation (%) |
|---|---|
| 1.0 | ± 39 |
| 0.1 | ± 32 |
| 0.01 | ± 32 |
| 0.001 | ± 39 |

For example, a mean prediction of 15 dB at 0.01% yields upper/lower bounds of ± 32 % or ± 4.8 dB. This results in a prediction range for the path attenuation, from the Global Model, of 10.2 dB to 19.8 dB, with a mean value of 15 dB.

### 2.2.4.3 Two-Component Model

The two-component rain model is an extension of the global model provided by Crane to include statistical information on the movement and size of rain cells, and to add several improvements to the original global model for the prediction of rain attenuation statistics. The two-component model was first introduced about two years after the global model (Crane, 1982), with later revisions (Crane, 1985)(Crane, 1996).

The model separately addresses the contributions of rain showers (volume cells) and the larger regions of lighter rain intensity surrounding the showers (debris). The rain distribution for each climate zone is modeled as a "two-component" function, consisting of a volume cell component and a debris component. The probability associated with each component is calculated, and the two values are summed independently to provide the desired total probability. The rain climate regions of the original Global Model are used in the Two-Component Model

Results from a 3-year radar measurement program in Goodland, Kansas were used to establish the statistical descriptions of the volume cells and debris regions. Data from 240,000 volume cells gathered from 25 storm days were utilized.

The measured rain rate distribution produced by the volume cells was found to be well approximated by an exponential distribution. The debris region distribution function was found to be nearly lognormal over the range 0.001% to 5% of the year.

The total rain distribution function is given by

$$P(r \geq R) = P_C e^{-\frac{R}{R_C}} + P_D N\left(\frac{\ln R - \ln R_D}{\sigma_D}\right) \qquad (2.2.4.3\text{-}1)$$

**Volume Cell** (exponential) **Debris** (log normal)

where:

$P(r \geq R)$ is the probability that the observed rain rate r exceeds the specified rain rate R
N is the normal probability distribution function,
$P_C$ is the probability of a cell,
$R_C$ is the average cell rain rate,
$P_D$ is the probability of debris,
$R_D$ is the average rain rate in the debris, and
$\sigma_D$ is the standard deviation of the natural log of the rain rate.

The input parameters required for the two-component model are:

f: the frequency of operation, in GHz
$\theta$: the elevation angle to the satellite, in degrees
$\varphi$: the latitude of the ground station, in degrees N or S.
$h_S$: the altitude of the ground station above sea level, in km.
$\tau$ : the polarization tilt angle with respect to the horizontal, in degrees.

The step by step procedure for the two-component model follows.

***Step 1)*** **Determine Rain Climate Zone and Cell Parameters**

Determine the global model rain climate zone for the ground station of interest from the global maps, Exhibits 2.2.4.2-1, 2.2.4.2-2, and 2.2.4.2-3, which show the climate zones for the Americas, Europe and Africa, and Asia, respectively. Exhibits 2.2.4.2-4 and 2.2.4.2-5 present the climate zones in more detail for North America and for Western Europe, respectively. Once the climate zone has been selected, obtain the five cell parameters $P_C$, $R_C$, $P_D$, $R_D$, and $\sigma_D$ from Exhibit 2.2.4.3-1.

| Rain Zone | Cell Parameters | | Debris Parameters | | | R for $P(r \geq R)=0.01\%$ (mm/h) |
|---|---|---|---|---|---|---|
| | $P_C$ (%) | $R_C$ (mm/h) | $P_D$ (%) | $R_D$ (mm/h) | $\sigma_D$ | |
| A | 0.009 | 11.3 | 3.0 | 0.20 | 1.34 | 10 |
| $B_1$ | 0.016 | 15.2 | 9.0 | 0.24 | 1.26 | 15 |
| B | 0.018 | 19.6 | 7.0 | 0.32 | 1.23 | 18 |
| $B_2$ | 0.019 | 23.9 | 7.0 | 0.40 | 1.19 | 22 |
| C | 0.023 | 24.8 | 9.0 | 0.43 | 1.15 | 26 |
| $D_1$ | 0.030 | 25.7 | 5.0 | 0.83 | 1.14 | 36 |
| $D_2$ | 0.037 | 27.8 | 5.0 | 1.08 | 1.19 | 49 |
| $D_3$ | 0.100 | 15.0 | 5.0 | 1.38 | 1.30 | 62 |
| E | 0.120 | 29.1 | 7.0 | 1.24 | 1.41 | 100 |
| F | 0.016 | 20.8 | 3.0 | 0.35 | 1.41 | 10 |
| G | 0.070 | 39.1 | 9.0 | 1.80 | 1.19 | 95 |
| H | 0.060 | 42.1 | 9.0 | 1.51 | 1.60 | 245 |

Exhibit2.2.4.3-1
Two-Component Model Rain Distribution Parameters
*[Source: Crane (1982)]*

***Step 2)*** **Determine the Specific Attenuation Coefficients a, b**

The specific attenuation is based on the relationship:

$$\gamma_R = a\, R^b \qquad (2.2.4.3\text{-}1)$$

where $\gamma_R$ is the specific attenuation in (dB/km) and a and b are frequency dependent specific attenuation coefficients.

The coefficients are calculated using the regression coefficients $k_H$ , $k_V$ , $\alpha_H$ , and $\alpha_V$ from Exhibit 2.2.4.1-5. The subscripts H and V represent horizontal and vertical polarization, respectively. The values have been tested for frequencies up to 40 GHz.

For those frequencies not listed in the table, the $k_H$, $k_V$ coefficients are determined by logarithmic interpolation with frequency; and the $\alpha_H$ and $\alpha_V$ terms are determined by linear interpolation with frequency. Finally a and b (for the specific attenuation calculation) are calculated as

$$a = [k_H + k_V + (k_H - k_V)\cos^2\theta \cos 2\tau]/2 \qquad (2.2.4.3\text{-}2)$$

$$b = [k_H \alpha_H + k_V \alpha_V + (k_H \alpha_H - k_V \alpha_V)\cos^2\theta \cos 2\tau]/2a \qquad (2.2.4.3\text{-}3)$$

where $\theta$ is the path elevation angle and $\tau$ is the polarization tilt angle with respect to the horizontal.

***Step 3)*** **Determine Volume and Debris Cell Heights**

The volume cell height, $H_C$, and the debris height, $H_D$, in km, are found from

$$H_C = 3.1 - 1.7\sin[2(\phi - 45)] \qquad (2.2.4.3\text{-}4)$$

$$H_D = 2.8 - 1.9\sin[2(\phi - 45)] \qquad (2.2.4.3\text{-}5)$$

The maximum projected cell and debris path lengths, $D_C$ and $D_D$ are determined from

For $\theta \geq 10^0$

$$D_{C,D} = \frac{(H_{C,D} - h_S)}{\tan\theta} \qquad (2.2.4.3\text{-}6)$$

For all $\theta$

$$D_{C,D} = \frac{2(H_{C,D} - h_S)}{\tan\theta + \left[\tan^2\theta + \frac{2(H_{C,D} - h_S)}{8500}\right]^{\frac{1}{2}}} \qquad (2.2.4.3\text{-}7)$$

***Step 4)*** **Initial Volume Cell Rain Rate**

Pick an attenuation value of interest, A, in dB, and calculate the initial volume cell rain rate estimate, $R_i$, from

$$R_i = \left( \frac{A \cos\theta}{2.671a} \right)^{\frac{1}{b-0.04}} \qquad (2.2.4.3\text{-}8)$$

where a and b are the attenuation coefficients from Step 1.

***Step 5)*** **Volume Cell Horizontal Extent**

Calculate the volume cell horizontal extent, $W_C$, in km, from,

For $D_C > W_C$

$$W_C = 1.87 R_i^{-0.04} \qquad (2.2.4.3\text{-}9)$$

For $D_C \leq W_C$

$$W_C = D_C \qquad (2.2.4.3\text{-}10)$$

***Step 6)*** **Adjustment for Debris**

Calculate the adjustment for debris associated with the volume cell from

$$C = \frac{1 + 0.7(D_C - W_C)}{1 + (D_C - W_C)} \qquad (2.2.4.3\text{-}11)$$

***Step 7)*** **Volume Cell Size Parameters**

Calculate the volume cell size parameters $T_C$ and $W_T$, in km, from,

$$T_C = 1.6 R_i^{-0.24} \qquad (2.2.4.3\text{-}12)$$

and

If $W_C < W_T$

$$W_T = \frac{2T_C}{\tan\theta + \left( \tan^2\theta + \frac{2T_C}{8500} \right)^{\frac{1}{b}}} \qquad (2.2.4.3\text{-}13)$$

If $W_C \geq W_T$

$$W_T = W_C \qquad (2.2.4.3\text{-}14)$$

***Step 8)*** **Final Volume Cell Rain Rate**

Calculate the final value of the Cell Rain Rate estimate from,

$$R_f = \left( \frac{CA\cos\theta}{aW_C} \right)^{\frac{1}{b}} \qquad (2.2.4.3\text{-}15)$$

***Step 9)*** **Probability of Volume Cell Intersection**

Determine the probability of intersecting a volume cell on the propagation path from,

$$P_f = P_C \left( 1 + \frac{D_C}{W_T} \right) e^{-\frac{R_f}{R_C}} \qquad (2.2.4.3\text{-}16)$$

This completes the steps in the calculation of the first probability associated with the selected value of attenuation for the volume cell component. Next the process is continued for the debris component.

***Step 10)*** **Initial Debris Rain Rate**

Determine the initial debris rain rate estimate, $R_a$, for the selected attenuation A, from,

$$R_a = \left( \frac{A\cos\theta}{29.7a} \right)^{\frac{1}{b-0.34}} \qquad (2.2.4.3\text{-}17)$$

where a and b are the attenuation coefficients from Step 1.

***Step 11)*** **Debris Horizontal Extent**

Calculate the debris horizontal extent $W_D$, in km from,

For $D_D > W_D$

$$W_D = 29.7 R_a^{-0.34} \qquad (2.2.4.3\text{-}18)$$

For $D_D \leq W_D$

$$W_D = D_D \qquad (2.2.4.3\text{-}19)$$

***Step 12)*** **Debris Size Parameters**

Calculate the debris size parameters $T_D$ and $W_D$, in km, from,

$$T_D = (H_D - h_S)\left\{\frac{1+\left[\frac{1.6}{(H_D - h_S)}\right]\ln(R_a)}{1-\ln(R_a)}\right\} \qquad (2.2.4.3\text{-}20)$$

and

If $W_D < W_L$

$$W_L = \frac{2T_D}{\tan\theta + \left(\tan^2\theta + \frac{2T_D}{8500}\right)^{\frac{1}{2}}} \qquad (2.2.4.3\text{-}21)$$

If $W_D \geq W_L$

$$W_L = W_D \qquad (2.2.4.3\text{-}22)$$

***Step 13)*** **Final Debris Rain Rate**

Calculate the final value of the Debris Rain Rate from,

$$R_z = \left(\frac{A\cos\theta}{aW_D}\right)^{\frac{1}{b}} \qquad (2.2.4.3\text{-}23)$$

***Step 14)*** **Probability of Debris Intersection**

Determine the probability of intersecting a debris region on the propagation path from,

$$P_g = P_D\left(1+\frac{D_D}{W_L}\right)\frac{1}{2}erfc\left[\frac{\ln\left(\frac{R_z}{R_D}\right)}{\sqrt{2}\,\sigma_D}\right] \qquad (2.2.4.3\text{-}24)$$

where *erfc* is the complimentary error function.

***Step 15)*** **Probability of exceedance for Attenuation A**

The probability of exceeding the selected attenuation A, P(a > A), is found as the sum of $P_f$, found in step 9, and $P_g$, found in Step 14, i.e.,

$$P(a > A) = P_f + P_g \qquad (2.2.4.3\text{-}25)$$

This completes the calculation for the single selected attenuation value A.

***Step 15)*** **Probability for Other Values of Attenuation**

Repeat Steps 4 through 15 for each other value of attenuation, A, desired. The total attenuation distribution P(a > A) is then obtained.

### 2.2.4.4 DAH Model ("USA Model")

The DAH rain attenuation model is an extension to the ITU-R model described in Section 2.2.4.1. The DAH model is often referred to as the USA model since its original submission to the ITU was through the USA delegation without authors names (Dissanayake & Allnut, 1992). The DAH designation acknowledges the authors: Dissanayake, Allnutt, and Haidara. The model has since been published in the open literature (Dissanayke, et al, 1997). The model accounts for the inhomogeneity in rain in the horizontal and vertical directions. The model is applicable across the frequency range 4 to 35 GHz and 0.001% to 10% outages. A step-by-step implementation is provided.

1) Calculate the rain height $h_R$ from the latitude of the ground receiver site.

The rain height $h_R$ is determined from:

$$h_R(\varphi) = \begin{cases} 5 - 0.075(\varphi - 23) & \text{for} \quad |\varphi| \geq 23^\circ \\ 5 & \text{for} \quad 0^\circ \leq |\varphi| < 23^\circ \end{cases} \qquad (2.2.4.4\text{-}1)$$

where $\varphi$ is the latitude of the ground station receiver. The DAH rain height is the same as the ITU-R rain height for latitudes greater than -21°. The rain height is only valid for latitudes $|\varphi|$ less than 89.6°, as was the case for the ITU-R method.

2) Calculate the slant-path length $L_S$ and horizontal projection $L_G$ from the rain height and the altitude of the ground receiver site. [Same as Step 2 of ITU-R Rain Model, Section 2.2.4.1]

The slant path length $L_s$ is defined as the length of the satellite-to-ground path that is affected by a rain cell (see Exhibit 2.2.4.1-1).

The slant path length $L_S$, expressed in km, is determined from

$$L_S(\theta) = \begin{cases} \dfrac{(h_R - h_S)}{\sin\theta} & for \quad \theta \geq 5^\circ \\ \dfrac{2(h_R - h_S)}{\left[\sin^2\theta + \frac{2(h_R - h_S)}{R_e}\right]^{1/2} + \sin\theta} & for \quad \theta < 5^\circ \end{cases} \qquad (2.2.4.4\text{-}2)$$

where,

$h_R$ = the height of the rain (km),
$h_S$ = the altitude of the ground receiver site from sea level (km),
$\theta$ = the elevation angle,
$R_E$= 8500 km (effective earth radius).

For angles greater than or equal to 5°, the slant path length is derived from the geometry from Exhibit 2.2.4.1-1. This equation for $L_S$ can result in negative values when the rain height is smaller than the altitude of the ground receiver site. If a negative value occurs, $L_S$ is set to zero.

The horizontal projection is calculated as

$$L_G = L_S \cos \theta \qquad (2.2.4.4\text{-}3)$$

where $L_S$ and $L_G$ are in kilometers.

3) Determine the rain rate $R_{0.01}$ (for 0.01% of an average year). [Same as Step 3 of ITU-R Rain Model, Section 2.2.4.1]

Select the value of rain rate at 0.01 % outage from the table of Exhibit 2.2.4.1-2, for the location of interest. The rain zones (A through Q) are associated with different geographic regions around the world, as shown in Exhibits 2.2.4.1-3, 2.2.4.1-4, 2.2.4.1-5.

4) Obtain the specific attenuation $\gamma_R$ .

The specific attenuation is based on the relationship:

$$\gamma_R = k\, R^{\alpha} \qquad (2.2.4.4\text{-}4)$$

where $\gamma_R$ is the specific attenuation in (dB/km) and $\{k, \alpha\}$ are frequency dependent variables calculated using the regression coefficients $k_H$ , $k_V$ , $\alpha_H$ , and $\alpha_V$ from Exhibit 2.2.4.1-5. The subscripts H and V represent horizontal and vertical polarization, respectively. The values have been tested for frequencies up to 40 GHz.

5) Calculate the horizontal path adjustment factor $rh_{0.01}$ for 0.01% of the time from:

$$rh_{0.01} = \frac{1}{1 + 0.78\sqrt{\frac{L_G \gamma_R}{f}} - 0.38[1 - e^{-2L_G}]} \qquad (2.2.4.4\text{-}5)$$

where $L_G$ is the horizontal projection of the slant-path from step 2, $\gamma_R$ is the specific attenuation from step 4, and $f$ is the frequency in GHz.

6) Calculate the adjusted rain path length $L_r$ (km) from:

$$L_r = \begin{cases} \dfrac{L_G \mathrm{rh}_{0.01}}{\cos\theta} & for \quad \zeta > \theta \\ \dfrac{h_R - h_S}{\sin\theta} & for \quad \zeta \le \theta \end{cases} \qquad (2.2.4.4\text{-}6)$$

where,

$$\zeta = \tan^{-1}\left[\frac{h_R - h_S}{L_G \mathrm{rh}_{0.01}}\right] \qquad (2.2.4.4\text{-}7)$$

and,

$h_R$ = the height of the rain (km)
$h_S$ = the altitude of the ground receiver site from sea level (km)
$\theta$ = the elevation angle.

7) Calculate the vertical path adjustment factor $rv_{0.01}$ for 0.01% of the time:

$$\mathrm{rv}_{0.01} = \frac{1}{1 + \sqrt{\sin\theta}\left[31\left(1 - e^{-\theta/[1+\chi]}\right)\frac{\sqrt{L_r \gamma_R}}{f^2} - 0.45\right]} \qquad (2.2.4.4\text{-}8)$$

where,

$$\chi = \begin{cases} 36 - |\phi| & for \quad |\phi| < 36° \\ 0 & for \quad |\phi| \ge 36° \end{cases} \qquad (2.2.4.4\text{-}9)$$

and $\phi$ is the latitude of the ground station receiver.

8) Calculate the effective path length through rain $L_e$ (km):

$$L_e = L_r \, rv_{0.01} \text{ (km)}. \qquad (2.2.4.4\text{-}10)$$

9) Calculate the attenuation $A_{0.01}$ exceeded for 0.01% of an average year:

$$A_{0.01} = \gamma_R \, L_e \quad \text{(dB)}. \qquad (2.2.4.4\text{-}11)$$

10) Calculate the attenuation $A_P$ exceeded P% of the time where P is the link outage:

$$A_{\mathrm{P}} = A_{0.01}\left(\frac{P}{0.01}\right)^{-(0.655+0.033\ln P-0.045\ln A_{0.01}-z\sin\theta(1-P))} \qquad (2.2.4.4\text{-}12)$$

where for P < 1%

$$z=\begin{cases} 0 & for \quad |\phi| \geq 36° \\ -0.005(|\varphi|-36) & for \quad \theta \geq 25° \quad and \quad |\phi| < 36°. \\ -0.005(|\varphi|-36)+1.8-4.25\sin\theta & for \quad \theta < 25° \quad and \quad |\phi| < 36° \end{cases} \qquad (2.2.4.4\text{-}13)$$

and for P ≥ 1%, z = 0.

### 2.2.4.5 ExCell Rain Attenuation Model

The ExCell Rain Attenuation Model (Capsoni, et. al., 1987) is loosely based on the ITU-R rain attenuation model, described in Section 2.2.4.1. The ITU-R model is based on point rainfall statistics. The ExCell method, however, also utilizes the concept of spatial distribution of rain cells. The structure of a rain cell is assumed to be exponential (hence the name EXponential Rain CELL), unlike the rectangular ITU-R assumption, and is characterized by two parameters, the peak intensity and the cell radius. The ExCell model is to be used for frequencies > 10 GHz.

The input parameters required for the ITU-R Rain Model are:

f: the frequency of operation, in GHz
$\theta$: the elevation angle to the satellite, in degrees
$\tau$: the polarization tilt angle with respect to the horizontal.
$\varphi$: the latitude of the ground station, in degrees N or S.
$h_s$: the altitude of the ground station above sea level, in km.

The step by step procedure follows:

1) Calculate the effective rain height $h_{fr}$ from the latitude of the ground receiver site using the ITU-R rain height procedure (ITU-R P.618-5, 1997).

The freezing rain height (or 0 °C isotherm) is the upper atmosphere altitude at which rain is in the transition state between rain and ice. The rain height is defined in km above sea level. Rain height is calculated as a function of ground station latitude ($\varphi$). The rain height, latitude and elevation angle are then used to calculate the slant path $L_S$ through a rain cell and the horizontal component of the slant path $L_G$.

The ITU-R rain height assumes that the rain height is a function of latitude ($\varphi$). The rain height $h_R$ is found as follows:

$$h_R(\varphi) = \begin{cases} 5 - 0.075(\varphi - 23) & \text{for} \quad \varphi > 23° \\ 5 & \text{for} \quad -21° \le \varphi \le 23° \\ 5 + 0.1(\varphi + 21) & \text{for} \quad -71° \le \varphi \le -21° \\ 0 & \text{for} \quad \varphi < -71° \end{cases} \qquad (2.2.4.5\text{-}1)$$

where $\varphi$ is the latitude of the ground station receiver. Positive $\varphi$ corresponds to the Northern Hemisphere, and negative $\varphi$ corresponds to the Southern Hemisphere. The rain height is expressed in km and is expected to be a value greater than zero. The rain height calculation is only valid for latitudes ($\varphi$) less than 89.6° (or greater than -89.6°).

2) Calculate the slant-path length $L_S$ and horizontal projection $L_G$ from the rain height and the altitude of the ground receiver site using the ITU-R procedure.

Rain attenuation is directly proportional to the slant path length. The slant path length $L_s$ is defined as the length of the satellite-to-ground path that is affected by a rain cell (see Exhibit 2.2.4.1-1).

The slant path length $L_S$, expressed in km, is determined from

$$L_S(\theta) = \begin{cases} \dfrac{(h_R - h_S)}{\sin\theta} & for \quad \theta \geq 5° \\ \dfrac{2(h_R - h_S)}{\left[\sin^2\theta + \frac{2(h_R - h_S)}{R_e}\right]^{1/2} + \sin\theta} & for \quad \theta < 5° \end{cases} \qquad (2.2.4.5\text{-}2)$$

where,

$h_R$ = the height of the rain (km), from Step 1
$h_S$ = the altitude of the ground receiver site from sea level (km),
$\theta$ = the elevation angle,
$R_E$= 8500 km (effective earth radius).

For angles greater than or equal to 5°, the slant path length is derived from the geometry shown in Exhibit 2.2.4.1-1. This equation for $L_S$ can result in negative values when the rain height is smaller than the altitude of the ground receiver site. If a negative value occurs, $L_S$ is set to zero.

The horizontal projection is calculated as

$$L_G = L_S \cos\theta \qquad (2.2.4.5\text{-}3)$$

where $L_S$ and $L_G$ are in kilometers.

3) Determine the rain intensity cumulative distribution using the following mathematical model for *P(R)*:

$$P(R) = P_o \ln^n(R^*/R), \qquad (2.2.4.5\text{-}4)$$

with the following steps:

a) Determine the maximum rain rate $R_{0.001}$ for the location of interest ITU-R Rain Region, shown highlighted in Exhibit 2.2.4.5-1. The rain zones (A through Q) are associated with different geographic regions around the world, as shown in Exhibits 2.2.4.1-3, 2.2.4.1-4, 2.2.4.1-5. Determine the value of R* equal to four times the maximum rain rate $R_{0.001}$:

$$R^* = 4\, R_{0.001}. \qquad (2.2.4.5\text{-}5)$$

| | ITU Rain Regions | | | | | | | | | | | | | | |
|---|---|---|---|---|---|---|---|---|---|---|---|---|---|---|---|
| % Outage | A | B | C | D | E | F | G | H | J | K | L | M | N | P | Q |
| **0.001** | **22** | **32** | **42** | **42** | **70** | **78** | **65** | **83** | **55** | **100** | **150** | **120** | **180** | **250** | **170** |
| 0.003 | 14 | 21 | 26 | 29 | 41 | 54 | 45 | 55 | 45 | 70 | 105 | 95 | 140 | 200 | 142 |
| 0.01 | 8 | 12 | 15 | 19 | 22 | 28 | 30 | 32 | 35 | 42 | 60 | 63 | 95 | 145 | 115 |
| 0.03 | 5 | 6 | 9 | 13 | 12 | 15 | 20 | 18 | 28 | 23 | 33 | 40 | 65 | 105 | 96 |
| 0.1 | 2 | 3 | 5 | 8 | 6 | 8 | 12 | 10 | 20 | 12 | 15 | 22 | 35 | 65 | 72 |
| 0.3 | 0.8 | 2 | 2.8 | 4.5 | 2.4 | 4.5 | 7 | 4 | 13 | 4.2 | 7 | 11 | 15 | 34 | 49 |
| 1 | <0.1 | 0.5 | 0.7 | 2.1 | 0.6 | 1.7 | 3 | 2 | 8 | 1.5 | 2 | 4 | 5 | 12 | 24 |

Exhibit 2.2.4.5-1: ITU-R Rain Regions. Rain Rate in mm/h

b) For any given values {Ri, Pi} from the ITU-R rain regions, compute:

$$x_i = \ln(\ln(R^*/R_i)) \text{ , and} \quad (2.2.4.5\text{-}6)$$

$$y_i = \ln(P_i) . \quad (2.2.4.5\text{-}7)$$

The points selected are $R_i$, $P_i = \{R_{0.1}, 0.1\}$ and $R_j$, $P_j = R_{0.001} = 0.001$.

c) Determine the slope (n) of the regression line:

$$y_i = nx_i + b . \quad (2.2.4.5\text{-}8)$$

The slope is computed from the points $\{x_1 (R_{0.1}), y_1 (0.1)\}$ and $\{x_2 (R_{0.001}), y_2 (0.001)\}$ where

$$n = \frac{y_2 - y_1}{x_2 - x_1} . \quad (2.2.4.5\text{-}9)$$

If $n \leq 2$ then this procedure is not valid, and computation via the ExCell model is halted.

3) Calculate the y-intercept ($b$) of the regression line:

$$b = y_i - nx_i . \quad (2.2.4.5\text{-}10)$$

Compute $P_o$:

$$P_o = \exp(b) . \quad (2.2.4.5\text{-}11)$$

4) Compute the parameters k and $\alpha$ from the ITU-R regression coefficients.

The $k$ and $\alpha$ parameters are frequency dependent variables calculated using the regression coefficients $k_H$ , $k_V$ , $\alpha_H$, and $\alpha_V$ from Exhibit 2.2.4.1-5. The subscripts H and V represent horizontal and vertical polarization, respectively. The values have been tested for frequencies up to 40 GHz.

For those frequencies not listed in the table, the $k_H$, $k_V$ coefficients are determined by logarithmic interpolation with frequency; and the $\alpha_H$ and $\alpha_V$ terms are determined by linear interpolation with frequency. Finally $k$ and $\alpha$ (for the specific attenuation calculation) are calculated as

$$k = [k_H + k_V + (k_H - k_V)\cos^2\theta \cos 2\tau]/2 \qquad (2.2.4.5\text{-}12)$$

$$\alpha = [k_H \alpha_H + k_V \alpha_V + (k_H \alpha_H - k_V \alpha_V)\cos^2\theta \cos 2\tau]/2k \qquad (2.2.4.5\text{-}12)$$

where $\theta$ is the path elevation angle and $\tau$ is the polarization tilt angle with respect to the horizontal.

5) Set $A = L_s \cdot K \cdot 2^{\alpha}$ . Then determine the auxiliary variable $R_e$ from:

$$R_e = \left(\left(\frac{A}{kL_s}\right) - 2^{\alpha}\right)^{1/\alpha}. \qquad (2.2.4.5\text{-}13)$$

6) Evaluate the integral summation formula giving the probability of the attenuation being exceeded:

$$P(A) = \Delta \sum_{k=i}^{N} E_k \cdot \left[\frac{1}{2}\ln^2\left(\frac{R_k}{R_e}\right) + r_k \cdot \ln\left(\frac{R_k}{R_e}\right)\right] \cdot P_k'''(\ln(R_k)). \qquad (2.2.4.5\text{-}14)$$

This is the integration over all the partial contributions to the probability due to the various cells. It is accomplished by determining a series of "N" regularly spaced values of ln ($R_k$) between ln($R_e$) and ln(R*):

$$\ln(R_k) = \ln(\mathrm{Re}) + (k - \tfrac{1}{2}) \cdot \Delta; \quad 1 \le k \le N \qquad (2.2.4.5\text{-}15)$$

with:

$$\Delta = \frac{1}{N} \cdot \ln\left(\frac{R^*}{R_e}\right); \qquad N \text{ not less than } 15. \qquad (2.2.4.5\text{-}16)$$

Then, for each k, determine:

$$t_k = \left(\frac{R_e}{R_k}\right)^{\alpha}, \qquad (2.2.4.5\text{-}17)$$

$$P_o^{\min,k} = \frac{1}{8} \cdot L_G \alpha \frac{t_k(3 - t_k)}{(1 - t_k)}, \qquad (2.2.4.5\text{-}18)$$

$$< P_{o,k} >= 2.71 R_k^{-0.26}, \quad (2.2.4.5\text{-}19)$$

$$E_k = \exp(-P_o^{\min,k} / < P_{o,k} >), \quad (2.2.4.5\text{-}20)$$

$$r_k = L_G / (4\pi \cdot < P_{o,k} >), \quad (2.2.4.5\text{-}21)$$

$$P_k'''(\ln(R_k)) = P_o \cdot n(n-1)(n-2)\ln^{(n-3)}(\tfrac{R^*}{R_k}), \quad (2.2.4.5\text{-}22)$$

and perform the summation for *P(A)* given by Equation (2.2.4.5-14).

**Note:** The interpolation algorithm may interpolate differently on different platforms due to rounding errors. The performance of this method can be noticeable improved in the high probabilities range by applying a "specialized" fit forcing for low rain (as opposite to the "full range" fit forcing used so far). It is suggested to apply the algorithm again by using only R ≤ 10 mm/h if at least two points in the cumulative distribution are given (the maximum value R* is unchanged). Then take the value of attenuation given by:

i) "full range" fit forcing (as shown above) for P < 0.04,
ii) "specialized" fit forcing (R…10 mm/h) for P ≥ 0.04.

8) For high outage probabilities, P ≥ 0.04, repeat step 7, equations 2.2.4.5-15 –2.2.4.5-22, and recalculate the summation for *P(A)*.

### 2.2.4.6 Manning Model

A rain attenuation prediction model was developed as part of the Advanced Communications Technology Satellite (ACTS) program at Lewis Research Center (LeRC). The model was developed by Dr. Robert Manning. The model is also referred to as the ACTS Rain Attenuation Prediction Model

The Manning Model consists of two separate elements or components. The first element of the model generates long term rain attenuation statistics for a slant path originating at specific geographic locations. The model that emerged from this effort is referred to as the ***Static Model*** (Manning, 1986)]. The static model currently supports 59 sites throughout the U.S.

The second element of the Manning Model was developed to capture the dynamic features of rain attenuation. The ***Dynamic Model*** evaluates link variations on the order of minutes and hours. Location dependence for the dynamic model is gained through a connection to the static model (Manning, 1987).

The static model was derived from extreme value statistical theory using long-term (up to 55 years in length) rain intensity curves and average rain fall amount data, provided by the U.S. Weather Service. The static model relates rain rate statistics for a particular location to attenuation statistics along a slant path.

The dynamic model was modeled as a Markov process. Based on observation of rain rates, the time rate of change of the rain rate is proportional to the rain rate. The rain attenuation process is modeled as a product of many random time-varying attenuation components, following an analogous argument used for rain rates. This attenuation process approaches a log-normal process for a large number of individual contributing attenuation processes. An intermediate quantity was introduced by standardizing the above log-normal process using the log of the mean of the attenuation process and the standard deviation of the log of the attenuation process. The same reasoning was applied to this intermediate quantity as for rain rate. That is, the time rate of change of this intermediate quantity is proportional to the quantity itself. This formed the basis for the stochastic differential equation used. The Markov property arises from the fact that the product of the time dependent conditional probability density functions imply independence.

The inputs parameters required for either model, with units in parentheses, are given as follows:

- Link operating frequency (1 GHz $\geq f \leq$ 1000 GHz).
- Longitude of the satellite in geostationary orbit (degress.minutes West)
- Longitude of the site (degrees.minutes $\geq$ 70 degrees, $\leq$ 125 degrees West)
- Latitude of the site (degrees.minutes $\geq$ 25 degrees, $\leq$ 50 degrees)
- Height of the terminal above sea level (feet), average yearly rainfall at terminal site (inches).

The outputs generated by the model are:

Static Model

- Probability of attenuation on the link (% of the year).
  *This is the probability that an attenuation event will occur on the slant path.*
- Mean attenuation on the link (dB)

Dynamic Model

- Standard deviation of log-attenuation.
- Fade duration and probability of occurrence.
  *These probabilities are for continuous attenuation duration from >0 to 30 minutes They are computed for fade levels 3, 5, 8, 10, 15 and 20 dB.*

The Manning Model is not structured to allow for a step by step procedure to be implemented for the general case of evaluation of a satellite path for a given location. Further information on the procedure is available from the developer of the model, R. Manning, at NASA Lewis Research Center, Cleveland, Ohio.

### 2.2.5 Rain Depolarization

The prediction of depolarization due to rain has evolved from early developments to empirical procedures that determine the cross polarization discrimination, XPD, from the copolarized attenuation, A. Prediction methods developed by Chu and by the ITU-R are provided. The contribution of ice to the XPD is also included in the ITU-R model.

### 2.2.5.1 Chu Empirical Models

This section describes the procedures and modeling techniques developed by Chu for the determination of rain induced depolarization on earth-space paths (Chu, 1974, 1980, 1982). The section begins with a development of the matrix representation utilized in the development of the modeling procedures.

Rain depolarization can be modeled using techniques similar to those applied to rain attenuation. The essential difference is that in examining depolarization, the raindrops are assumed to be oblate spheroids. Exhibit 2.2.5.1-1 shows the geometry for a dual linear polarized (LP) wave incident on an oblate spheroidal raindrop. The raindrop is at an arbitrary orientation with respect to the direction of propagation of the wave. The orientation is specified by the angle $\alpha$, between the propagation vector and the raindrop's symmetry axis. The plane containing $\alpha$ will be referred to as the plane of incidence.

$E_x$ and $E_y$ are electric field vectors of two orthogonal LP waves. They are in a plane normal to the propagation vector, and each one can be resolved into two components: a component in the plane of incidence, and a component normal to it. Parallel to these components, we define two symmetry axes, labeled I and II in the figure. The projection of the raindrop into the plane containing the electric field vectors is an ellipse, and axes I and II are its minor and major axes, respectively. Exhibit 2.2.5.1-2 shows this ellipse and how the electric fields are resolved into their "I" and "II" components.

The total electric field magnitudes in the I and II directions ($E_I$ and $E_{II}$) are given by

$$\begin{bmatrix} E_I \\ E_{II} \end{bmatrix} = \begin{bmatrix} \cos\theta & -\sin\theta \\ \sin\theta & \cos\theta \end{bmatrix} \begin{bmatrix} E_x \\ E_y \end{bmatrix} = R \begin{bmatrix} E_x \\ E_y \end{bmatrix} \qquad (2.2.5.1\text{-}1)$$

where $\theta$, the canting angle, is the angle between the x and I axes.

Now consider a region of space containing many identical raindrops with the same orientation distributed throughout it. According to scattering theory, the effect of many scatterers along the propagation path of a wave is to multiply the electric field vector by a transmission coefficient of the form

$$T = e^{[-(a-j\phi)L]} \qquad (2.2.5.1\text{-}2)$$

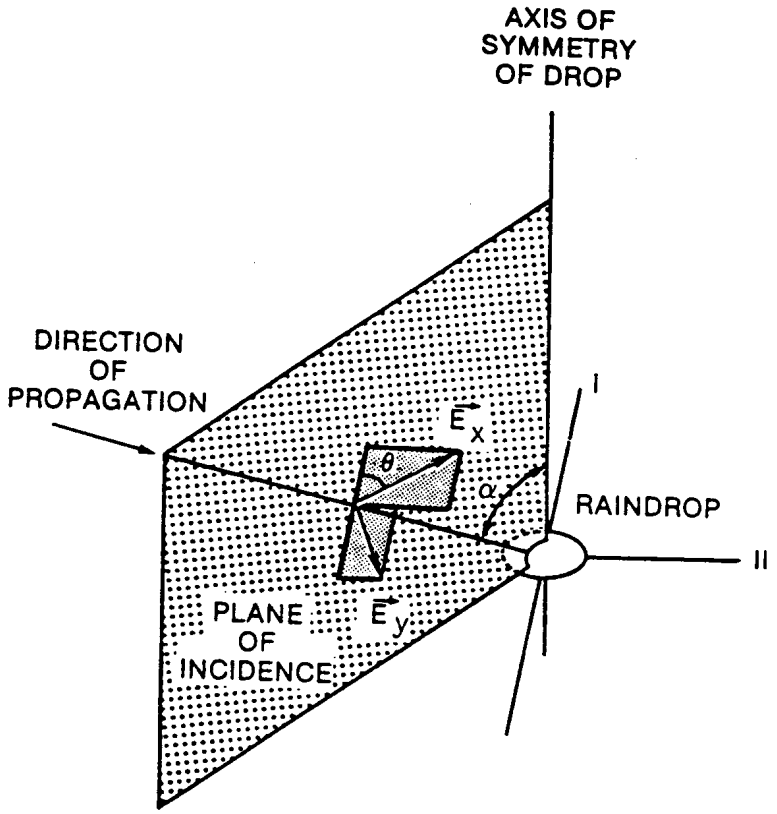


Exhibit 2.2.5.1-1. Geometry for Rain Depolarization Analysis

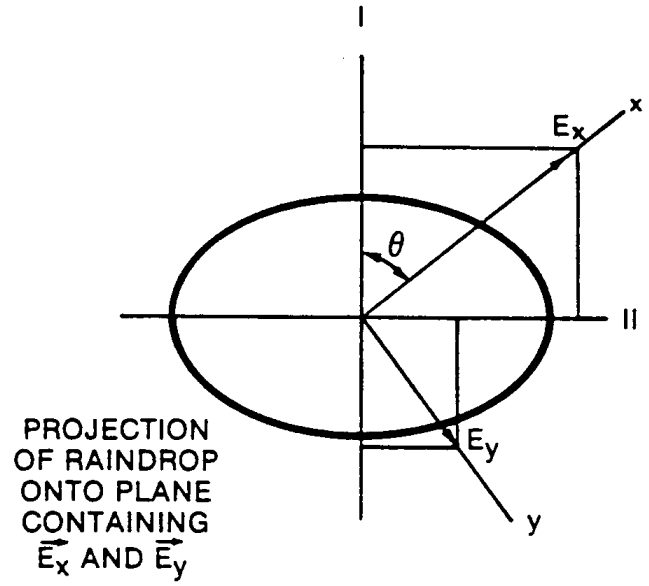


Exhibit 2.2.5.1-2. Resolution of Electric Fields into I and II Components

where L is the path length through the scattering region. The 'a' term of the exponent produces attenuation of the wave, and the $\phi$ termproduces a phase lag. This phase lag is in addition to the normal free-space phase retardation of the fields. Instead of a and $\phi$ , which have units of nepers per unit length and radians per unit length, respectively, the more useful parameters, A and $\Phi$, are normally used:

A = specific attenuation of power flux density of wave, in dB/km.
$= 20 (\log_{10} e)\, a = 8.686\, a$

$\Phi$ = specific phase lag of wave, in degrees/km.
$= (180/\pi)\, \phi$

A region filled with oblate spheriodal raindrops is characterized by two transmission coefficients: $T_I$, applied to the "I" component of the electric field, and $T_{II}$, applied to the "II" component. Denoting the fields of the wave incident on the scattering region by a subscript i, and the fields of the wave exiting the region by s (for scattered), we can write

$$\begin{bmatrix} E_{Is} \\ E_{IIs} \end{bmatrix} = \begin{bmatrix} T_I & 0 \\ 0 & T_{II} \end{bmatrix} \begin{bmatrix} E_{Ii} \\ E_{IIi} \end{bmatrix} = T \begin{bmatrix} E_{Ii} \\ E_{IIi} \end{bmatrix} \qquad (2.2.5.1\text{-}3)$$

The coordinate rotation R, defined above, can be applied to get an equation for the effect of the scattering region on the field vectors in the x and y directions.

$$\begin{bmatrix} E_{xs} \\ E_{ys} \end{bmatrix} = R^{-1} T R \begin{bmatrix} E_{xi} \\ E_{yi} \end{bmatrix} = T' \begin{bmatrix} E_{xi} \\ E_{yi} \end{bmatrix} \qquad (2.2.5.1\text{-}4)$$

Exhibit 2.2.5-3 shows how the three component transformations are successively applied to produce T'. The overall transformation matrix T' can be evaluated to yield

$$T' = \begin{bmatrix} t_{xx} & t_{xy} \\ t_{yx} & t_{yy} \end{bmatrix}$$
$$t_{xx} = T_I \cos^2\theta + T_{II} \sin^2\theta \qquad (2.2.5.1\text{-}5)$$
$$t_{yy} = T_I \sin^2\theta + T_{II} \cos^2\theta$$
$$t_{xy} = t_{yx} = \frac{1}{2}(T_{II} - T_I) \sin^2\theta$$

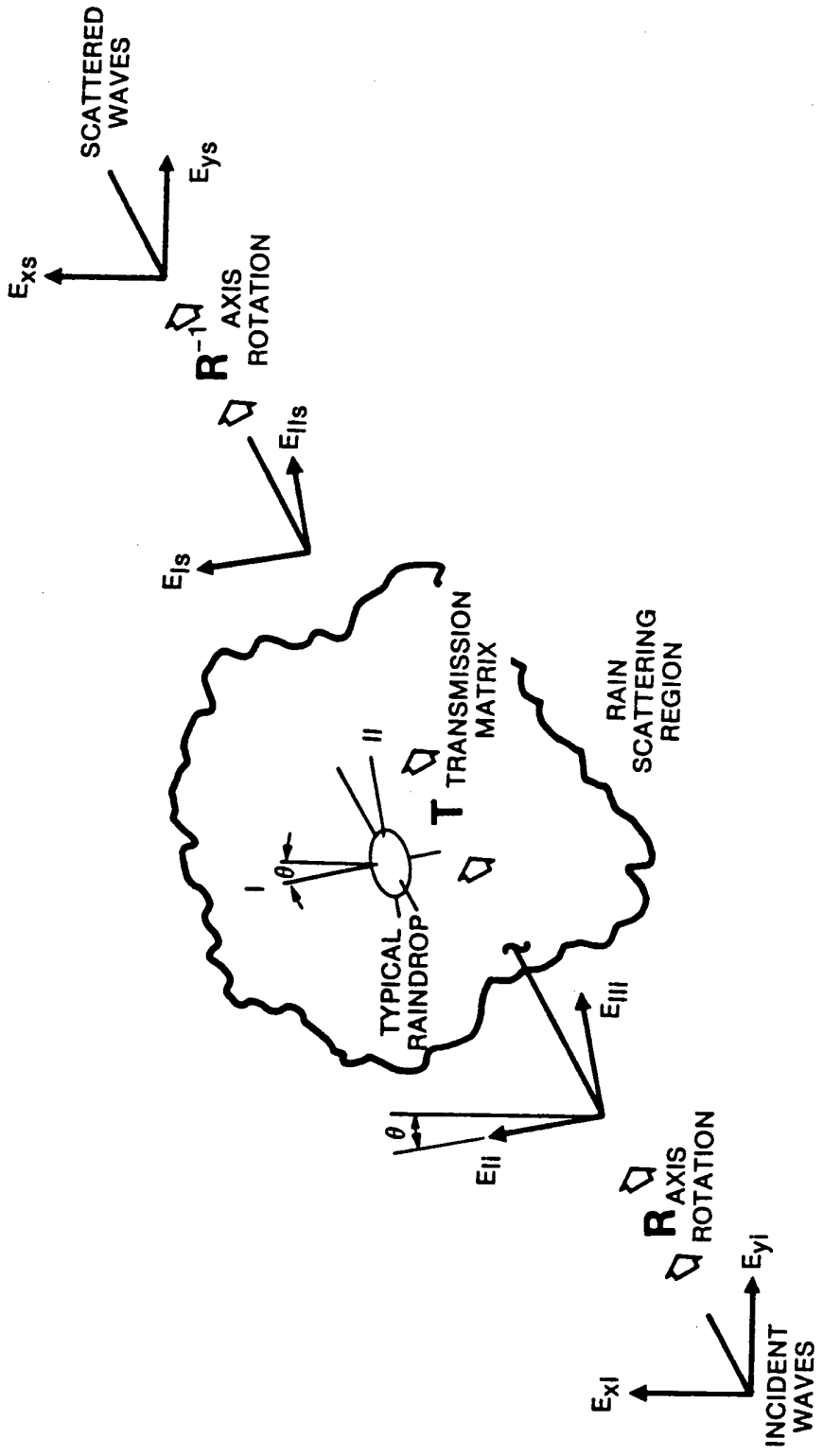


Exhibit 2.2.5.1-3. Components of Overall Transformation Matrix 'T' Describing Rain Depolarization

If we specify the LP wave polarized in the x direction the copolarized wave, we can now obtain expressions for the cross polarization discrimination, XPD:

$$\begin{aligned} XPD_x &= 10\log\frac{\left|E_{xs}\right|^2}{\left|E_{ys}\right|^2} \quad \text{with } E_{yi=0} \\ &= 10\log\frac{\left|t_{xx}\right|^2}{\left|t_{yx}\right|^2} \\ &= 20\log\frac{1+\gamma\tan^2\theta}{(\gamma-1)\tan\theta} \end{aligned} \tag{2.2.5.1-6}$$

where

$$\gamma = \frac{T_{II}}{T_I} = e^{[-(a_{II}-a_I)L+j(\phi_{II}-\phi_I)L]}$$

Or, if we specify the y- direction as the copolarized state,

$$\begin{aligned} XPD_y &= 10\log\frac{\left|E_{ys}\right|^2}{\left|E_{xs}\right|^2} \quad \text{with } E_{xi=0} \\ &= 10\log\frac{\left|t_{yy}\right|^2}{\left|t_{xy}\right|^2} \\ &= 20\log\frac{\gamma+\tan^2\theta}{(\gamma-1)\tan\theta} \end{aligned} \tag{2.2.5.1-7}$$

For the case of circular polarization

$$XPD_c = 10\log\left(\left|\frac{t_{xx}}{t_{yx}}\right|^2\right)_{\theta=45^o} = 20\log\frac{\gamma+1}{\gamma-1} \tag{2.2.5.1-8}$$

which is independent of the sense of rotation of the copolarized wave.

Thus far, we have assumed that all raindrops are of equal size and have the same orientation. The model must account for the distribution of sizes and shapes of raindrops and the distribution of angles $\theta$ and $\alpha$ that are present in the rain along the path. Scattering theory allows for this. The scattering effect of a single raindrop is determined as a function of some parameter (like size),

then the distribution of that parameter over the population of raindrops is used in calculating the transmission coefficients. The transmission coefficients (more exactly, the specific attenuation and phase lag, A and $\Phi$) have been calculated in this manner as a function of rain rate by several authors. The first calculations (Chu,1974) (Watson and Arbabi, 1973a) used oblate spheroidal raindrops. The drops were assumed to be distributed according to the well-known Laws and Parsons distribution, and to have eccentricities that were directly related to their sizes, with the largest drops being the most deformed. Later work has considered the more realistic drop shapes Pruppacher-Pitter (1971) and (Oguchi, 1977). Exhibit 2.2.5.1-4 (from Morrison, et al, 1973) is an example of the results of these calculations. These curves give the difference in the specific attenuation and phase between the I and II axes. The angle between the direction of propagation and the raindrop symmetry axis, $\alpha$ , is a parameter, and the canting angle, $\alpha$, is set to $25^o$. The differential attenuation and phase are of most interest because they actually determine XPD. As can be seen from the curves, the worst case for differential attenuation and phase corresponds to $\alpha = 90^o$. This agrees with intuition, since the projection ellipse of the drop onto the plane containing the field vectors has the greatest eccentricity for that case. For values of $\alpha$ different from $90^o$, Chu (1974) shows that the following approximation is true:

$$\begin{aligned} A_{II} - A_I &= \sin^2 \alpha \, [(A_{II} - A_I)]_{\alpha=90^o} \\ \Phi_{II} - \Phi_I &= \sin^2 \alpha \, [(\Phi_{II} - \Phi_I)]_{\alpha=90^o} \end{aligned} \qquad (2.2.5.1\text{-}9)$$

Accounting for the distribution of $\alpha$ and $\alpha$ is more difficult than doing so for drop size and shape. We have little information about the distribution of the orientation of raindrops. It is expected that wind and wind gusts produce an appreciable spatial correlation in the orientation. In the absence of wind, a fairly symmetric distribution about the vertical would be expected.

The $\alpha$ component of drop orientation is usually considered to be equal to a constant $90^o$ for line-of-sight (horizontal) paths and the complement of the elevation angle for satellite (oblique) paths. The effect of $\alpha$ on XPD is apparently so small compared with the canting angle dependence that allowing for a distribution of $\alpha$ is not worthwhile.

### 2.2.5.1.1 Chu Two-Tiered Rain Depolarization Model

Chu (1980) employed a "two-tiered" Gaussian model to account for the canting angle variations. It assumes first that the instantaneous canting angle has a Gaussian distribution with mean $\phi_m$ and standard deviation $S_\phi$. Second, the mean angle $\phi_m$, which varies with time, is itself assumed to be Gaussian. The distribution of $\phi_m$ has zero mean and standard deviation $S_m$. Chu states that the values of these parameters that give the best agreement with experimental data are $S_\phi = 30^o$ and $S_m = 3^o$.

Based on this two-tiered model, Chu (1982) derived a semi-empirical formula for depolarization versus attenuation that agrees with experimental results over a wide range of frequency, polarization tilt angle and elevation angle.

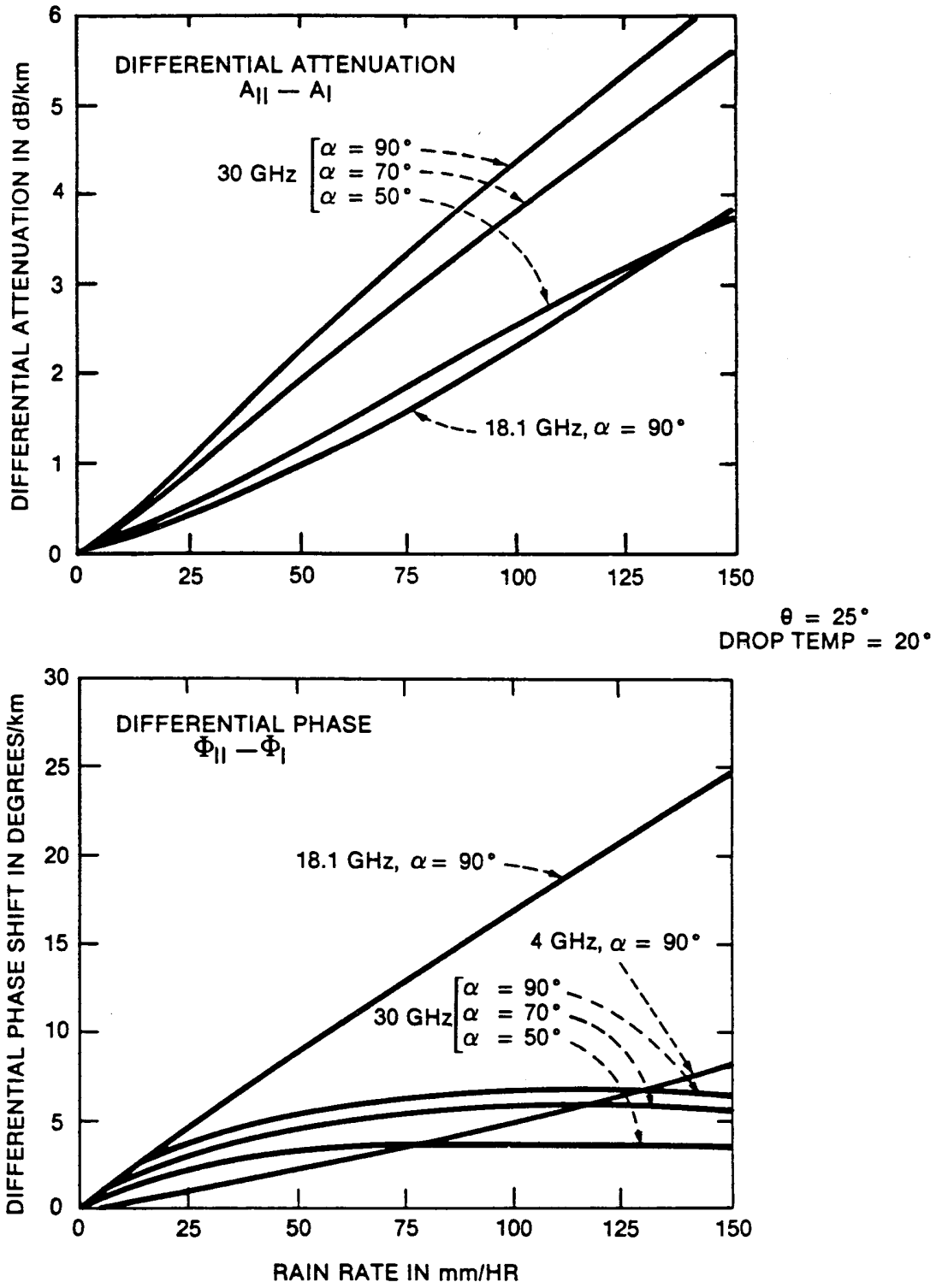


Exhibit 2.2.5.1-4. Differential Attenuation and Phase for Rain
*[Source: Morrison et. al., (1973)]*

To calculate long-term statistics of depolarization from rain attenuation statistics the following parameters are required:

$A_p$: rain attenuation (dB) exceeded for the required percentage of time, $p$, for the path in question, commonly called co-polar attenuation, CPA,

$\tau$: tilt angle of the linearly polarized electric field vector with respect to the horizontal

$f$: frequency (GHz),

$\theta$: path elevation angle (degrees).

Step 1) Determine the Cross-polarization discrimination, XPD.

a) For circular polarization, $XPD_c$ , in decibels, is given by

$$XPD_c = 11.5 + 20\log f - 20\log A_p - 40\log(\cos\theta) \qquad (2.2.5.1\text{-}10)$$

b) For linear polarization,

$$\begin{aligned} XPD_L &= 11.5 + 20\log f - 20\log A_p - 40\log(\cos\theta) \\ &-10\log\left[\frac{1}{2}(1 - 0.978\cos 4\tau)\right] - 0.075 A_p \cos^2\theta\cos 2\tau \end{aligned} \qquad (2.2.5.1\text{-}11)$$

### 2.2.5.2 ITU-R Rain Depolarization Model

This section presents the latest ITU-R rain depolarization method as described in ITU-R P.618-5 (ITU-R, 1997).

To calculate long-term statistics of depolarization from rain attenuation statistics the following parameters are needed:

$A_p$: rain attenuation (dB) exceeded for the required percentage of time, $p$, for the path in question, commonly called co-polar attenuation, CPA,

$\tau$: tilt angle of the linearly polarized electric field vector with respect to the horizontal (for circular polarization use $\tau = 45°$),

$f$: frequency (GHz),

$\theta$: path elevation angle (degrees).

The method described below to calculate cross-polarization discrimination (XPD) statistics from rain attenuation statistics for the same path is valid for 8 GHz $\leq f \leq$ 35 GHz and $\theta \leq 60°$. The procedure for scaling to frequencies down to 4 GHz is given in steps 8 and 9 below.

1) Calculate the frequency-dependent term:

$$C_f = 30\log f \qquad \text{for } 8 \leq f \leq 35 \text{ GHz.} \qquad (2.2.5.2\text{-}1)$$

2) Calculate the rain attenuation dependent term:

$$C_A = V(f)\log A_p \qquad (2.2.5.2\text{-}2)$$

where:

$$V(f) = 12.8 f^{0.19} \qquad \text{for } 8 \leq f \leq 20 \text{ GHz,}$$

$$V(f) = 22.6 \qquad \text{for } 20 < f \leq 35 \text{ GHz.}$$

3) Calculate the polarization improvement factor:

$$C_\tau = -10\log[1 - 0.484(1 + \cos 4\tau)] \qquad (2.2.5.2\text{-}3)$$

The improvement factor $C_\tau = 0$ for $\tau = 45°$ and reaches a maximum value of 15 dB for $\tau = 0°$ or 90°.

4) Calculate the elevation angle-dependent term:

$$C_\theta = -40\log(\cos\theta) \qquad \text{for } \theta \le 60° \qquad (2.2.5.2\text{-}4)$$

5) Calculate the canting angle dependent term:

$$C_\sigma = 0.0052\sigma^2 \qquad (2.2.5.2\text{-}5)$$

$\sigma$ is the effective standard deviation of the raindrop canting angle distribution, expressed in degrees; $\sigma$ takes the value 0°, 5°, 10° and 15° for 1%, 0.1%, 0.01% and 0.001% of the time, respectively.

6) Calculate rain XPD not exceeded for $p$% of the time:

$$XPD_{rain} = C_f - C_A + C_\tau + C_\theta + C_\sigma \qquad \text{dB} \qquad (2.2.5.2\text{-}6)$$

7) Calculate the ice crystal dependent term:

$$C_{ice} = XPD_{rain} \times (0.3 + 0.1\log p)/2 \qquad \text{dB} \qquad (2.2.5.2\text{-}7)$$

8) Calculate the XPD not exceeded for $p$% of the time, including the effects of ice:

$$XPD_p = XPD_{rain} - C_{ice} \qquad \text{dB} \qquad (2.2.5.2\text{-}8)$$

In this prediction method in the frequency band 4 to 6 GHz where path attenuation is low, $A_p$ statistics are not very useful for predicting XPD statistics. For frequencies below 8 GHz, the frequency-scaling formula of step 9 can be used to scale cross-polarization statistics calculated for 8 GHz down to the 6 to 4 GHz band.

9) Long-term XPD statistics obtained at one frequency and polarization tilt angle can be scaled to another frequency and polarization tilt angle using the semi-empirical formula:

$$XPD_2 = XPD_1 - 20\log\left[\frac{f_2\sqrt{1-0.484(1+\cos 4\tau_2)}}{f_1\sqrt{1-0.484(1+\cos 4\tau_1)}}\right] \qquad \text{for } 4 \le f_1, f_2 \le 30 \text{ GHz} \qquad (2.2.5.2\text{-}9)$$

where $XPD_1$ and $XPD_2$ are the XPD values not exceeded for the same percentage of time at frequencies $f_1$ and $f_2$ and polarization tilt angles, $\tau_1$ and $\tau_2$, respectively.

Equation 2.2.5.2-9 is based on the same theoretical formulation as the prediction method of steps 1-8, and can be used to scale XPD data that include the effects of both rain and ice depolarization, since it has been observed that both phenomena have approximately the same frequency dependence at frequencies less that about 30 GHz.

### 2.2.6 Ice Depolarization

The second major cause of depolarization on Earth-space paths, besides rain, is the presence of ice crystals in clouds at high altitudes. Ice crystal depolarization is different from rain depolarization in that it is not accompanied by appreciable co-polarized attenuation. This is because the depolarization is caused primarily by differential phase shifts, rather than differential attenuation, which is responsible for rain depolarization. Another distinguishing characteristic is that the amplitude and phase of the cross-polarized signal often undergo abrupt, coincident changes with large excursions.

The change an electric field experiences in passing through a depolarizing medium can be represented by

$$[E]=[D]\ \left[E^{i}\right] \tag{2.2.6-1}$$

where $[E^i]$ is the matrix representation of the field associated with the plane wave incident on the depolarizing medium, [E] is the matrix for the field arriving at the receiver, and the depolarization matrix is

$$[D]=\begin{bmatrix} D_{xx} & D_{xy} \\ D_{yx} & D_{yy} \end{bmatrix}. \tag{2.2.6-2}$$

In a clear air medium, [D] is the identity matrix, and the electric field is unchanged by the medium. The propagation direction is taken to be along the *z*-axis, and the wave polarization plane is the *xy*-plane with the *x* direction being fixed as horizontal.

The effect of the depolarizing medium on a communication system depends upon the polarization of the antennas. The dual-polarized receiving antenna can be represented by a response matrix

$$[\mathrm{A_R}]=\begin{bmatrix} \cos\gamma_{\mathrm{c}} & \sin\gamma_{\mathrm{c}}\mathrm{e}^{-\mathrm{j}\delta_{\mathrm{c}}} \\ \cos\gamma_{\mathrm{x}} & \sin\gamma_{\mathrm{x}}\mathrm{e}^{-\mathrm{j}\delta_{\mathrm{x}}} \end{bmatrix}, \tag{2.2.6-3}$$

where ($\gamma_c$, $\delta_c$) and ($\gamma_x$, $\delta_x$) are conventional polarization parameters (Kraus and Carver, 1973) for the copolarized and cross-polarized channels. The complex voltages at the output ports of the receiving antenna are then found from

$$\begin{bmatrix} V_c \\ V_x \end{bmatrix}=[A_R]\ [E]=[A_R]\ [D]\ \left[E^{i}\right]. \tag{2.2.6-4}$$

System performance can then be evaluated using the complex depolarization ratio

$$C = \frac{V_x}{V_c}. \qquad (2.2.6\text{-}5)$$

The cross-polarization ratio is defined as CPR = $|C|^2$. The inverse of CPR is the cross-polarization discriminator, XPD.

### 2.2.6.1 Tsolakis and Stutzman Model

A complete model for ice media propagation would require a knowledge of ice particle sizes, shapes, and quantities. Such information about ice media is at best incomplete. Nevertheless, a great deal can be accomplished with a model that employs some simplifying assumptions about the ice medium. Definitive information on ice particle sizes and shapes is not available, but needle and plate shapes appear to occur frequently. It is customary to approximate the ice needle shape by a long narrow prolate spheroid and the ice plate shape by a flat oblate spheroid.

The flexibility introduced by using sophisticated computational methods is not required in most situations because of the lack of information on ice particle sizes and shapes. Usually, some form of the Rayleigh approximation is employed to provide simplicity in calculation. Forward scattering from ice crystals can be computed using Rayleigh scattering concepts, since the particles are small in relation to the wavelength. The Rayleigh scattering approach has been taken to be valid up to 50 GHz.

To compute ice depolarization matrix, the following parameters are needed:

$\varepsilon$: path elevation angle (degrees),

$\psi$: projection of the tilt angle of the particles onto the *xy*-plane (for both plates and needles) (degrees),

$\phi$: azimuth rotation angle (out of the *xy*-plane) of the axis of symmetry for ice needles (degrees),

m: complex index of refraction of ice (unitless),

$\delta$: phase difference between $E_y$ and $E_x$, $-180° \le \delta \le +180°$,

V: volume of the spheroid ($m^3$),

$\rho$: ice particle number density (number per cubic meter of volume, $m^{-3}$),

L: thickness of the ice cloud (m), and

<V>: average ice particle volume ($m^3$).

A step by step procedure is now provided for the prediction model.

1) Compute the intermediate value:

$$p_x^2 = 1 + \cos^2\varepsilon(\cos 2\phi + \cos 2\psi) + \cos 2\psi \cos 2\phi(1 + \sin^2\varepsilon) + \sin^2\varepsilon + 2\sin 2\psi \sin 2\phi \sin\varepsilon \quad (2.2.6.1\text{-}1)$$

2) Compute the intermediate value:

$$p_y^2 = 1 + \cos^2\varepsilon(\cos 2\phi - \cos 2\psi) - \cos 2\psi \cos 2\phi(1 + \sin^2\varepsilon) + \sin^2\varepsilon - 2\sin 2\psi \sin 2\phi \sin\varepsilon \quad (2.2.6.1\text{-}2)$$

3) Compute the intermediate value:

$$p_x p_y = 2\cos 2\psi \sin 2\phi \sin\varepsilon - \sin 2\psi \cos^2\varepsilon - 2\sin 2\psi \cos 2\phi(1 + \sin^2\varepsilon) \quad (2.2.6.1\text{-}3)$$

4) Compute the f (plates) matrix:

$$[f']_{plate} = (m^2 - 1)\begin{bmatrix} 1 + \dfrac{1-m^2}{m^2}\cos^2\delta\ \sin\psi & \dfrac{1-m^2}{2m^2}\cos^2\delta\ \sin 2\psi \\ \dfrac{1-m^2}{2m^2}\cos^2\delta\ \sin 2\psi & 1 + \dfrac{1-m^2}{m^2}\cos^2\delta\ \cos^2\psi \end{bmatrix}, \quad (2.2.6.1\text{-}4)$$

where

$$[f]_{plate} = \frac{k_0^2 V}{4\pi}\ [f']_{plate}. \quad (2.2.6.1\text{-}5)$$

5) Compute the f (needles) matrix:

$$[f']_{needle} = \frac{2(m^2-1)}{m^2+1}\begin{bmatrix} 1 + \frac{1}{8}(m^2-1)p_x^2 & \frac{1}{8}(m^2-1)p_x p_y \\ \frac{1}{8}(m^2-1)p_x p_y & 1 + \frac{1}{8}(m^2-1)p_y^2 \end{bmatrix}, \quad (2.2.6.1\text{-}6)$$

where

$$[f]_{needle} = \frac{k_0^2 V}{4\pi}\ [f']_{needle}. \quad (2.2.6.1\text{-}7)$$

6) Compute the k matrix:

$$k = \begin{bmatrix} k_{11} & k_{12} \\ k_{21} & k_{22} \end{bmatrix}, \quad (2.2.6.1\text{-}8)$$

$$k_{11} = \frac{k_o}{2} \rho L \langle V \rangle \left\{ P \left\langle \left[ f_{11}^{'} \right]_{plate} \right\rangle + (1-P) \left\langle \left[ f_{11}^{'} \right]_{needle} \right\rangle \right\}, \quad (2.2.6.1\text{-}9)$$

$$k_{22} = \frac{k_o}{2} \rho L \langle V \rangle \left\{ P \left\langle \left[ f_{22}^{'} \right]_{plate} \right\rangle + (1-P) \left\langle \left[ f_{22}^{'} \right]_{needle} \right\rangle \right\}, \quad (2.2.6.1\text{-}10)$$

$$k_{12} = k_{21} = \frac{k_o}{2} \rho L \langle V \rangle \left\{ P \left\langle \left[ f_{12}^{'} \right]_{plate} \right\rangle + (1-P) \left\langle \left[ f_{12}^{'} \right]_{needle} \right\rangle \right\}, \quad (2.2.6.1\text{-}11)$$

where $k_o = 2\pi f / 0.3$. The shape distribution is bimodal with $P$ being the fraction of plates and $1\text{-}P$ being the fraction of needles. The tilt angle of all particles (angle of plate axis of rotation from vertical and angle of needle axis of rotation from horizontal) is Gaussian distributed with mean $\langle \psi \rangle$ and standard deviation $\sigma_\psi$. The orientation angle of needles in the horizontal (azimuth) plane, $\phi$, is assumed to be Gaussian distributed with mean $\langle \phi \rangle$ and standard deviation $\sigma_\phi$. $[f']_{\text{plate}}$ and $[f']_{\text{needle}}$ are found from Eq.'s 2.2.6.1-4 and 2.2.6.1-6 with the following replacements:

$$\cos 2\psi \rightarrow e^{-2\sigma\psi^2} \cos\left(2\langle\psi\rangle\right),$$
$$\sin 2\psi \rightarrow e^{-2\sigma\psi^2} \sin\left(2\langle\psi\rangle\right),$$
$$\cos 2\phi \rightarrow e^{-2\sigma\phi^2} \cos\left(2\langle\phi\rangle\right),$$
$$\sin 2\phi \rightarrow e^{-2\sigma\phi^2} \sin\left(2\langle\phi\rangle\right).$$

It is convenient to introduce an ice content factor and define it as IC=ρL<V>. It is a measure of the total ice encountered by a wave passing through the cloud. Introduction of this parameter combines three unknowns into one, reducing the complexity of the problem. The value of IC can be estimated. Choosing an average volume of $10^{-12}$ $m^3$ (from an average radius of about 0.1 mm) and a particle density of $10^6$ $m^{-3}$ gives an ice concentration of $10^{-6}$ $m^3/m^3$. This average volume is approximate and will actually depend upon the distributions of particle sizes and shapes. Antar et al. (1982) deduces from radar observations ice concentrations of 0.25 x $10^{-6}$ and 1.05 x $10^{-6}$ $m^3/m^3$ in two clouds. A cloud thickness of 1 to 5 km gives values of IC from $10^{-3}$ to 5 x $10^{-3}$ $m^4/m^3$. This thickness is consistent with the few estimates from radar measurements by Antar et al. (1982) of 2 to 3 km maximum vertical thickness of ice clouds.

7) Compute the ice depolarization matrix:

$$[D] = \frac{1}{\lambda_1 - \lambda_2} \begin{bmatrix} (k_{22} - \lambda_2) e^{-j\lambda_2} - (k_{22} - \lambda_1) e^{-j\lambda_1} & k_{12}\left(e^{-j\lambda_1} - e^{-j\lambda_2}\right) \\ k_{12}\left(e^{-j\lambda_1} - e^{-j\lambda_2}\right) & (k_{22} - \lambda_2) e^{-j\lambda_1} - (k_{22} - \lambda_1) e^{-j\lambda_2} \end{bmatrix} \quad (2.2.6.1\text{-}12)$$

where

$$\lambda_1 = \tfrac{1}{2}\left\{k_{11} + k_{22} + \left[(k_{11} - k_{22})^2 + (2k_{12})^2\right]^{1/2}\right\}, \qquad (2.2.6.1\text{-}13)$$

$$\lambda_2 = \tfrac{1}{2}\left\{k_{11} + k_{22} - \left[(k_{11} - k_{22})^2 + (2k_{12})^2\right]^{1/2}\right\}. \qquad (2.2.6.1\text{-}14)$$

The ice depolarization matrix can now be used to compute the XPD as shown in the introduction of this section.

### 2.2.6.2 ITU-R Ice Depolarization Prediction

The ITU-R Rain Depolarization procedure described in Section 2.2.5.2 includes a means of estimating the contribution of ice depolarization to the total XPD for the link. Steps 7 and 8 in that section computes the ice crystal dependent term and the XPD including the effect of ice.

The ice crystal dependent term is determined from;

$$C_{ice} = XPD_{rain} \times (0.3 + 0.1 \log p)/2 \qquad \text{dB} \qquad (2.2.6.2\text{-}1)$$

The XPD not exceeded for $p$% of the time, including the effects of ice is then found from

$$XPD_p = XPD_{rain} - C_{ice} \qquad \text{dB} \qquad (2.2.6.2\text{-}2)$$

where $XPD_{rain}$ is the cross polarization discrimination due to rain and $p$ is the percentage of time. The determination of the ice component by this method is on a statistical basis, i.e. the calculation is based on rain attenuation exceedance values for the percentage of the time $p$.

### 2.2.7 Wet Surface Effects

The need to model wet surface effects on the antenna dish, and feed was realized through the experience gained from the many rain attenuation experiments that have been conducted over the past several decades. There is no complete model allowing a link budget calculation for wet surface effects, however some experiments have been conducted and some modeling approaches have been proposed.

Experimental measurements of wet surface effects on ACTS terminals were described by Acosta, et al (1997), and preliminary modeling concepts were described by Crane et al (1997) and Ramachandran (1997). Results of their work are summarized here.

Exhibit 2.2.7-1 illustrates the first level of the problem. Atmospheric effect models can predict the power at ($P_1$) but it cannot be easily measured. The power at the receiver ($P_2$) is not predicted well because propagation models do not include wet antenna effects. The power $P_2$ is easily measured and compared to propagation models. The antenna adds a new attenuation dependence that is not part of the atmospheric effects but does cause significant losses. The losses are dependent on the material, type of coating on the antenna, and the elevation angle of the antenna.

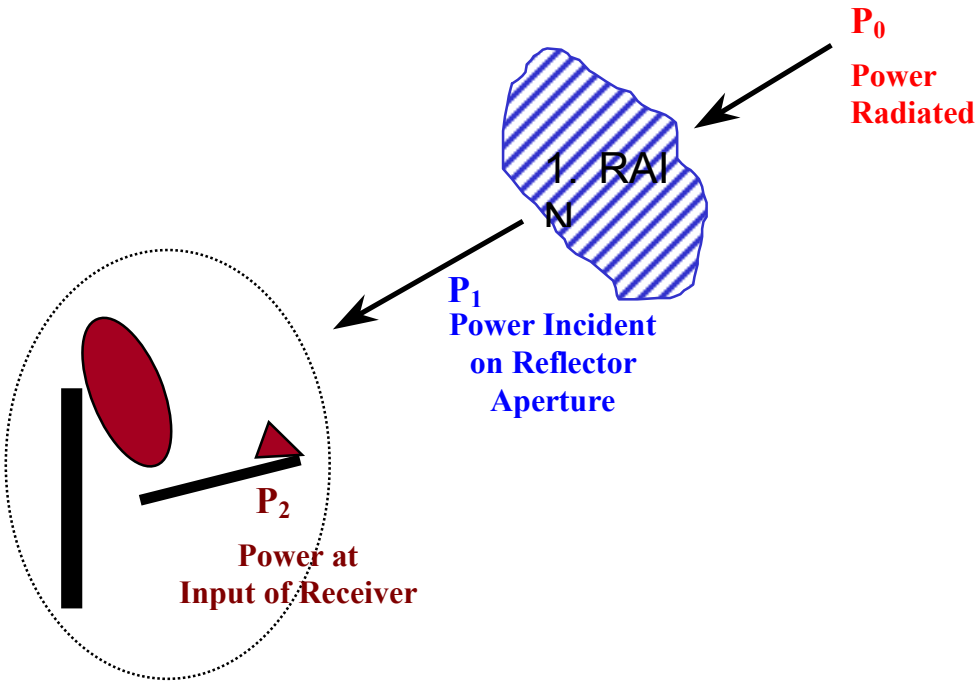


Exhibit 2.2.7-1: The Wet Antenna Concept
(Acosta et al, 1997)

### 2.2.7.1 Wet Antenna Surface Experiments

The effect of water at the surface of the antenna is of growing interest in satellite communications. Experimenters speculate that the effect could be responsible for more than 3 dB of attenuation at Ka-band, however few experiments have been conducted.

The ACTS propagation experiment has conducted several of these wet antenna experiments using various methods. Acosta et al.(1997) of NASA Lewis Research Center defined four regions at which a water cell can cause signal degradation. Exhibit 2.2.7.1-1 illustrates these regions.

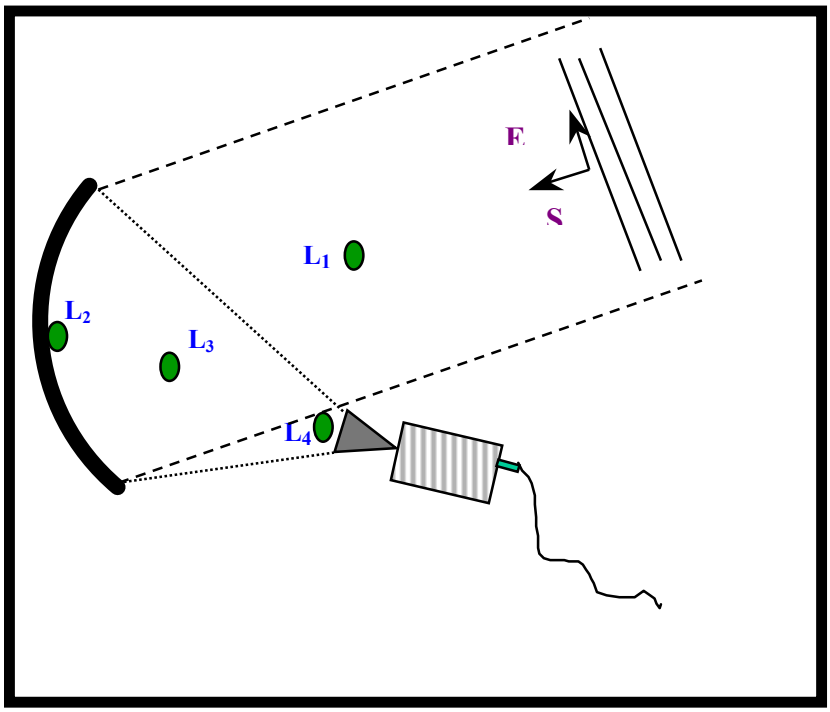


Exhibit 2.2.7.1-1
Four Water Cell Regions for a Parabolic Antenna.
(Acosta et al, 1997)

Location #1 ($L_1$) represents the region only effected by constituents in the atmosphere. Many models exist to predict the effect of propagation through a water cell in this region. Location #2 ($L_2$) represents a water cell located on the antenna dish. A water cell at this location causes the dish to reflect in a non-symmetrical fashion, causing an over all degradation in the systems performance. Location #3 ($L_3$) represents a water cell falling between the feed horn and the dish of the antenna. Location # 4 ($L_4$) represents a water cell on the feed horn itself. Water on the feed horn causes attenuation of all parts of the signal being directed to the feed from the dish, thus, a water cell at $L_4$ is expected to cause more attenuation than the water cells located at $L_2$ and $L_3$.

Using the ACTS satellite, Acosta performed an experiment in which he measured the effect of a spherical water cell with a diameter of 0.35m placed at each of these locations. The volume of the water cell was 1.56 $in^3$. The antenna used in the experiment was a parabolic reflector with an off-axis feed and F/D=0.6. The results given in Exhibit 2.2.7.1-2 illustrate the relative severity of the effect of a water cell at each location.

| Location of Water Cell | Measured Attenuation (dB) |
|---|---|
| $L_1$ | 0.25 |
| $L_2$ | 0.44 |
| $L_3$ | 1.13 |
| $L_4$ | 9.50 |

Exhibit 2.2.7.1-2
Static Water Cell Effects Experiment. Frequency: 20.8 GHz
(Acosta et al, 1997)

Establishing the wet surface effects on attenuation requires an investigation of water on the feed ($L_4$) and water on the parabolic surface ($L_2$) of the antenna.

#### 2.2.7.1.1 Wet Antenna Effects and Antenna Size

Acosta's experimental evidence illustrates that the attenuation due to water on the feed is much greater than attenuation due to water on the reflector. This conclusion is somewhat controversial since the effect has also been found to change with the age of the feed. Crane et al (1997) and Ramachandran (1997) theorized that the water layer on the reflector surface caused more attenuation than a water layer on the feed. They also found that attenuation due to water on the feed increases with the age of the feed, indicating that hydrophobic coating on the feed wears off quickly. Measured values for attenuation due to water on the feed (FA) were found to differ significantly for a new feed and a one-year-old feed. The attenuation measurement taken with the new feed, indicated that FA is only about 0.6 dB. A year later, FA was again measured to be 2.2 dB. Exhibits 2.2.7.1-3 and 2.2.7.1-4 illustrate these effects for two antennas of different sizes.

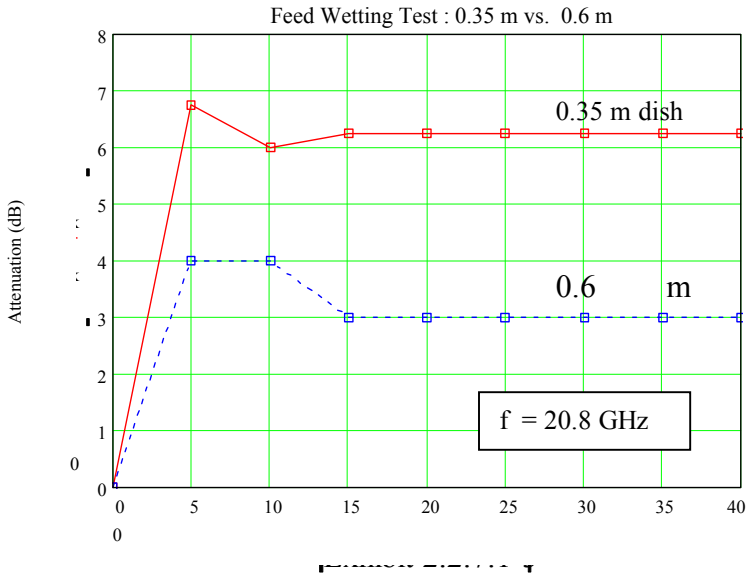


Feed Wetting Experiment for 0.35 m and 0.6 m parabolic antennas with F/D=0.6
(Acosta et al, 1997)

Exhibit 2.2.7.1-3 illustrates that water on the feed of the antenna causes a greater attenuation on a smaller antenna then it does on the larger antenna. Additionally, the peak value, reached after some amount of water has accumulated on the feed, appears to occur around the same time for both antennas, a time independent of antenna size.

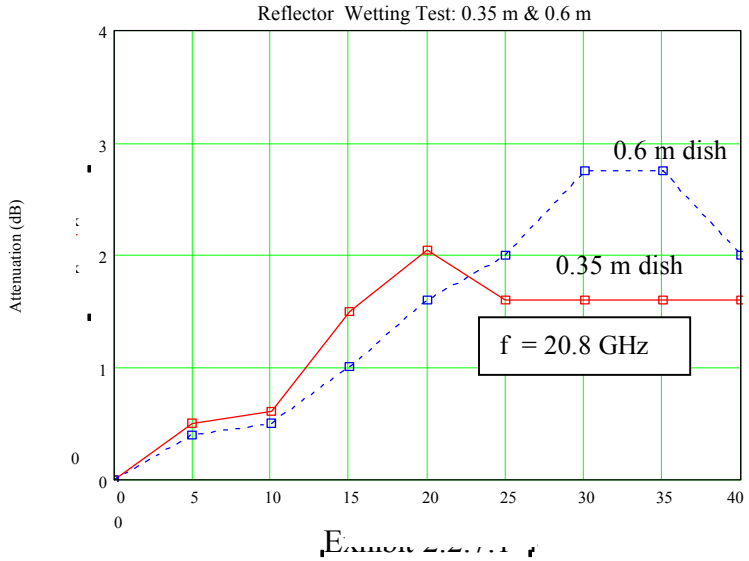


Dish Wetting Experiment for 0.35 m and 0.6 m parabolic antennas with F/D=0.6
(Acosta et al, 1997)

Exhibit 2.2.7.1-4 illustrates that water on the reflector of the antenna causes a greater attenuation on a larger antenna then it does on a smaller antenna. Additionally, the time that it takes to reach the peak value is greater for the larger antenna than for the smaller antenna.

### 2.2.7.1.2 The Antenna Wetting Factor

Another experiment performed in 1997 included the use of two identical antennas to measure the Antenna Wetting Factor. One of the antennas was placed under a rain shelter, and the other was left out in the open. The shelter did not interfere with the clear air signal, but protected the antenna from wet surface effects. The Antenna Wetting Factor (Acosta et al, 1997) is the difference between the power received at the input of the protected receiver minus the power received at the input of the unprotected receiver. Exhibit 2.2.7.1-5 compares the fade distributions of the protected and unprotected receivers for the duration of the experiment.

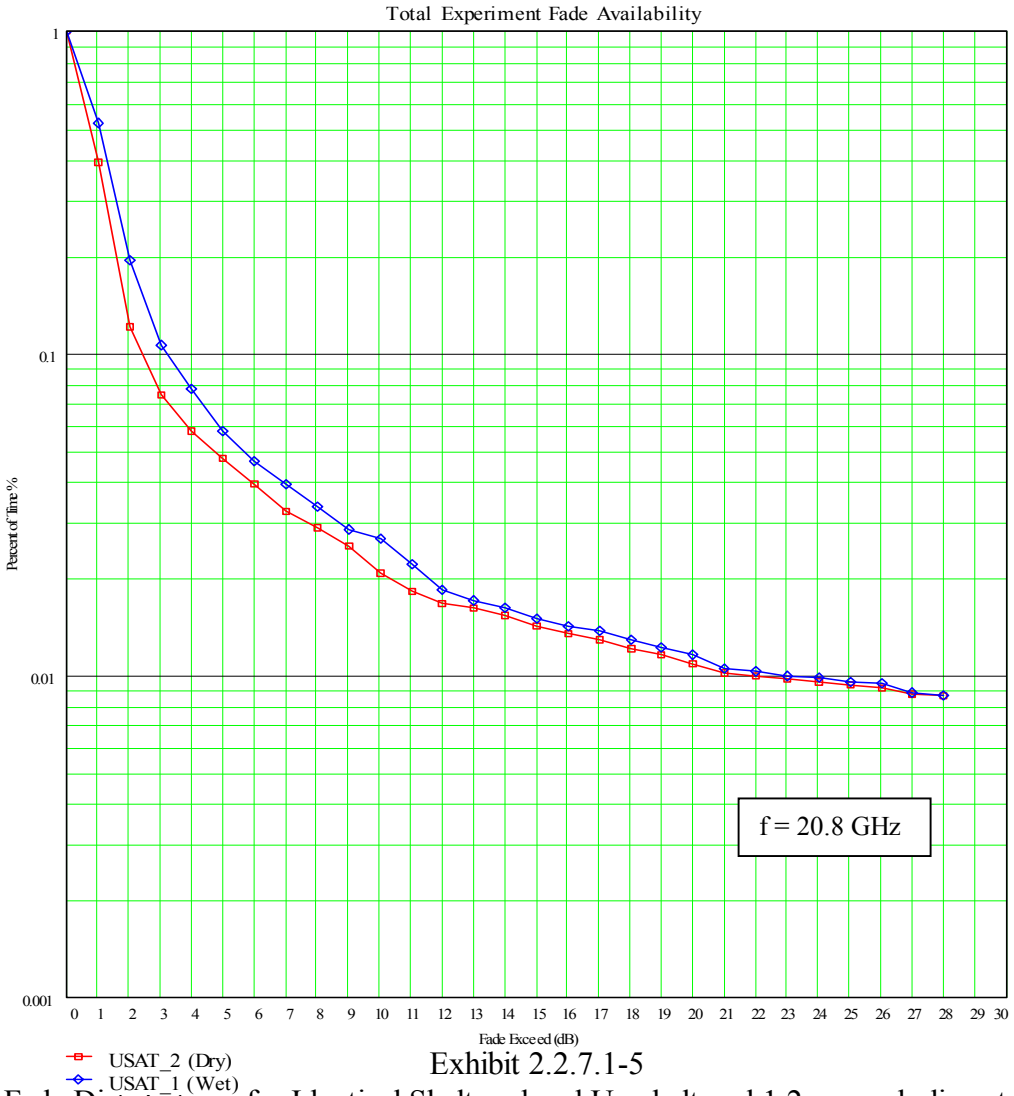


Exhibit 2.2.7.1-5
Fade Distributions for Identical Sheltered and Un-sheltered 1.2 m parabolic antennas
(Acosta et al, 1997)

**Acosta's Experimental Results (Frequency = 20.8 GHz):**

- *The antenna-wetting factor for the 1.2 m antennas is very similar to the 0.35 m antennas.*
- *Maximum antenna wetting factor was measured to be between 3 and 4 dB.*
- *Wet antenna fade availability differed from dry antenna fade availability by 2 dB at lower fades (5-10 dB)*
- *Higher antenna wetting factors tend to occur at rain rates of the order of 10 - 40 mm/hr.*
- *At very high rain rates and high fades both antennas (dry and wet) have a negligible wetness factor.*

### 2.2.7.2 Wet Antenna Effects Modeling

In order to understand the effect of a wet antenna on the system margin and availability, the effect of the size and coating material must be considered for a given antenna. Through the ACTS experiment some attempts to model wet surface effects are in progress, however, testing of these models is incomplete.

Wet surface effects models must account for two physical effects: (1) the flow of water over the surface, and (2) the propagation of electromagnetic waves through the water on the surface. The most complete wet surface effects model is the Crane-Ramachandran model (Ramachandran, 1997), (Crane et al, 1997). The model was developed along side experiments to determine the effects of water on the reflector surface and water on the feed.

The Crane-Ramachandran model is derived from Maxwell's equations. The attenuation due to water on the surface of the antenna and water on the feed are modeled as consecutive mediums of varied indices of refraction with transmissions and reflections at each boundary.

#### 2.2.7.2.1 Attenuation Due to Water on the Reflector Surface

This section describes the Crane-Ramachandran model for Attenuation due to water on the surface of a parabolic receiver with an offset feed. The smooth conductor surface model is described and the most recent results for more complicated cases are presented.

##### 2.2.7.2.1.1 The Smooth Conductor Model

A three-boundary smooth conductor model illustrates the basic concept of the wet surface model. The model uses Maxwell's equations and with Snell's Law to derive the amplitudes of forward and backward moving waves propagating through three mediums. Exhibit 2.2.7.2.1.1-1 illustrates the reflections and transmissions at each boundary.

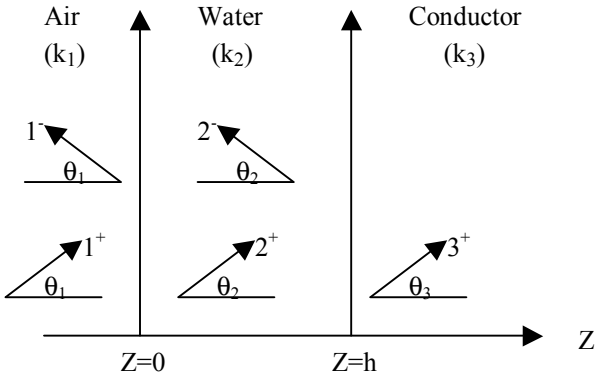


Exhibit 2.2.7.2 –1
Boundary Conditions for Water on a
Conducting surface.

Crane and Ramachandran, used these boundary conditions to solve for the attenuation due to a layer of water on a smooth conducting surface:

$$\text{Atten} = 20\ \text{Log}\left(\frac{E^{ml-}}{E^{ml+}}\right) \tag{2.2.7.2-1}$$

where $E^{ml-}$ and $E^{ml+}$ are the amplitudes of the backward and forward moving waves respectively.

The ratio of the two amplitudes for vertical polarization is given by:

$$\frac{E_v^{\,ml-}}{E_v^{\,ml+}} = \frac{(\eta_2\cos\theta_2 - \eta_1\cos\theta_1) - D_v(\eta_2\cos\theta_2 + \eta_1\cos\theta_1)}{(\eta_2\cos\theta_2 + \eta_1\cos\theta_1) - D_v(\eta_2\cos\theta_2 - \eta_1\cos\theta_1)} \tag{2.2.7.2-2}$$

where $\eta = (\mu/\varepsilon_c)^{1/2}$ is the intrinsic impedance of the medium in ohms and $D_v$ is given by:

$$D_v = \frac{\eta_2\cos\theta_2 - \eta_3\cos\theta_3}{\eta_2\cos\theta_2 + \eta_3\cos\theta_3} e^{-2h(\theta_m)\gamma_2\cos\theta_2} \tag{2.2.7.2-3}$$

and $\gamma_1$ is a complex medium dependent constant given by:

$$\gamma_1 = \sqrt{j\omega\mu(\sigma + j\omega\varepsilon_c)} = j\omega\sqrt{\mu\varepsilon_c} \tag{2.2.7.2-4}$$

where $\mu$ is the permeability of the medium in H/m, $\sigma$ is the conductivity of the medium in 1/ohms, and $\varepsilon$ is the permittivity of the medium a in F/m.

For horizontal polarization, the ratio of the [illegible]litudes becomes:

$$\frac{E_h^{m1-}}{E_h^{m1+}} = \frac{(\eta \quad - D_h(\eta_2 \cos\theta_1 + \eta_1 \cos\theta_2)}{(\eta \quad - D_h(\eta_2 \cos\theta_1 - \eta_1 \cos\theta_2)} \qquad (2.2.7.2\text{-}5)$$

and

$$\theta_{mh} \qquad (2.2.7.2\text{-}6)$$

From viscosity relations paired with the ge[illegible]enna,

$$h(\theta_m) = \sqrt[3]{\frac{3R\sin(\theta_m + \alpha)X(w)\mu}{\rho g \sin\theta_m}} \qquad (2.7.2.2\text{-}7)$$

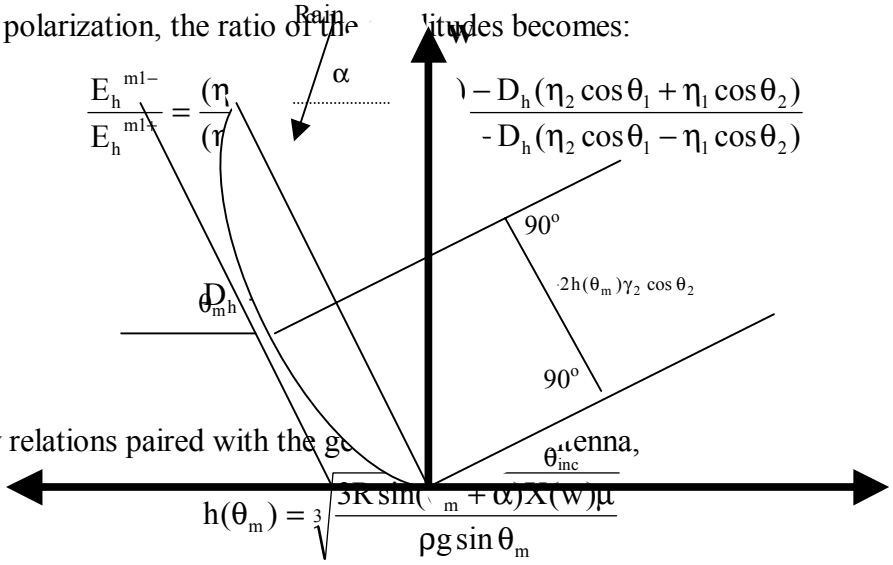


where R is the rain rate, ρ is the density, g is acceleration due to gravity equal to 9.81 m/s, α is the falling rain angle with respect to horizontal, and X(w) is given by:

$$X(w) = a\log\left(\sec\left(\tan^{-1}\frac{w(\theta_n)}{2a}\right) + \frac{w(\theta_n)}{2a}\right) + \frac{w(\theta_n)}{2}\sec\left(\tan^{-1}\frac{w(\theta_n)}{2a}\right) \qquad (2.7.2.2\text{-}8)$$

where

$$w(\theta_n) = 2a\tan\theta_n \qquad (2.7.2.2\text{-}9)$$

and "a" is the focal length of the antenna and $\theta_n = 180 - (\theta_m + \theta_{inc})$. The reflector geometry is shown in Exhibit 2.2.7.2-2.

Exhibit 2.2.7.2-2: Parabolic Dish Antenna Geometry
(for a reflector with an offset feed)

### 2.2.7.2.1.2 The ACTS Reflector Model

The principles applied for the smooth conductor case, can be applied to a more complicated situation such as the ACTS reflector, where six layers are present. Crane and Ramachandran are currently working to apply these principles to the ACTS reflector. For the ACTS reflector, the boundary conditions are determined by the six medium interfaces, illustrated in Exhibit 2.2.7.2-3.

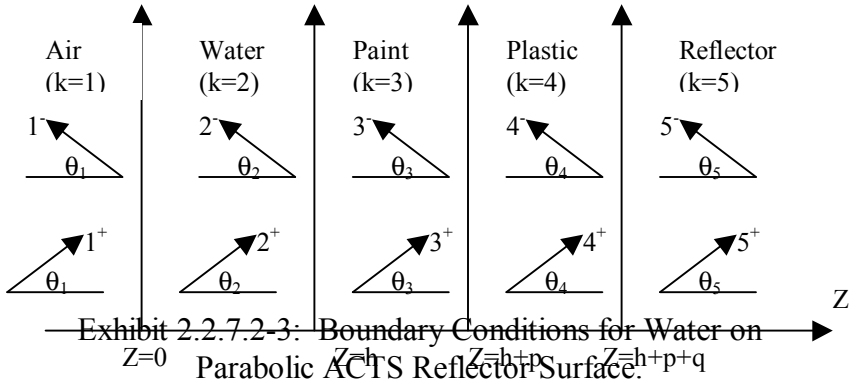


Exhibit 2.2.7.2-3: Boundary Conditions for Water on Parabolic ACTS Reflector Surface.

Since the derivation and output equations from this method are extremely complicated, the derivation will not be described here. However, Crane and Ramachandran have conducted some simulations using this method. The results are illustrated in Exhibits 2.2.7.2-4 and 2.2.7.2-5.

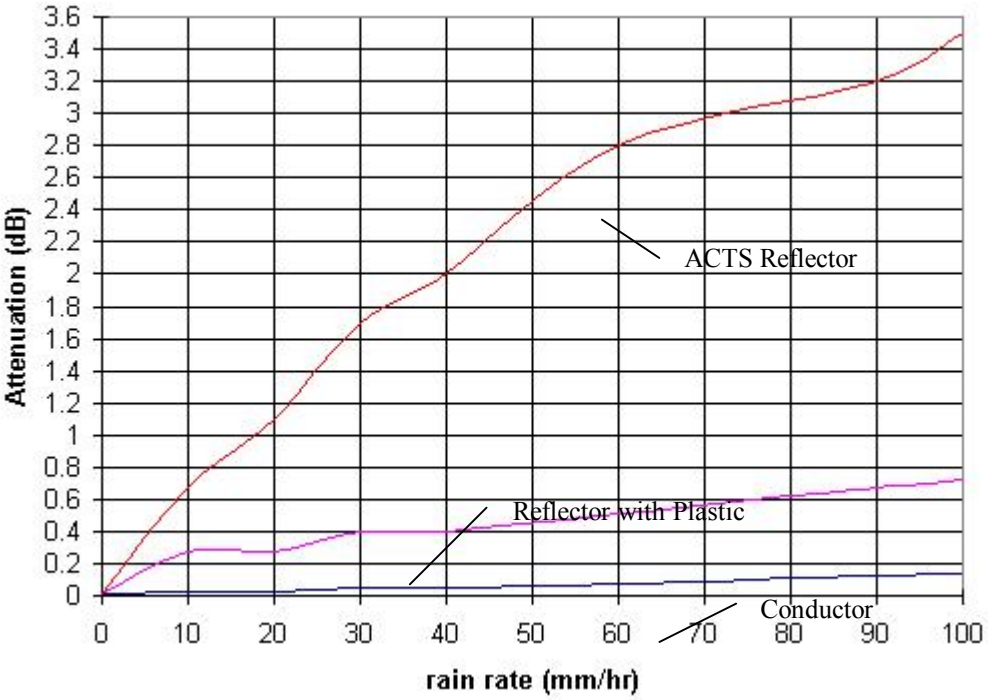


Exhibit 2.2.7.2-4: Attenuation due to Wet Reflector Surface for an ACTS reflector at 20 GHz.

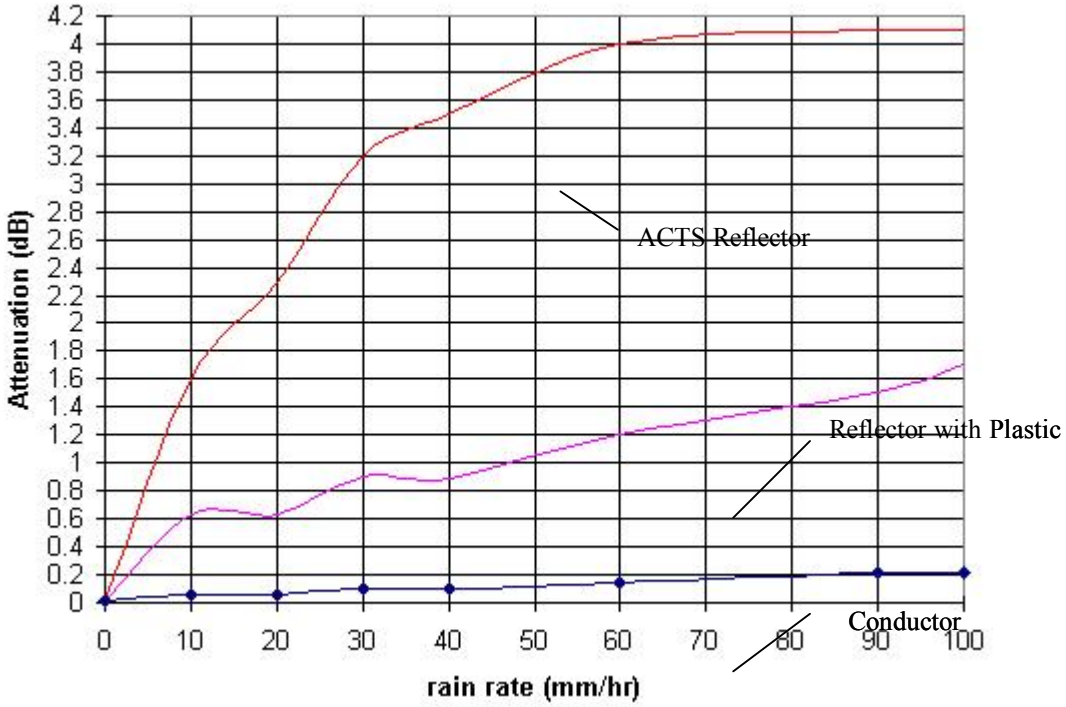


Exhibit 2.2.7.2-5: Attenuation due to Wet Reflector Surface for an ACTS reflector at 27 GHz

### 2.2.7.2.2 Attenuation Due to Water on the Feed

The principles applied for the smooth conductor case, can also be applied to predict attenuation due to a wet feed. Crane and Ramachandran are currently working to apply these principles to the ACTS feed, the boundary conditions are determined by a four medium interface, illustrated in Exhibit 2.2.7.2-6.

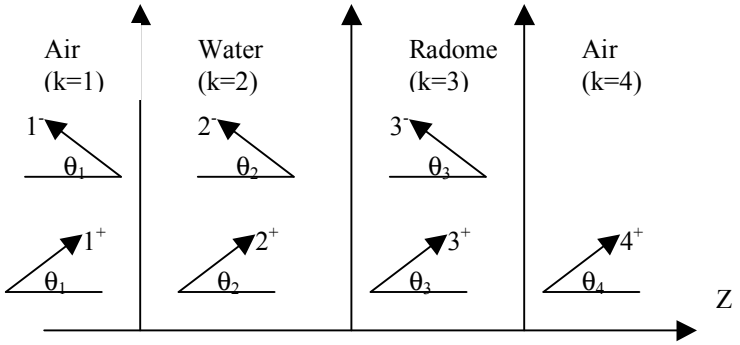


Exhibit 2.2.7.2-6: Boundary Conditions for Water on the Antenna Feed.

Since the derivation and output equations from this method are extremely complicated, the derivation will not be described here. However, Crane and Ramachandran have conducted some simulations using this method. The results are illustrated in Exhibit 2.2.7.2-7.

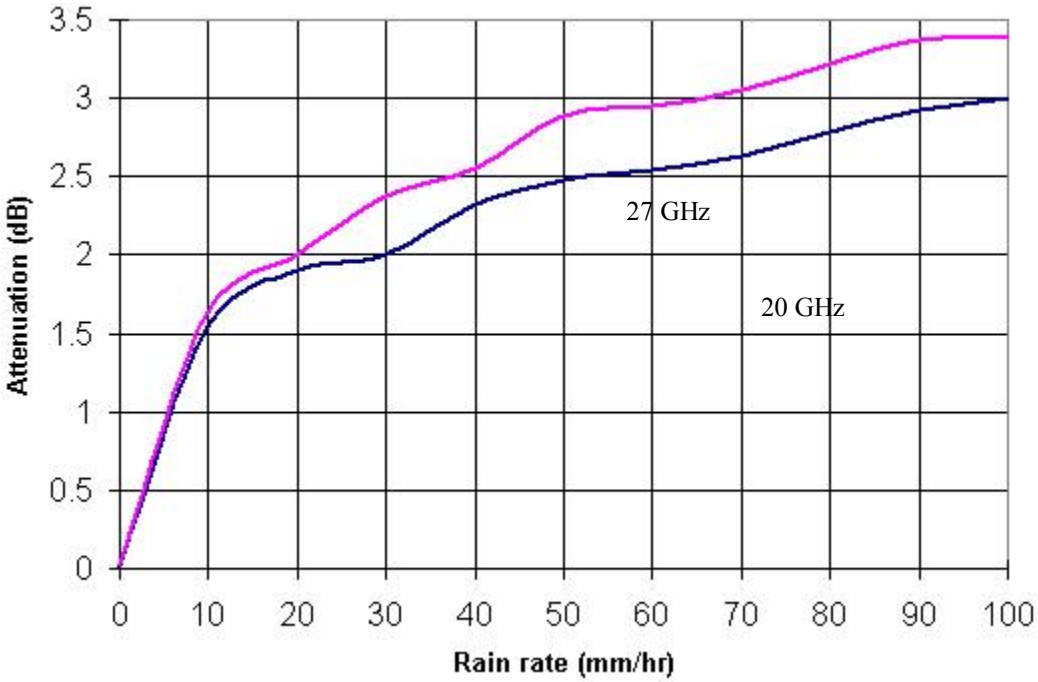


Exhibit 2.2.7.2-7: Attenuation Due to Water on the Feed.
(Rain Angle $\alpha = 20°$)

## 2.2.8 Scintillation

This section presents methods and models for the prediction of scintillation on earth-space paths produced in the troposphere. Tropospheric scintillation tends to be most noticeable for systems operating at frequencies above about 3 GHz, and at low elevation angles. The effects of tropospheric scintillation are observed as fluctuations in the amplitude of a signal received on an earth-space link. Typically, at frequencies above about 3 GHz, the effects of rain attenuation are the dominant atmospheric effect on earth-space paths; however, for high frequencies and/or low margin systems, scintillation effects must be considered.

Section 2.2.8.1 presents statistical prediction models for the evaluation of scintillation caused by tropospheric turbulence. Section 2.2.8.2 provides a prediction method for cloud scintillation. [Note: Ionospheric scintillation, which is significant for frequencies below about 3 GHz, is discussed in Section 2.1.1]

## 2.2.8.1 Tropospheric Scintillation

### 2.2.8.1.1 The Karasawa Model

The current ITU-R model (ITU-R Rec. P.618-5, 1997) for predicting scintillation outage is based on the model proposed by Karasawa et al. (1988). For time periods smaller than about 5 minutes, rapid fluctuations in received signal power caused by atmospheric turbulence (or more simply "scintillation") are modeled as a log-normal random process (normal in decibels). The standard deviation of scintillation fluctuations (scintillation intensity) varies slowly with time as a function of temperature and atmospheric water vapor concentration.

Karasawa et al. proposed a bivariate statistical model for scintillation. The probability density function (pdf) can be written as the product of a normal density function, which describes the short-term behavior of scintillation, and a gamma density function, which describes the long-term changes in scintillation intensity.

The bivariate density function depends on a single computed parameter, the mean monthly scintillation intensity. This parameter is computed as a function of both system and environmental parameters.

From experimental data, Karasawa quantified scintillation in terms of the following statistical parameters.

- $X \equiv$ instantaneous signal amplitude in dB
- $\sigma_x \equiv$ standard deviation of $X$ (scintillation intensity)
- $P_1(X/\sigma_x) \equiv$ pdf for stationary Gaussian random process (constant $\sigma_x$)
- $P_2(\sigma_x) \equiv$ gamma pdf

Histograms of $\sigma_x$ measurements, compiled over one-month periods, are shown to agree closely with the pdf for a gamma distributed random variable. Cumulative time distributions of scintillation can be estimated from the following bivariate pdf

$$P(X, \sigma_x) = P_1(X/\sigma_x)\, P_2(\sigma_x) \qquad (2.2.8.1\text{-}1)$$

where $P_1$ describes scintillation for short (< 1 hour) periods while $P_2$ describes the slower variations (month) in $\sigma_x$.

Given $P(X, \sigma_x)$, the likelihood of a scintillation fade exceeding a threshold $\gamma$ dB is given by

$$p(X \geq \gamma) = 1 - \int_{-\infty}^{\gamma} \int_{0}^{\infty} P(X, \sigma_x) d\sigma_x dX \,. \qquad (2.2.8.1\text{-}2)$$

Scintillation must be considered in combination with gaseous absorption, rain, and cloud attenuation when computing link availability estimates. The scintillation intensity varies as a function of temperature and atmospheric water vapor concentration. Scintillation is also a function of elevation angle, signal frequency (weak), and path length. The dependence of scintillation on environmental and system parameters can be reduced to a single parameter $\sigma_{\sigma x}$ , which defines the standard deviation of the scintillation intensity for a one-month period.

The normal pdf for short-term scintillation fluctuations given a constant scintillation intensity $\sigma_x$ can be written as,

$$P_1(X|\sigma_x) = \frac{1}{\sqrt{2\pi\sigma_x^2}} \exp(-X^2 / 2\sigma_x^2) \,. \qquad (2.2.8.1\text{-}3)$$

The gamma pdf (for long-term scintillation fluctuations) for $\sigma_x$ is as follows,

$$P_2(\sigma_x) = \frac{\beta^\alpha}{\Gamma(\alpha)} \sigma_x^{\alpha-1} \exp(-\beta\sigma_x) \qquad (2.2.8.1\text{-}4)$$

where

$$\beta = \frac{m}{\sigma_{\sigma x}^2}, \qquad (2.2.8.1$$

$$\alpha = \frac{m^2}{\sigma_{\sigma x}^2}, \qquad (2.2.8.1$$

$$m = \langle \sigma_x \rangle, \text{ and} \qquad (2.2.8.1\text{-}7)$$

$$\sigma_{\sigma x} = \text{var}(\sigma_\chi) \qquad (2.2.8.1\text{-}8)$$

Karasawa demonstrated a linear relationship between the mean ($m$) and the standard deviation ($\sigma_{\alpha x}$) of the scintillation intensity

$$\sigma_{\alpha x} = .32m \tag{2.2.8.1-9}$$

Therefore,

$$\beta = \frac{10}{\sigma_{\alpha x}} \text{ , and} \tag{2.2.8.1-10}$$

$$\alpha = 9.8 \tag{2.2.8.1-11}$$

Thus, the pdf for scintillation is completely specified by a single parameter, $\sigma_{\alpha x}$,

$$P(X, \sigma_x) = \left[ \frac{e^{-x^2/(2\sigma_x)}}{\sqrt{2\pi\sigma_x^2}} \right] \left[ \left( \frac{10}{\sigma_{\alpha x}} \right)^{9.8} \left( \frac{1}{\Gamma(9.8)} \right) \sigma^{8.8} e^{-(10\sigma_x/\sigma_{\alpha x})} \right]. \tag{2.2.8.1-12}$$

Once the $\sigma_{\alpha x}$ parameter is determined for the scintillation pdf in equations (2.2.8.1-1) or (2.2.8.1-12), this pdf may be combined with other atmospheric pdfs to calculate the required system margin.

### 2.2.8.1.2 ITU-R Scintillation Prediction Method

The ITU-R model (ITU-R Rec. P.618-5, 1997) for predicting scintillation outage provides a quick and effective method to estimate the statistics of tropospheric scintillation from local environmental parameters. The ITU-R model calculates the parameter $\sigma_{\alpha x}$, the standard deviation of the instantaneous signal amplitude (amplitude expressed in dB). This parameter $\sigma_{\alpha x}$ is often referred to as the **scintillation intensity**. $\sigma_{\alpha x}$ is determined from the following system and environmental parameters:

(1) antenna size and efficiency,

(2) antenna elevation angle,

(3) RF frequency,

(4) average local monthly temperature, and

(5) average local monthly relative humidity.

Scintillation intensity increases with increasing RF frequency, temperature and humidity, and decreases with increasing antenna size and elevation angle as specified by the ITU-R model.

The ITU-R procedures has been tested at frequencies between 7 and 14 GHz, but is recommended for applications up to at least 20 GHz. (ITU-R Rec. 618-5, 1997).

The input parameters required for the ITU-R method are:

- $t$: average surface ambient temperature (°C) at the site for a period of one month or longer,
- H: average surface relative humidity (%) at the site for a period of one month or longer,
- $f$: frequency (GHz), where 4 GHz ≤ $f$ ≤ 20 GHz,
- θ: path elevation angle, where θ ≥ 4°,
- $D$: physical diameter (m) of the earth-station antenna, and
- η: antenna efficiency; if unknown, η = 0.5 is a conservative estimate.

The step by step procedure for the ITU-R prediction model is provided here.

1) For the value of $t$, calculate the saturation water vapor pressure, $e_s$, (kPa), (see ITU-R Rec. 453-6, 1997):

$$e_s = 6.1121 \exp\left(\frac{17.502t}{t + 240.97}\right) \qquad (2.2.8.1\text{-}13)$$

2) Compute the wet term of the radio refractivity, $N_{wet}$, corresponding to $e_s$, $t$ and $H$ (see ITU-R Rec. 453-6, 1997):

$$N_{wet} = \frac{3732 H e_s}{(273 + t)^2} \qquad (2.2.8.1\text{-}14)$$

3) Calculate the standard deviation of the signal amplitude, $\sigma_{ref}$, used as reference:

$$\sigma_{ref} = 3.6 \text{ x } 10^{-3} + 10^{-4} \text{ x } N_{wet} \quad \text{dB.} \qquad (2.2.8.1\text{-}15)$$

4) Calculate the effective path length L according to:

$$L = \frac{2h_L}{\sqrt{\sin^2\theta + 2.35x10^{-4}} + \sin\theta} \quad m \qquad (2.2.8.1\text{-}16)$$

where $h_L$ is the height of the turbulent layer; the value to be used is $h_L$ = 1000 m.

5) Estimate the effective antenna diameter, $D_{eff}$, from the geometrical diameter $D$, and the antenna efficiency η:

$$D_{eff} = \sqrt{\eta D} \quad m. \qquad (2.2.8.1\text{-}17)$$

6) Calculate the antenna averaging factor from:

$$g(x) = \sqrt{3.86\left(x^2 + 1\right)^{11/12} \times \sin\left[\frac{11}{6}\arctan\frac{1}{x}\right] - 7.08x^{5/6}} \qquad (2.2.8.1\text{-}18)$$

with

$$x = 1.22\, D^2_{eff}\,(f/L) \qquad (2.2.8.1\text{-}19)$$

where $f$ is the carrier frequency (GHz).

7) Calculate the standard deviation of the signal of the considered period and propagation path:

$$\sigma = \sigma_{ref} f^{7/12} \frac{g(x)}{(\sin\theta)^{1.2}}. \qquad (2.2.8.1\text{-}20)$$

8) Calculate the time percentage factor $a(p)$ for the time percentage, $p$, of concern in the range $0.01 < p \leq 50$:

$$a(p) = -0.061\,(\log_{10}p)3 + 0.072\,(\log_{10}p)2 - 17.71\,\log_{10}p + 3.0 \qquad (2.2.8.1\text{-}21)$$

where p is the percentage outage.

9) Calculate the scintillation fade depth for the time percentage $p$ by:

$$A_s(p) = a(p) \cdot \sigma \qquad dB. \qquad (2.2.8.1\text{-}22)$$

### 2.2.8.1.3 Scintillation Dynamics

For many low elevation angle systems, the majority of fades below a desired threshold are scintillation induced. Exhibit 2.2.8.1-1 illustrates a scenario in which the mean fade level caused

by gas and clouds is above the given threshold, but the strongest scintillations cause short outages.

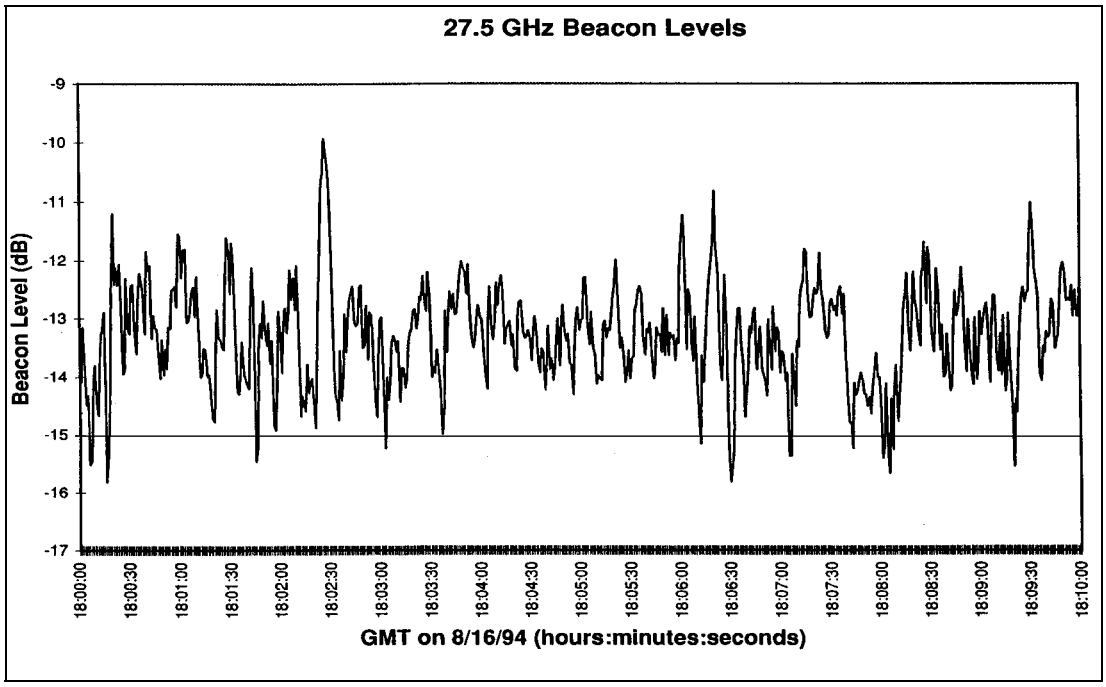


Exhibit 2.2.8.1-1

Beacon Data from Alaska ACTS Terminal (Elevation Angle 8°)

The cdf's for signal fade levels due to combined atmospheric effects are used to estimate the percentage of time a signal will fall below a given threshold, but static cdf's alone do not provide information on the frequency of fade/scintillation occurrence.

The frequency of fade and mean fade duration can be estimated using the static cdf and the well known "level crossing formula" where the expected fade rate of a normal random process is computed from the pdf and the power spectral density function of the process.

The model for estimating frequency of fade, which will be described in this section, was developed at Stanford Telecommunications and presented at the 1996 IEEE / URSI conference in Baltimore, Maryland (Weinfield, J. and T. Russell, 1996).

### 2.2.8.1.3.1 The Level Crossing Formula

Let $\boldsymbol{x}(t)$ denote a differentiable random process, and let $n_a(T)$ denote the number of times $\boldsymbol{x}(t)$ crosses a threshold $a$ in an interval of length $T$. The level crossing formula can be written as

$$E\{ n_a(T)\} = Tf_x(a)E\{|\boldsymbol{x}'(t)|, \boldsymbol{x}(t) = a\}. \quad (2.2.8.1\text{-}23)$$

Recall that scintillation is modeled as a stationary normal random process for short time periods. A differentiable normal random process can be shown to be statistically independent of its first derivative. Therefore, the conditional dependence of $\boldsymbol{x}'(t)$ on $a$ is not relevant, so

$$E\{ n_a(T)\} = Tf_x(a)E\{|\boldsymbol{x}'(t)|\} = Tf_x(a)\eta_x \quad (2.2.8.1\text{-}24)$$

where mean fade slope is defined as

$$\eta_x \equiv E\{|\boldsymbol{x}'(t)|\} \ . \quad (2.2.8.1\text{-}25)$$

### 2.2.8.1.3.2 Relating Mean Slope to Power Spectral Density

The mean fade slope $\eta_x$ can be expressed in terms of $S_x(f)$, the power spectrum of $\boldsymbol{x}(t)$

$$\eta_x = \sqrt{\frac{-2R''(0)}{\pi}} = 8\pi\sqrt{\int_{-\infty}^{\infty} f^2 S_x(f)df} \quad (2.2.8.1\text{-}26)$$

where $R(t)$ is the autocorrelation of $x(t)$.

Recall that the standard deviation of a stationary random process may be written in terms of the power spectral density of the process as follows

$$\sigma_x = \sqrt{R(0)} = \sqrt{\int_{-\infty}^{\infty} S_x(f)df} \ . \quad (2.2.8.1\text{-}27)$$

The power spectral density for scintillation fading seen by a point receiver was derived by Tatarskii (1971), and Haddon and Vilar (1986) have derived a modified form of the power spectrum which reflects the effect of antenna aperture smoothing.

The approximate form of the power spectrum is given by

$$S_x(f) = \frac{K(f_c, f_s, \sigma_x)\exp(-f^2 / f_s^2)}{[1+(f / f_c)^2]^{4/3}[1+f / f_s]^{1/2}} \quad (2.2.8.1\text{-}28)$$

where

$f_c = v_t/(\lambda L)$, $\lambda$ is the wavelength,
$f_s = 0.659 v_t/D$,
$\sigma_x \equiv$ scintillation intensity,
$D \equiv$ effective antenna diameter,
$L \equiv$ path length through troposphere, and
$v_t \equiv$ transverse wind velocity.

The antenna aperture causes an effective band limiting of scintillation, which is reflected in the parameter $f_s$. Note that $f_s$ is inversely proportional to antenna diameter. The power spectral density approaches Tatarskii's expression for the power spectrum of a point receiver, as the diameter $D$ approaches 0.

Equation (2.2.8.1-28) is an example of a temporal power spectrum. Temporal spectra illustrate frequency domain characteristics of nonstationary random processes by "freezing" time varying parameters such as the transverse wind velocity $v_t$ in the scintillation spectrum. Note that equations (2.2.8.1-26) and (2.2.8.1-27) hold for temporal spectra, as well as standard power spectra for stationary random processes.

### 2.2.8.1.3.3 Estimating Frequency of Fade

The relationship between mean fade slope and scintillation intensity $\sigma_x$, which has been measured extensively, is implemented.

The level crossing formula can be written as

$$\lambda_a = E\{ n_a(T)/T\} = \boldsymbol{f_x}(a)\ \eta_{\boldsymbol{x}} = \sigma_x f_x(a)(\ \eta_{x/}\sigma_x) \qquad (2.2.8.1\text{-}29)$$

where the parameter $\lambda_a$ defines the expected frequency with which the fade level $\boldsymbol{x}(t)$ crosses threshold $a$.

The ratio $\eta_{x/}\sigma_x$ is a constant and can be computed by substituting the expression for the power spectrum in (2.2.8.1-28) into equations (2.2.8.1-26) and (2.2.8.1-27), using typical average values for the time varying parameters. The constant $K$ cancels out and the integrals can be computed numerically. As equation (2.2.8.1-29) illustrates, $\lambda_a$ is linearly proportional to $\sigma_x$.

### 2.2.8.1.3.4 Numerical Example- Scintillation Dynamics

Assume a satellite ground station with the following system and environmental input parameters:

- 20 GHz receive frequency,
- 1.5 m dish,
- 10 ° elevation angle,
- average transverse wind velocity $v_t$ = 4 m/sec, and
- average scintillation intensity $\sigma$ = 1 dB.

Assume that it is a clear day, so all atmospheric attenuation is caused by gaseous absorption and scintillation. The attenuation due to gaseous absorption is assumed to be a constant 6 dB. At this level of attenuation, the system fade margin is 3 dB.

Given this scenario, scintillation will cause the received power to fade below threshold, resulting in a system outage approximately 5.1 times per hour. The received power will be above threshold over 99% of the time.

If the gaseous absorption were increased from 6 dB to 7 dB, decreasing the fade margin to 2 dB, system outages would occur approximately once a minute, while the system availability would be approximately 98%.

### 2.2.8.2 Cloud Scintillation

Traditional models for turbulence induced scintillations are based on long-term statistics measured over a period of months [ITU-R Rec. P.618-5 (1997), Karasawa et.al. (1988), and Otung (1996)]. However, it is often useful to make predictions based on short-term data as in the case of a scintillation event spanning several minutes. Recently, a method was developed by Vanhoenacker, et al. (1993) that utilizes information recorded for a single scintillation event, and constructs a model which can be used to make predictions of performance for broadband signals. In this section, the basis of this method is described. In the next section, a general procedure is provided.

The model proposed by Vanhoenacker simulates the effects of turbulence in cumulus clouds under dry conditions. Wind and variations in temperature generate turbulent eddies with varying refractive index values. The presence of these eddies introduces phase shifts and attenuation in the transmitted fields. For this problem, the weak fluctuation theory introduced by Tatarski (1961, 1971) is applied at microwave frequencies under the relaxed conditions specified by Strohbehn (1968), Ishimaru (1977), and Clifford (1970). Additional physical assumptions are also made:

1. The scintillation event is stationary (Gaussian statistics).
2. Frozen turbulence.
3. Depolarization is negligible.
4. A thin turbulent layer.
5. The turbulence is related to presence of cumulus clouds.
6. Diffraction effects are negligible.

Using these assumptions, the geometry of the atmospheric turbulence can be related in a straightforward manner to physical and statistical parameters obtained from experimental measurements.

Scintillations in the absence of rain are caused by tropospheric turbulence. A thin turbulent layer occurs at an altitude range of 1.5-3 km in which eddies form with size $L$ in the range $l_0 < L < L_0$ (where $l_0 \cong 1$ mm and 10 m $< L_0 <$ 100 m). To model propagation through the turbulent layer, the turbulent eddies are grouped along the paths through the turbulent layer and treated as a homogeneous dielectric cylinders. The length of a particular cylinder corresponds to the local thickness of the turbulent layer, and the radius is related to the size of the eddies it contains. The permittivity of the each cell depends the humidity levels of the eddies contained within it. Finally, the network of cells is pushed across the link at a specified cross-path wind speed to create the scintillation mechanism.

The fields are computed at the receiver location using the Kirchoff-Huygens approximation in which the effects of edge diffraction on the cylinders are neglected. The presence of the cylinder adds only a phase shift and a small attenuation to part of the received field. This is a reasonable approximation since the difference in permittivity between the turbulent cell and the surrounding medium is small. The voltage received at the terminals of a circular aperture antenna (such as a

parabolic dish) can be calculated by taking the receiving pattern and effective aperture diameter into account.

It is possible to characterize the network of cells by using a combination of scintillation event measurements and turbulence theory. Each cell geometry is chosen such that its simulated log-amplitude peak conforms to the distribution of the measured event. Additionally, parameters are constrained to fit turbulence theory for a thin turbulent layer. The resulting turbulent geometry yields simulated results that approximately fit the experimental measurements. Simulations were used to obtain values for the following event parameters: mean variance, peak-to-peak log-amplitude, spectrum corner frequency, and number of zero dB crossings (of the log-amplitude) per minute. Comparisons with measurements from the Olympus satellite at 12.5, 20, and 30 GHz showed that the average differences of these parameters were, when considered together and averaged, less than 20%.

#### 2.2.8.2.1 Vanhoenacker Model

The following information is based on descriptions provided in several references of Vanhoenacker and colleagues (1990), (1993), (1995), (1997). The implementation of the method is not trivial; hence, the procedure given here is intended as an introduction to the method rather than as an algorithm development tool.

The first step in applying this method is to obtain a description of the atmospheric turbulence based on experimental information obtained from an observed scintillation event. Exhibit 2.2.8.2-1 depicts the assumed atmospheric geometry: of a set of homogeneous dielectric cylinders moving across the earth-space path.

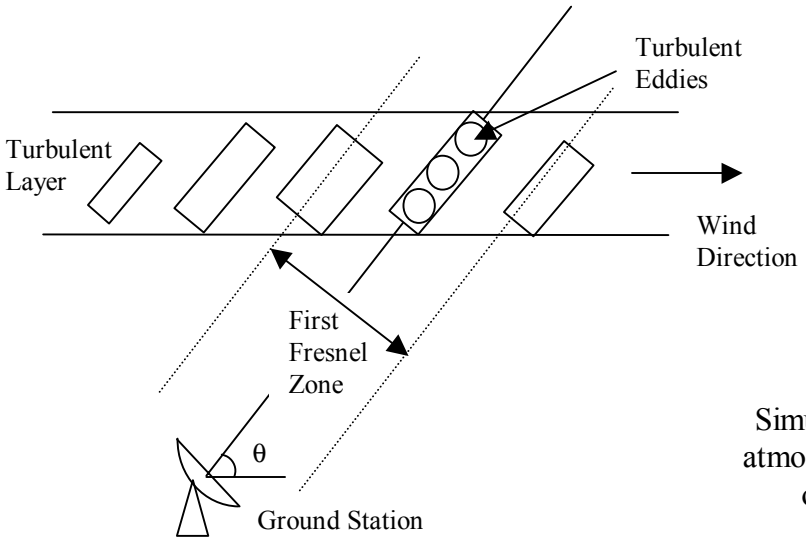


Exhibit 2.2.8.2-1
Simulation geometry depicting atmospheric turbulence as a set of dielectric cylinders.

To extract the lengths, radii, and permittivities for each cell, the following procedure is used:

1. The total number of turbulent cells, $N$, is computed from the number of zero dB crossings, $f$, observed over the event duration:

$$N = 0.25 N_c (12.5/f)^{1/2} (1.2)^{(f/12.5-1)} \quad (2.2.8.2\text{-}1)$$

2. For a single cell, the following quantities are incremented over their respective ranges in a nested loop:

   - Relative humidity within the cell over the range: 98%-107% (loop #1).
   - Cell length $T$ over the range: 10 m-100 m (loop #2).

3. A cell offset is randomly generated (within the first Fresnel zone radius) in the direction normal to the plane containing the earth-space path and the wind direction.

4. Refractive indexes inside ($n_1$) and outside ($n_2$) of the cell are computed based on the procedures outlined in Vanhoenacker et al. (1993), Hallikainen (1984), and Ray (1972).

5. The geometry parameters for the cylindrical cell are computed as follows:

$$C_n^2 = \sigma_\chi^2 / \left(42.478 k^{7/6} T z^{5/6}\right) \quad (2.2.8.2\text{-}2)$$

$$D_n(r) \cong (5/8)(n_1 - n_2) \quad (2.2.8.2\text{-}3)$$

$$r = \left( \frac{D_n(r)}{C_n^2} \right)^{3/2} \quad (2.2.8.2\text{-}4)$$

where

$C_n^2$ = average refractive structure parameter
$D_n(r)$ = refractive structure function
$r$ = cell radius (m)
$T$ = cell length (m)
$\sigma_\chi^2$ = measured variance ($dB^2$)
$n_1$ = refractive index inside cell
$n_2$ = refractive index outside cell

6. Test the resulting cell to determine if it fits the measured log-amplitude distribution:

- Partition the lower portion ($p$ < 50%— representing peak values) of the measured distribution into 0.2 dB sections on the log-amplitude axis.
- Map the time percentage corresponding to each section to a fraction of the total number of cells found in step 1.
- Use the simulation described below to compute the peak log-amplitude caused at the receiver for the single cell under consideration.
- If the resulting peak log-amplitude value fills an available section in the log-amplitude partition, then store the current cell geometry.

7. Repeat steps 2-5 until the total number of cells is obtained.

The resulting turbulence geometry can now be used to simulate scintillation on the link. The following equation gives the voltage at the terminals of the receiving antenna. The integral is evaluated for the each cell, and a superposition of the resulting voltages gives the received signal.

$$V = \xi_0 \sqrt{A} \frac{\exp(-jk_0 R)}{R}\left[1 + \frac{jD}{2Ad_2}(\exp(-\gamma d) - 1) I_2\right] \qquad (2.2.8.2\text{-}6)$$

$$I_2 = \iint_{S_2} \exp(-j\alpha r^2) \frac{J_1(k_0 D/2\sin\theta_2)}{\sin\theta_2} r dr d\phi \qquad (2.2.8.2\text{-}7)$$

where

$A$ = effective aperture ($m^2$)
$\xi_0$ = transmitted field amplitude
$\gamma$ = propagation constant of the cell ($m^{-1}$)
$k_0$ = propagation constant ($m^{-1}$)
$R$ = distance from transmitter to receiver (m)
$d_2$ = distance form receiver to turbulence (m)
$\theta_2$ = angle from antenna boresite to source point on the turbulent cell (rad)
$r$ = distance from earth-space path to source point on turbulent cell (m)
$\phi$ = angle from x-axis measured at the turbulent cell (rad)
$D$ = effective diameter of the receiving aperture ($m^2$)
$d$ = cell length (m)
$S_2$ = surface of the base of the turbulent cell (closest to the receiver)
$\alpha = (k_0 R)/(2d_2)$ ($m^{-1}$)

The voltages for each time step over the duration of the simulation. The following types of output can be obtained:

- Log-amplitude time series

- Transfer function $H(f) = E_0/E_T$ ($E_0$ = field at the receiver in the absence of turbulence, $E_T$ = field at the receiver with turbulence included)
- Power spectral density
- Log-amplitude distribution
- Scintillation variance
- Group delay

### 2.2.9 Worst Month Statistics

Communications systems performance is often specified in terms of 'worst month' or 'any month' criteria, rather than the annual or yearly performance criteria. Propagation margins for rain are then specified as not to exceed values over the 'worst month', rather than not to exceed values for an average year, or annual basis. The worst month specification is particularly prevalent in the broadcast industry, and specification of broadcast satellite service (BSS) performance requirements often are in terms of monthly rather than annual time references

An unambiguous definition of worst month is important to assure that performance specifications are consistent and will be correctly implemented. The ITU-R presented a concept of worst month, which attempts to provide a global standard for the telecommunications industry (ITU-R Rec. P.581-2, 1997). The definitions are:

1. *the fraction of time during which a pre-selected threshold is exceeded in the worst month of a year is referred to as "the annual worst-month time fraction of excess";*

2. *the statistic relevant for the performance criteria referring to "any month" is the long-term average of the annual worst-month time fraction of excess;*

3. *the worst month of a year for a pre-selected threshold for any performance degrading mechanism, [is] that month in a period of twelve consecutive calendar months, during which the threshold is exceeded for the longest time. The worst month is not necessarily the same month for all threshold levels [underline by author].*

The underlined text highlights the fact that the worst month may be different for each desired threshold value.

The direct determination of worst month statistics is most often developed from extension of annual statistics obtained from direct measurement or from application of a rain attenuation prediction model, such as one of the models provided in Section 2.2.4. The following section provides a procedure developed by the ITU-R for the conversion of annual statistics to worst-month statistics.

#### 2.2.9.1 ITU-R Worst Month Prediction Model

The ITU-R has developed a recommended procedure for the determination of the attenuation value exceeded for a time percentage, $p_w$, of the worst month, from average annual time percentages, p (ITU-R Rec. P.841, 1997).

The step by step procedure is now provided:

***Step 1)***

Obtain the distribution of the annual time percentage, p, for the location and operating frequency of interest. The distribution can be determined from direct measurements, or by the recommended prediction models provided in Section 2.2.4.

***Step 2)***

Determine the location dependent parameters $Q_1$ and $\beta$ required for the calculation. Exhibit 2.2.9.1-1 provides values of $Q_1$ and $\beta$ for locations where measured data is available. Parameter values are provided primarily for rain attenuation conditions, with a limited selection for multipath conditions.

For locations not in the table, the global values of

$$Q_1 = 2.85 \quad \text{and} \quad \beta = 0.13$$

should be used.

| Location | Propagation Effect | | | |
|---|---|---|---|---|
| | Rain on slant path | | Multipath | |
| | $Q_1$ | $\beta$ | $Q_1$ | $\beta$ |
| **Global** | **2.85** | **0.13** | **2.85** | **0.13** |
| USA<br>Virginia | 2.7 | 0.15 | | |
| JAPAN<br>Yamaguchi | 4.0 | 0.15 | | |
| JAPAN<br>Kashima | 2.7 | 0.15 | | |
| EUROPE<br>North West | 3.1 | 0.16 | 4.0 | 0.13 |
| EUROPE<br>Mediterranean | 3.1 | 0.16 | | |
| EUROPE<br>Nordic | 3.8 | 0.16 | | |
| EUROPE<br>Alpine | 3.8 | 0.16 | | |

Exhibit 2.2.9.1-1
$Q_1$ and $\beta$ values for various propagation effects and locations
*[Source: ITU-R Rec. P.841 (1997)]*

***Step 3)***

Determine the conversion factor Q, for each value of p, from:

$$
\begin{aligned}
Q(p) &= 12 && \text{for} && p < \left(\frac{Q_1}{12}\right)^{\frac{1}{\beta}} \% \\
&= Q_1 p^{-\beta} && \text{for} && \left(\frac{Q_1}{12}\right)^{\frac{1}{\beta}} < p < 3\% \\
&= Q_1 3^{-\beta} && \text{for} && 3\% < p < 30\% \\
&= Q_1 3^{-\beta}\left(\frac{p}{30}\right)^{\frac{\log\left(Q_1 3^{-\beta}\right)}{\log(0.3)}} && \text{for} && 30\% < p
\end{aligned}
\qquad (2.2.9.1\text{-}1)
$$

Exhibit 2.2.9.1-2 shows a plot of the conversion factor Q for the global parameters $Q_1 = 2.85$ and $\beta = 0.13$.

***Step 4)***

Determine the annual worst month time percentage of excess, $p_w$, for each annual time percentage, p, from

$$p_w = Q(p)\,p \qquad (2.2.9.1\text{-}2)$$

where $1 < Q(p) < 12$, and p and $p_w$ refer to the same threshold levels.

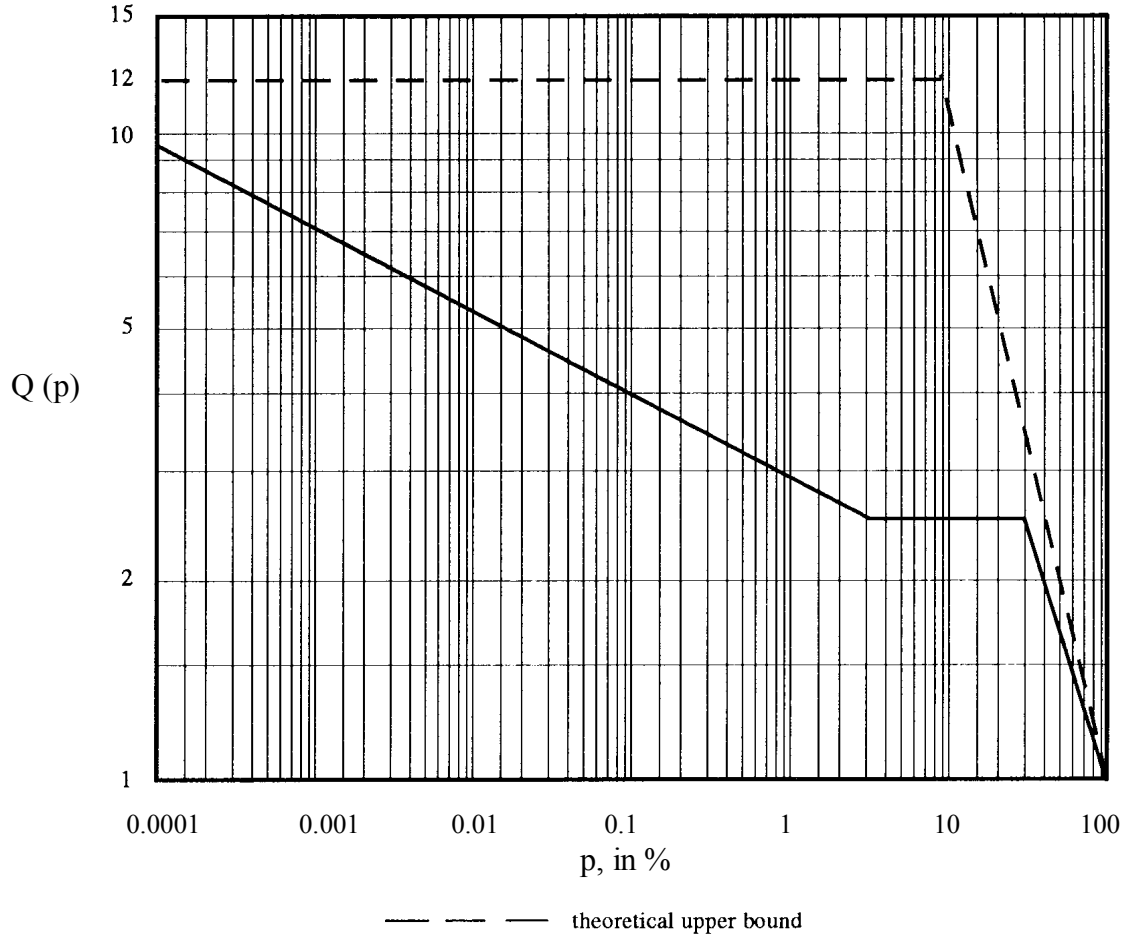


Exhibit 2.2.9.1-2
The Worst Month Conversion Factor Q, for the global parameters $Q_1 = 2.85$ and $\beta = 0.13$ (solid line)
*[Source: ITU-R Rec. P.841 (1997)]*

#### 2.2.9.1.1 Inverse Relationship

The average annual time percentage of excess, p, can be determined from the average annual worst-month time percentage of excess, $p_w$, through the inverse relationship

$$p = \frac{p_w}{Q(p)} \tag{2.2.9.1-3}$$

Utilizing Equations (2.2.9.1-1) and (2.2.9.1-3), and setting

$$p_o \equiv \left( \frac{Q_1}{12} \right)^{\frac{1}{\beta}} \tag{2.2.9.1-4}$$

the conversion factor is found as

For $12\, p_o < p_w\,(\%) < Q_1 3^{(1-\beta)}$,

$$Q(p_w) = Q_1^{\,1/(1-\beta)}\, p_w^{\,-\beta/(1-\beta)} \tag{2.2.9.1-5}$$

Then, for the global parameters, $Q_1 = 2.85$ and $\beta = 0.13$, the relationship between p and $p_w$ is found as

For $.00019 < p_w\,(\%) < 7.8$,

$$p = 0.30\, p_w^{\,1.15} \tag{2.2.9.1-6}$$

This result allows for the determination of the threshold value (margin) required for a specified worst month link performance when the annual time exceedance distribution is available. For example, if the performance requirement is for 0.1 % of the worst month, the threshold value is found as the threshold at the annual distribution value of

$$p = 0.30(0.1)^{\,1.15} = 0.0212\,\%$$

### 2.2.9.1.2 Variability of Worst Month Estimation

The natural variability of the propagation phenomena will affect the year-to-year variation of the annual worst month statistics for a communications link. If we define $W_R$ as the annual worst-month time fraction of excess associated with a return period of R years, the expected variation about a long-term average predicted value can be estimated from the curves of Exhibit 2.2.9.1-3.

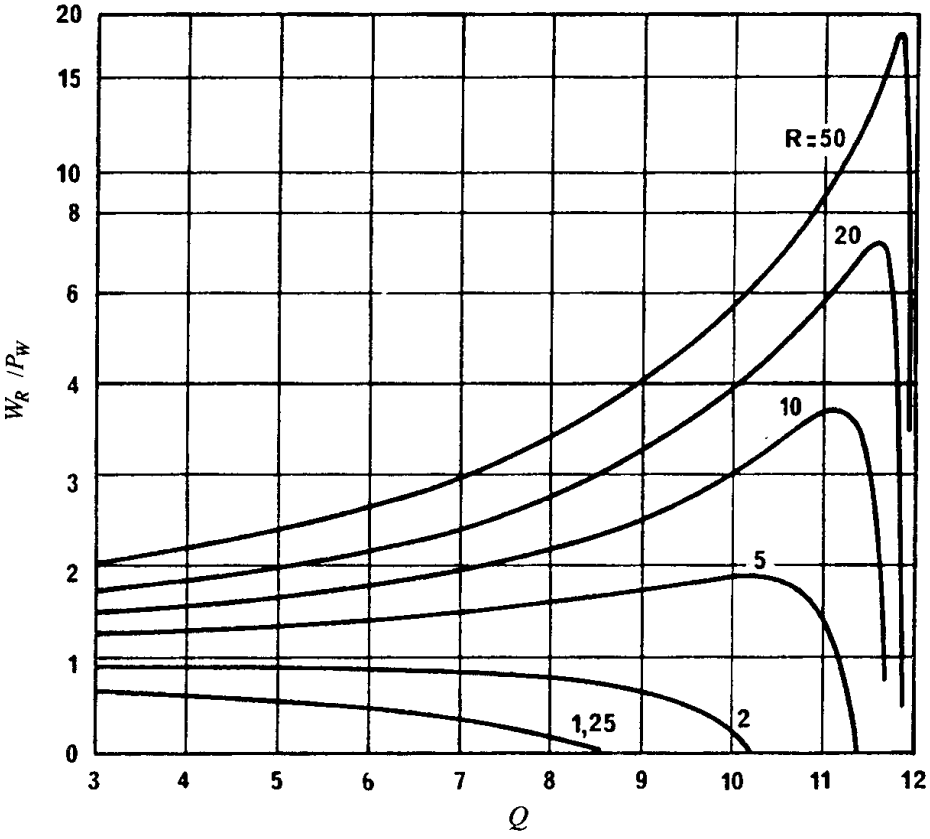


$p_w$: average annual worst-month time fraction of excess
R: return period, in years
$W_R$: annual worst month time fraction of excess associated with the return period of R years
Q: worst-month conversion factor

Exhibit 2.2.9.1-3
Estimation of Year-to-year Variations in Worst-Month Statistics
*[Source: ITU-R Rec. P.678-1 (1997)]*

$W_R/p_w$ is plotted in Exhibit 2.2.9.1-3 as a function of Q for return values from 1 to 50 years. Note that $p_w$, $W_R$, and Q are referred to the same pre-selected threshold value for the plots shown.

The return period is the average time duration between two consecutive occurrences of a defined stochastic event. For a long series of observation the value of the return period is $1/P$ (times the unit time between two subsequent observations) where $P$ is the probability of occurrence of the event. For example, the median value of a long series of annual worst-month time fraction of excess values would have a two-year return period (ITU-R Rec. P.678-1, 1997).

### 2.2.10 Fade Rate and Fade Duration

This section discusses the calculation of fade rate statistics and fade duration statistics. Fade rate and fade duration statistics provide important information about how long a fade of a given attenuation can be expected to last, as well as how fast the fade will occur (Pratt et al, 1993). The following sections discuss methods for calculating fade rate and fade duration.

#### 2.2.10.1 Fade Rate

Fade Rate, Rate of Fade, and Fade Slope are all terms used to describe the rate at which the signal level fades or varies with time. A fade may be due to a rain event, gaseous absorption or depolarization of the signal to name a few possible causes. Three procedures for calculating the fade slope were proposed by experimenters involved in the Olympus program. The procedures were described and compared in an OPEX (Olympus Propagation Experimenters) document edited by Poiares Baptista and Davies (1994).

##### 2.2.10.1.1 Method 1

The first method was used by British Telecom Labs (Howell, et al, 1992). The fade slope is calculated from the following equation:

$$\text{Fade Slope} = \frac{S(\Delta t) - A_T}{\Delta t} \qquad (2.2.10.1\text{-}1)$$

where,

$A_T$ = A threshold attenuation being exceeded
$S(\Delta t)$ = The signal level at a specified time interval $\Delta t$ after the signal level has exceeded some preset attenuation threshold $A_T$.

The fade slope can be calculated for different attenuation thresholds $A_T$. In the OPEX experiment, this method showed no significant differences between the rate of fade during clear air and the rate of fade during a rain event. The conclusion was that the slopes were masked by noise.

##### 2.2.10.1.2 Method 2

The second method used during the OPEX experiment implements a two-step filtering process (Rucker, 1991, 1993). A moving average (MA) is calculated for time intervals of 10s. Then the slope is calculated from a least squares fit (LSF) of the averaged data. This procedure was found to yield significantly higher fade slopes during the rain event than after the event, however the rate of fade before the event and during the event were found to be of the same order of magnitude. The latter effect was attributed to scintillation.

#### 2.2.10.1.3 Method 3

In the third method used in the OPEX experiment, the fade slope is calculated as the difference of two samples from filtered time series data. The time series data is first run through a cosine-squared shaped filter with a time constant of 100 sec to remove any noise and scintillation effects. The data is sampled at a frequency of 1Hz. Using this method, a difference in the fade slopes during a rain event and the fade slopes during clear air was observed. Before and after a rain event, the fade slopes were found to be very low while during a rain event higher fade slopes were found. The higher fade slope during the rain event was found to correlate well with the measured signal level.

### 2.2.10.2 Fade Duration

The duration of a rain fade is the amount of time that a specified value of attenuation is exceeded. Fade duration is typically computed for incremental attenuation values. Statistics of fade duration are mostly given in terms of $n_s$ or $n_d$ where $n_s$ is the total time (number of seconds) an attenuation threshold is exceeded and $n_d$ is the number of individual fades of duration d. The parameters are directly proportional where:

$$n_s = d\, n_d \qquad (2.2.10.2\text{-}1)$$

No significant dependence of these distributions on fade depth is evident in most measurements for fades of less than 20 dB. Significant departures from log-normal seem to occur for fade durations of less than 30 seconds. Fade duration at specified fade levels tend to increase with decreasing elevation angle.

For ISDN connections via satellite, data are needed on the contribution of attenuation events shorter than 10 seconds to the total fading time. This information is particularly useful for the attenuation level corresponding to the outage threshold. Events longer than 10 seconds may contribute to system down time, while shorter events affect system performance during available time. Some Examples of fade duration calculations are given Exhibits 2.2.10.2-1 and 2.2.10.2-2.

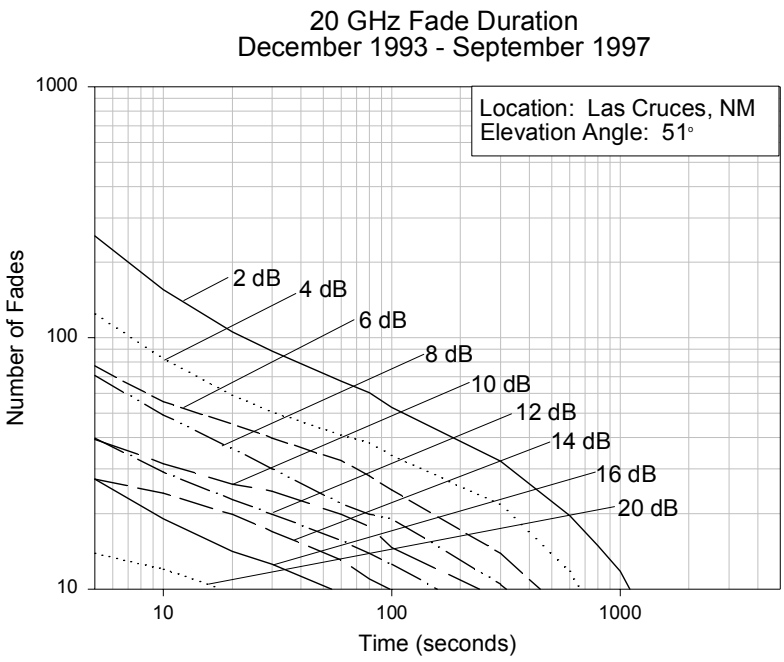


Exhibit 2.2.10.2-1: Fade Duration Calculated from New Mexico ACTS 20.2 GHz beacon data.

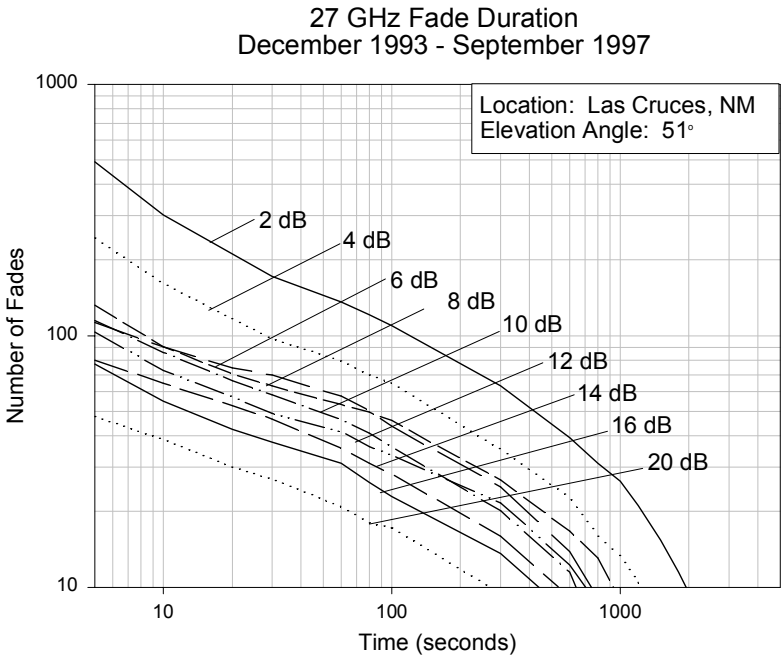


Exhibit 2.2.10.2-2: Fade Duration Calculated from New Mexico ACTS 27.5 GHz beacon data.

### 2.2.11 Combined Effects Modeling

Traditional systems of the past operate differently from modern systems. Traditional systems are designed with availability on the order of 99.99%. In order to maintain link closure 99.99% of the time, the system must be able to operate through high rain rates. At the time a traditional system's propagation margin is exceeded, rain attenuation will often be at least an order of magnitude larger than all other atmospheric attenuators combined. For this reason, traditional propagation prediction techniques have focused on accurately predicting the rain attenuation and adding the rain margin value to a small mean gaseous absorption value.

Modern systems are often designed for much lower availabilities; availability values on the order of 99.0-99.9% are typical. In this case, much less severe weather will lead to a loss of link closure. The primary impact to the system designer is that, at the time of link outage, secondary effects such as water vapor, oxygen, and cloud attenuation, will contribute a larger percentage of the total attenuation. Rain is usually still the dominant attenuator in modern systems, however the secondary attenuators can no longer be assumed to have only minor statistical significance.

Combined effects models provide techniques for assessing the cumulative effect of multiple attenuators that occur simultaneously along a propagation link. The ITU-R has not approved any model as a formal recommendation, and no particular model can be considered a standard. However, when calculating availability for modern systems, it is probably a wise choice to investigate some of the combined effects models that have been proposed. Three current combined effects techniques are discussed here.

#### 2.2.11.1 Feldhake Combined Effects Model

This section describes a procedure developed by Feldhake (1997) for the evaluation of the cumulative effects of multiple attenuators on a satellite path.

Consider a system operating with the following parameters:

| | |
|---|---|
| frequency: | 20 GHz |
| elevation angle: | 20° |
| availability: | 99.5% |
| location: | Washington, DC |
| latitude: | 38.4°N |
| average temperature: | 14.4°C |
| average humidity: | 9.0 g/m$^3$ |

It may be shown that with the given parameters, the system may operate with the losses listed in Exhibit 2.2.11.1-1.

| | |
|---|---|
| Rain Attenuation | 5.3 dB |
| Gaseous Absorption | 0.8 dB |
| Cloud Attenuation | 0.2 dB |
| Tropospheric Scintillation | 0.4 dB |
| **Total Margin Requirement** | **6.7 dB** |

Exhibit 2.2.11.1-1
Attenuating Contributions of Multiple, Simultaneous Atmospheric Effects

The total attenuation value of 6.7 dB is a simple summation of each of the component attenuation levels using traditional techniques. In order to determine the range of possible attenuation levels occurring for 99.5% availability, a statistical approach may be used which considers the complete distributions of each weather effect. This approach does not lend itself to quick, "back-of-the-envelope" calculations but may be qualitatively described in a step-by-step procedure.

*Step 1)*

Collect distributions of weather data for absolute humidity, cloud liquid water, and rain rate. These distributions may come from several sources.

- Absolute humidity distributions are easily derived. There are many climatic databases available that provide daily or even hourly long-term records of local temperature and humidity values. Often, such data can be found on world wide web sites. The data can be compiled to create long term distributions of local values. Another possible source is ITU-R Recommendation P.836-1 (1997). The recommendation provides global maps of surface and integrated water vapor content for various percentages of time. The disadvantage of the ITU-R maps is that not all locations are based on local measurements. Also, the time percentages for which maps are provided are spaced rather widely. Estimating water vapor for other percentages of time requires an interpolation.

- Cloud liquid distributions are slightly more difficult to obtain. One possibility is to use radiosondes (weather balloons). Several empirical detection algorithms are available to estimate the amount of cloud liquid water present along a vertical path from a single radiosonde sounding. Radiosonde data is available in many parts of the world and is relatively inexpensive. A second possible source of cloud liquid water data comes from ITU-R Recommendation P.840-2 (1997). Like the ITU-R recommendation for water vapor, P.840 provides global maps of cloud liquid water for various percentages of time.

- Rain rate data is the most difficult to obtain. The two primary sources are the Crane global rain maps and the maps provided in ITU-R Recommendation P.837-1 (1997). Both maps divide the world into climatic regions. Each region has it's own unique rain rate distributions assigned to it. The European Space Agency has recently published a third set of rain maps. These maps are based on global remote sensing data. They divide the world into 1.5° latitude x 1.5° longitude grid squares. Each grid square has it's own unique rain rate distribution.

*Step 2)*

Apply the entire distributions of weather effects to the appropriate propagation models. That is to say, use the rain rate distribution with a rain attenuation prediction model to obtain a rain attenuation distribution. Similarly, a distribution of cloud liquid water contents may be applied to a cloud attenuation model to obtain a cloud attenuation distribution. The same applies for humidity and gaseous absorption.

Rain attenuation may be calculated using the ITU-R or the DAH rain attenuation models described in Sections 2.2.4.1 and 2.2.4.4, respectively. For water vapor and cloud liquid water, the most accurate model to use is the Liebe complex refractivity model, described in Section 2.2.1.1. If it is appropriate to give up a small amount of accuracy in order to have simplified calculations, the ITU-R (Section 2.2.1.2) provides models that may be more suitable. The ITU-R models will provide attenuation estimates for water vapor and clouds respectively. Both the Liebe and ITU-R models for gaseous absorption include the effects of oxygen with the water vapor attenuation.

*Step 3)*

Create two distributions of total attenuation by assuming statistical correlation and decorrelation between the effects. The assumption of perfect correlation between the atmospheric effects produces a worst case scenario. In this case as one atmospheric effect increases in severity, they all will increase. In some cases the assumption is good. For example, the assumption of perfect correlation between the effects will predict that the highest rain rates will come from the clouds with the most water. However, the assumption will also predict that whenever the humidity is high, rain will also occur.

Statistical correlation may be modeled in the total attenuation through equiprobable summation of the individual attenuation values at a specific probability level. This relationship may be represented by

$$A(P)_{Total} = A_{Rain}(P) + A_{Gas}(P) + A_{Cloud}(P) + A_{Scintillation}(P) \qquad (2.2.11.1\text{-}1)$$

where $A_X(P)$ is the Attenuation in dB due to Effect *X* experienced no more than P percent of the time. An example of this is the summation performed in Exhibit 2.2.11.1-1. Each of the individual attenuation values represented in the table are the values not exceeded 99.5% of the time. The total attenuation produced by summing them is the value of total attenuation not exceeded more than 99.5% of the time in a worst case sense. The process is also presented graphically in Exhibit 2.2.11.1-2.

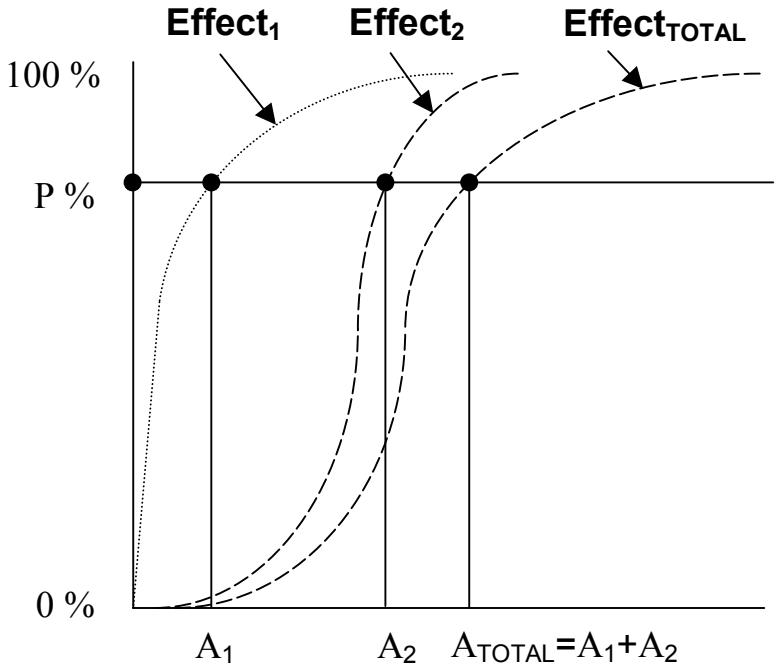


Exhibit 2.2.11.1-2
Graphical example of equiprobable summation

Perfect decorrelation between the effects assumes that there is no statistical relationship between the effects. In some cases this assumption is valid. For example, as the rain intensity within an event grows from 2 mm/hr to 4 mm/hr, it is not reasonable to expect the humidity to also experience a 100% increase. However, this assumption also creates the possibility that rain may fall from a clear blue sky.

Statistical decorrelation may be modeled by convolving the cumulative distribution function, CDF, of attenuation due to one effect with the probability density function, PDF, of attenuation due to another effect. This may be performed by:

$$P(A_{Total}) = \int_{-\infty}^{A_{Total}} p_1(A)\, P_2(A_{Total} - A)\, dA \qquad (2.2.11.1\text{-}2)$$

where $p_x(A)$ is the PDF of attenuation due to atmospheric effect $X$, and $P_Y(A)$ is the CDF of attenuation due to effect $Y$. The resulting distribution will be the CDF of the independent joint statistic. Additional effects may be included in the total distribution by convolving additional PDFs with each successive joint CDF. A graphical representation of this operation is presented in Exhibit 2.2.11.1-3.

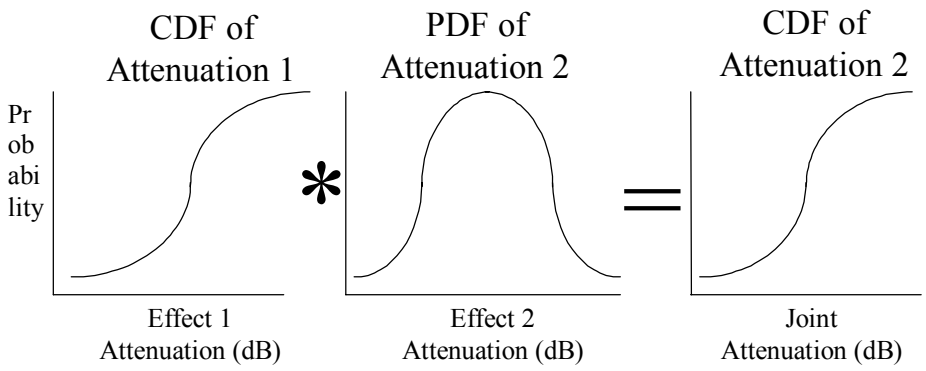


Exhibit 2.2.11.1-3
Graphical example of convolution

By superimposing the dependent and independent cases on top of each other, a set of statistical bounds may be established that will represent the most realistic, optimistic and pessimistic cases. A more optimistic case could be derived if an assumption is made of negative correlation, however at frequencies below about 30 GHz, this is probably not a realistic condition.

*Step 4)* (Optional)

If monthly or seasonal meteorological data is available, it is useful to first combine the attenuation distributions into dependent and independent monthly or seasonal basis. This will serve to help the optimistic and pessimistic bounds converge toward a single distribution.

The four, seasonal, dependent case curves can be combined into a single annual curve using the following formula.

$$P_{Year} = P_{Win} \cdot P_{Win}(A) + P_{Spr} \cdot P_{Spr}(A) + P_{Sum} \cdot P_{Sum}(A) + P_{Aut} \cdot P_{Aut}(A) \quad (2.2.11.1\text{-}3)$$

where $P_{Xxx}$ is the probability that season Xxx occurs in the year and $P_{Xxx}(A)$ is the probability level associated with attenuation, A, occurring during season Xxx. For a quick calculation it may be assumed that PXxx is 0.25; however, not all seasons contain exactly the same number of minutes. The same process can then be applied to the independent case. If monthly data is available, the data may be divided into twelve dependent and independent case distributions.

An example output for the system parameters discussed above is provided in Exhibit 2.2.11.1-4. The chart shows two sets of dependent and independent curves. The outer pair of curves (marked with circles) represents the dependent and independent cases using only data collected on an annual basis. The inner pair of curves (marked with triangles) were generated using the same data but after first dividing it into monthly distributions.

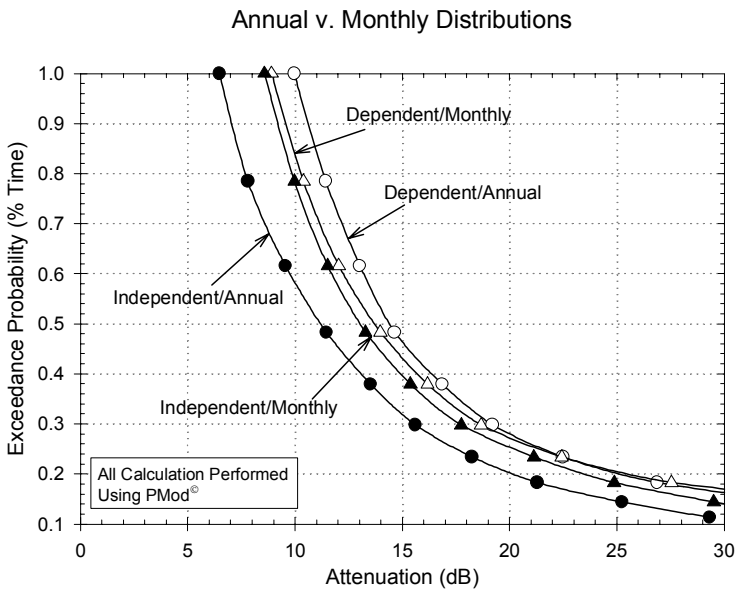


Exhibit 2.2.11.1-4
Dependent and independent total attenuation curves using annual data and data segmented by month.

This method shows promise when compared to traditional approaches and measured data. Traditional approaches involve accurately estimating rain attenuation only. A mean absorption loss is then added to the rain attenuation to create a total atmospheric attenuation margin requirement. Exhibits 2.2.11.1-5 and 2.2.11.1-6 show measured propagation data from the ACTS satellite to Reston, VA at 20 and 27 GHz. The dependent, independent and traditional prediction curves are overlaid on the measured data.

Both figures show that the traditional techniques tend to under predict attenuation particularly at high exceedance probabilities (low system availabilities). The measured data follows the dependent and independent curves to attenuation values exceeded at least 1% of the time while the traditional method falls back toward a value at the mean annual gas loss. At lower probability levels (higher system availabilities), the measured data falls somewhere between the predicted bounds.

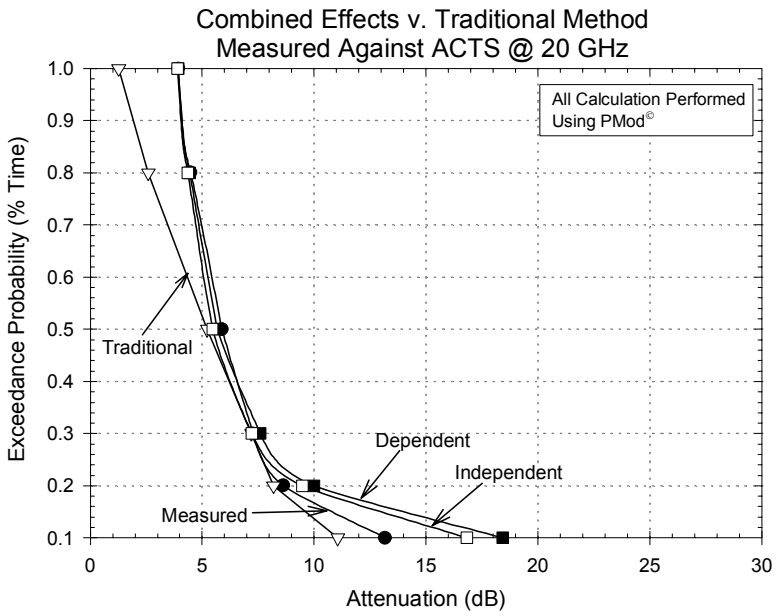


Exhibit 2.2.11.1-5
Independent, Dependent, and Traditional Prediction Techniques
Compared with Measured ACTS Data at 20.185 GHz.

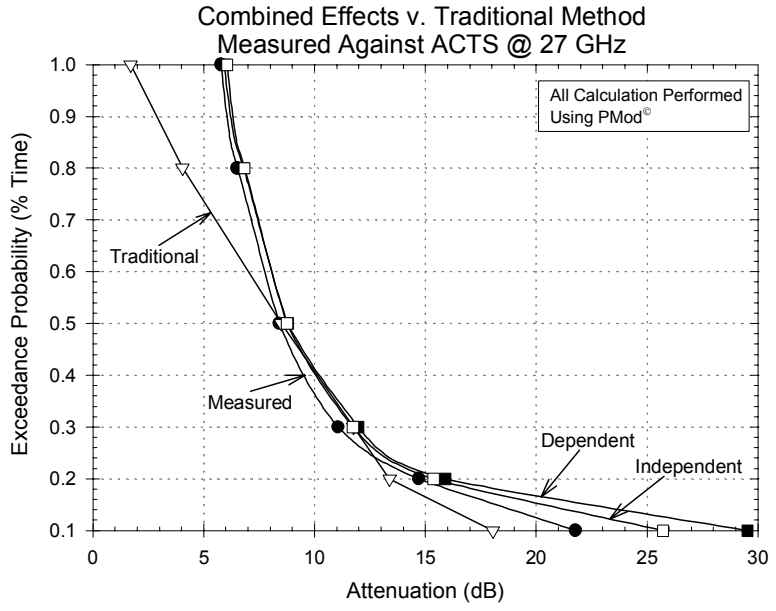


Exhibit 2.2.11.1-6
Independent, Dependent, and Traditional Prediction Techniques
Compared with Measured ACTS Data at 27.505 GHz.

### 2.2.11.2 DAH Combined Effects Model

The prediction model developed by Dissanayake, Allnutt, and Haidara (DAH) takes a different approach to solving the combined effects problem (Dissanayke, A., et.al., 1997). The DAH model is an empirical model that works on the premise that large rain attenuation and small clear-air attenuation are relatively straightforward to characterize. The difficulty lies in trying to calculate the transition region when water vapor and cloud losses may be elevated, but rain is not yet the overwhelming source of signal degradation. To this end, the DAH model provides not only a system for combining atmospheric effects, but new models for calculating the attenuation due to different atmospheric components.

The effects considered by the DAH model are rain, water vapor, oxygen, clouds, melting layer, and tropospheric scintillation. The attenuation due to each effect may be calculated for a specific percentage of time, then combined for a total attenuation. The following steps describe the procedure:

*Step 1)*

Calculate rain attenuation, $A_r$, using the DAH Rain Model. This model is an empirical model that performs well when compared to measured data. A step-by-step procedure for the DAH rain model is given in Section 2.2.4.4 of this handbook.

*Step 2)*

Calculate water vapor and oxygen attenuation, $A_g$, using the atmospheric gaseous absorption model provided by the ITU-R. A step-by-step procedure for the ITU-R gaseous attenuation model is given in Section 2.2.1.2.2 of this handbook. Although this standard model was not developed specifically for use with the DAH combined effects algorithm, the authors of the DAH model recommend its use.

Inputs to the ITU-R gaseous absorption model include the absolute humidity for the location of interest and at the desired probability level. If this data is not available, the authors of the DAH model suggest a technique for estimating the distribution. Absolute humidity can be assumed to have a distribution that follows a normal probability law. The average annual water vapor density is used as the mean; the standard deviation of the distribution is equal to about ¼ of the mean value.

*Step 3)*

Calculate cloud attenuation, $A_c$, using the DAH cloud model. This model is not discussed elsewhere and is unique to the DAH combined effects algorithm. The DAH cloud attenuation model is based on empirical fits between cloud attenuation measurements and long-term cloud cover observations for four specific cloud types. With this model, cloud attenuation may be calculated in a four-step process.

a) Determine the specific attenuation due to each of the four cloud types using:

$$\alpha_{ci} = 0.4343\left(\frac{3\pi\upsilon}{32\lambda\rho}\right)\mathrm{Im}\left(\frac{1-\varepsilon}{2+\varepsilon}\right) \qquad (2.2.11.2\text{-}1)$$

where

| | |
|---|---|
| $\upsilon$ | cloud liquid water density ($g/m^3$) given in Exhibit 2.2.11.2-1, |
| $\lambda$ | wavelength (m), |
| $\rho$ | density of water ($g/m^3$), |
| $\varepsilon$ | complex dielectric constant of water, |
| Im | imaginary part of a complex number, and |
| i | one to four for the four cloud types. |

The parameters of the four cloud types are presented in Exhibit 2.2.11.2-1.

| Cloud Type | Vertical Extent (km), Hc | Horizontal Extent (km), Lc | Water Content ($g/m^3$), $\upsilon$ |
|---|---|---|---|
| Cumulonimbus | 3.0 | 4.0 | 1.0 |
| Cumulus | 2.0 | 3.0 | 0.6 |
| Nimbostratus | 0.8 | 10.0 | 1.0 |
| Stratus | 0.6 | 10.0 | 0.4 |

Table 2.2.11.2-1
Average Properties of Four Cloud Types Used in the DAH Model

b) Determine the total attenuation for the path through each cloud type. Zenith path attenuation is given by

$$A_{ci} = \alpha_{ci} \cdot H_{ci} \qquad (2.2.11.2\text{-}2)$$

where $H_{ci}$ is the vertical extent of cloud type i. Path attenuation due to clouds may be derived for elevations other than 90º, by assuming clouds to be vertically oriented cylinders of the size given in Exhibit 2.2.11.2-1.

c) Derive the conditional cloud attenuation distribution curve by numerically ordering the four cloud attenuation values on the line given by:

$$P(A > A_c) = \frac{P_o}{2}\,\mathrm{erfc}\left(\frac{\ln A - \ln \overline{A_c}}{\sqrt{2\sigma_c}}\right) \qquad (2.2.11.2\text{-}3)$$

where

| | |
|---|---|
| $P(A>A_c)$ | probability that the cloud attenuation, $A_c$, does not exceed A, |
| $\tilde{A}_c$ | average value of $A_c$, |
| $\sigma_c$ | standard deviation of $A_c$, and |
| $P_o$ | probability of cloud cover from the long term observations. |

c) Fit a curve through the five points calculated in c) assuming a lognormal relationship to arrive at the total distribution of cloud attenuation.

*Step 4)*

Calculate the attenuation due to the melting layer, $A_m$. The DAH model also provides its own model of melting layer attenuation. This is a relatively simple model that estimates the attenuation as a function of the rain rate.

$$A_m = \alpha_m \cdot L_m \qquad (2.2.11.2\text{-}4)$$

This is accomplished by first calculating the specific attenuation of the melting layer, $\alpha_m$, and then multiplying it by the path length through the melting layer, $L_m$. The specific attenuation of the melting layer, $\alpha_m$, is given by:

$$\alpha_m = a\,R^b \qquad (2.2.11.2\text{-}5)$$

where R is the rain rate, in mm/r, and

$$a = e^{1.58 \cdot \ln(f) - 6.23}$$
$$b = e^{0.029 \cdot \ln(f) - 0.031}$$

The parameter f is the frequency in GHz.

The vertical thickness of the melting layer is assumed to be 0.5 km so the path length, $L_m$, is given by:

$$L_m = \frac{0.5}{\sin\theta} \qquad (2.2.11.2\text{-}6)$$

where

$\theta$ is elevation angle, and

$L_m \le 10$ km. If $L_m > 10$ km (i.e. $\theta < 2.9^o$), then assume $L_m$=10.0 km.

*Step 5)*

Calculate tropospheric scintillation using the ITU-R scintillation prediction model. A step-by-step procedure for the ITU-R scintillation model is provided in Section 2.2.8.1.2. This model estimates the effect of changes in the refractivity of the atmosphere. The ITU-R model performs well when tested against measured data, however DAH does add one minor adjustment as a correction for elevation angles below 5º. The adjustment consists of a modified standard deviation, $\sigma_t$, given by:

$$\sigma_t = \sigma_\chi + \sigma_o\left(e^{0.11(5-\theta)} - 1.0\right) \qquad (2.2.11.2\text{-}7)$$

where

$\sigma_o$ ITU-R model reference scintillation standard deviation value,

$\sigma_\chi$ ITU-R model standard deviation of the scintillation,

*Step 6)*

Combine the effects into a single total attenuation value. The method for combining the effects is frequency dependent. Two different algorithms are used for frequencies above and below 10 GHz. The technique for combining the effects approaches the problem by dividing the distribution into three regions. The first is a clear air region where there is no rain. The second is a transition region where light rains are accompanied by gaseous absorption as well as cloud and melting layer components. The third region is the heavy rain region, where rain is the dominant attenuator. Exhibit 2.2.11.2-2 shows a graphical representation of the three regions.

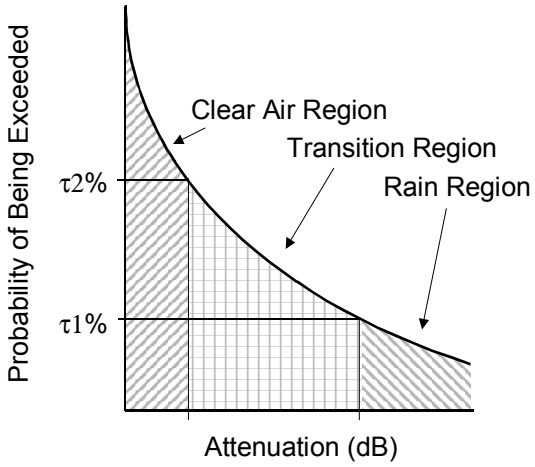


Exhibit 2.2.11.2-2
The three regions considered by the DAH combined effects model

The probabilities used to separate the three regions are located at $\tau_1$ and $\tau_2$. When the frequency of interest is between 4 GHz and 10 GHz, the $\tau_1$ and $\tau_2$ are arbitrarily set to 0.5% and 10.0% respectively. At frequencies above 10 GHz, $\tau_1$ becomes dependent on the rain climate, and $\tau_2$ becomes dependent on elevation angle. In this case, $\tau_1$ is equal to 1% or the probability that the rain rate exceeds 2 mm/hr, whichever is greater, and

$$\tau_2 \begin{cases} = 10 & \text{for } \theta \le 10^o \\ = 5 & \text{for } \theta \ge 30^o \\ = 10 - \dfrac{\theta - 10}{4} & \text{for } 10^o < \theta < 30^o \end{cases} \qquad (2.2.11.2\text{-}8)$$

where $\theta$ is the elevation angle.

For the following sets of equations, the following variables will be used:

$A(P)$ is the total attenuation at a percentage of time, P,
$A_R(P)$ is the attenuation due to rain at a percentage of time, P,
$A_G(P)$ is the attenuation due to gas at a percentage of time, P,
$A_C(P)$ is the attenuation due to clouds at a percentage of time, P,
$A_M(P)$ is the attenuation due to the melting layer at a percentage of time, P,
$A_{CM}(P)$ is the combined attenuation due to clouds and melting layer at a percentage of time, P,
$A_{RCM}(P)$ is the combined attenuation due to rain, clouds and melting layer at a percentage of time, P, and
$A_S(P)$ is the attenuation due to scintillation at a percentage of time, P,

At probabilities greater than $\tau_2$%, it is assumed that any attenuation is due to clear air. This assumption applies to both frequency ranges. The total attenuation in this region of the distribution is given by:

$$A(P) = \sqrt{\left(A_C(P) + A_G(P)\right)^2 + A_S(P)^2} \qquad (2.2.11.2\text{-}9)$$

In the range $\tau_1 \le P \le \tau_2$, there is a transition from attenuation dominated by clouds and the melting layer to attenuation dominated by rain. In this region the technique for combining the various sources of attenuation is dependent on frequency.

In the frequency range of 4 GHz to 10 GHz, the distribution is assumed to change log-normally from being dominated by clouds and the melting layer at $\tau_2$(=10%) to being dominated by rain at $\tau_1$(=0.5%). The value of $A_{RCM}(P)$ is calculated by

$$A_{RCM}(P) = I_{ln\,m}\left(A_R(0.5\%), A_{CM}(10\%)\right) \qquad (2.2.11.2\text{-}10)$$

where $I_{lnm}$ represents the log-normal interpolation between the value predicted for rain attenuation at the 0.5% probability level and the value predicted jointly for clouds and the melting layer at the 10% probability level. In this case,

$$A_{CM}(P) = \sqrt{A_C(P)^2 + A_M(P)^2} \qquad (2.2.11.2\text{-}11)$$

In the frequency range of 10 GHz to 35 GHz, the distribution of $A_{RCM}(P)$ is determined from

$$A_{RCM}(P) = \frac{\tau_2 - P}{\tau_2 - \tau_1} \cdot A_R(P) + \frac{P - \tau_1}{\tau_2 - \tau_1} \cdot A_{CM}(P) \qquad (2.2.11.2\text{-}12)$$

Once $A_{RCM}(P)$ has been determined by either Eq's (2.2.11.2-10) or (2.2.11.2-12), A(P) is given by:

$$A(P) = \sqrt{\left(A_{RCM}(P) + A_G(P)\right)^2 + A_S(P)^2} \qquad (2.2.11.2\text{-}13)$$

At probabilities less than $\tau_1$%, it is assumed across both ranges of frequencies that the total attenuation will be primarily due to rain, gaseous absorption, and scintillation. In this case

$$A(P) = \sqrt{\left(A_R(P) + A_G(P)\right)^2 + A_S(P)^2} \qquad (2.2.11.2\text{-}14)$$

This completes the steps for the DAH combined effects procedure.

### 2.2.11.3 ESA Combined Effects Studies

The European Space Agency, ESA, has been conducting studies for several years on the combined effects of attenuation and scintillation phenomena. A comprehensive summary or prediction procedure for the work accomplished is not currently available in the open literature. The most complete description of efforts on the combination problem is available in an ESA report (Salonen, et al, 1994), also summarized in an OPEX (Olympus Propagation Experimenters) report (ESA, 1994).

The method is briefly described in Salonen et al, (1992). A study of the combination of gases and clouds is provided in Salonen (1993), while a study of scintillation and attenuation is presented in van de Kamp, et al (1997).

## 2.3 RADIO NOISE

Radio noise can be introduced into the transmission process of a satellite communications system from both natural and human-induced sources. Any natural absorbing medium in the atmosphere which interacts with the transmitted radiowave will not only produce a signal amplitude reduction (attenuation), but will also be a source of thermal noise power radiation. The noise associated with these sources, referred to as radio noise, or sky noise, will directly add to the system noise through an increase in the antenna temperature of the receiver. For very low noise communications receivers radio noise can be the limiting factor in the design and performance of the system.

Radio noise is emitted from many sources, both natural (terrestrial and extra-terrestrial origin) and human made.

Terrestrial sources include:
- emissions from atmospheric gases (oxygen and water vapor)
- emissions from hydrometers (rain and clouds).
- radiation from lightning discharges (atmospheric noise due to lightning);
- re-radiation from the ground or other obstructions within the antenna beam

Extra-terrestrial sources include;
- cosmic background radiation
- solar and lunar radiation
- radiation from celestial radio sources (radio stars)

Human induced sources include:
- unintended radiation from electrical machinery, electrical and electronic equipment
- power transmission lines
- internal combustion engine ignition
- emission from other communications systems.

This chapter describes the major radio noise sources in satellite communications, and provides concise methods to calculate the noise and evaluate effects on system performance.

### 2.3.1 Specification of Radio Noise

The thermal noise emission from a gas in thermodynamic equilibrium, from Kirchoff's Law, is equal to its absorption, and this equality holds for all frequencies. The noise temperature, $t_b$, observed by a ground station in a given direction through the atmosphere (also referred to as the brightness temperature), is given by radiative transfer theory, (Waters, 1976, Wulfsberg, 1964)

$$t_b = \int_0^\infty t_m \gamma e^{-\tau} dl + t_\infty e^{-\tau_\infty} \qquad (2.3.1\text{-}1)$$

where $t_m$ is the ambient temperature, $\gamma$ is the absorption coefficient, and $\tau$ is the optical depth to the point under consideration. Also,

$$\tau = 4.343\,A \qquad \text{dB} \tag{2.3.1-2}$$

where A is the absorption over the path in question , in dB. For frequencies above 10 GHz, the second term on the righthand side of Equation (2.3.1-1) reduces to 2.7 K, the cosmic background component (unless the sun is in the beam of the aperture).

For an isothermal atmosphere ($t_m$ constant with height), Equation (2.3.1-1) further reduces to

$$\begin{aligned} t_b &= t_m\left(1-e^{\tau}\right) \\ t_b &= t_m\left(1-10^{-\frac{A}{10}}\right) \qquad \text{K} \end{aligned} \tag{2.3.1-3}$$

where A is again atmospheric absorption in dB. The value of $t_m$ in Equation (2.3.1-3) ranges from 260 to 280 K. Wulfsburg (1964) provided a relationship to determine the value of $t_m$ from surface measured temperature,

$$t_m = 1.12t_s - 50 \qquad \text{K} \tag{2.3.1-4}$$

where $t_s$ is the surface temperature, in K.

Noise from individual sources such as atmospheric gases, the Sun, the Earth's surface, etc., are usually given in terms of their brightness temperature. The antenna temperature is the convolution of the antenna pattern and the brightness temperature of the sky and ground. For antennas whose patterns encompass a single distributed source, the antenna temperature and brightness temperature are the same.

The noise in a communications system is expressed in terms of an equivalent noise temperature, $t_a$ , in degrees Kelvin, and a noise factor, $F_a$ , in dB,given by

$$F_a(\text{dB}) = 10\log\left(\frac{t_a}{t_0}\right) \tag{2.3.1-5}$$

where $t_0$ is the ambient reference temperature, set to 290 K. Equivalently, the noise factor can be expressed as

$$F_a(\text{dB}) = 10\log\left(\frac{p_a}{kt_0b}\right) \tag{2.3.1-6}$$

where $p_a$ is the available noise power at the antenna terminals, k is Boltzman's constant, and b is the noise power bandwidth of the receiving system.

Exhibit 2.3.1-1 summarizes the median expected noise levels produced by sources of external radio noise in the frequency range applicable to practical space communications (ITU-R Rec PI.372-6, 1997). Noise levels are expressed in terms of both noise temperature, $t_a$, (right vertical axis), and Noise Factor, $F_a$(dB) (left vertical axis). Between about 30 MHz to 1 GHz, galactic noise (curves B and C) predominates, but will generally be exceeded by man-made noise in populated areas (curve A). Above 1 GHz, the absorptive constituents of the atmosphere, i.e. oxygen, water vapor (curves E), also act as noise sources and can reach a maximum value of 290 K under extreme conditions.

The Sun is a strong variable noise source, reaching values of 10,000 K and higher when observed with a narrow beamwidth antenna (curve D), under quiet Sun conditions. The cosmic background noise level of 2.7 K (curve F) is very low and is not a factor of concern in space communications.

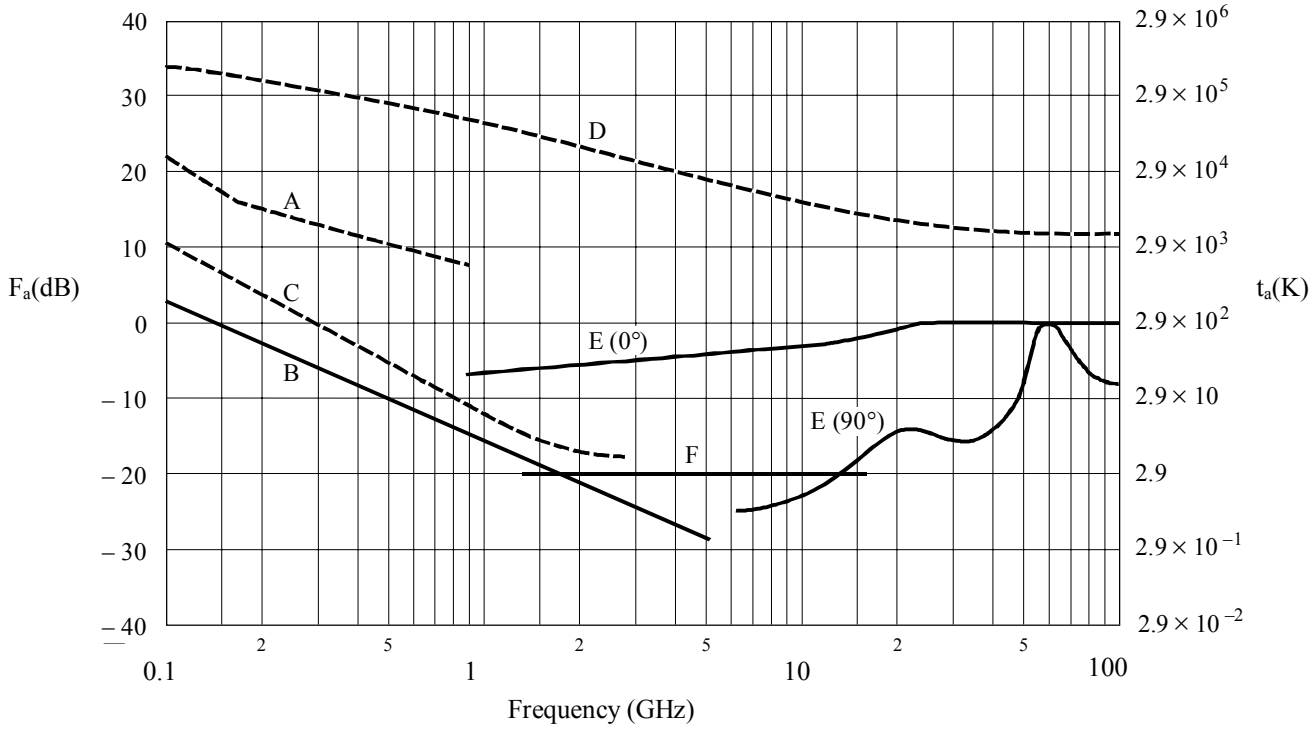


A: estimated median business area man-made noise
B: galactic noise
C: galactic noise (toward galactic centre with infinitely narrow beamwidth)
D: quiet Sun ($\frac{1}{2}^\circ$ beamwidth directed at Sun)
E: sky noise due to oxygen and water vapour (very narrow beam antenna); upper curve, 0° elevation angle; lower curve, 90° elevation angle
F: black body (cosmic background), 2.7 K
minimum noise level expected

Exhibit 2.3.1-1
Noise Factor and Brightness Temperature from External Sources
*[Source: ITU-R PI.372-6 (1994)]*

### 2.3.2 Noise from Atmospheric Gases

The gaseous constituents of the Earth's atmosphere interact with a radiowave through a molecular absorption process that results in attenuation of the signal. This same absorption process will produce a thermal noise power radiation that is dependent on the intensity of the absorption, through Equation 2.3.1-3.

The major atmospheric gases that affect space communications are oxygen and water vapor. The sky noise temperature for oxygen and water vapor, for an infinitely narrow beam, at various elevation angles, was calculated by direct application of the radiative transfer equation, at frequencies between 1 and 340 GHz (Smith, 1982). Exhibits 2.3.2-1 and 2.3.2-2 summarize the results of these calculations for representative atmospheric conditions (ITU-R Rec. PI.372-6, 1994). Exhibit 2.3.2-1 represents moderate atmospheric conditions (7.5 $g/m^3$ water vapor, 50 % relative humidity). Exhibit 2.3.2-2 provides an expanded frequency scale version for use with frequencies below 60 GHz. The curves are calculated using a radiative transfer program for seven different elevation angles and an average atmosphere as stated on the Exhibits. The cosmic noise contribution of 2.7 K or other extra-terrestrial sources are not included. The 1976 United States Standard Atmosphere is used for the dry atmosphere. A typical water vapor contribution is added above the tropopause.

**Brightness temperature (clear air) for 7.5 g/m³ water vapour concentration (surface temperature and pressure equal to 15° C and 1 023 mb); θ is the elevation angle**

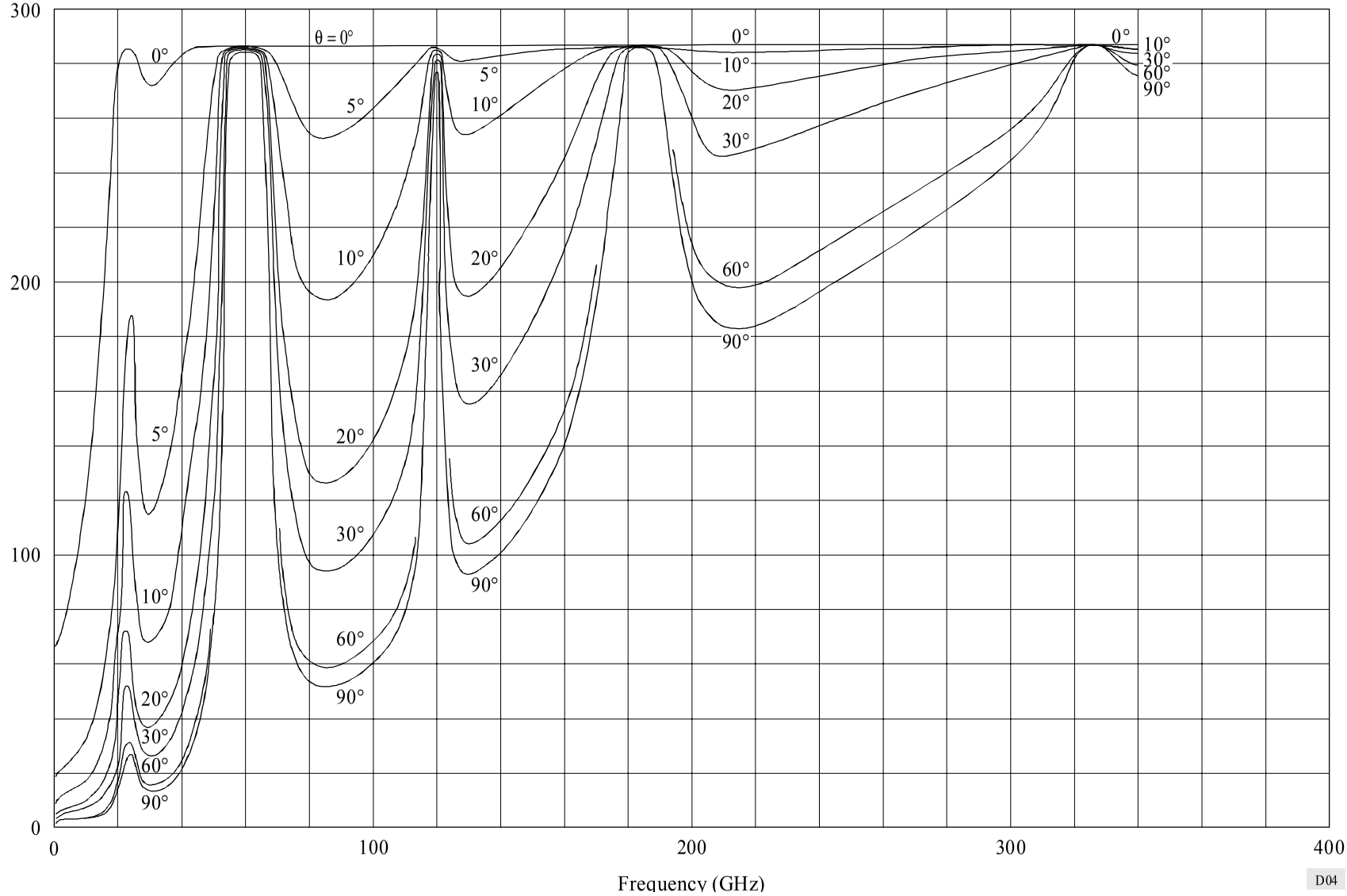

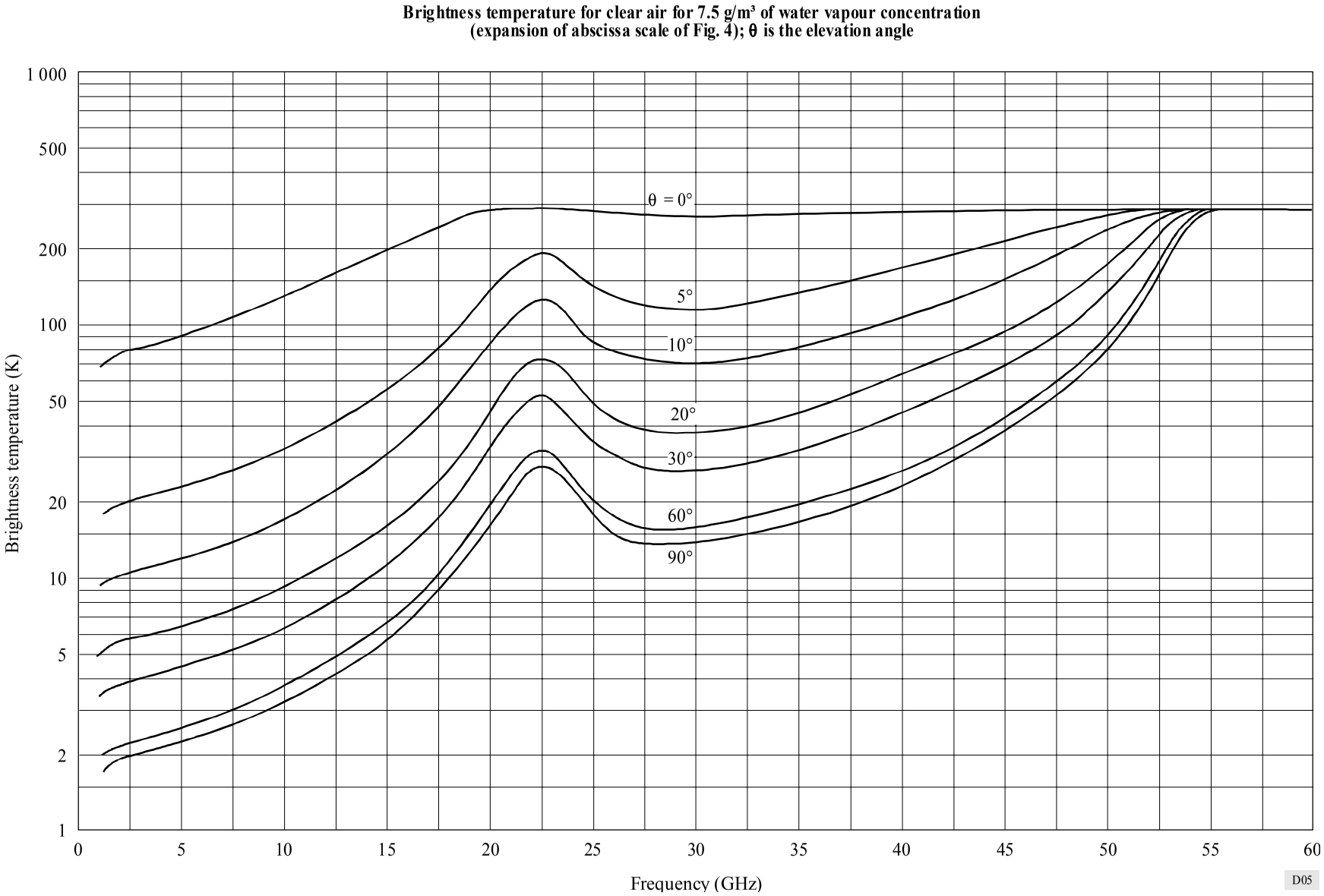
Brightness temperature for clear air for 7.5 g/m³ of water vapour concentration
(expansion of abscissa scale of Fig. 4); θ is the elevation angle
1 000
500
200
100
50
20
10
5
2
1
Brightness temperature (K)
θ = 0°
5°
10°
20°
30°
60°
90°
0
5
10
15
20
25
30
35
40
45
50
55
60
Frequency (GHz)
D05

### 2.3.3 Sky Noise Due to Rain

Sky noise due to absorption in rain can also be determined from the radiative transfer approximation methods described in Section 2.3.1. The noise temperature due to rain, $t_{r,}$ can be determined directly from the rain attenuation from (see Eq. 2.3.1-3)

$$t_r = t_m\left(1-10^{-\frac{A_r(dB)}{10}}\right) \qquad K \qquad (2.3.3\text{-}1)$$

where $t_m$ is the mean path temperature, in $^o$ K, and $A_r$(dB) is the total path rain attenuation, in dB. Note that the noise temperature is independent of frequency, i.e., for a given rain attenuation, the noise temperature produced will be the same, regardless of the frequency of transmission.

The mean path temperature, $t_m$, as described in Section 2.3.1, can be estimated from the surface temperature $t_s$ by,

$$t_m = 1.12t_s - 50 \qquad K \qquad (2.3.3\text{-}2)$$

where $t_s$ is the surface temperature in $^o$K.

A direct measurement of $t_m$ is difficult to obtain. Simultaneous measurements of rain attenuation and noise temperature on a slant path using satellite propagation beacons can provide a good estimate of the statistical range of $t_m$. Good overall statistical correlation of the noise temperature and attenuation measurements occurs for $t_m$ between 270 K and 280 K for the vast majority of the reported measurements (Ippolito, 1971), (Strickland, 1974), (Hogg and Chu, 1975).

Exhibit 2.3.3-1 shows the noise temperature calculated from Eq. 2.3.3-1 as a function of total path rain attenuation for the range of values of $t_m$ from 270 K to 280 K. The noise temperature approaches 'saturation', i.e., the value of $t_m$, fairly quickly above attenuation values of about 10 dB. Below that value the selection of $t_m$ is not very critical. The centerline ($t_m$ = 275 K) serves as the best prediction curve for $t_r$. The noise temperature rises quickly with attenuation level. It is 56 K for a 1 dB fade, 137 K for a 3 dB fade, and 188 K for a 5 dB fade level.

The noise temperature introduced by rain will add directly to the receiver system noise figure, and will degrade the overall performance of the link. The noise power increase occurs coincident with the signal power decrease due to the rain fade; both effects are additive and contribute to the reduction in link carrier to noise ratio.

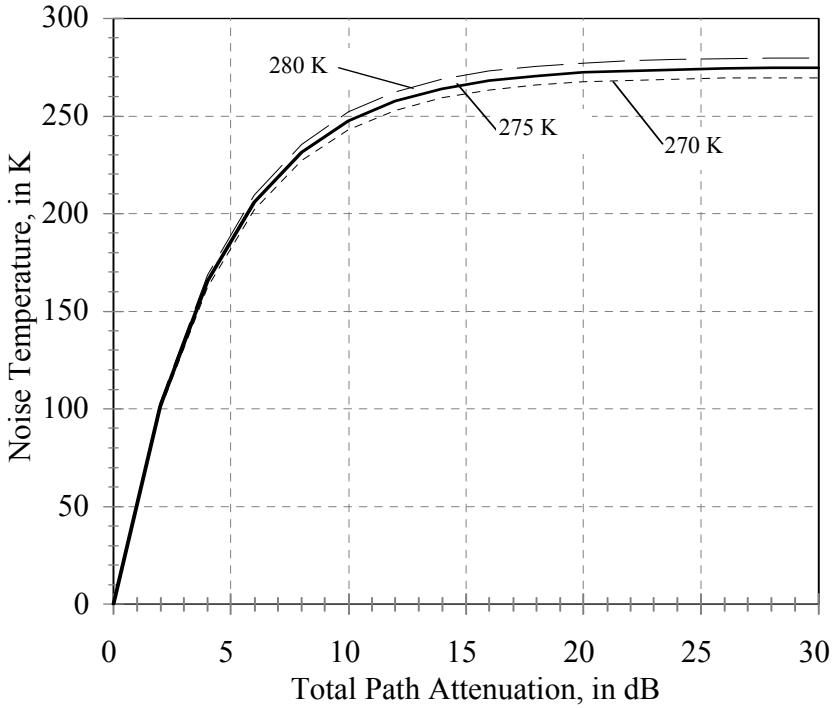


Exhibit 2.3.3-1
Noise Temperature as a function of Total Path Attenuation, for
Mean Path Temperatures of 270, 275, and 280 K.

### 2.3.4 Sky Noise Due to Clouds

Sky noise from clouds can be determined from radiative transfer approximations in much the same way as given in the previous section for sky noise from rain. The temperature and cloud absorption coefficient variations along the path must be defined, and Equations 2.3.1-1 through 2.3.1-4 can be applied.

Slobin (1982) provided calculations of cloud attenuation and cloud noise temperature for several locations in the United States, using radiative transfer methods and a four layer cloud model. Details of the Slobin model, including characteristics of cloud types and the calculation procedure, are described in Section 2.2.2.3. Exhibit 2.3.4-1 summarizes the zenith ($90^o$ elevation angle) sky noise temperature as calculated by Slobin for several frequencies of interest. Cloud temperatures for other elevation angles can be estimated from

$$t_\theta = \frac{t_z}{\sin\theta} \qquad 90 \le \theta \le 10 \text{ degrees} \tag{2.3.4-1}$$

where $t_z$ is the zenith angle cloud temperature, and $t_\theta$ is the cloud temperature at the path elevation angle $\theta$.

| Frequency (GHz) | Light Thin Cloud | Light Cloud | Medium Cloud | Heavy Clouds I | Heavy Clouds II | Very Heavy Clouds I | Very Heavy Clouds II |
|---|---|---|---|---|---|---|---|
| 6 / 4 | $< 6^o$ | $< 6^o$ | $< 13^o$ | $< 13^o$ | $< 13^o$ | $< 19^o$ | $< 19^o$ |
| 14 / 12 | 6 | 10 | 13 | 19 | 28 | 36 | 52 |
| 17 | 13 | 14 | 19 | 28 | 42 | 58 | 77 |
| 20 | 16 | 19 | 25 | 36 | 52 | 77 | 95 |
| 30 | 19 | 25 | 30 | 56 | 92 | 130 | 166 |
| 42 | 42 | 52 | 68 | 107 | 155 | 201 | 235 |
| 50 | 81 | 99 | 117 | 156 | 204 | 239 | 261 |

Exhibit 2.3.4-1
Sky Temperature from Clouds at Zenith ($90^o$ Elevation Angle)
*[Source: Ippolito(1986)]*

Slobin also developed annual cumulative distributions of zenith cloud sky temperature for specified cloud regions at fifteen frequencies from 8.5 to 90 GHz. Slobin divided the U.S. into fifteen regions of statistically "consistent" clouds (see Exhibit 2.2.2.3-3). The region boundaries are highly stylized and should be interpreted liberally. Some boundaries coincide with major mountain ranges (Cascades, Rockies, and Sierra Nevada), and similarities may be noted between the cloud regions and the rain rate regions of the Global Model. Each cloud region is characterized by observations at a particular National Weather Service observation station. The locations of the observation sites are shown with their three-letter identifiers on the map. For each of these stations, an "average year" was selected on the basis of rainfall measurements. The "average year" was taken to be the one in which the year's monthly rainfall distribution best matched the 30-year average monthly distribution. Hourly surface observations for the "average year" for each station were used to derive cumulative distributions of zenith attenuation and noise temperature due to oxygen, water vapor, and clouds.

Exhibit 2.3.4-2, a through d, shows examples of zenith sky temperature cumulative distributions for four of the Slobin cloud regions; Denver, New York, Miami, and Oakland, at frequencies of 10, 18, 32, 44, and 90 GHz. Plots for all fifteen cloud regions are available in Slobin (1982).

The distributions give the percent of the time the noise temperature is the given value or less. For example, at Denver, the noise temperature was 12 K or less for 0.5 (50 %) of the time at 32 GHz. Values of noise temperature in the distribution range 0 to 0.5 (0 to 50 %) may be regarded as the range of clear sky conditions. The value of noise temperature at 0 % is the lowest value observed for the test year.

Sky temperature values can be approximated from cloud attenuation values by application of Equation (2.3.1-3) with $t_m$, the mean path temperature for clouds, set to 280 K.

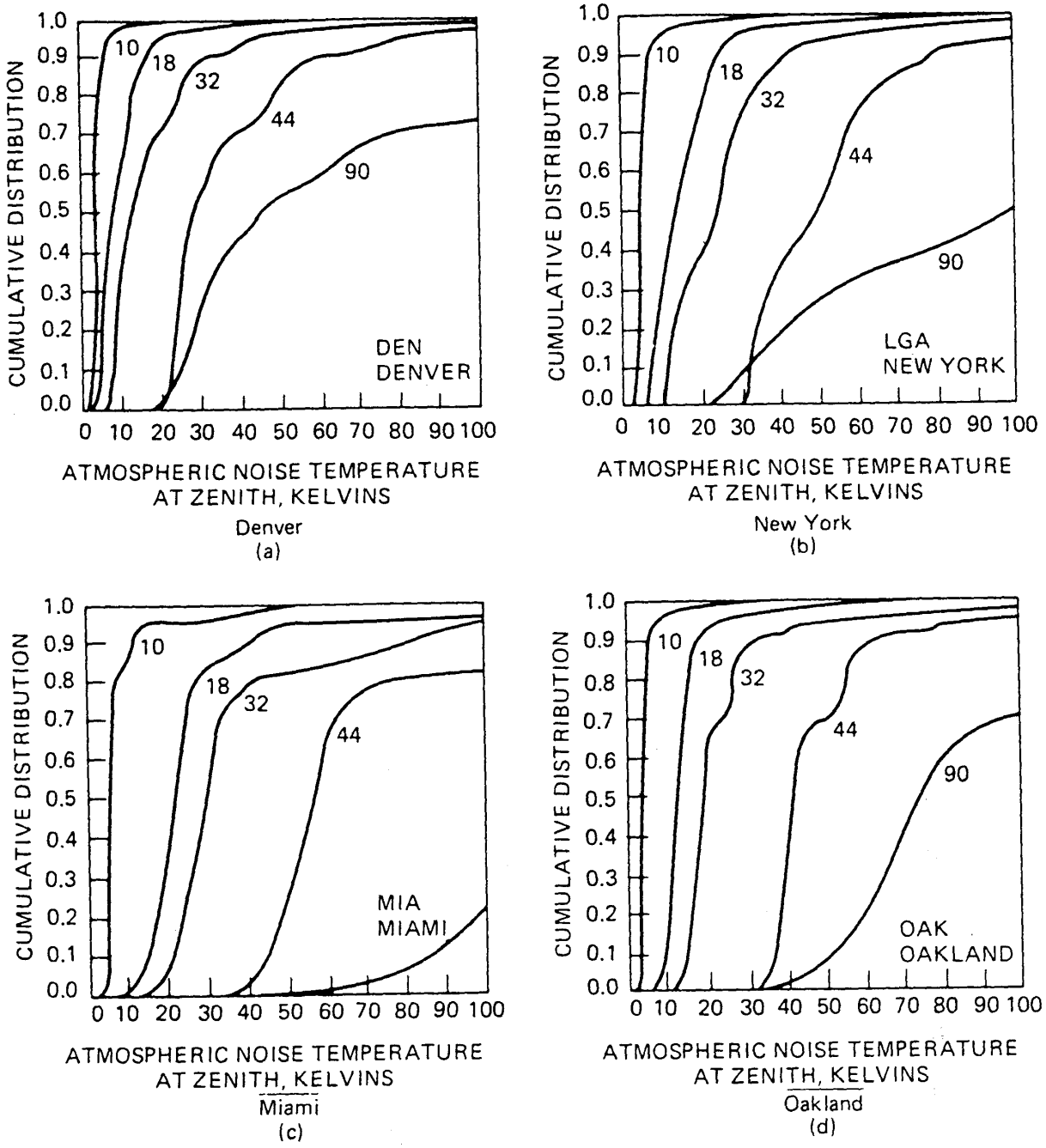


Exhibit 2.3.4-2
Cumulative Distributions of Zenith Sky Temperature for Four Locations,
From the Slobin Cloud Model
*[Source: Ippolito (1986)]*

### 2.3.5 Noise From Extra-Terrestrial Sources

Sky noise from sources outside the earth can be present for both uplinks and downlinks, and will depend to a large extent on the included angle of the source and the frequency of operation. The brightness temperature range for the common extra-terrestrial noise sources in the frequency range 0.1 to 100 GHz is shown in Exhibit 2.3.5-1.

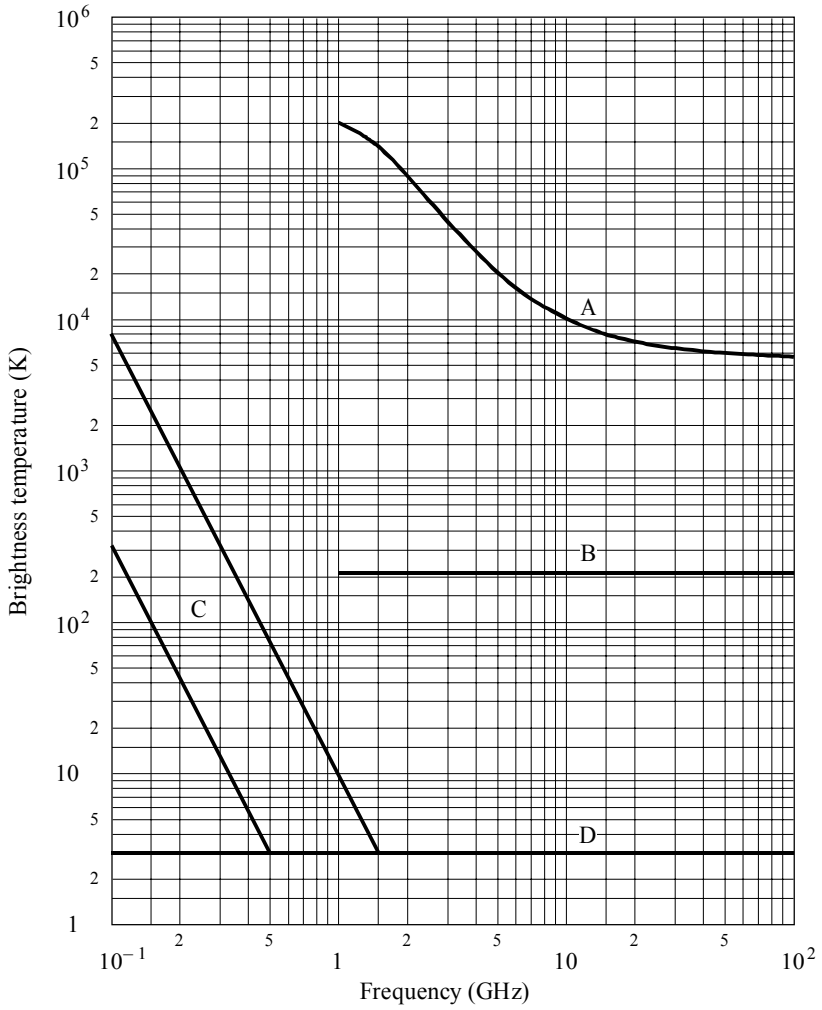


Exhibit 2.3.5-1
Extraterrestrial Noise Sources
*[Source: ITU-R Rec. PI.372-6 (1994)]*

Above 2 GHz, one need consider only the Sun, the Moon, and a few very strong non-thermal sources such as Cassiopeia A, Cygnus A and X and the Crab nebula. The cosmic background contributes only 2.7 K and the Milky Way appears as a narrow zone of somewhat enhanced intensity.

### 2.3.5.1 Cosmic Background Noise

Consider first the background noise in the general sky. Exhibit 2.3.5-1 shows that at low frequencies, galactic background noise will be a present, dropping off quickly with frequency up to about 2 GHz.

For communications below 2 GHz, only the Sun and the galaxy (the Milky Way), which appears as a broad belt of strong emission, are of concern. For frequencies up to about 100 MHz, the median noise figure for galactic noise, neglecting ionospheric shielding, is given by:

$$NF_m = 52 - 23 \log f \qquad (2.3.5.1\text{-}1)$$

where f is the frequency in MHz

Plots of sky temperature for the Milky Way are provided in Exhibits 2.3.5.1-1 and 2.3.5.1-2. The plots give the total radio sky temperature at 408 MHz smoothed to 5° angular resolution. The displays are given in equatorial coordinates, declination δ (latitude) and right ascension α (hours eastward around equator from vernal equinox).

The regions displayed in each plot are:

| | Right Ascension α | Declination δ |
|---|---|---|
| Exhibit 2.3.5.1-1 | 0000 h to 1200 h | $0^o$ to $+90^o$ |
| Exhibit 2.3.5.1-2 | 0000 h to 1200 h | $0^o$ to $-90^o$ |

The contours are directly in K above 2.7 K. The accuracy is 1 K. The contour intervals are:

- 2 K below 60 K,
- 4 K from 60 K to 100 K,
- 10 K from 100 K to 200 K,
- 20 K above 200 K.

Arrows on unlabelled contour lines point clockwise around a minimum in the brightness distribution. The dashed sinusoidal curve between ± 23.5° defines the ecliptic that crosses the Milky Way close to the galactic center. The strongest point sources are indicated by narrow peaks of the temperature distribution, while weaker sources are less apparent owing to the limited angular resolution.

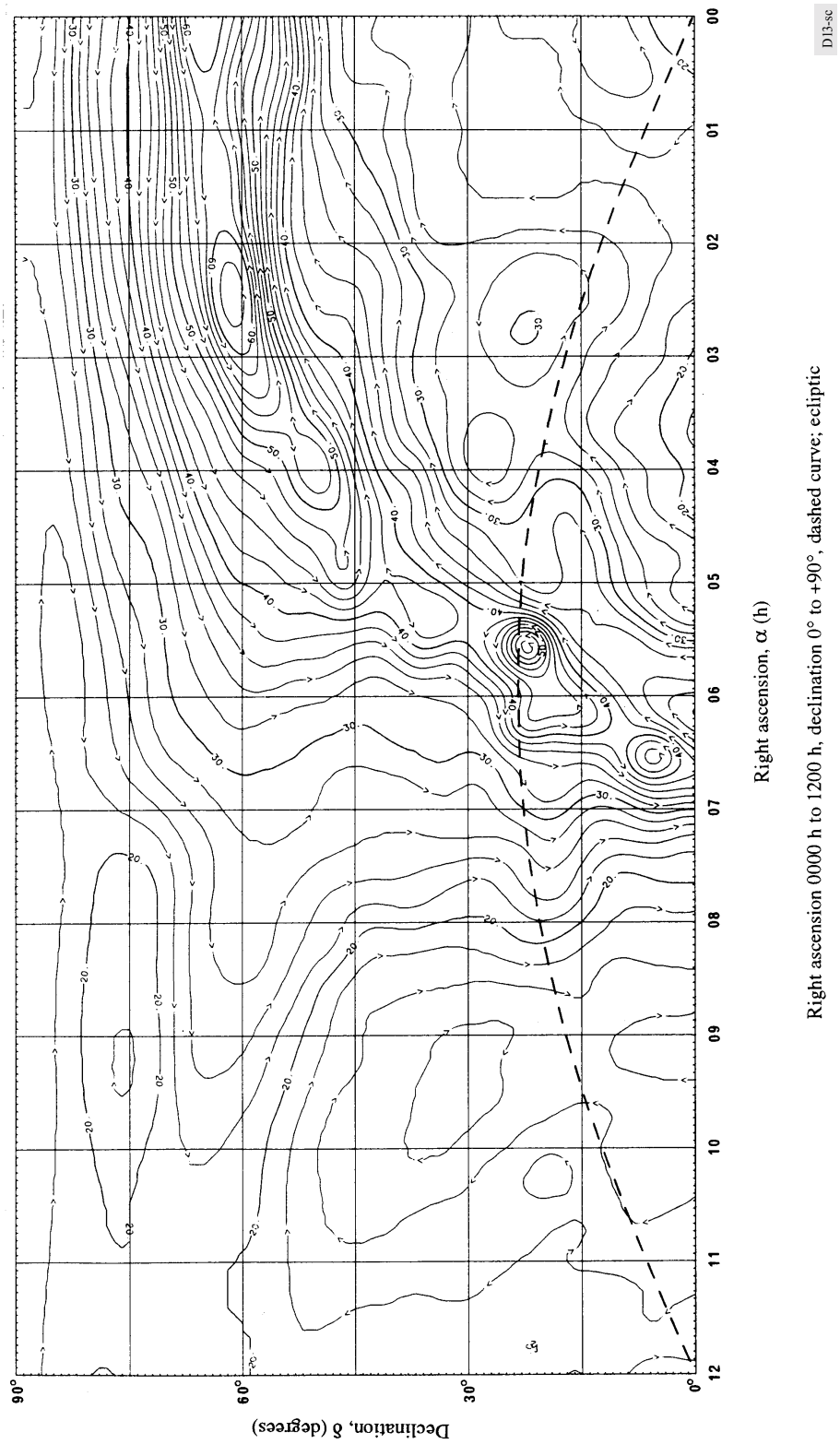


Exhibit 2.3.5.1-1 Radio Sky Temperature at 408 MHz
*[Source: ITU-R PI.372-6 (1994)]*

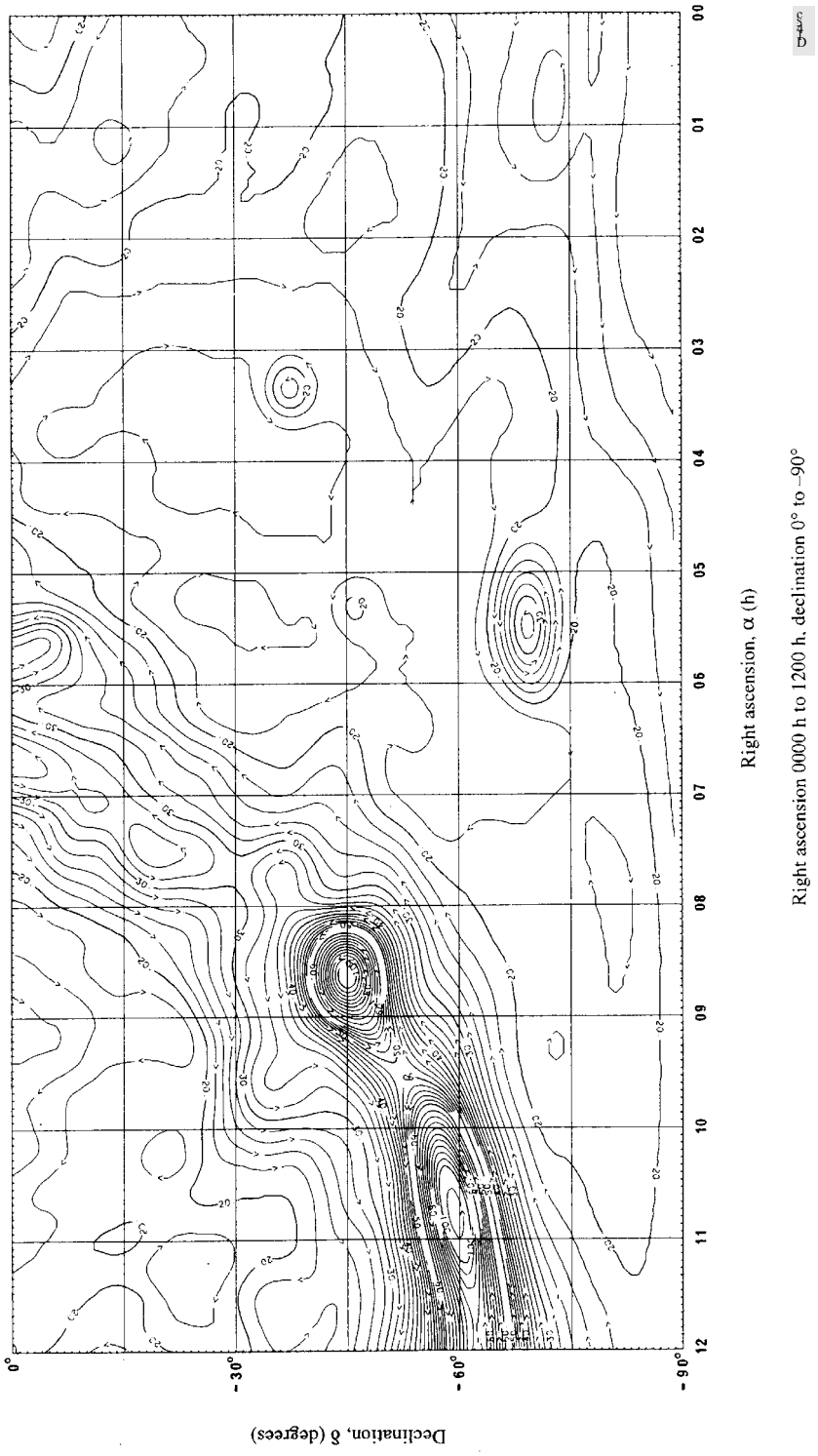


Exhibit 2.3.5.1-2 Radio Sky Temperature at 408 MHz
*[Source: ITU-R PI.372-6 (1994)]*

A early mapping of cosmic background by Ko and Kraus (1957) provided contour maps of the radio sky for galactic and stellar sources. Exhibit 2.3.5.1-3 shows a plot of the radio sky at 250 MHz in equatorial coordinates (declination versus right ascension). A geostationary satellite as seen from the Earth appears as a horizontal line of fixed declination between $+8.7^o$ and $-8.7^o$ , shown by the shaded band on the figure.

The contours of Exhibit 2.3.5.1-3 are in units of 6 K above 80 K, the values corresponding to the coldest parts of the sky. For example, at 1800 h and $0^o$ declination, the contour value is 37. The brightness temperature at 250 MHz is then 6 x 37 + 80 = 302 K. The brightness temperature for another frequency, $f_i$, is found from

$$t_b(f_i) = t_b(f_o)\left(\frac{f_i}{f_o}\right)^{-2.75} + 2.7 \qquad (2.3.5.1\text{-}2)$$

For example, the brightness temperature at 1 GHz can be determined from the value of at 250 MHz from:

$$t_b(1\,\text{GHz}) = 302\left(\frac{1}{.25}\right)^{-2.75} + 2.7 = 9.4\,\text{K}$$

At 4 GHz:

$$t_b(4\,\text{GHz}) = 302\left(\frac{4}{.25}\right)^{-2.75} + 2.7 = 2.8\,\text{K}$$

Several relatively strong non-thermal sources, such as Cassiopeia A, Cygnus A and X, and the Crab Nebula are shown on the figure (marked A through D). They are not in the zone of observation for geostationary satellites, and would only be in view for non-geostationary orbits for a very small segment of time.

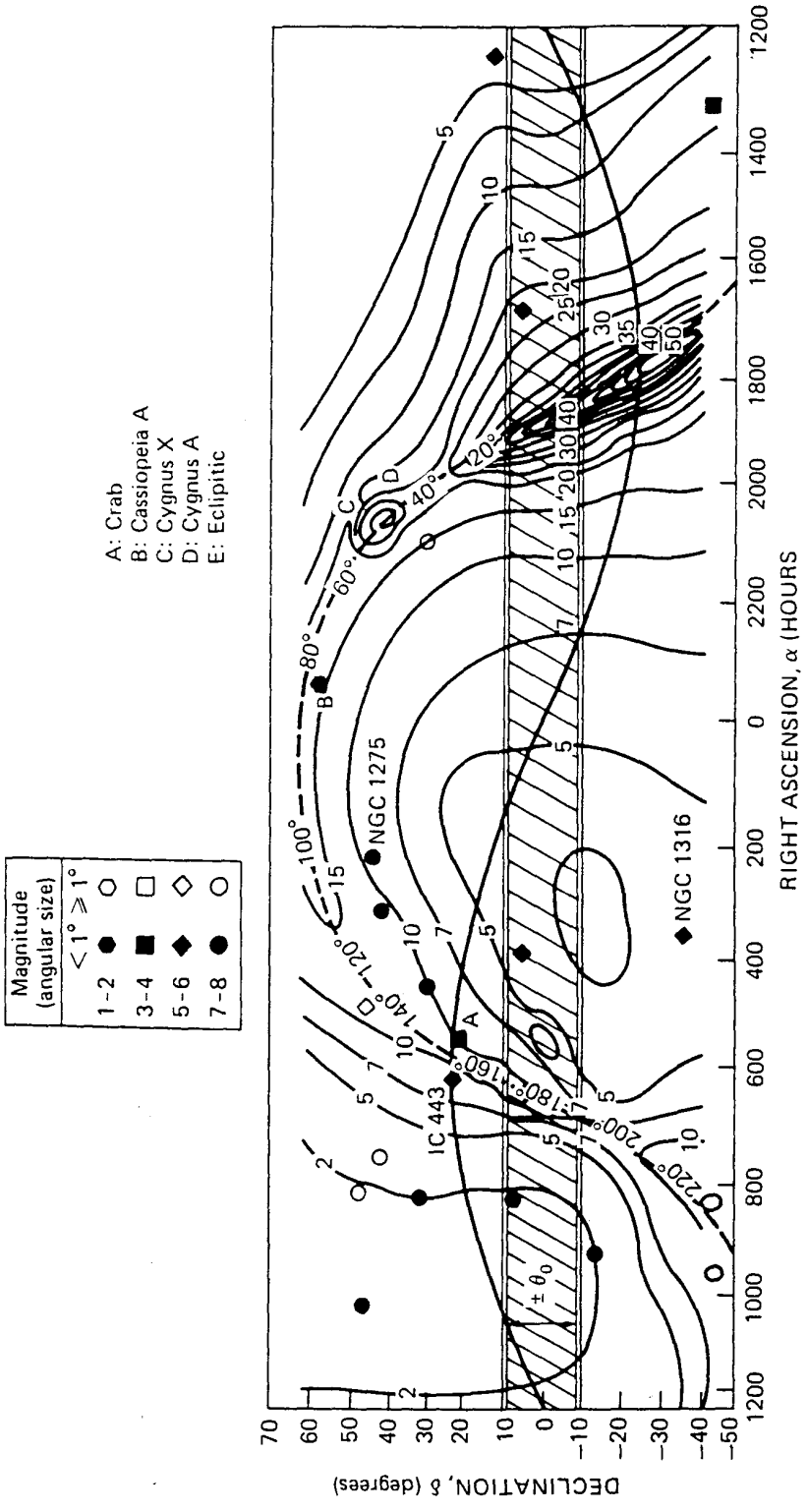


Exhibit 2.3.5.1-3
The radio sky at 250 MHz in the region around the geostationary orbital arc
[Source: Ko & Krouse (1957)]

### 2.3.5.2 Solar Noise

The sun generates very high noise levels and will contribute significant noise when it is collinear with the Earth station-satellite path. For geostationary satellites, this occurs near the equinoxes, for a short period each day. The power flux density generated by the sun is given as a function of frequency in Exhibit 2.3.5.2-1 (Perlman, et al, 1960). Above about 30 GHz the sun noise temperature is practically constant at 6000 K (Kraus, 1986).

The presence of solar noise can be quantitatively represented as an equivalent increase in the antenna noise temperature by an amount $t_{sun}$. $t_{sun}$ depends on the relative magnitude of the receiver antenna beamwidth compared with the apparent diameter of the sun ($0.48^o$), and how close the sun approaches the antenna boresight. The following formula, after Baars (1973), gives an estimate of $t_{sun}$ (in degrees K) when the sun, or another extraterrestrial noise source, is centered in the beam.

$$t_{sun} = \frac{1 - e^{-\left(\frac{\delta}{1.2\theta}\right)^2}}{f^2\delta^2} \log^{-1}\left(\frac{S+250}{10}\right) \qquad (2.3.5.2\text{-}1)$$

where

$\delta$ = apparent diameter of the sun, deg
$f$ = frequency, GHz
$S$ = power flux density, dBw/Hz-m$^2$
$\theta$ = antenna half-power beamwidth, deg

For an Earth station operating at 20 GHz with a 2 meter diameter antenna (beamwidth about $0.5^o$), the maximum increase in antenna temperature that would be caused by a quiet sun transit is found to be about 8100 K.

The sun's flux has been used extensively for measuring tropospheric attenuation. This is done with a sun-tracking radiometer, which monitors the noise temperature of an antenna that is devised to automatically remain pointed at the sun.

### 2.3.5.3 Lunar Noise

The moon reflects solar radio energy back to the Earth. Its apparent size is approximately 0.5 degrees in diameter, similar to the sun angle. The noise power flux density from the moon varies directly as the square of frequency, which is characteristic of radiation from a "black body." The power flux density from the full moon is about -202 dBW/Hz-m$^2$ at 20 GHz. The maximum antenna temperature increase due to the moon, for the 20 GHz 2m antenna considered in the previous section, would be 320 K. The phase of the moon and the ellipticity of its orbit cause the

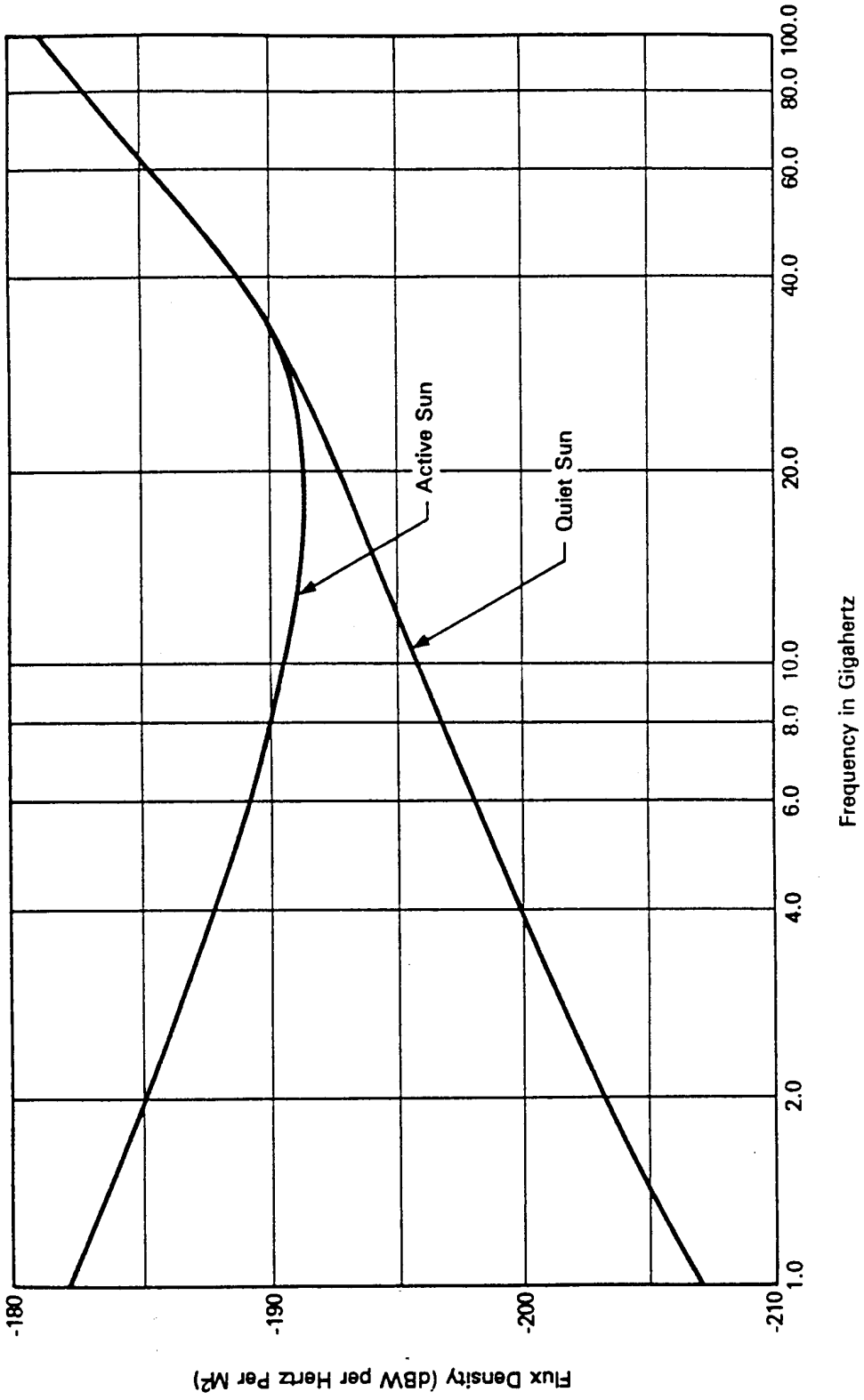


Exhibit 2.3.5.2-1 Power Flux Density for Quiet and Active Sun
*[Source: Perlman, et al (1960)]*

apparent size and flux to vary widely, but in a regular and predictable manner. The moon has been used to measure Earth station antenna characteristics (Johannsen and Koury, 1974).

### 2.3.5.4 Radio Stars

The strongest radio stars are ten times weaker than the lunar emission. The strongest stars (Wait, et al, 1974) emit typically -230 dBW/Hz-$m^2$ in the 10 to 100 GHz frequency range. Three of these strong sources are Cassiopeia A, Taurus A and Orion A. These sources are often utilized for calibration of ground station antenna G/T. During the calibrations the attenuation due to the troposphere is usually cancelled out by comparing the sky noise on the star and subtracting the adjacent (dark) sky noise.

## 2.4 GENERAL MODELING PROCEDURES

This section presents a number of modeling procedures and considerations that do not fit directly into the previous sections, but are important to a full evaluation of atmospheric effects on satellite links. The importance of obtaining useful data is discussed and reasonable criteria for determining the usefulness of a data set are presented. General modeling procedures for frequency scaling, predicting the statistical attenuation ratio, elevation angle scaling, altitude scaling, polarization scaling, and latitude correction are provided.

### 2.4.1 Application of Statistical Data to Link Prediction and Modeling

Statistical distributions of data are often used to evaluate or validate prediction models, or used directly to make predictions for a link budget. Scaling techniques may be used on a given data set to make link budget predictions. When using data for these purposes, the data must comply with certain standards in order for the techniques to be valid. This section on data describes guidelines for determining if it is valid to apply these methods to a given distribution of data. Additionally, some sources of data are discussed.

#### 2.4.1.1 Statistical Distributions of Attenuation from Data

Statistical distributions of data are categorized and modeled by the effect causing the attenuation. In propagation effects evaluations, three letter acronyms are often used to describe these distributions. The most important distributions (ACA, AFS, and ARD) are described in this section.

##### 2.4.1.1.1 Attenuation with Respect to Free Space (AFS)

The attenuation with respect to free space, AFS, is the usual designation for attenuation due to ALL attenuation (signal level loss) effects produced by the atmosphere (other than free space path loss). These effects could include one or more of the following:

- gaseous absorption
- rain attenuation
- cloud attenuation
- fog attenuation
- scintillation

Measurements made on a satellite link with a continuous beacon provide a direct measure of AFS. Consider a slant path link which is monitoring the signal level from a satellite beacon at a frequency f. The signal level measured at the receiver, S, will be

$$S = AFS + L_{FS} \qquad (dB) \qquad (2.4.1.1\text{-}1)$$

where $L_{FS}$ is the free space loss,

$$L_{FS} = 20\log\left(\frac{4\pi r}{\lambda}\right) \qquad (2.4.1.1\text{-}2)$$

and r is the range, $\lambda$ is the wavelength.

If the range and wavelength is specified in meters, and the frequency specified in GHz,

$$L_{FS} = 20\log f + 20\log r + 32.5 \qquad dB \qquad (2.4.1.1\text{-}3)$$

AFS is a useful parameter to evaluate the total attenuation effects on a space link, but it is difficult to apply directly to the prediction and modeling of propagation effects since all effects are present and it is usually not possible to separate out the individual components of the attenuation.

#### 2.4.1.1.2 Attenuation with Respect to Clear Air (ACA)

The attenuation with respect to clear air, ACA, is the attenuation with respect to free space, AFS, less the attenuation due to gaseous absorption, AGA.

$$ACA = AFS - AGA. \qquad (2.4.1.1\text{-}4)$$

ACA is usually determined from beacon measurements by estimating AGA from radiometric measurements and subtracting it from the measured (AFS) value. The quantity ACA does not include effects due to clouds and scintillation. Rain attenuation is the most severe effect and ACA is typically compared directly to rain attenuation models.

#### 2.4.1.1.3 Radiometer Derived Attenuation (ARD)

Propagation measurement programs often employ total power radiometers to find the absolute reference level of the beacon signals. Two recent examples are the ACTS and the OLYMPUS measurement campaigns. The radiometers are used to remove diurnal variations and can be used to predict path attenuation within limitations.

The radiometer measures the sky background temperature at a given frequency. The measurement can be used to calculate the atmospheric gaseous attenuation (AGA). This is accomplished by assuming that the sky background temperature is about 110 K during clear sky conditions. The

calculated rain-gas threshold attenuation, AT, is then 2.17 dB. Then the atmospheric gaseous attenuation is given by:

$$AGA = \begin{cases} ARD & \text{for} \quad ARD < AT \\ AT & \text{for} \quad ARD > AT \end{cases} \qquad (2.4.1.1\text{-}5)$$

### 2.4.1.2 Criteria for Determining the Applicability of Data

Propagation data sets giving the statistical distributions for ACA may be used to predict losses due to rain for a link budget, scaled or compared to rain models. When a data set is going to be used for any of these purposes, the data should meet certain criteria.

1) The attenuation data should be collected at the location of interest, or at a site with similar statistical rain rate distributions. This is important since the rain rate can vary widely from site to site. There are two sets of maps available which divide the earth into rain regions. The maps can be used to estimate the rain rate when the information is not otherwise available (see section 2.2.4).

2) Typically, rain attenuation models predict attenuation for availabilities specified as a percentage of an average year. It is generally accepted that ten years of statistical data are necessary to include year to year weather variations, thus the rain models are expected to be accurate when compared to ten years of data. Since the duration of most propagation experiment campaigns is much less than ten years, annual data sets are often used instead. The models appear to be reasonably accurate for considerably less data, as long as the data set contains data for at least 85% of a full year. If the data set contains more than one year, it must contain data for at least 85% of the last year. A statistical distribution for rain attenuation calculated for less than 85% of a full year may be missing part or all of the rainy season. This will cause the distribution to seriously under predict the attenuation at a given availability. If the data set is missing part of a dry season, the attenuation is over predicted by the statistical distribution of the data set.

3) The data set should be for the elevation angle of interest. If the data was collected at a different elevation angle, then an elevation angle correction can be computed via the methods described in section 2.4.3.

4) The data set should be for the correct signal polarization. If the data was collected at a different polarization, then the polarization can be corrected via the methods described in section 2.4.4.2.

5) The data should be collected at a latitude and altitude close to the one of interest. If the data was collected at another location within the same rain region, then a correction factor can be calculated via the method described in section 2.4.4.1.

6) The attenuation data should be for the correct frequency. If the attenuation data is for the correct frequency and meets all of the other criteria, then the attenuation for the necessary availability can be taken directly from the statistical distribution. However, even if the data is not for the correct frequency, the data can be scaled in frequency via the methods described in section 2.4.2.

When data is available, it is generally better to use frequency scaling of data instead of rain attenuation models to predict attenuation due to rain. The ITU frequency scaling method is recommended since the method is currently considered the most accurate, however several methods are described in section 2.4.2.

### 2.4.1.3 ITU Method for Error Calculation

When comparing statistical distributions of rain attenuation data to rain models, or frequency scaled data collected at another frequency, the error is generally computed via the ITU error calculation method (ITU-R Reccommendation P.618-5, 1997). The error at the availability ρ, error (ρ), is given by:

$$\text{error}(\rho) = \begin{cases} 100 \times \ln\left(\dfrac{A_p(\rho)}{A_m(\rho)}\right) \times \left(\dfrac{A_m(\rho)}{10}\right)^{0.2} & \text{for} \quad A_m \le 10\text{dB} \\ 100 \times \ln\left(\dfrac{A_p(\rho)}{A_m(\rho)}\right) & \text{for} \quad A_m > 10\text{dB} \end{cases} \tag{2.4.1.3-1}$$

where $A_p(\rho)$ is the predicted attenuation and $A_m(\rho)$ is the measured attenuation at the availability $\rho$ .

### 2.4.2 Frequency Scaling and Attenuation Ratio

While the statistical rain attenuation models (see section 2.2.4) are useful for predicting the loss due to rain for a given link budget calculation, there is no good substitute for actual data. The rain attenuation models are the best approach when investigating the dependence of attenuation statistics on elevation angle, polarization and rain rate. However, if reliable data measured at one frequency are available, the ITU-R recommends frequency scaling the data to predict attenuation at other frequencies.

If data are not available, or if various effects such as the elevation angle dependence are being considered, refer to section 2.2.4 for rain model implementation procedures. The rain attenuation models can also be compared to the data to check the reliability of the data set before frequency scaling is used. Large errors from these models may indicate error in the data set.

In the following sections, two types of attenuation scaling, statistical and instantaneous, are introduced. Eight statistical attenuation scaling methods in common use are described.

#### 2.4.2.1 Statistical Attenuation Scaling

This section describes frequency scaling models that can be used to scale the attenuation values of a given statistical distribution of data collected at one frequency to the attenuation values expected at another frequency. Two models are described. The models incorporate a transfer function between two attenuation values at different frequencies. This transfer function is called the Statistical Attenuation Ratio (ARS).

##### 2.4.2.1.1 Statistical Attenuation Ratio (ARS)

The statistical attenuation ratio (ARS) is defined as the ratio of the attenuation values from two statistical distributions. For example, ARS calculated from two ACA distributions is defined as:

$$\mathrm{ARS} = \frac{\mathrm{ACA}(f_U, p)}{\mathrm{ACA}(f_L, p)} \qquad (2.4.2.1\text{-}1)$$

where $f_L$ is the lower frequency, $f_U$ is the upper frequency and p probability of the of the ACA attenuation being scaled. Examples plots of the attenuation ratio calculated from ACA and AFS are given in Exhibits 2.4.2.1-1 and 2.4.2.1-2.

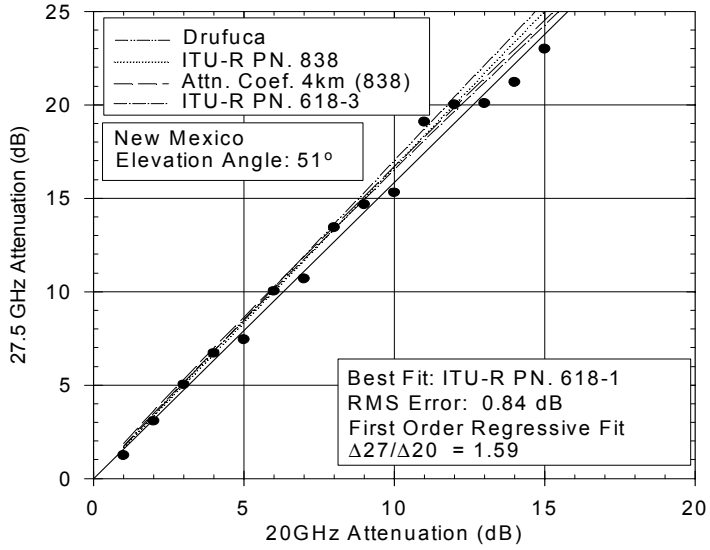


Exhibit 2.4.2.1-1. ARS plot calculated from two ACA distributions of ACTS data collected at 20.2 GHz and 27.5 GHz**.**

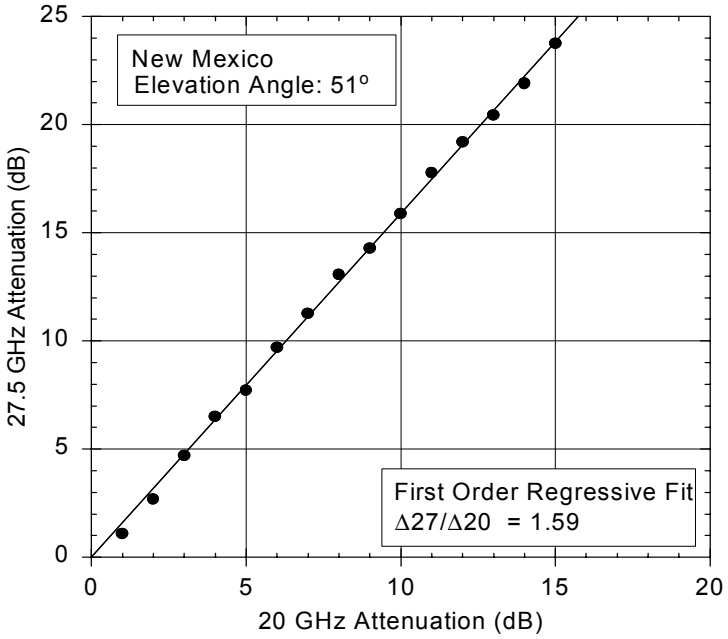


Exhibit 2.4.2.1-2. ARS plot calculated from two AFS Distributions of ACTS data collected at 20.2 GHz and 27.5 GHz

### 2.4.2.1.2 ITU-R Frequency Scaling Model

The current ITU frequency-scaling model is considered the most accurate method for predicting attenuation when it is applicable. The method is valid for the frequency range 7 to 50 GHz. This section describes the latest version of the ITU-R model, as presented in ITU-R Recommendation P.618-5 (1997). A step-by-step implementation procedure is provided.

1) Calculate the frequency dependent parameters $\varphi_1(f_1)$ and $\varphi_2(f_2)$ where $f_1$is the frequency of the data, $f_2$ is the desired frequency and $\varphi(f)$ is defined as follows:

$$\varphi(f) = \frac{f^2}{1+10^{-4} f^2} \qquad (2.4.2.1\text{-}2)$$

2) Calculate the perturbation factor $H(\varphi_1, \varphi_2, A_{p1})$ where $A_{p1}$ is the attenuation at the availability (p) of interest.

$$H(\varphi_1, \varphi_2, A_{p1}) = 1.12 \times 10^{-3} (\varphi_2/\varphi_1)^{0.5} (\varphi_1 A_{p1})^{0.55} \qquad (2.4.2.1\text{-}3)$$

3) Calculate the attenuation ratio $A_{p2} / A_{p1}$.

$$\frac{A_{p2}}{A_{p1}} = \left(\frac{\varphi_2}{\varphi_1}\right)^{1-H(\varphi_1,\varphi_2,A_1)} \qquad (2.4.2.1\text{-}4)$$

4) Calculate the attenuation $A_{p2}$ at the frequency of interest.

$$A_{p2} = A_{p1}\left(\frac{\varphi_2}{\varphi_1}\right)^{1-H(\varphi_1,\varphi_2,A_1)} \qquad (2.4.2.1\text{-}5)$$

### 2.4.2.1.3 Hodge Frequency Scaling Model

A scaling model developed by Hodge (1977) assumes that the rain rate along the path on a given link is a Gaussian function. A step-by-step implementation procedure is provided.

1) Formulate the instantaneous attenuation:

$$A = \int_0^L a\left[R_0 e^{-(x/l_0)^2}\right]^b dx \qquad (2.4.2.1\text{-}6)$$

where $R_o$ is the peak rain rate along the link path length L, $l_o >> L$ is a measure of the cellular rain structure and x is the distance measured from the maximum rain-rate intensity point.

2) The attenuation ratio is then calculated from:

$$\frac{A_2}{A_1} = \frac{k_2}{k_1}\sqrt{\frac{\alpha_1}{\alpha_2}}\left(\frac{A_1}{k_1}\sqrt{\frac{\alpha_1}{\pi}}\right)^{\left(\frac{\alpha_2}{\alpha_1}-1\right)} \qquad (2.4.2.1.-7)$$

where $\alpha_1$, $k_1$, $\alpha_2$, and $k_2$ are the attenuation coefficients calculated from the values found in Exhibit 2.2.4.1-5.

### 2.4.2.1.4 CCIR Frequency Scaling Model

The CCIR(now the ITU-R) in 1990 provided a frequency scaling method, which was replaced with the current ITU-R version, described in Section 2.4.2.1.2. The earlier version, found in CCIR report 721-3 (1990), is still in use, so it is included here for completeness.

A step-by-step procedure is provided.

1) Calculate the frequency dependent parameters $\varphi(f_L)$ and $\varphi(f_U)$ where $f_L$ is the frequency of the data, $f_U$ is the desired frequency and $\varphi(f_1)$ is defined as follows:

$$\varphi(f) = \frac{f^{1.72}}{1+3\times10^{-7}f^{3.44}} \qquad (2.4.2.1-8)$$

2) Calculate the attenuation ration ARS = $A_p(f_U)/ Ap(f_L)$

$$\mathrm{ARS} = \frac{A_P(f_U)}{A_P(f_L)} = \frac{\varphi(f_U)}{\varphi(f_L)} \qquad (2.4.2.1-9)$$

### 2.4.2.1.5 Simple Frequency Scaling Model

This model is a power law scaling model based on the assumption that the attenuation ratio is directly proportional to the ratio of the frequencies squared. Due to its simplicity, this method is very useful for making estimates.

1) Calculate the scaled attenuation $A_{p2}$ at the frequency of interest.

$$A_{p2} = A_{p1}\left(\frac{f_2}{f_1}\right)^2 \qquad (2.4.2.1-10)$$

The method is derived from the more general relationship:

$$A_{fu} = A_{fL}\left(\frac{f_U}{f_L}\right)^n \qquad (2.4.2.1-11)$$

Various values of n have been proposed for different frequency ranges. Ro (1973) and Drufuca (1974) proposed that n=1.72 for frequencies between 11.2 GHz and 18.7 GHz. Owalabi and Ajayi (1980) investigated specific attenuation for a Laws and Parson drop size distribution and found that the relationship hods over the 10-20 GHz range for n=2. They also noticed a trend of decreasing n with increasing rain rate.

### 2.4.2.1.6 Kheirallah Frequency Scaling Method

This model, first proposed by Kheirallah & Olsen (1982), is derived from the ITU-R rain attenuation model by assuming that the parameters L and r are the same at both frequencies so that:

$$\frac{A_1}{A_2} = \frac{\gamma_{R1} L_{s1} r_1}{\gamma_{R2} L_{s2} r_2} = \frac{\gamma_{R1}}{\gamma_{R2}} \tag{2.4.2.1-12}$$

where $\gamma$ is the specific attenuation (dB/km), R is the rain rate (mm/h), L (km) is the effective path length through the rain and k and $\alpha$ are tabulated parameters dependent on frequency and the drop size distribution (DSD). Then the specific attenuation is given by:

$$\gamma = kR_p^{\alpha} \tag{2.4.2.1-13}$$

and

$$\frac{A_1}{A_2} = \frac{\gamma_{R1}}{\gamma_{R2}} = \frac{k_1 R_p^{\alpha_1}}{k_2 R_p^{\alpha_2}} \tag{2.4.2.1-14}$$

By making some approximations, Kheirallah & Olsen concluded that:

$$A_2 \approx k_2 \left( \frac{A_1}{k_1} \right)^{\alpha_2/\alpha_1} \tag{2.4.2.1-15}$$

### 2.4.2.1.7 Battesti Frequency Scaling Method for Terrestrial Links

This method, proposed by Battesti (1981) suggests that, for terrestrial links, the attenuation is proportional to a linear function of the frequency. The method was obtained by examining the specific attenuation for spatially uniform rain events with a typical drop size distribution (DSD). His study resulted in the following relationship:

$$ARS = \frac{A(f_U)}{A(f_L)} = \begin{cases} \dfrac{f_U - 6}{f_L - 6} & \text{for} \quad f_L, f_U \le 20 \text{ GHz} \\ \dfrac{f_U - 10}{f_L - 10} & \text{for} \quad f_L, f_U > 20 \text{ GHz} \\ 1.4\left(\dfrac{f_U - 10}{f_L - 6}\right) & \text{for} \quad f_L < 20 \text{ GHz}, f_U > 20 \text{ GHz} \end{cases} \qquad (2.4.2.1\text{-}16)$$

#### 2.4.2.1.8 Rue Frequency Scaling Model

The Rue (1980) model stems from a simplification of the Misme-Fimbel (1975) rain attenuation model. A step-by-step implementation procedure is provided.

1) Determine the portion of the slant path length through a cylindrical rain cell with a diameter of 3.0 km:

$$D = \begin{cases} L_{3km} & \text{for} \quad L < 27 \\ 27 & \text{for} \quad L \ge 27 \end{cases} \qquad (2.4.2.1\text{-}17)$$

2) Then the attenuation is calculated from:

$$A_2 = k_2 5^{\alpha_2} D + 3k_2 \left(\frac{A_1 - k_1 5^{\alpha_1} D}{3k_1}\right)^{\alpha_2/\alpha_1} \qquad (2.4.2.1\text{-}18)$$

where $\alpha_1$, $k_1$, $\alpha_2$, and $k_2$ are the attenuation coefficients calculated from the values found in Exhibit 2.2.4.1-5.

The Misme-Fimbel model, a model most applicable for high rain rates of ≥ 20mm/h, is based on a log-normal approximation to the cumulative rain rate distribution. The model assumes that a rain cell is a compact core of constant rain rate surrounded by a much larger area of light residual rain. Rue's model is a simplification of this model in which the residual rain rate is assumed to be 5mm/h, and the cylindrical rain core is assumed to be 3.0 km in diameter (hence the numeric values 5 and 3 appear in equation 2.4.2.1-18).

### 2.4.2.1.9 Examples: Frequency Scaling Model Comparison

This section gives an example of statistical attenuation scaling using the ACTS Las Cruces, NM data (Pinder, et al, 1997). Exhibit 2.4.2.1-3 compares ARS values calculated from each model, to ARS values calculated from the ACTS data. Plot illustrates that the ITU-R model best predicts ARS. The Simple model is the worst predictor. All of the models over predict ARS.

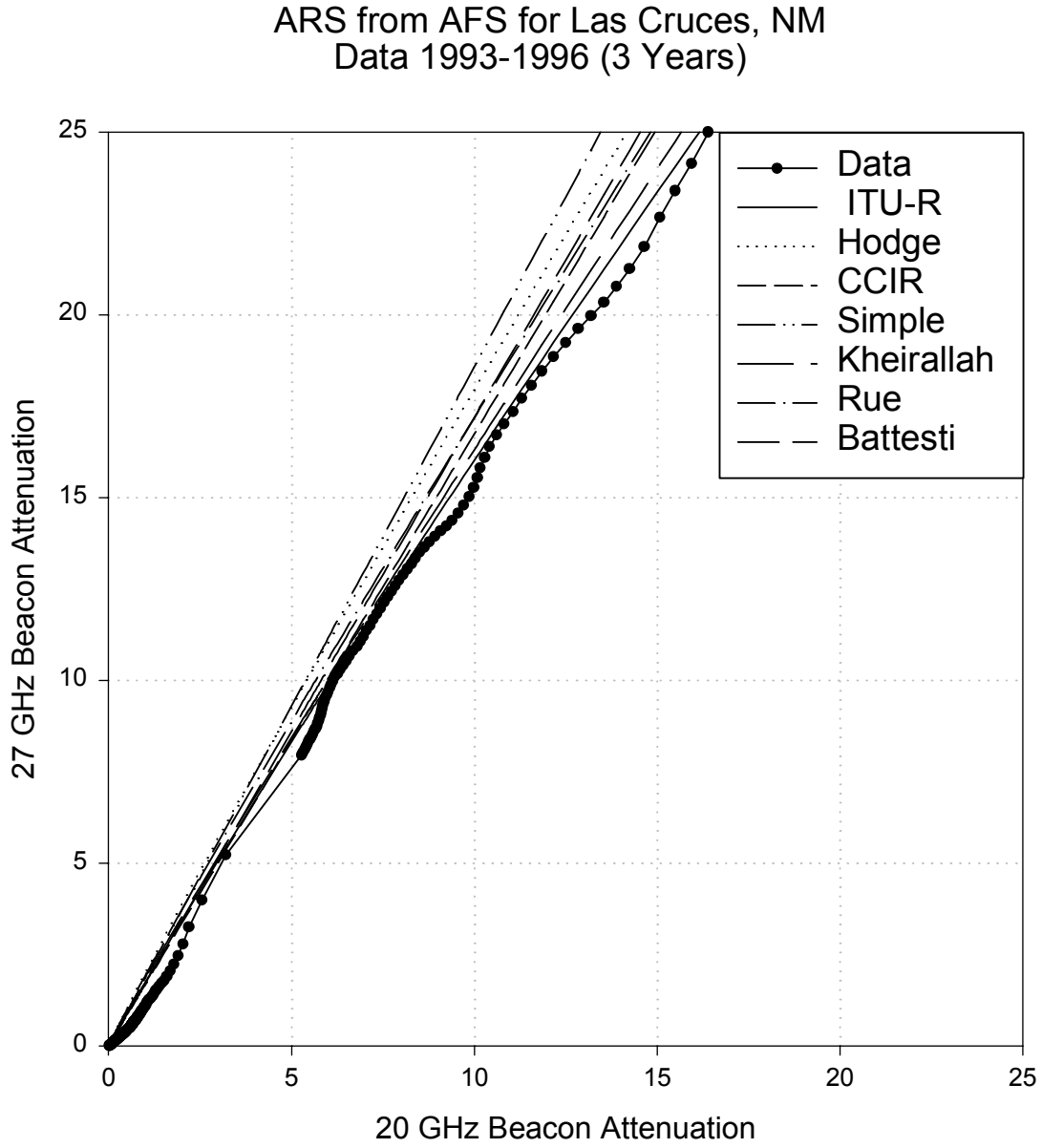


Exhibit 2.4.2.1-3: Comparison of ARS predicted by models to ARS calculated from ACTS Las Cruces, NM data.

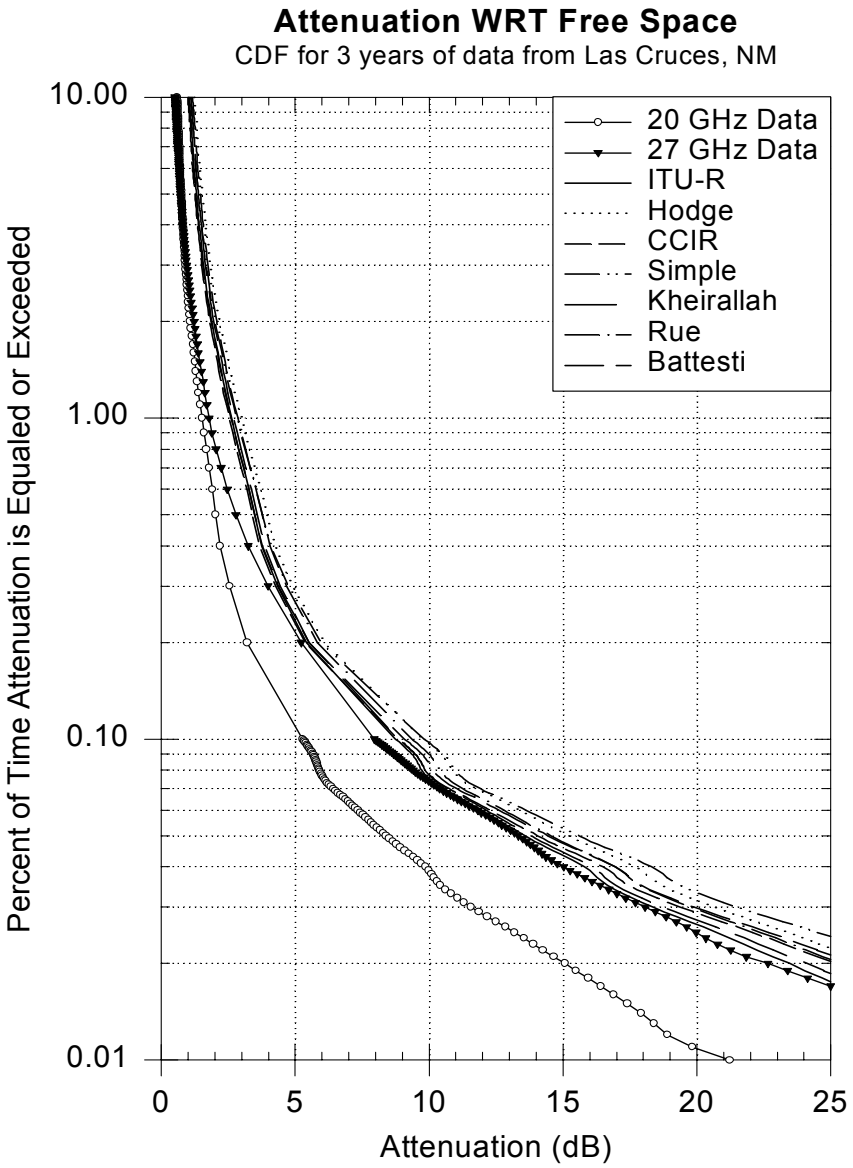


Exhibit 2.4.2.1-4: Comparison of AFS predicted by models to AFS calculated from ACTS data

Exhibit 2.4.2.1-4 compares the scaled statistical distributions for each model to the 27 GHz ACTS data for Las Cruces, NM. The models were used to scale the 20 GHz data to 27 GHz. The plot illustrates that the scaled distributions over predicted the 27 GHz data. The data is best predicted by the ITU-R model, which falls within 1.5 dB of the actual data, even at high attenuation levels where models tend to have the greatest error. By comparison, the Simple model, having the largest error for the actual data, over predicts the data by 4-5 dB, for attenuation levels between 15 and 25 dB.

### 2.4.2.2 Instantaneous Attenuation Scaling

The instantaneous attenuation ratio (RA) is the ratio of attenuation $A(f_U)$ measured at a frequency $f_U$ to the attenuation $A(f_L)$ measured at some lower frequency $f_L$.

$$RA = \frac{A(f_U)}{A(f_L)} \qquad (2.4.2.2\text{-}1)$$

To date, no models have been proposed to predict RA. Calculations of RA preformed by Laster and Stutzman (1993) using OLYMPUS data show that RA varies rapidly as a function of time. Thus, any RA model must quantify these fluctuations statistically by necessity.

## 2.4.3 Elevation Angle Scaling

The amount of attenuation in a given communications path through the atmosphere is highly dependent of the elevation angle. The primary effect of elevation angle on attenuation is that it changes the path length through the medium causing the attenuation. The following sections describe models that may be used to scale attenuation data collected at one elevation angle to estimate the attenuation at another elevation angle.

### 2.4.3.1 Elevation Angle Scaling to Zenith for AGA

The primary effect of elevation angle on attenuation is that it changes the path length through the medium causing the attenuation. During clear air, the attenuation is due to gaseous absorption and scintillation. Scintillation effects are small for elevation angles greater than 10°. Since the atmosphere is modeled as homogenous spherical layers, made up of various constituents, AGA measured at elevation angle $\theta_1$ can be scaled to estimate the AGA at a different elevation angle $\theta_2$ without considering dependencies on frequency, latitude, or other variables. The procedure for scaling AGA measured at $\theta_1$ to an estimated AGA at 90° was defined in CCIR Report 719-1, 1982. Given the attenuation measured at $\theta_1$, the attenuation at 90°, is estimated by:

$$A_{90^\circ} = A_{\theta 1} \ \operatorname{cosec} \theta_1 \qquad (2.4.3.1\text{-}1)$$

### 2.4.3.2 Independent Elevation Angle Scaling for ACA

Data collected at an elevation angle θ can be scaled to other elevation angles. The following technique was used with reasonably accurate results to compare attenuation measurements collected at the same frequency but different elevation angles at Virginia Tech. The method can be derived from the ITU-R rain attenuation model by assuming the precipitation to be horizontally stratified in the region of the elevation angle variations. For elevation angles greater than 10°, the attenuation measured at elevation angle $\theta_1$ is scaled to elevation angle $\theta_2$ from the relationship:

$$\frac{A(\theta_1)}{A(\theta_2)} = \frac{\sin\theta_2}{\sin\theta_1} \qquad (2.4.3.2\text{-}1)$$

The attenuation is assumed to be for the same location, frequency and polarization.

Exhibits 2.4.3.2-1 and 2.4.3.2-2 give the statistical distributions of two data sets collected at different elevation angles in the late seventies. The data scaled from 21° under predicts the attenuation at 41°. The discrepancy is due to differences in the rain rate for each year and polarization angle. The data at 21° was collected during a high rain rate year. Scaling from a lower elevation angle to a higher angle under predicts the attenuation. Scaling from a high elevation angle to a lower angle under predicts the attenuation.

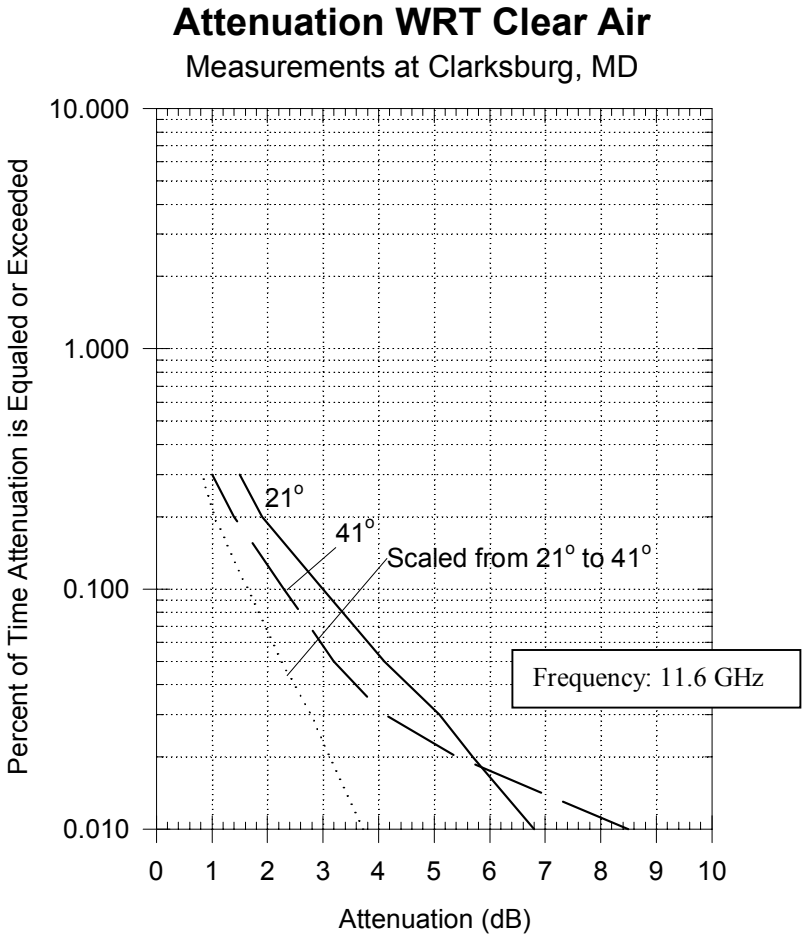


Note: The $21^0$ data was collected in CY 1977 with a maximum rain rate of 92.1 mm/h
The $41^0$ data was collected in CY 1978 with a maximum rain rate of 65.0 mm/h.

Exhibit 2.4.3.2-1
Evaluation of Elevation Angle Scaling
using 11.6 GHz data collected at Clarksburg, MD.

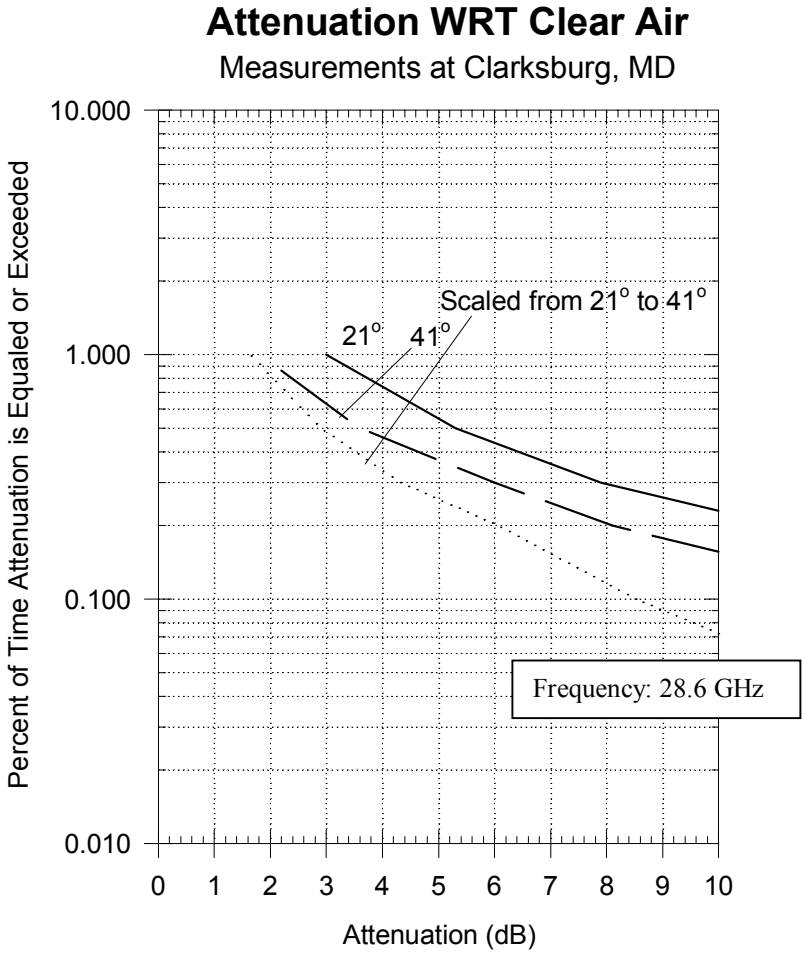


Note: The $21^0$ data was collected in CY 1977 with a maximum rain rate of 92.1 mm/h
The $41^0$ data was collected in CY 1978 with a maximum rain rate of 65.0 mm/h.

Exhibit 2.4.3.2-2
Evaluation of Elevation Angle Scaling
using 28.6 GHz data collected at Clarksburg, MD.

### 2.4.4 Simultaneous Latitude, Altitude, and Elevation Angle and Polarization Angle Scaling from the ITU-R Rain Attenuation Model

The ITU-R rain attenuation model can be used to scale a given ACA distribution of data collected at a latitude $\varphi_1$, altitude $h_1$, elevation angle $\theta_1$ and polarization tilt angle $\tau_1$ to a any other latitude $\varphi_2$, altitude $h_2$, elevation angle $\theta_2$ and polarization tilt angle $\tau_2$. The method allows site corrections on ACA data providing that the data collection latitude $\varphi_1$ and the latitude of interest $\varphi_2$ are in the same rain rate region. The approach is two-fold.

Two correction factors can be extracted from the ITU rain attenuation model by noting that the ratio of two given attenuations can be written as:

$$\frac{A_1}{A_2} = \frac{\gamma_{R1} L_{s1} r_1}{\gamma_{R2} L_{s2} r_2} = \left[\frac{\gamma_{R1}}{\gamma_{R2}}\right]\left[\frac{L_{s1} r_1}{L_{s2} r_2}\right] = \gamma' \; L' \qquad (2.4.4\text{-}1)$$

where $\gamma'$ is the ratio of the specific attenuations and L' is the ratio of the slant path length terms. The following sections describe how these terms can be used to scale ACA distributions.

#### 2.4.4.1 Latitude, Altitude, and Elevation Angle Scale Factor (L')

This section describes the method for determining L' for a given data set. The slant path scaling term L' is really a function of seven variables:

$$L'(f, \theta_1, \theta_2, \varphi_1, \varphi_2, hs_1, hs_2) = \left[\frac{L_{s1} r_1}{L_{s2} r_2}\right] \qquad (2.4.4.1\text{-}1)$$

where f is the frequency, $\theta_1$ and $\theta_2$ are the elevation angles, $\varphi_1$ and $\varphi_2$ are the latitudes, and $hs_1$ and $hs_2$ are the altitudes of the sites. If the elevation angles are the same, or if the elevation angle scaling method described in section 2.4.3.2 has been used, $\theta_1 = \theta_2$ for these calculations.

1) To determine the site correction factor, first calculate the effective rain heights $h_r$ for each site:

$$h_{fr}(\varphi) = \begin{cases} 5 - 0.075(\varphi - 23) & for \quad \varphi > 23° \\ 5 & for \quad -21° \le \varphi \le 23° \\ 5 + 0.1(\varphi + 21) & for \quad -71° \le \varphi \le -21° \\ 0 & for \quad \varphi < -71° \end{cases} \qquad (2.4.4.1\text{-}2)$$

See section 2.2.4.1 for more information about the effective rain height.

2) Next, calculate the slant-path lengths for each site.

$$L_S(\theta) = \begin{cases} \dfrac{(h_R - h_S)}{\sin\theta} & \text{for} \quad \theta \geq 5° \\ \dfrac{2(h_R - h_S)}{\left[\sin^2\theta + \dfrac{2(h_R - h_S)}{R_E}\right]^{1/2} + \sin\theta} & \text{for} \quad \theta < 5° \end{cases} \tag{2.4.4.1-3}$$

where,

$h_R$ = the effective rain height (km),
$h_S$ = the altitude of the ground receiver site from sea level (km),
$\theta$ = the elevation angle,
$R_E$= 8500 km (effective earth radius).

3) Calculate the horizontal projection of the slant path lengths $L_G$ for each site.

$$L_G = L_S \cos\theta \tag{2.4.4.1-4}$$

4) Calculate the reduction factors $r_p$ for each site from the rain rate as follows:

$$r_{0.01} = \frac{1}{1 + L_G / L_0} \tag{2.4.4.1-5}$$

where

$$L_0 = \begin{cases} 35e^{-0.015R_p} & \text{for} \quad R_p \leq 100\text{mm/h} \\ 35e^{-0.015(100)} & \text{for} \quad R_p > 100\text{mm/h} \end{cases} \tag{2.4.4.1-6}$$

and $L_G$ is the horizontal projection calculated in step 3.

5) Calculate the slant path correction factor L':

$$L' = \frac{L_{s1} r_{p1}}{L_{s2} r_{p2}} \tag{2.4.4.1-7}$$

6) If $\theta_1 = \theta_2$ and the polarization angles $\tau_1 = \tau_2$ then,

$$\frac{A_1}{A_2} = \gamma' \quad L' = L' \tag{2.4.4.1-8}$$

where $\gamma'$ is the ratio of specific attenuations.

### 2.4.4.2 Polarization Angle Scaling from ITU-R 813-5

The polarization dependence of the ITU-R rain attenuation model comes from the experimentally determined power law relationship inherent in the specific attenuation calculation. From equation 2.4.4-1, the latitude and altitude corrections are completely contained in the slant path term L'. The next step is to compensate for polarization angle differences. The polarization angle dependence of the ITU-R rain model is completely contained in the ratio of the specific attenuations $\gamma'$. This section describes the method for determining $\gamma'$. The specific attenuation scaling term $\gamma'$ is really a function of six variables:

$$\gamma'(f, R, \theta_1, \theta_2, \tau_1, \tau_2) = \left[\frac{\gamma_1}{\gamma_2}\right] \qquad (2.4.4.2\text{-}1)$$

where f is the frequency, $\theta_1$ and $\theta_2$ are the elevation angles, and $\tau_1$ and $\tau_2$ are the polarization tilt angles for each site. If the elevation angles are the same, or if the elevation angle scaling method described in section 2.4.2.2 has been used, $\theta_1 = \theta_2$ for these calculations.

1) Using the table given for the attenuation coefficients in Exhibit 2.2.4.1-5, calculate k and $\alpha$ for each site:

$$k_1 = [k_H + k_V + (k_H - k_V)\cos^2\theta_1 \cos 2\tau_1]/2 \qquad (2.4.4.2\text{-}2)$$
$$k_2 = [k_H + k_V + (k_H - k_V)\cos^2\theta_2 \cos 2\tau_2]/2$$

$$\alpha_1 = [k_H \alpha_H + k_V \alpha_V + (k_H \alpha_H - k_V \alpha_V)\cos^2\theta_1 \cos 2\tau_1]/2k \qquad (2.4.4.2\text{-}3)$$
$$\alpha_2 = [k_H \alpha_H + k_V \alpha_V + (k_H \alpha_H - k_V \alpha_V)\cos^2\theta_2 \cos 2\tau_2]/2k$$

2) Calculate the specific attenuation for each site from the rain rate:

$$\gamma_1 = \alpha_1 R_p^{\alpha_1} \qquad (2.4.4.2\text{-}4)$$
$$\gamma_2 = \alpha_2 R_p^{\alpha_2}$$

where $R_p$ can be taken from the ITU-R distribution of the rain rates (Exhibit 2.2.4.1-2) or from a map of the ITU-R rain regions (Exhibits 2.2.4.1-3, 4, 5).

3) Then calculate the specific attenuation scale factor:

$$\gamma' = \frac{\gamma_1}{\gamma_2} \qquad (2.4.4.2\text{-}5)$$

4) Then,

$$\frac{A_1}{A_2} = \gamma' \; L' \qquad (2.4.4.2\text{-}6)$$

## 2.5 LINK RESTORATION MODELS

This section presents a compilation of models and procedures for the determination of methods of restoral of the link performance that may be affected by degradations from atmospheric conditions. The predominate effect, particularly for systems operating above 10 GHz, is rain attenuation.

A satellite link which is subject to weather dependent path attenuation is designed to operate at an acceptable performance level by allowing adequate power margins on the uplink and the downlink segments. This can be accomplished directly by increasing antenna size or increasing the RF transmit power, or both. When the expected path attenuation exceeds the power margins available, and this can easily occur in the Ku, Ka, and V-bands for many regions of the earth, then additional methods must be considered to overcome the severe attenuation conditions and restore acceptable performance on the links.

Restoration techniques discussed in this section include site diversity, orbit diversity, link power control and adaptive forward error correction.

### 2.5.1 Site Diversity

Site diversity is a technique used to improve overall link performance by taking advantage of the spacially inhomogeneous nature of rain. Through site diversity, two or more ground stations are used to receive a common signal from a single transmitting satellite. Ideally, two sites located in different places will not simultaneously experience equal rain attenuation. Therefore, by monitoring whichever signal is the less attenuated, overall system throughput is enhanced. While experiments are presently being conducted using three or more ground stations, models typically focus on a two site configuration.

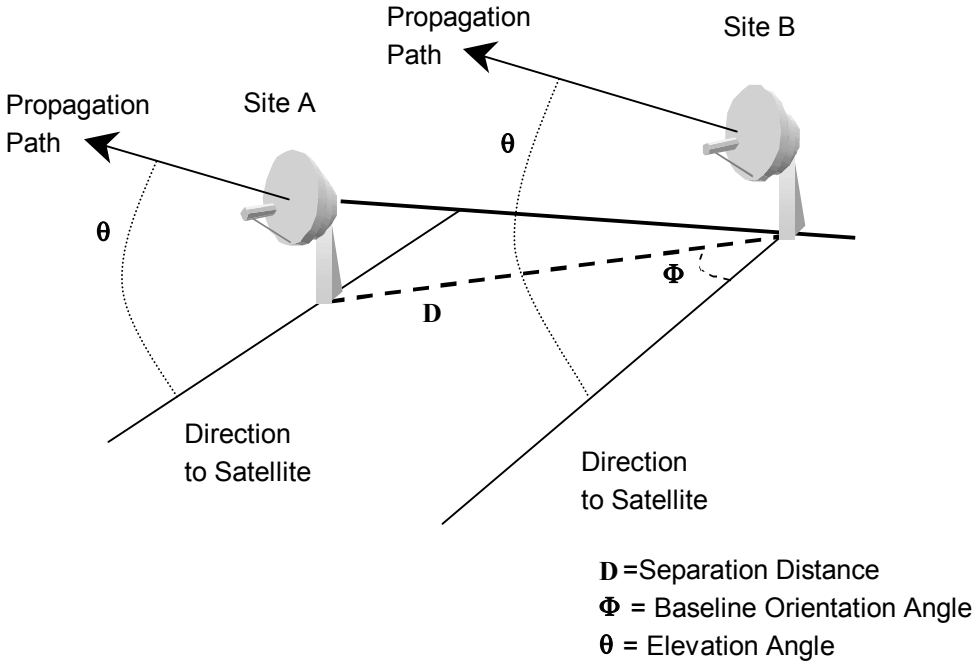


Exhibit 2.5.1-1 – An example of a two site diversity configuration.

The two primary parameters which influence the gain achieved by site diversity are site separation and baseline orientation. Site separation, D, is typically at least as wide as a rain cell (i.e. a few km). If the sites are too closely space, the probability is increased that the propagation paths will pass through the same rain event. As D increases, the instantaneous correlation of rain attenuation between sites becomes less. The second important factor to site diversity is the baseline orientation angle, $\Phi$. An optimal condition exists when $\Phi = 90°$. Geometrically, a 90° baseline orientation angle provides the widest separation between propagation paths. When $\Phi = 0°$, one propagation path will look over the top of the other and the overall gain is reduced.

The data available from early diversity experiments in New Jersey and Ohio (Hodge, 1974, Wilson, 1970, Wilson and Mammel, 1973, Gray, 1973) were used to develop an empirical model for the dependence of diversity gain on separation distance, d, and single site attenuation, A, (Hodge-1976).

The Hodge model was extended and improved by the ITU-R and adopted in Recommendation P.618. The improvement in overall link performance through site diversity may be measured in two ways: Diversity Gain and a Diversity Improvement Factor. The ITU-R provides models for both (ITU-R Rec. P.618-5, 1997). Both models are recommended for use between 10 and 30 GHz and for exceedance percentages below 0.1%.

The following sections present the original Hodge diversity model and the later ITU-R models that were derived from it.

### 2.5.1.1 Hodge Site Diversity Model

The Hodge (1976) site diversity model is based on an assumed empirical relation of the form

$$G_D = a' (1-e^{-b'D}) \quad (2.5.1.1\text{-}1)$$

where the coefficients a' and b' depend upon the single site attenuation according to

$$a' = A - 3.6 (1-e^{-0.24A}) \quad (2.5.1.1\text{-}2)$$

$$b' = 0.46 (1-e^{-0.26A}) \quad (2.5.1.1\text{-}3)$$

The original diversity gain model was improved by Hodge (1982) to include other factors besides single-site attenuation and separation distance. Based on data from thirty-four diversity experiments, the improved model takes into account the following variables, listed in decreasing degree of dependence

| | |
|---|---|
| Separation distance | d |
| Single-site attenuation | A |
| Link frequency | f |
| Elevation angle | EL |
| Baseline-to-path angle | $\triangle$ |

The variable $\triangle$ is the angle between the inter-site baseline and the ground projection of the Earth-space propagation path, measured such that $\triangle \leq 90^o$.

The improved model also eliminated the implication of the earlier model that diversity gain approaches a constant (3.6 dB) for very deep fades.

The model then gives the diversity gain as

$$G_D = G_d G_f G_E G_{\triangle} \quad (2.5.1.1\text{-}4)$$

where each factor contains the dependence of the variable denoted by its subscript. The first factor is the same as the gain of the earlier model:

$$G_d = a(1-e^{-bd}) \quad (2.5.1.1\text{-}5)$$

The regression coefficients are given by

$$a = 0.64A - 1.6 (1 - e^{-0.11A}) \quad (2.5.1.1\text{-}6)$$

$$b = 0.585 (1 - e^{-0.98A}) \quad (2.5.1.1\text{-}7)$$

The remaining factors are

$$G_f = 1.64\ e^{-0.025f} \qquad (2.5.1.1\text{-}8)$$

$$G_E = 0.00492(EL) + 0.834 \qquad (2.5.1.1\text{-}9)$$

$$G_{\triangle} = 0.00177\ \triangle + 0.887 \qquad (2.5.1.1\text{-}10)$$

where, d is in kilometers, A is in dB, f is in GHz, and EL and $\triangle$ are in degrees.

The improved model predictions were compared with the original data set and produced an rms error of 0.73 dB. The data set used consisted of the results of thirty-four diversity experiments covering a wide range of variable values.

### 2.5.1.2 ITU-R Site Diversity Model

The ITU-R Site Diversity Model is an empirically derived model that is based on the revised Hodge Model. The input parameters required are;

frequency, $f$ (GHz),
elevation angle, $\theta$ (°),
site separation, D (km),
baseline orientation angle, $\Phi$ (°), and
attenuation threshold, A (dB)

The model predicts the overall improvement in system performance in terms of diversity gain, G(dB).

The procedure for calculating G is implemented in a straight forward, step-by-step process which determines the gain component due to each of the input variables (ITU-R Rec. P.618-5, 1997).

Step 1: Calculate the gain contributed by the spatial separation from:

$$G_D = a \cdot (1 - e^{-bD}) \qquad (2.5.1.2\text{-}1)$$

where:

$$a = 0.78 \cdot A - 1.94 \cdot (1 - e^{-0.11 \cdot A}) \qquad (2.5.1.2\text{-}2)$$

$$b = 0.59 \cdot (1 - e^{-0.1 \cdot A}) \qquad (2.5.1.2\text{-}3)$$

Step 2: Calculate the gain contributed by the frequency dependence from:

$$G_f = e^{-0.025 \cdot f} \qquad (2.5.1.2\text{-}4)$$

Step 3: Calculate the gain contributed by the elevation angle dependence from:

$$G_\theta = 1 + 0.006 \cdot \theta \qquad (2.5.1.2\text{-}5)$$

Step 4: Calculate the gain contributed by the baseline orientation angle dependence from:

$$G_\Phi = 1 + 0.002 \cdot \Phi \qquad (2.5.1.2\text{-}6)$$

Step 5: Compute the net diversity gain as the product of individual components:

$$G = G_D \cdot G_f \cdot G_\theta \cdot G_\Phi \quad (\text{dB}) \qquad (2.5.1.2\text{-}7)$$

### 2.5.1.3 ITU-R Diversity Gain - Sample Calculation

Assume a theoretical system operating with the following parameters:

frequency: 20 GHz
elevation angle: 20°
availability: 99.9%
latitude: 38.4°N
rain region: K.

It may be shown using the ITU-R rain model that this system will experience an attenuation, A, of 11.31 dB. If this attenuation level is unacceptable to system designers, it may be reduced by an amount equal to the diversity gain.

Suppose a second, identical site were added to the system where:

D = 10 km and
$\Phi = 85°$

The diversity gain is calculated by:

Step 1: Calculate the gain contributed by the spatial separation from:

$$a = 0.78 \cdot A - 1.94 \cdot (1 - e^{-0.11 \cdot A}) = 0.78 \cdot 11.31 - 1.94 \cdot (1 - e^{-0.11 \cdot 11.31}) = 7.44$$

$$b = 0.59 \cdot (1 - e^{-0.1 \cdot A}) = 0.59 \cdot (1 - e^{-0.1 \cdot 11.31}) = 0.40$$

$$G_D = a \cdot (1 - e^{-bD}) = 7.44 \cdot (1 - e^{-0.40 \cdot 10}) = 7.30$$

Step 2: Calculate the gain contributed by the frequency dependence from:

$$G_f = e^{-0.025 \cdot f} = e^{-0.025 \cdot 20} = 0.61$$

Step 3: Calculate the gain contributed by the elevation angle dependence from:

$$G_\theta = 1 + 0.006 \cdot \theta = 1 + 0.006 \cdot 20 = 1.12$$

Step 4: Calculate the gain contributed by the baseline orientation angle dependence from:

$$G_\Phi = 1 + 0.002 \cdot \Phi = 1 + 0.002 \cdot 85 = 1.17$$

Step 5: Compute the net diversity gain as the product of individual components:

$$G = G_D \cdot G_f \cdot G_\theta \cdot G_\Phi = 7.30 \cdot 0.61 \cdot 1.12 \cdot 1.17 = 5.84$$

Therefore, the new system attenuation threshold level is $A - G = 11.31 - 5.84 = 5.47$ dB.

Plots of diversity gain, G, for the example system above using other separations and baseline orientations are presented in Exhibit 2.5.1.3-1.

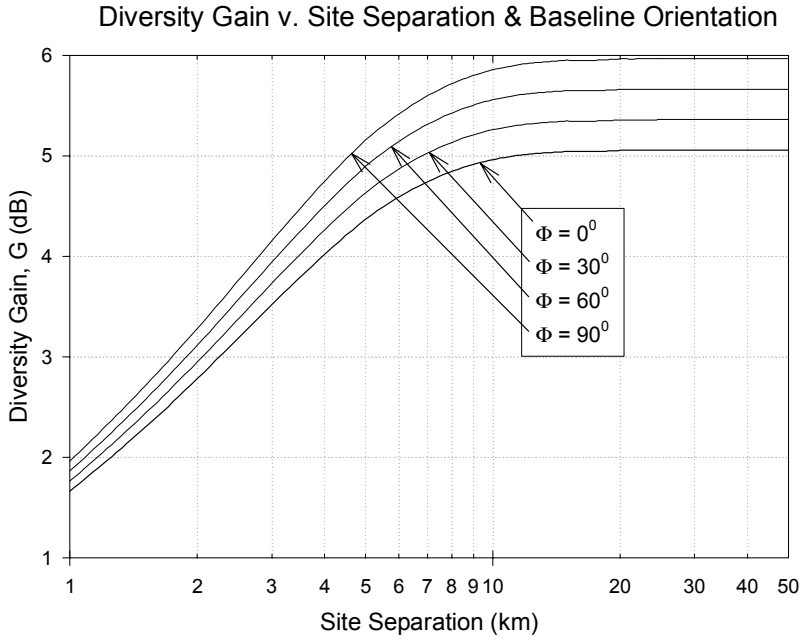


Exhibit 2.5.1.3 –1 Diversity Gain v. Site Separation and Baseline Orientation for a Theoretical System

### 2.5.1.4 ITU-R Diversity Improvement Factor

The ITU-R (Rec. P.618-5, 1997) also provides a procedure for calculating the Diversity Improvement, a complementary parameter to Diversity Gain. Rather than calculating a dB level of gain, the diversity improvement, I, is measured as a ratio of the single site exceedance time percentage to the two-site exceedance time percentage.

Diversity improvement is a function of the exceedance time and the site separation only. It may be calculated by the following:

Step 1: Calculate the empirical coefficient, $\beta^2$

$$\beta^2 = 10^{-4} \cdot D^{1.33} \qquad (2.5.1.4\text{-}1)$$

Step 2: Calculate the diversity improvement factor, I

$$I = \frac{P_1}{P_2} = \frac{1}{\left(1+\beta^2\right)} \cdot \left(1 + \frac{100 \cdot \beta^2}{P_1}\right) \approx 1 + \frac{100 \cdot \beta^2}{P_1} \qquad (2.5.1.4\text{-}2)$$

### 2.5.1.5 ITU-R Diversity Improvement – Sample Calculation

Considering the theoretical system in section 2.5.1.3 where:

frequency: 20 GHz,
elevation angle: 20°,
availability: 99.9%,
latitude: 38.4°N,
rain region: K, and
attenuation: 11.31 dB

with a second, identical site located at:

D = 10 km and
$\Phi$ = 85°,

the diversity improvement factor, I, may be calculated.

Step 1: Calculate the empirical coefficient, $\beta^2$

$\beta^2 = 10^{-4} \cdot D^{1.33} = 10^{-4} \cdot 10^{1.33} = 2.14 \cdot 10^{-3}$

Step 2: Calculate the diversity improvement factor, I

$$I = \frac{P_1}{P_2} = \frac{1}{\left(1+\beta^2\right)} \cdot \left(1 + \frac{100 \cdot \beta^2}{P_1}\right) \approx 1 + \frac{100 \cdot \beta^2}{P_1} = 1 + \frac{100 \cdot 2.14 \cdot 10^{-3}}{0.1} = 3.14$$

where $P_1$ = 100-Availability = 0.1.

Therefore, for a system with an overall attenuation threshold of 11.31 dB the addition of the second site improved system availability from 99.90% to:

$$100 - P_2 = 100 - \frac{P_1}{I} = 100 - \frac{0.1}{3.14} = 99.97\%$$

Plots of diversity improvement factor, I, for various separation distances are presented in Exhibit 2.5.1.5-1.

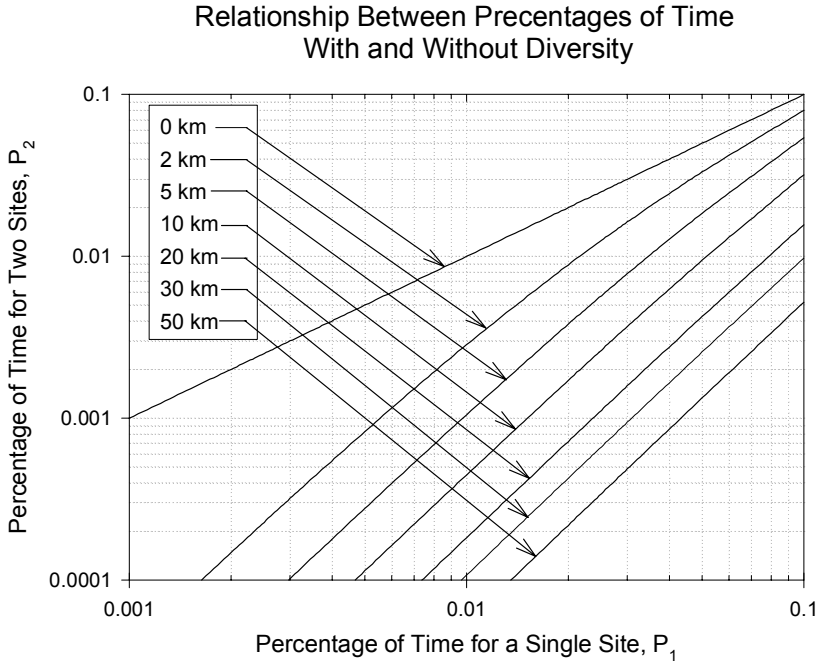


Exhibit 2.5.1.5-1 Relationship between $P_1$ and $P_2$.

### 2.5.1.6 Considerations When Modeling Site Diversity

The ITU-R models provide good methods for estimating the gain achieved through diversity techniques, however there are a few points to keep in mind.

- Both the diversity gain and diversity improvement models are empirically derived from a limited amount of data. They are considered valid only between 10 and 30 GHz and for availabilities of at least 99.9% (i.e. P<0.1%).
- The diversity gain and diversity improvement models were independently derived. Calculations for the same site diversity configuration using both models may provide slightly different results.
- The diversity gain model typically shows a lack of additional gain after about 10 or 20 km (See Exhibit 2.5.1.2-1). More recent research has shown that this is a product of the empirical data from which the model was derived. Some additional gain can be achieved with increasing distance beyond 50 km (Ortgies, 1996), however models are not yet available to represent this effect.

### 2.5.2 Orbit Diversity

Orbit diversity refers to the use of two satellites at separate orbital positions, which provide two paths to a single ground terminal (Ippolito,1986). Orbit diversity is generally less effective than site diversity for rain fade mitigation because the diversity paths are more highly correlated. Nevertheless, orbit diversity has the advantage that the two satellites can be shared (as part of a resource-sharing scheme) with many ground sites. This is in contrast to the case of site diversity, where the redundant ground site can generally be dedicated to only one primary ground site (Matricciani, 1987). Therefore, site diversity is somewhat inefficient in the sense that the redundant ground site is not used most of the time. On the other hand, if an orbit diversity scheme does not take advantage of its capability for resource-sharing with several ground sites it, too, is inefficient and is likely to prove too expensive for the amount of diversity gain that it does provide.

Operational considerations other than rain fades can also make the use of orbit diversity more attractive. Examples of such operational considerations include satellite equipment failures and sun transit by the primary satellite, both of which require hand-over to a redundant satellite to maintain communication. The use of a redundant satellite for other reasons in addition to rain fades can help to make orbit diversity economically practical.

If a ground terminal is to take full advantage of orbit diversity, it should have two antenna systems, so that the switching time between propagation paths can be minimized. If the terminal has only one antenna system with a relatively narrow beamwidth, switching time can be excessive because of the finite time required to slew the ground antenna from one satellite to another, and because of the finite time needed for the receivers to re-acquire the uplink and downlink signals. Of course, the use of two spatially separated ground antennas provides an opportunity for site diversity in addition to orbit diversity.

Satellites in geostationary orbit are desirable for orbit diversity because they appear to the ground station to be fixed in space. Such orbits simplify satellite acquisition and tracking, and alleviate satellite handover problems. However, satellite coverage of high northern and southern latitudes is limited - requiring ground antennas at these latitudes to operate at low elevation angles. In addition, rain attenuation is greater at low elevation angles because of the longer path lengths through rain cells. To overcome this difficulty with high-latitude stations, elliptical orbits whose apogees occur at high latitudes can be used, allowing satellite coverage for a relatively large fraction of the orbit period. However, not only are the advantages of geostationary orbits then lost, but in addition several satellites must be used in order to provide coverage at all times.

Data concerning the improvement achievable with orbit diversity are sparse. An early analysis was conducted by Matricciani (1987). The elements of the evaluation were,

1. A ground station at Spino d'Adda in Northern Italy
2. Satellite 1 (Italsat) at 13 deg. E longitude
3. Satellite 2 (Olympus) at 19 deg. W longitude.

The predicted single-path and double-path statistics for a 20 GHz downlink are shown in Exhibit 2.5.2-1. The diversity (double path) predictions shown in this figure assume that Satellite 1 is normally used, and that Satellite 2 is switched in only when the rain attenuation for Satellite 1 exceeds some selected value. Because Satellite 2 would therefore be used only a small fraction of the time, it can be time shared with several ground stations for large-scale orbit diversity. The predictions are based on single-path measurements of the rain-rate probability distribution, and the joint distribution for the double-path attenuation is assumed to be log-normal.

Measurements of orbit diversity improvement have been made by Lin, et al (1980) for a configuration consisting of:

1. A ground station at Palmetto, GA
2. Path 1 - 18 GHz radiometer pointed in direction of COMSTAR D1 at 128 deg. W longitude
3. Path 2 - 19 GHz beacon of COMSTAR D2 at 95 deg. W longitude.

Exhibit 2.5.2-2 shows measurement results at 18 and 19 GHz. One might expect the diversity gain to improve markedly as the angle subtended increases. However, it can be shown that, except when the single-path attenuation is large to begin with, the diversity gain actually increases rather slowly with the subtended angle (Ippolito, 1986). This is because most of the rain attenuation is at low altitudes, so that even widely diverging propagation paths often pass through the same rain cell.

The measurements in Exhibit 2.5.2-2 cannot be directly compared with the predictions in Exhibit 2.5.2-1 because the rain statistics and geometrical configurations differ. Nevertheless, the limited measurements and calculations that have been made both indicate that a modest diversity gain is achievable from orbit diversity. In any case, orbit diversity gain is less than that achievable with site diversity. Predictions from the ITU-R Diversity Gain procedure, for example, shows that one can expect roughly five dB site diversity gain when the average single-site rain attenuation is 10 dB. Exhibits 2.5.2-1 and 2.5.2-2, on the other hand, show that one can expect only two or three dB gain from orbit diversity.

Orbit diversity is of great interest for systems employing non-GSO (geosynchronous orbit) constellations, particularly for systems operating in the Ka or V bands. Measured data is expected to be available over the next several years as the new generation of broadband FSS systems operating in the Ka and V bands join the existing GSO satellite systems.

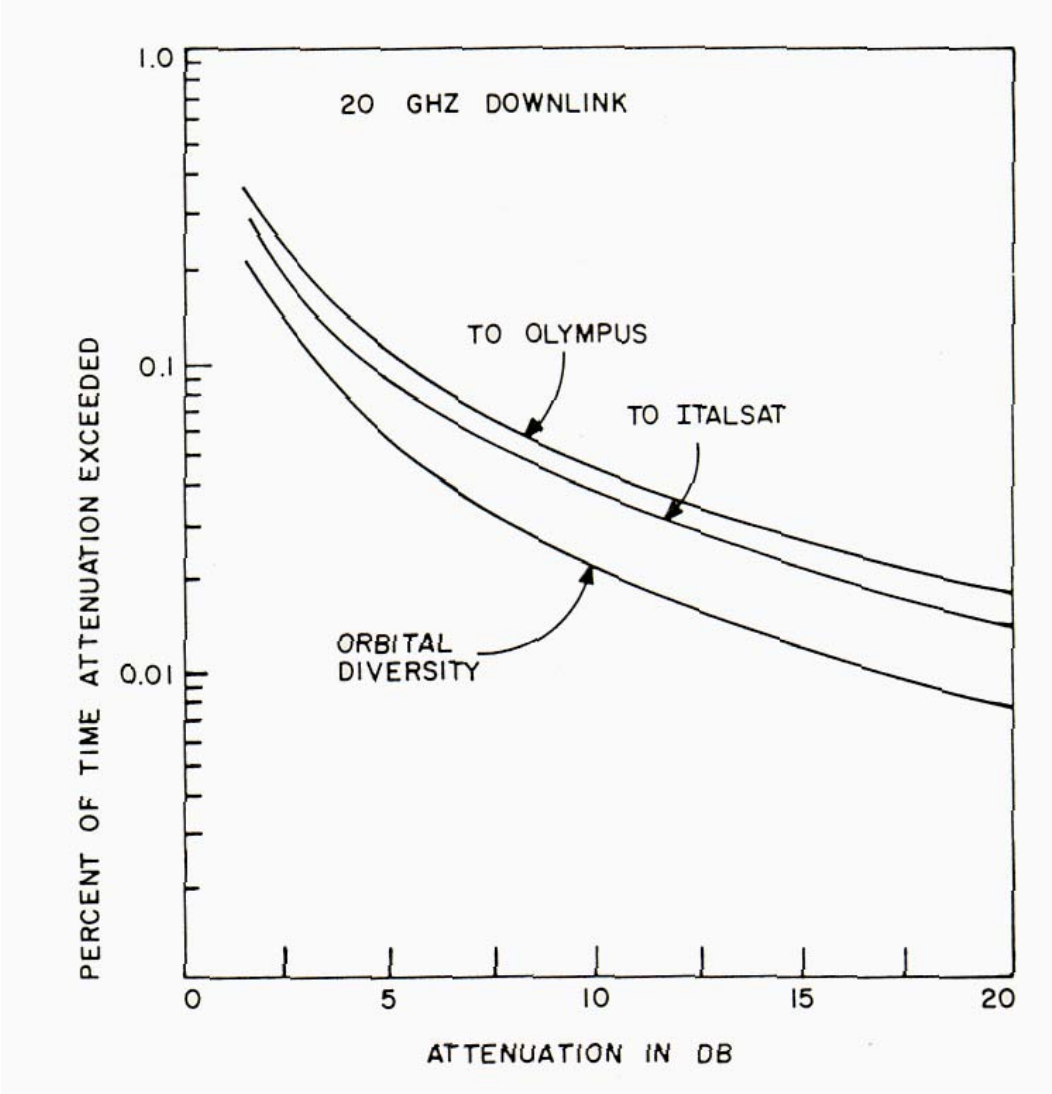


Exhibit 2.5.2-1
Predicted Orbit Diversity Performance for Spino d'Adda, Italy
*[Source: Matricciani (1987)]*

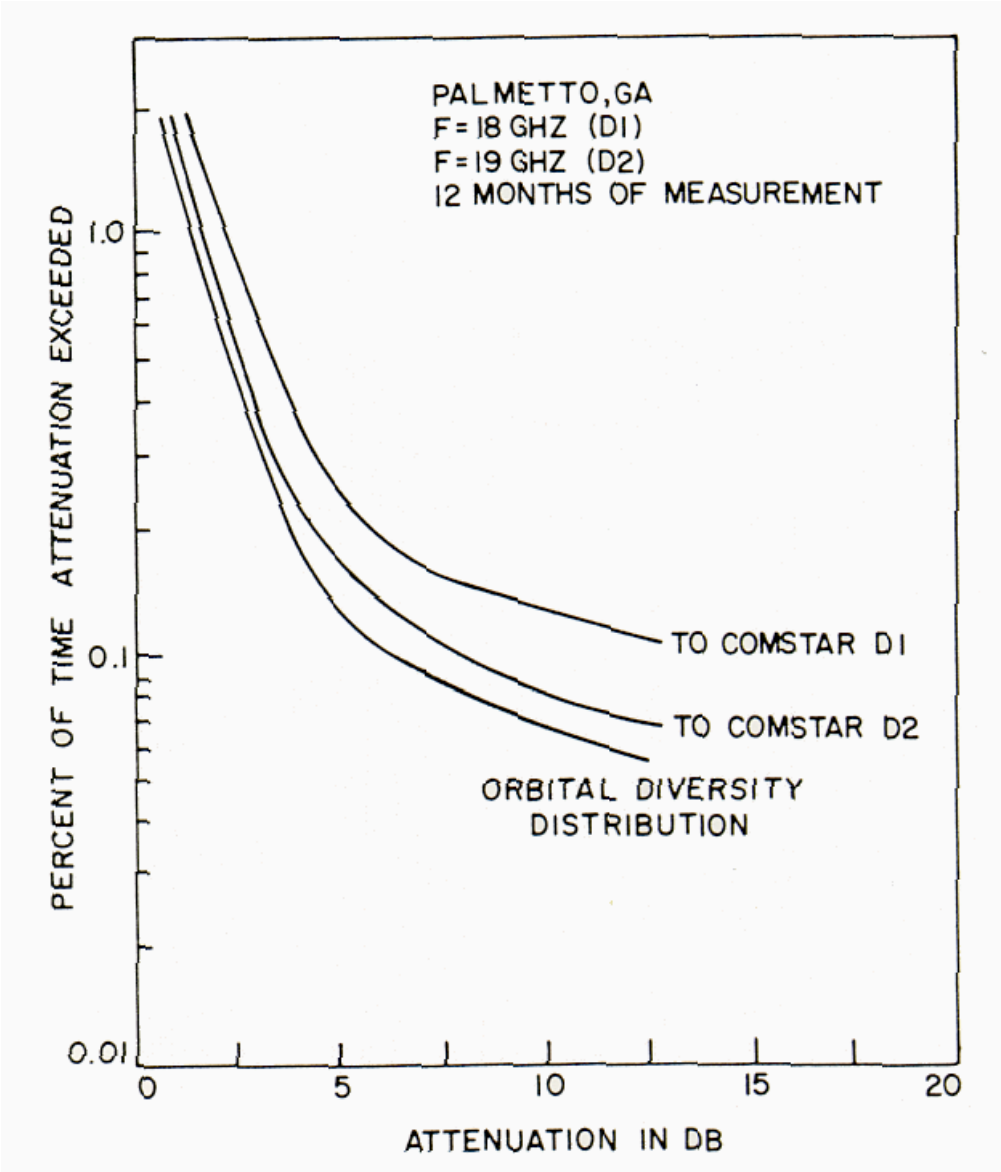


Exhibit 2.5.2-2
Orbit Diversity Measurements at Palmetto, GA
*[Source: Lin, et al (1980)]*

### 2.5.3 Link Power Control

The objective of power control is to vary the transmitted power in direct proportion to the attenuation on the link, so that the received power stays constant through rain fades. This can be employed, in principle, on either the uplink or downlink. There are two reasons for using power control rather than a very high transmitted power level to mitigate rain fades. When used on the uplink, power control a) can prevent the transponder on the satellite from being overdriven, and b) can maintain the power balance among several uplink carriers using the same transponder. (When multiple carriers share a non-linear transponder near saturation, variations in the input level of one of them are enhanced at the output.) When used on the downlink, power control can provide a temporary power boost to combat fades on selected links while requiring only a modest increase in satellite solar array power. The array power not needed during clear-sky operation is used to charge batteries, which supply the energy needed to transmit the added power during fades.

Through power control, the maximum amount of rain attenuation that can be compensated is equal to the difference between the maximum output of the Earth station or satellite power amplifier and the output required under clear-sky conditions. The effect of power control on availability, assuming that control is perfect, is the same as having this power margin at all times. A perfect power control system varies the power exactly in proportion to the rain attenuation. Errors in the power control result in added outages, effectively decreasing this margin. Maseng and Baaken (1981) have studied this effective margin reduction due to power control delay.

A drawback of power control is a potential increase in intersystem interference. A power boost intended to overcome rain attenuation along the direct Earth-space path will produce an increase in power on interfering paths as well. If the same rain fade does not exist on these paths, the interference power received by the victim earth station, such as other terrestrial stations, will increase. Due to the inhomogeneity of heavy rain, attenuation on interfering paths at large angles from the direct earth-space path will often be much less than the attenuation on that path. Terrestrial system interference caused by the earth station, although tolerable under clear-sky conditions, may therefore become intolerable in the presence of rain when uplink power control is used. Downlink power control will likewise increase the potential for interference with earth stations using adjacent satellites. A downlink power boost for the benefit of a receiving station experiencing a rain fade will be seen as an increase in interference by vulnerable stations that are not experiencing fades.

#### 2.5.3.1 Uplink Power Control

A frequency-division multiple-access (FDMA) satellite communication system with large spatial and time variations in rain fades will experience significant nonlinear distortion when fades are mitigated by the use of large power margins alone. Nonlinear distortion, which occurs when the satellite transmitter is operated near saturation, includes AM-to-PM conversion and generation of intermodulation products.

By continually adjusting the uplink power from each ground station in accordance with uplink fade conditions, variations in the operating point of the satellite TWTA can be minimized, thereby minimizing nonlinear distortion. However, this does not completely solve the problem because downlink rain fades must also be considered. Lyons (1974, 1976) showed that if the uplink power control algorithm accounts not only for uplink fades but also for downlink fades, good performance can be achieved in the presence of fading on both links by using uplink power control alone. Although individual signal levels at the satellite receiver will vary widely in this situation, the TWTA operating point will still remain relatively fixed so long as there is a sufficiently large number of users, all having controlled access to the satellite. If deep fades occur on only a few of the uplink and downlink paths, variations in the received downlink signal levels will be relatively small, thus requiring smaller fade margins.

Uplink power control requires that each station accessing the satellite possess knowledge not only of its uplink fade characteristics, but also of the downlink fade characteristics for all stations to which it is transmitting. Power control of all transmitting stations can be achieved from a single location at the cost of control delays, which result in relatively slow fade mitigation. If instead, we have distributed control in the sense that each station controls its own transmitted power, delays are minimized. However, performance may suffer because the total received uplink power at the satellite can no longer be maintained approximately constant under widely fluctuating propagation conditions. Furthermore, with distributed control, fade information must be exchanged continually among all participating stations to make the system work.

These arguments indicate that if the uplink power control algorithm does not take into account the downlink fade characteristics, then power control can likely be applied only to single-service, single-user links. For such links, there are two types of uplink power control that can be used. The first is a closed-loop system that adjusts uplink power in accordance with the satellite received signal level returned to the transmitting station via telemetry. The second is an open-loop system that adjusts uplink power in accordance with either the downlink signal (or beacon) level, or the attenuation calculated from ground-based radiometer or radar measurements. Exhibits 2.5.3.1-1 and 2.5.3.1-2 illustrate closed-loop and open-loop uplink power control for single-carrier links (Ippolito, 1986).

### 2.5.3.2 Downlink Power Control

More and more satellite systems are moving to on-board signal processing, not only to improve bit error rate performance, but also to improve terminal interconnectivity and to make downlink performance independent of the uplink. On-board processing simplifies power control for rain fade mitigation (especially in FDMA systems) because the uplink power control algorithm no longer needs to take into account downlink fade conditions. Uplink and downlink power control can be done independently, which alleviates many problems associated with the use of FDMA during rain fades. This assumes that on-board processing includes demodulation to baseband, followed by remodulation onto a downlink

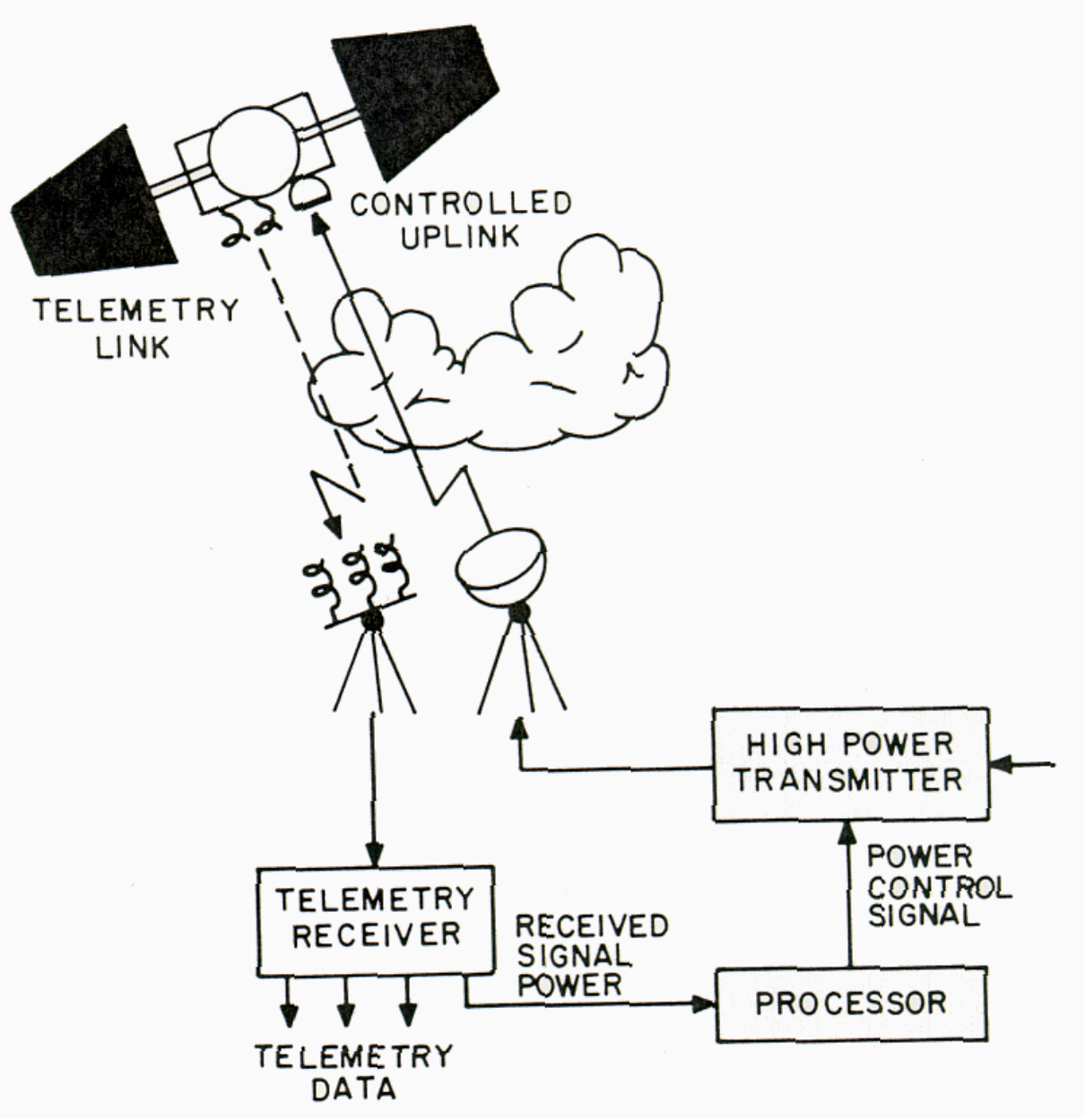


Exhibit 2.5.3.1-1
Closed Loop Uplink Power Control
*[Source: Ippolito (1986)]*

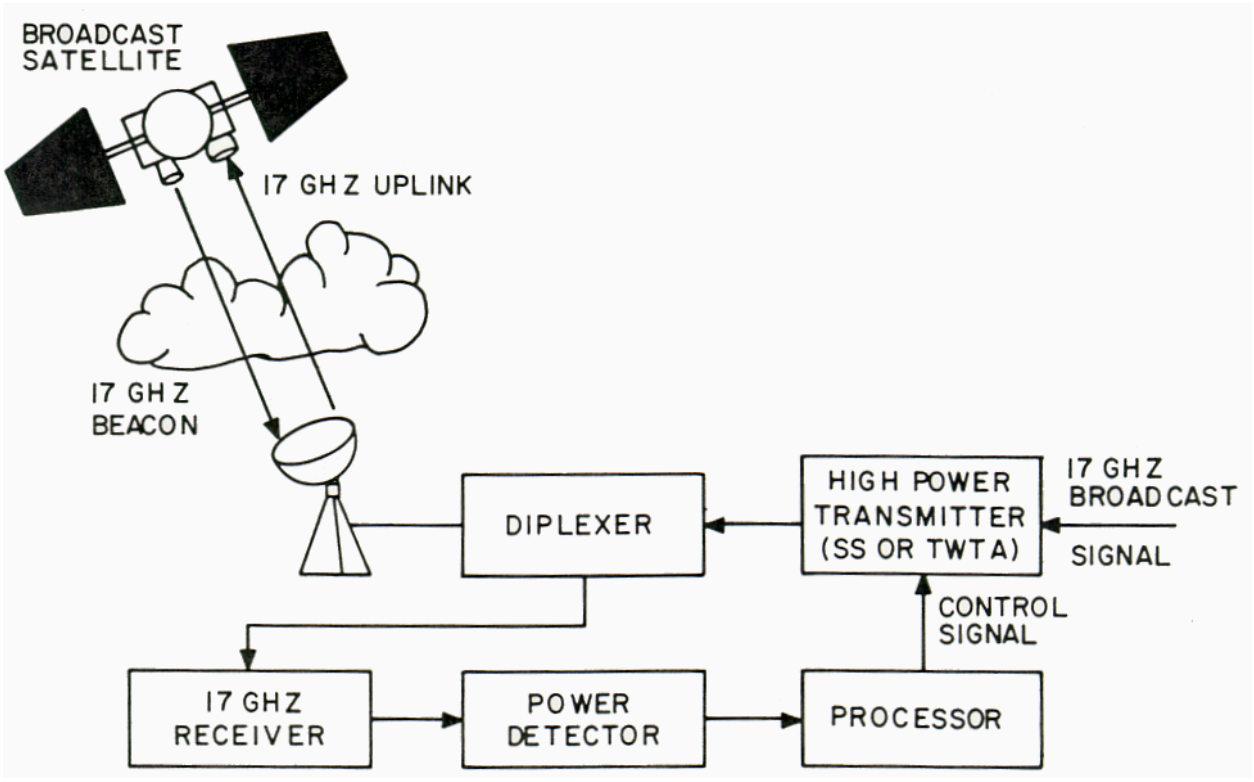


Exhibit 2.5.3.1-2
Open Loop Uplink Power Control
*[Source: Ippolito (1986)]*

carrier. The following discussion assumes that downlink power control can be accomplished essentially independent of the uplink regardless of whether or not on-board processing is being used.

The satellite transmitter usually has only one or two switchable output power levels, so downlink power control for rain fade mitigation is less flexible than uplink power control. This problem with downlink power control is somewhat alleviated by the use of switchable spot beams on the satellite. The antenna footprints are relatively small, thereby allowing added downlink power to be directed only to those terminals that require it. In fact, switching to spot beams is, in itself, an effective technique for mitigating rain fades, even when satellite transmitter power is not controlled. The use of downlink power control together with switchable antenna beams might better be called EIRP control rather than power control.

## 2.5.4 Adaptive FEC

Time Division Multiple Access (TDMA) systems assign each earth station a time interval during which it alone may access the entire satellite bandwidth. The time between accesses by a given station is the TDMA frame period, and each station is assigned a fixed fraction of the frame. This fraction is proportional to the traffic the station is carrying, or to its average bit rate. By leaving a portion of the frame period unassigned, those stations experiencing rain fades can be temporarily assigned a larger fraction of the frame for fade mitigation. One very effective technique available to exploit this additional time resource is to apply forward error correction (FEC). The same number of information bits is transmitted each frame period as before. However FEC reduces the required received signal level, thereby at least partially off-setting the loss in received power experienced during rain fades. Alternatively, the additional allotted time allows a reduction in data rate during rain fades. Exhibit 2.5.4-1 shows the typical elements of a communications system employing forward error correction.

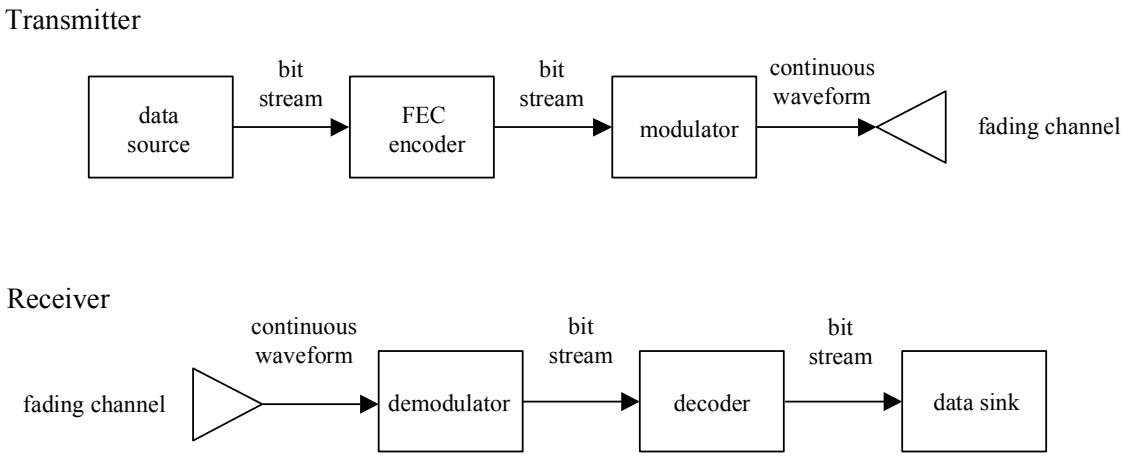


Exhibit 2.5.4-1
Elements of a communications system
with forward error-correction (FEC)

Coding increases the effective SNR by adding redundancy to the data being transmitted. However, the addition of coding overhead reduces the bandwidth available for data content. One way to balance the advantages with the disadvantages of coding is through the use of *adaptive coding*. With adaptive coding, little or no coding is used in clear air (unfaded) conditions, maximizing data throughput. If a fade occurs, the application of coding can preserve the link at low SNR, although at a reduced data rate. Such an implementation of adaptive coding requires a *feedback* system, in which the state of the propagation channel is measured periodically to detect fading conditions, or to estimate the extent of a fade. The results of the channel measurements are used to determine if coding is required, and a command is sent to both transmitter and receiver to act accordingly.

This scheme is adaptive in the sense that FEC is applied only when the rain attenuation has exceeded a selected threshold. When FEC is used, the symbol timing hardware still operates at the same fixed rate. Adaptive FEC can be implemented in software, which may be advantageous in some systems.

There is a limit to the mitigation that coding can provide. This is because minimum symbol energy must be maintained to ensure proper recovery of symbol timing in the receiver. Therefore, because the symbol rate is fixed, a minimum received signal power level must be maintained. The fade margin achieved with FEC must be traded off against the reduction in total system capacity that occurs. As propagation conditions worsen, the fraction of the frame duration needed for fade mitigation must increase, thereby reducing the fraction available for use during clear weather.

FEC can be used to mitigate either uplink or downlink fades. A station affected by uplink fades would encode its entire burst - lengthening its burst period by its allotted reserve time. Each station receiving that station's burst must decode the data in that burst. In contrast, a receiving station affected by downlink fading will receive all its data in coded form. Transmitting stations must encode that portion of the data that is transmitted to the affected station. It is apparent that a central control station must dynamically assign the extra time to the stations that require it. Furthermore, all stations in the network must know which stations require coding.

A satellite using on-board signal processing essentially decouples the downlink from the uplink, which allows the reserve time to be used more efficiently. Only those transmitting stations experiencing uplink fades then need to encode their data. The satellite would not only demodulate the uplink signal, but would also decode those uplinks affected by fading. The satellite would then encode for downlink transmission only those signals affected by downlink fades. The reserve time used by faded uplinks is, in effect, freed up to be used by faded downlinks.

Acampora (1979, 1981) studied the performance of a system using FEC coding to mitigate downlink fades. The hypothetical TDMA system studied operated in the 12/14 GHz band, using a bent-pipe transponder. The traffic model used assigned traffic between the 100 most populous U.S. cities in proportion to their population ranking. The Earth stations were given a built-in fade margin, and the reduction in this margin made possible by time resource sharing was found, using a convolutional FEC code that gave a 10 dB power saving. A typical result of this analysis showed that reserving six percent of the frame period as a shared resource provided an outage of 30 minutes per year (.0057% of the time) with 9 dB less rain margin than would otherwise be needed.

#### 2.5.4.1 Block Codes

Block coding adds redundancy to a "block" of symbols by mapping it to a larger block. Block coding maps $k$-symbol source words to $n$-symbol code words, where $n > k$. The lengthening of

symbol words requires that the (uncoded) data rate be reduced to accommodate the coding overhead, or that the bandwidth of the signal be increased. The code rate is the ratio of the size of the data blocks to the size of the coded blocks, or

$$r = \frac{k}{n} \tag{2.5.4.1-1}$$

Examples of block codes are:

- Reed-Solomon (used in TDMA systems)
- Hamming codes ("perfect" single error-correcting codes)
- RS codes (can correct bursts of errors)

The bit error rate for block codes is described by

$$\text{BER} \cong \frac{(n-1)!}{t!(n-1-t)!} P_e^{t+1} \tag{2.5.4.1-2}$$

where $t$ is the maximum number of errors that can be corrected by a code, $n$ is the number of bits in each code word, and $P_e$ is the probability of error for each individual bit.

### 2.5.4.2 Convolutional codes

Convolutional codes are codes with memory, meaning that a set of $n$ symbols output from the convolutional encoder is not only a function of the input $k$ symbols, but the previous $K$ - 1 sets of $k$ input symbols. A convolutional encoder is implemented with a shift register with length $k*K$, where $k$ bits at a time are shifted into the registers. Taps are taken from the shift register (from locations defined by the code) and led to $n$ modulo-2 adders (XOR gates), which are sequentially sampled to produce $n$ output bits for each $k$ input bits. The code rate of the convolutional encoder is, as for block codes

$$r = \frac{k}{n} \tag{2.5.4.2-1}$$

The parameter $k$ controls the amount of memory in the code. Encoders with larger values of $k$ have better performance than those with small $k$, but require more hardware (larger shift registers).

Computation of coding gain for convolutional codes requires a complete state description of the code being evaluated, which is beyond the scope of this handbook. However, bounds on coding gain have been tabulated, and are shown in Exhibits 2.5.4.2-1 and 2.5.4.2-2.

| Rate 1/2 codes | | | Rate 1/3 codes | | |
|---|---|---|---|---|---|
| $K$ | $d_f$ | Upper bound (dB) | $K$ | $d_f$ | Upper bound (dB) |
| 3 | 5 | 3.97 | 3 | 8 | 4.26 |
| 4 | 6 | 4.76 | 4 | 10 | 5.23 |
| 5 | 7 | 5.43 | 5 | 12 | 6.02 |
| 6 | 8 | 6.00 | 6 | 13 | 6.37 |
| 7 | 10 | 6.99 | 7 | 15 | 6.99 |
| 8 | 10 | 6.99 | 8 | 16 | 7.27 |
| 9 | 12 | 7.78 | 9 | 18 | 7.78 |

Exhibit 2.5.4.2-1 Coding Gain Upper Bounds for Some Convolutional Codes
Source: Bhargava et al (1981)

| Uncoded | Code rate | | 1/3 | | 1/2 | | | 2/3 | | 3/4 | |
|---|---|---|---|---|---|---|---|---|---|---|---|
| *Eb/No* (dB) | $P_B$ | $K$ | 7 | 8 | 5 | 6 | 7 | 6 | 8 | 6 | 9 |
| 6.8 | $10^{-3}$ | | 4.2 | 4.4 | 3.3 | 3.5 | 3.8 | 2.9 | 3.1 | 2.6 | 2.6 |
| 9.6 | $10^{-5}$ | | 5.7 | 5.9 | 4.3 | 4.6 | 5.1 | 4.2 | 4.6 | 3.6 | 4.2 |
| 11.3 | $10^{-7}$ | | 6.2 | 6.5 | 4.9 | 5.3 | 5.8 | 4.7 | 5.2 | 3.9 | 4.8 |
| Upper bound | | | 7.0 | 7.3 | 5.4 | 6.0 | 7.0 | 5.2 | 6.7 | 4.8 | 5.7 |

Exhibit 2.5.4.2-1
Basic Coding Gain (dB) for Soft Decision Viterbi Decoding
*[Source: Jacobs (1974)]*

### 2.5.4.3 Concatenated Codes

Concatenated codes are constructed by placing block and convolutional codes in series.

Turbo codes are parallel concatenations of short convolutional codes with an intermediate interleaving to create a great effective free distance (immature technology).

### 2.5.4.4 Trellis codes

Trellis coded modulation combines coding and modulation: a larger alphabet reduces the uncoded performance, but adds coding redundancy.

### 2.5.4.5 Comparison of Coding Methods

Block and convolutional coding schemes require additional bandwidth to accommodate the additional (redundant) symbols being transmitted. Trellis codes, however, increase the size of the symbol *alphabet*, thereby adding redundancy without increasing the required bandwidth.

| Coding | Decoding | Coding Gain (dB) at BER of $10^{-5}$ | Complexity |
|---|---|---|---|
| Block BCH | Algebraic | 1.5 - 4 | Low to moderate (1) |
| Block | Majority - hard decision | 1.5 - 3.5 | Low to moderate (1) |
| Convolutional | Threshold - hard decision | 1.5 - 3 | Low to moderate (1) |
| Convolutional | Viterbi - soft decision | 4.5 - 5.5 | High |
| Convolutional | Sequential - soft decision | 5 - 7 | High |
| In series - block - convolutional | Viterbi + algebraic | 6.5 - 7.5 | Very high |

(1) Dependent on the number of correctable errors.

Exhibit 2.5.4.5-1
Comparison of Coding Methods
*[ Source: ITU-R (1988)]*

## 2.6 REFERENCES – SECTION 2


Acampora, A.S. (1979), "A Shared Resource TDMA Approach to Increase the Rain Margin of 12/14-GHz Satellite Systems," BSTJ, Vol. 58, No. 9 (Nov.) pp. 2097-2111.

Acampora, A.S. (1981), "Rain Margin Improvement Using Resource Sharing in 12-GHz Satellite Downlinks," BSTJ, Vol. 60, No. 2 (Feb), pp 167-192.

Acosta, Roberto J., R. Reinhart, D. Kifer, C. Emrich and N.Goldshan (1997), "Wet Antenna Studies an LeRC," *Proceedings of the Twenty-second NASA Propagation Experimenters Meeting (NAPEX XXII) and Advanced Communications Technology Satellite (ACTS) Propagation Studies Miniworkshop*, Nassar Goldshan, ed., Boca Raton, FL, prepared by Jet Propulsion Laboratory, California Institute of Technology, November 1997.

Allnutt, J. E. (1989), *Satellite-to-ground radiowave propagation*, Peter Peregrinus Ltd., London.

Altshuler, E.A. (1984), "A Simple Expression for Estimating Attenuation by Fog at Millimeter Wavelengths," IEEE Trans. Ant. & Prop., Vol. AP-32, No. 7, pp. 757-758.

Antar, Y. M., A. Hendry, J. J. Schlesak, and R. L. Olsen (1982), Measurements of ice depolarization at 28.56 GHz using the COMSTAR beacon simultaneously with a 16.5 GHz polarization diversity radar, IEEE Trans. Antennas Propagation, AP-30, 858-866.

Baars, J.W.M. (1973), "The Measurement of Large Antennas with Cosmic Radio Sources," IEEE Trans. Ant. Prop., Vol. AP-21, No. 4, pp. 461-474.

Barbaliscia, F., M. Boumis, & E. Fionda (1996), "First Results of the Measurement Campaign on Cloud Structure and Propagation Effects," *Proceedings of the URSI Commission F Workshop on Climatic Parameters in Radiowave Propagation Prediction*, Oslo, Norway, pp. 28-29.

Battesti, J. (1981), On the subject of the frequency dependence of rain attenuation, Annals of Telecommunications, V. 36, pp. 274-275, Mar.-Apr. 1981.

Bhargava, V.K., D. Haccoun, R. Matyas, and P. Nuspl (1981), *Digital Communications by Satellite*, John Wiley & Sons, Inc., New York.

Capsoni, C.F., F. Fedi and A. Paraboni (1987), "A Comprehensive, Meteorologically Oriented Methodology for the Prediction of Wave Propagation Parameters in Telecommunications Applications Beyond 10 GHz," Radio Science, Vol. 22, No 3, May-June 1987.

CCIR, Rep. 719-1 (1982), Attenuation By Atmospheric Gases, *Recommendations and Reports of the CCIR, 1982*, *Vol. V, Propagation in Non-Ionized Media*, International Telecommunications Union, Geneva.

CCIR, Rep. 721-3 (1990), Attenuation By Hydrometers, in Particular Precipitation, and Other Atmospheric Particles, *Reports of the CCIR, 1990, Annex to Volume V, Propagation in Non-Ionized Media*, International telecommunications Union, Geneva

Chu, T.S. (1974), "Rain-Induced Cross-Polarization at Centimeter and Millimeter Wavelengths,"Bell Syst. Tech. Jrnl, Vol. 58, No. 8, pp. 1557-1579.

Chu, T.S. (1980), "Microwave Depolarization of an Earth-Space Path," Bell Syst. Tech. Jrnl, Vol. 59, No. 6 (July-Aug) pp. 987-1107.

Chu, T.S. (1982), "A Semi-Empirical Formula for Microwave Depolarization Versus Rain Attenuation on Earth-Space Paths," IEEE Trans. on Communications, Vol. COM-30, No. 12, (Dec) pp 2550-2554.

Clifford S. and Strohnbehn J. (1970), "The theory of microwave line-of-sight propagation through a turbulent atmosphere, IEEE Trans. Ant. Prop., vol. AP-18, no. 2, pp. 264-274.

Cole R., Ho K., Mavrokoukoulakis N. (1978), "The effect of the outer scale of turbulence and wavelength on scintillation fading at millimeter wavelengths," IEEE Trans. Ant. Prop., vol. AP-26, no. 5, pp. 712-715.

Crane, R.K. (1980), "Prediction of Attenuation by Rain", IEEE Trans. Comm., vol. COM-28, no.9, Sept. 1980.

Crane, R.K. (1982), "A Two-Component rain model for the prediction of Attenuation Statistics," Radio Science, Vol. 17, No. 6, pp. 1371-1387, November-December 1982.

Crane, R.K. (1996), *Electromagnetic Wave Propagation Through Rain*, John Wiley & Sons, Inc., New York.

Crane, R.K., D. Ramachadran, P. Robinson, X. Wang (1997), "ACTS Propagation Studies in Oklahoma", *Proceedings of the Twenty-first NASA Propagation Experimenters Meeting (NAPEX XXI) and Advanced Communications Technology Satellite (ACTS) Propagation Studies Miniworkshop*, Nassar Goldshan, ed., El Segundo, CA, prepared by Jet Propulsion Laboratory, California Institute of Technology, June 1997.

Dissanayake, A.W. and Allnut (1992), "USA: Prediction of Rain Attenuation in Low-Latitude Regions," *ITU-R SG3 Document 92/4*, USA, March 17, 1992.

Dissanayake, A.W., Allnut, J.E., and Fatim Haidara (1997) "A Prediction Model that Combines Rain Attenuation and Other Propagation Impairments Along Earth-Satellite Paths," IEEE Trans. Antennas and Propagation, V 45, No. 10, October 1997.

Drufuca, G. (1974), "Rain attenuation statistics for frequencies above 10 GHz from rain gauge observations," Journal de Recherches Atmospheriques. Vol. 8, n.1-2, pp. 399-441 Jan.-Jun. 1974.

ESA (1994), "Combination of the different attenuation effects," Section 8.4 in Volume 1: *Reference Book on Attenuation Measurement and Prediction, Second Workshop of the OLYMPUS Propagation Experimenters*, ESA WPP-083, p. 136,November 1994.

Feldhake, G. (1997), "Estimating the Attenuation Due to Combined Atmospheric Effects on Modern Earth-Space Paths," IEEE Antennas & Propagation Magazine, pp. 26-34, August 1997.

Flock, W.L. (1979), *Electromagnetics and the Environment: Remote Sensing and Telecommunications*. Englewood Cliffs, NJ: Prentice Hall.

Flock, W.L. (1987), *Propagation Effects on Satellite Systems at Frequencies Below 10 GHz, A Handbook for Satellite Systems Design*, NASA Reference Publication 1108(02), Washington, D.C.

Gray, D.A. (1973), "Earth-Space Path Diversity: Dependence on Base Line Orientation," *1973 G-AP/URSI Meeting*, Boulder, Colorado.

Hadden, J, and E. Villar (1986), "Scattering Induced Microwave Scintillations from Clear Air and Rain on Earth Space Paths and the Influence of Antenna Aperture", IEEE Trans. Antennas Propagation., vol. AP-34, pp.646-657, May 1986.

Hallikainen M. (1884), *Dielectric properties of natural media*, Nordic Research Summer School, Lukeberg, Sweden.

Hanson, W.B. (1965), "Structures of the Ionosphere," in Johnson, F.S. (ed), *Satellite Environment Handbook*, Stanford U. Press.

Ho, H.C. and J.D. Kraus (1957), "A Radio Map of the Sky at 1.2 Meters," Sky and Telescope, Vol 16, pp160-161, February 1957.

Hodge, D.B. (1974), "Path Diversity for Reception of Satellite Signals," Journal de Recherches Atmospherique, Vol. 9, pp. 443.

Hodge, D.B. (1976), "An Empirical Relationship for Path Diversity Gain," IEEE Trans. Ant. Prop. Vol. AP-24, pp. 250.

Hodge, D.B. (1977), Frequency Scaling of Rain Attenuation, IEEE Trans., AP-25, 446-447, May.

Hodge, D.B. (1978), "Path Diversity for Earth-Space Communication Links," Radio Science, Vol. 13, pp. 481.

Hodge, D.B. (1982), "An Improved Model for Diversity Gain on Earth-Science Propagation Paths", Radio Science, Vol. 17, No. 6, pp. 1393-1399.

Hogg, D.C. and Ta-shing Chu (1975) , "The Role of Rain in Satellite Communications," Proc. of the IEEE, Vol. 63, No. 9, pp. 1308-1331, Sept. 1975.

Howell, R.G. et al (1992), Satellite co-polar measurements at BT Laboratories, BT Technology Journal, Vol. 10, No. 4, 34-51.

Ippolito, Louis J. Jr. (1986), *Radiowave Propagation in Satellite Communications*, Van Nostrand Reinhold, New York

Ippolito, Louis J. Jr., (1971), "Effects of precipitation on 15.3 and 31.65 GHz earth-space transmissions with the ATS-V satellite," Proc. of the IEEE, Vol. 59, pp. 189-205, Feb. 1971.

Ishimaru, A. (1977), "Theory and application of wave propagation and scattering in random media," Proc. of the IEEE, vol. 65, no. 7, pp. 1030-1061.

ITU-R (1988), *Handbook on Satellite Communications Fixed Satellite Service*. International Telecommunications Union, Geneva, p. 149.

ITU-R, Rec. P.372-6 (1994), *Radio Noise*, International Telecommunications Union, Geneva.

ITU-R, Rec. P.453-6 (1997): The Radio Refractive Index: Its Formula and Refrectivity Data, International Telecommunications Union, Geneva.

ITU-R, Rec. P.531-4 (1997): Ionospheric Propagation Data and Prediction Methods Required for the Design of Satellite Services and Systems, International Telecommunications Union, Geneva.

ITU-R, Rec. P.581-2 (1997): The Concept of Worst Month, International Telecommunications Union, Geneva.

ITU-R, Rec. P.618-5 (1997): Propagation Data and Prediction Methods Required for the Design of Earth-Space Telecommunications Systems, International Telecommunications Union, Geneva.

ITU-R, Rec. P.676-3 (1997): Attenuation by Atmospheric Gases, International Telecommunications Union, Geneva.

ITU-R, Rec. P.678-1 (1997): Characterization of the Natural Variability of Propagation Phenomena, International Telecommunications Union, Geneva.

ITU-R, Rec. P.680-2 (1997): Propagation Data Required for the Design of Earth-Space Maritime Mobile Telecommunications Systems, International Telecommunications Union, Geneva.

ITU-R, Rec. P.834-2 (1997): Effects of Tropospheric Refraction on Radiowave Propagation, International Telecommunications Union, Geneva.

ITU-R, Rec. P.835-2 (1997): Reference Standard Atmosphere for Gaseous Attenuation, International Telecommunications Union, Geneva.

ITU-R, Rec. P.836-1 (1997): Water Vapour: Surface Density and Total Columnar Content, International Telecommunications Union, Geneva.

ITU-R, Rec. P.837-1 (1997): Water Vapour: Characteristics of Precipitation for Propagation Modeling, International Telecommunications Union, Geneva.

ITU-R, Rec. P.838 (1997): Specific attenuation model for rain for use in prediction methods, International Telecommunications Union, Geneva.

ITU-R, Rec. P.840-2 (1997): Attenuation Due to Clouds and Fog, International Telecommunications Union, Geneva.

ITU-R, Rec. 841 (1997): Conversion of Annual Statistics to Worst Month Statistics, International Telecommunications Union, Geneva.

Jacobs, I.M. (1974), "Practical Applications of Coding," IEEE Trans. Inf. Theory, vol. IT20, May 1974, pp. 305-310.

Johannsen, K.G. and A. Koury (1974), "The Moon as a Source for G/T Measurements," IEEE Trans. Aerospace and Electronic Systems., Vol. AES-10, No. 5, pp. 718-727.

Karasawa, Y., M. Yamada, and J. E. Allnutt (1988), "A New Prediction Method for Tropospheric Scintillation in Satellite Communications", IEEE Trans., **AP-36,** pp. 1608-1614.

Kheirallah, H.N. and R.L. Olsen (1982), Comparison of a One and a Two Frequency Technique for Frequency Scaling of Rain Attenuation Statistics, submitted to Electronics Letters.

Kheirallah, H.N., Knight, J.P., Olsen, R.L., McCormick, K.S., and Segal, B. (1980), "Frequency dependence of effective path length in prediction of rain attenuation statistics," Electronic Letters, Vol. 16, pp. 448-450.

Klobuchar, J.A. (1978), "Ionospheric effects on satellite navigation and air traffic control systems," in *Recent Advances in Radio and Optical Progation for Modern Communication, Navigation, and Detection Systems*, AGARD Proceedings - LS - 93, ISBN 92-835-1280-4. NTIS: Springfield, VA 22161, April 1978.

Koester K. L. and L. H. Kosowsky (1970), "Attenuation of Millimeter Waves in Fog," *Fourteenth Radar Meteorology Conference*, November 17-20, Tuscon, Arizona.

Kraus, J.D. (1986), *Radio Astronomy*, 2nd Edition, Cygnus-Quasar Books.

Kraus, J. D., and K. R. Carver (1973), *Electromagnetics*, 2nd ed., chap. 11, McGraw-Hill, New York.

Laster, Jeff and W.L. Stutzman, (1993), "Attenuation scaling by frequency in the Ku/Ka Bands using the Olympus Satellite," JPL contract 958435 SATCOM Report No. 93-16.

Liebe, H.J. (1985), "An Updated Model for Millimeter Wave Propagation in Moist Air", Radio Science, **20**, pp. 1069-1089.

Liebe, H.J., Hufford, G.A., Cotton, M.G. (1993), Propagation Modeling of Moist Air and Suspended Water/Ice Particles at Frequencies Below 1000 GHz, *AGARD 52nd Specialists' Meeting of the Electromagnetic Wave Propagation Pane*l, Palma De Mallorca, Spain, 17-21 May 1993.

Lin, S.H., H.J. Bergmann, and M.V. Pursley, (1980), "Rain Attenuation on Earth-Satellite Paths-Summary of 10-Year Experiments and Studies," Bell System Technical Journal, Vol. 59, No. 2 (Feb.), pp. 183-228.

Lyons, R.G., (1974) "Combined Effects of Up- and Down-Link Fading Through a Power-Limiting Satellite Repeater," IEEE Trans. Comm., Vol. COM-22, No. 4 (March), pp. 350-352.

Lyons, R.G. (1976), "A Statistical Analysis of Transmit Power Control to Compensate Up- and Down-Link Fading in an FDMA Satellite Communications System," IEEE Trans. Comm., Vol. COM-24, No. 6 (June), pp. 622-636.

Manning, R.M. (1986), A Statistical Rain Attenuation Prediction Model with Application to the Advanced Communication Technology Satellite Project: I - Theoretical Development and Application to Yearly Predictions for Selected Cities in the United States, NASA CR-179498.

Manning, R.M. (1987), A Statistical Rain Attenuation Prediction Model with Application to the Advanced Communication Technology Satellite Project: II - Theoretical Development of a Dynamic Model and Application to Rain Fade Durations and Tolerable Control Delays for Fade Countermeasures, NASA TM-100242.

Maseng, T. and P.M. Bakken (1981), "A Stochastic Dynamic Model of Rain Attenuation," IEEE Trans. Comm., Vol. COM-29, No. 5 (May).

Matricciani, E., (1987), "Orbital Diversity in Resource-Shared Satellite Communication Systems Above 10 GHz," IEEE J. on Selected Areas in Comm., Vol. SAC-5, No. 4, pp. 714-723.

Mayer, C. E, B. E. Jaeger, R. K. Crane, and X. Wang (1997), "Ka-Band Scintillations: Measurements and Model Predictions," Proc. IEEE**,** vol. 85, no. 6, pp. 936-945, June 1997.

Misme, P. and J. Fimbel (1975), Theoretical and experimental determination of the rain attenuation on a propagation path, Annals of Telecommunications, V. 30, 149-158, May-June 1975.

Morrison, J.A., M.J. Cross, and T.S. Chu (1973), "Rain-Induced Differential Attenuation and Differential Phase Shift at Microwave Frequencies," Bell System Tech. J., Vol. 52, No. 4, pp. 599-604.

Nowland, W.L., R.L. Olsen, and I.P. Shkarofsky (1977), "Theoretical Relationship Between Rain Depolarization and Attenuation," Electronics Letters, Vol. 13, No. 22, pp. 676-677.

Oguchi, T. (1977), "Scattering Properties of Pruppacher-and-Pitter Form Raindrops and Cross Polarization Due to Rain: Calculations at 11, 13, 19.3 and 34.8 GHz," Radio Science, Vol. 12, pp. 41-51.

Ortgies, G. (1996), "Ka band Wave Propagation Activities at Deutsche Telecom," *CEPIT IV Meeting Proceedings*, Florence, Italy, September 23, 1996.

Otung, I. E. (1996), "Prediction of tropospheric amplitude scintillation on a satellite link," IEEE Trans. Ant. and Propag., vol. 44, no. 12, Dec. 1996.

Owolabi, I.E. and G.O. Ajayi (1980), Frequency Scaling Technique for Rainfall Attenuation Prediction on Terrestrial Microwave Links, presented *at URSI Commission F Symposium*, Lennoxville, Canada, May 1980.

Pinder, J., J. Feil, L.J. Ippolito and S. Horan (1997), ACTS Propagation Measurements Program, Final Report (Nineteenth Quarterly Report), Contract NAS3-26411, Stanford Telecom, Reston, VA, January 30, 1997.

Poiares Baptista, J. P. V. and P.G. Davies, ed. (1994), *OPEX Reference Book on Attenuation Measurement and Prediction*, vol. 1, Noordwijk, The Netherlands: OPEX, ESA-WPP083, 1994, pp. 49-64.

Pratt, T. et al (1993), Fade duration statistics from the Virginia Tech propagation experiment using the Olympus satellite 12, 20 and 30 GHz beacons, *Proc. of The 20th Meeting of Olympus Propagation Experimenters*, Darmstadt, 224-256

Pruppacher, H.R. and R.L. Pitter (1971), "A Semi-empirical Determination of the Shape of Cloud and Rain Drops," J. Atmos. Science, Vol. 28, pp. 86-94.

Ramachandran, Deepak (1997), "Effect of Water on Antenna Surface." Master of Science Thesis, School of Electrical and Computer Engineering. University of Oklahoma, Norman, OK.

Ray P.S. (1772), "Broadband complex refractive index of ice and water," Appl. Optics, vol. 11, no. 8, pp. 1836-1844.

Ro, C.U. (1973), Rain Attenuation Statistics Across Canada, M.Sc. Thesis, Dept. of Meteorology, McGill University, Montreal, March 1973.

Roddy, Dennis. (1989). *Satellite Communications*, 2nd Edition. Prentice-Hall Inc. Washington D.C.

Rucker, F. (1991), Description of the dynamic behaviour of the Olympus beacon signals by the signal variance and slope, *Proc. of The 15th Meeting of Olympus Propagation Experimenters*, Noordwijk, The Netherlands, 46-69.

Rucker, F. (1993), Frequency and attenuation dependent fade slope statistics, Electronic Letters, Vol. 29, No. 9, 744-746.

Rue, O. (1980), Radiowave Propagation at Frequencies Above 10 GHz. New Formulas for Rain Attenuation, *TELE*, English Edition, V. 32, No. 1, 11-17.

Russell, T, J. Weinfield, C. Pearson, and L. Ippolito (1995), "Modeling Ka-band and Low Elevation Angle Propagation Statistics", *Proceedings of the Nineteenth NASA Propagation Experimenters Meeting (NAPEX XIX)*, Boulder, Colorado, June 14-16, 1995.

Salonen, E, S. Karhu, P.Jokela, W. Zhang, S. Uppala, H. Aulamo, S.Sarkkula, (1990), "Study of Propagation Phenomena for Low Availabilities", Helsinki University of Technology, European Space Agency Contract Report, November 1990.

Salonen, E, S. Karhu, P.Jokela, W. Zhang, S. Uppala, H. Aulamo, S. Sarkkula, J.P. Poiares Baptista (1992), "Modeling and Calculation of Atmospheric Attenuation for Low Fade Margin Satellite Communications," ESA Journal, No. 3, pp. 299-317.

Salonen, E (1993), "Prediction Models of Atmospheric Gases and Clouds for Slant Path Propagation," Olympus Utilization Conference, *Proceedings of International Conference concerning Programme Results, ESA Publication WPP-60*, Sevilla, pp. 615-622, 20-22 April 1993.

Salonen, E., S. Karhu, S. Uppala, R. Hyvöen (1994), "Study of Improved Predictions," Final Report for ESA/ESTEC, Contract 9455/91/NL/LC(SC), December 1994.

Slobin, S.D., (1982), "Microwave Noise Temperature and Attenuation of Clouds: Statistics of These Effects at Various Sites in the United States, Alaska, and Hawaii", Radio Science; Vol. 17, No. 6, pp.1443-1454.

Smith, E.K. (1982), "Centimeter and Millimeter Wave Attenuation Nd Brightness Temperature Due to Atmospheric Oxygen and Water Vapor," Radio Science, Vol. 17, No. 6, pp. 1455-1464, Nov.-Dec. 1982.

Strickland, J.I. (1974), "The measurement of slant path attenuation using radar, radiometers and a satellite beacon," J. Res. Atmos., Vol. 8, pp. 347-358, 1974.

Strohbehn, J.W. (1968), "Line-of-sight propagation through the turbulent atmosphere," Proc. of the IEEE, vol.56, no. 8, pp. 1301-1318, August 1968.

Tatarskii, V. (1971), *The Effect of the Turbulent Atmosphere on Wave Propagation*, U.S. Dept. of Commerce, TT-68-50464, Springfield, Virginia.

Tatarskii, V.I. (1961), *Wave propagation in a turbulent medium*, McGraw-Hill, New York, 1961.

Tsolakis, A. and W. L. Stutzman (1983), Calculation of ice depolarization on satellite radio paths, Radio Science, Vol. 18, 1287-1293.

Van de Kamp, M.M.J.L., J. K. Tervonen, E.T. Salonen (1997), "Study of Low Elevation Angle Scintillation Modeling, Final Report for ESA/ESTEC Contract 10827/94/NL/NB(SC), September 1997

Vander Vorst A., Vasseur H., Vyncke C., Amaya Byrne C., and Vanhoenacker-Janvier D. (1997), "From electromagnetics to system performance: a new method for the error-rate prediction of atmospheric communications links," IEEE J. Selected Areas in Comm., vol. 15, No. 4, May 1997.

Vanhoenacker D. (1987). "Modèle radioélectrique pour la scintillation observée aux hyperfréquences sur les liaisons satellite-terre," Ph.D. Thesis, U.C. Louvain-la-Neuve.

Vanhoenacker D. and Vander Vorst A. (1990), "A multipath model for atmospheric scintillations at microwaves and millimeter waves," Int. J. Infared Millimeter Waves, 1990, V.11, No. 4.

Vanhoenacker D., Vasseur H., Amaya C., and Vander Vorst A. (1993), "Atmospheric model for cloud produced scintillation and evaluation of its impact on communication signals," E.S.A. Purchase Order nr. 113272, Microwave Laboratory, U.C. Louvain-la-Neuve, July 1993.

Vanhoenacker-Janvier D. and Vasseur H. (1995), "Prediction of scintillation effects on satellite communications above 10 GHz," IEE Proc.-Microw. Antennas Propag., Vol. 142. No. 2, April 1995.

Wait, D.F., W.C. Daywitt, M. Kanda and C.K.S. Miller (1974), "A Study of the Measurement of G/T Using Casseopeia A," National Bureau of Standards, Report. No. NBSIR 74-382.

Waters, J.W. (1976), "Absorption and Emissions by Atmospheric Gases," *Methods of Experimental Physics, Vol. 12B, Radio Telescopes*, Ed. M. L. Meeks, Academic Press, New York.

Watson, P.A., and M. Arbabi (1973a), "Rainfall Crosspolarization at Microwave Frequencies," Proc. IEE, Vol. 120, No. 4, pp. 413-418.

Watson, P.A., and M. Arbabi (1973b), "Cross-Polarization Isolation and Discrimination," Electronics Letters, Vol. 9, N. 22, pp. 516-519.

Weinfield, J., and T. Russell (1996), "Scintillation Fade Frequency Estimation", *1996 USNC/URSI Radio Science Meeting*, Baltimore, MD, p. 336.

Wilson, R.W., (1970), "A Three radiometer Path Diversity Experiment," Bell System Technical J., Vol. 49, p. 1239.

Wilson, R.W., and W.L. Mammel (1973), "Results from a Three Radiometer Path Diversity Experiment," *Proceedings of Conference on Propagation of Radio Waves at Frequencies above 10 GHz,* London, p. 23.

Wulfsberg, K.N. (1964), "Apparent Sky Temperatures at Millimeter- Wave Frequencies," Phys. Science Res. Paper No. 38, Air Force Cambridge Res. Lab., No. 64-590.